Emulating the Human Vasculature in a Multi-Organ-Chip Platform

Rheology and Vasculogenesis

vorgelegt von

Dipl.-Ing.

Tobias Hasenberg

geb. in Rostock

von der Fakultät III – Prozesswissenschaften
der Technischen Universität Berlin
zur Erlangung des akademischen Grades

Doktor der Ingenieurwissenschaften
- Dr.-Ing. –

genehmigte Dissertation

Promotionsausschuss:

Vorsitzende: Prof. Dr. Yuri Rappsilber
Gutachter: Prof. Dr. Roland Lauster
Gutachter: Prof. Dr. Peter Neubauer
Gutachter: Prof. Dr. Horst Spielmann

Tag der wissenschaftlichen Aussprache: 3. März 2017

Berlin 2018

All models are wrong;
some models are useful.

- George Box (1978)

Abstract

The Multi-Organ-Chip platform is a microphysiological system developed to evaluate toxicity and efficacy of drugs, and adverse effects of cosmetics, chemicals and alike in a sub-systemic mode. At the scale of a microscope glass slide, it comprises several compartments for the co-cultivation of human 3D tissue constructs. The organoids are physically separated, yet, interconnected through perfused microfluidics. The incorporated on-chip micropump provides pulsatile circulation at a microliter scale – enough to provide oxygen, nutrition and deplete excreted products from the cells. The system contains a minute volume of medium enabling crosstalk and interaction of the organoids. The resulting tissue-to-fluid ratio is more physiological-like than in comparable systems. The organoid cultures are, however, not sufficiently vascularised to overcome limitations in size and complexity. Hence, this dissertation's objective is to contribute to the recreation of a continuous endothelial barrier throughout the system.

For this, three major aspects were addressed: (1) Implementing a near-physiological, pulsatile flow. It should provide an *in vivo*-like shear stress regime, which is required for a phenotypical behaviour of some of the incorporated cell types, specifically the endothelial cells. The complex fluid dynamics created by the micropump were characterised and – where possible – optimised. (2) Creating an endothelial lining within the chip's microfluidic system. A prerequisite already set up in previous works. (3) Establishing capillary-like vessels in the cultivation compartments, preferably interconnected with the endothelialised microfluidics, as a direct route to the organoids. Fibrin hydrogels containing an endothelial / stromal cell co-culture enabled the self-organised formation of microcapillaries. This work will address issues of dynamic *versus* static cultivation environments, the stability of the hydrogel, along with the influence of the medium constituents on the cell behaviour.

The work will show that basic features of blood vessels could be emulated inside the Multi-Organ-Chip platform. A continuous endothelium is crucial for physiological-like interactions, regulation and homeostasis within organoid (co-)cultures as well as for long-term tissue cultivation. Moreover, it is a requirement for replacing medium with a full blood surrogate and to enable immunological queries.

Zusammenfassung

Die Multi-Organ-Chip Plattform ist ein mikrophysiologisches System, welches für die Beurteilung von Toxizität und Wirksamkeit von Medikamenten, sowie von negativen Auswirkungen von Kosmetika, Chemikalien und ähnlichem entwickelt wurde. Auf Größe eines Objektträgers enthält sie mehrere Kompartimente für jedwede subsystemische Co-Kultur dreidimensionaler Gewebekonstrukte. Diese Organoide sind zwar physisch voneinander getrennt, jedoch durch ein mikrofluidisches System strömungstechnisch miteinander verbunden. Die eingebaute *on-chip* Mikropumpe erzeugt eine pulsatile Strömung im Mikroliter-Maßstab – genug, um den Zellen Sauerstoff und Nährstoffe bereitzustellen und ausgeschiedene Produkte abzuführen. Das System verfügt über ein sehr geringes Volumen an Nährmedium und ermöglicht so den Austausch sowie Wechselwirkungen zwischen den Organoiden. Daraus resultiert auch ein Volumenverhältnis von Gewebe zu Medium, das näher an physiologischen Maßstäben liegt als in vergleichbaren Systemen. Die Gewebekonstrukte sind jedoch unzureichend vaskularisiert, um Beschränkungen in Größe und Komplexität zu überwinden. Gegenstand dieser Dissertation soll es daher sein, einen Beitrag zur Nachbildung der endothealen Barriere im gesamten System zu leisten.

Drei Bedingungen müssen dafür erfüllt werden: (1) Ein nahezu physiologischer, pulsatiler Volumenstrom muss zur Verfügung gestellt werden. Dieser soll eine geeignete Schubspannung aufbauen, welche für ein phänotypisches Verhalten der verwendeten Zelltypen – insbesondere der Endothelzellen – erforderlich ist. Die komplexen Strömungsverhältnisse, die die Mikropumpe hervorruft, wurden charakterisiert. Wo es möglich war, fand eine Optimierung statt. (2) Das mikrofluidische System der Plattform muss komplett endothealisiert sein. Eine Voraussetzung die bereits in vorhergehenden Arbeiten erfüllt wurde. (3) Als direkte Route in die Organoide hinein müssen kapillarartige Gefäße in den Kultivierungskompartimenten erzeugt werden, die möglichst mit der Mikrofluidik verbunden sind. Fibrinhydrogele, die eine Co-Kultur aus Endothel- und Stromazellen enthalten, ermöglichten die sich selbst organisierende Bildung von Mikrokapillaren. Diese Arbeit wird sich mit Fragestellungen bezüglich dynamischer *versus* statischer Kulturbedingungen befassen, sowie mit der Stabilität der Hydrogele und dem Einfluss der Medienzusammensetzung auf das Verhalten der Zellen.

Die Dissertation zeigt, dass grundlegende Charakteristika von Blutgefäßen innerhalb der Multi-Organ-Chip Plattform nachgebildet werden konnten. Ein durchgehendes Endothelium ist entscheidend für physiologische Interaktionen, Regulation und Homöostase innerhalb der Organoid(co)kulturen. Zudem ist es essentiell für Langzeitkultivierung der Gewebe. Darüber hinaus stellt es eine Voraussetzung dar, das Nährmedium mit einem Vollblutäquivalent zu ersetzen und immunologische Fragestellungen zu ermöglichen.

Content

List of Figures

List of Tables

Chapter 1

Introduction

1.1. Emulating human biology

With the forthcoming of microphysiological systems (MPS) the scientific community is more than ever committed to initiate a paradigm shift in the assessment of toxicity and efficacy testing (Marx et al., 2016). Essentially, an MPS comprises one or multiple microscopic models of human organs in a microfluidic device for the examination of an applied substance. The idea is to emulate the human biology *in vitro* as accurately as possible. The miniaturisation allows not only the control of physiological parameters but enables high-throughput experiments, too. With these new devices acquisitions of online parameters are possible that are not accessible in corresponding animal models, while still being able to recreate the same systemic interactions of the organs. With the ever-increasing complexity MPS are intended to, eventually, surpass nowadays technologies of animal tests and cell culture techniques in terms of being able to predict a substance's properties in humans – may it be in pharmacology, food, cosmetic and chemical industry, or even environmental science. The MPS created entirely new hopes and expectations. If successful a whole admission apparatus would stand on a completely new foundation. Drug candidates could be rejected earlier in the testing process, hence, reducing overall costs, reducing the risks for probands and consumers, and reducing the unnecessary expenditure of animal lives.

1.2. The MOC at a glance

The Multi-Organ-Chip (MOC) is a platform for perfusion experiments with low medium volumes (Maschmeyer et al., 2015a; Sonntag et al., 2010; Wagner et al., 2013). It is available in different layouts for up to five organs and prospectively even more. The system consists of micro-scale channels connecting an integrated micropump unit with cultivation compartments. The compartments are able to host three-dimensional (3D) tissue constructs. The chips are usually composed of three layers (Fig. 2.01B). The upper part – the adapter plate (AP) – is a bulky polycarbonate plate that provides access holes to the lower layers.

The middle part comprises the microfluidics and the micropump as well as valves. The layer is made of the polymer polydimethylsiloxane (PDMS). It is chemically inert, transparent and elastic. Moreover, it is permeable to oxygen, which – of course – is crucial for the cell survival. The silicon's high flexibility makes it prominent among researchers and developers for lab-on-a-chip devices. It receives, however, disapproval from manufacturers for its inability to be adopted for high-throughput production methods such as injection moulding. Furthermore, some criticise its absorption of low-weight hydrophobic substances, which the author will address later. Nevertheless, PDMS is successfully used in mid-range production scales, allowing even small laboratories to produce functional and leak-proof chips without the need for external contractors.

The bottom part is usually a microscopic glass slide. All layers are tightly sealed with one another creating a closed microfluidic system. No external pumps and medium-carrying

tubings need to be attached, which reduces the medium content considerably while raising the tissue-to-fluid ratio. The perfusion of the system is accomplished within the chip. The micropump consists of three consecutively arranged membranes that are actuated by pneumatic pressure. The perfusion is, then, carried out by the controlled lifting and lowering of the membranes. Valves prohibit backflow and direct the fluid in the desired direction.

1.3. Strategy behind the thesis

This work is split into two main chapters. Each introduces the given topic, elucidates on the methodology and results, as well as discusses the findings and puts them into perspective. Each chapter also concludes with an outlook on further developments.

By means of particle image velocimetry (PIV) it is possible to evaluate the micropump for its rheological properties without interfering with it too much. Particularly the flow rate, as a measure for medium turnover, and the wall shear stress need to be assessed and optimised. Therefore, a set of potentially influential factors must be screened for their impact. With this the work intends to recapitulate physiological relevant strain especially on the incorporated endothelial cells (ECs) and to emulate the *in vivo* situation. Moreover, PIV can be part of a quality management strategy to improve the robustness of chip manufacturing.

Furthermore, a strategy for perfusing not only the endothelialised microfluidics (Schimek et al., 2013) but also *de novo* formed microvessels and subjacent organoids will be presented. For this cell-laden fibrin scaffolds are introduced into the MOC system. The ECs incorporated self-organise into microvascular structures when co-cultivated with adipose-derived stromal cells (ASCs). To eventually emulate the human vasculature, however, distinct changes in the microfluidic design are required and presented later.

Chapter 2

Rheology in the Multi-Organ-Chip

2.1. Introduction – Why we need to know what is happening in the chip

With the rise of *in vitro* 3D cell cultures and the advent of organ-on-a-chip models great attention has been given to external stresses to which cells of the human body are exposed. In fact, external forces were shown to improve the behaviour of some cells *in vitro.* Endothelial cells, for example, react in manifold ways to physiological shear stresses (Ando and Yamamoto, 2009; Barakat and Lieu, 2003). Lung epithelial cells show improved transport capabilities when regularly stretched (Huh et al., 2010). Chondrocytes need not only hypoxic conditions for differentiation (Duval et al., 2012) but also pressure that recapitulates physiological strain on the cells (Elder and Athanasiou, 2009). Tissue engineered heart valves show improved mechanical characteristics that withstand physiological pressures, as soon as the constructs were cultivated with a certain load (Moreira et al., 2016). Further, the stiffness of the cells' substrate influences their route of differentiation (Engler et al., 2006). In a MPS like the MOC there is, thus, a great potential in precisely controling the forces emitted to the cells. Temperature, oxygen partial pressure and flow are key factors that are present and fairly easy to control. The latter transmits shear forces onto cells that are in direct contact with it. While this is a physiological force for some cells (for instance for ECs), it can be harmful to cells that *in vivo* are apart from the volumetric streams (like hepatocytes). Nevertheless, the flow ensures the proper distribution of nutrients and oxygen in the medium and removes excreted products from the cells' proximity. Controlling the flow ensures knowledge about the supply rate of the cells and the forces transmitted to those cells that require it. Both should ideally be in physiological proportions.

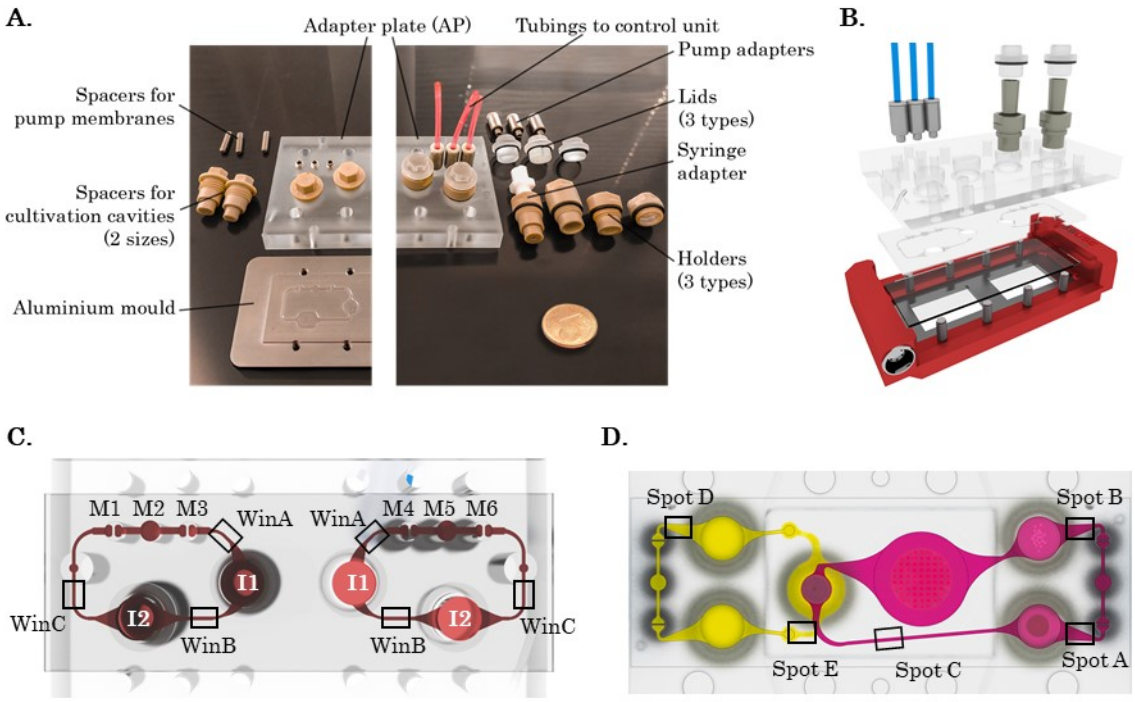

Figure 2.01: The Multi-Organ-Chip system and its components at a glance. (A) On the left side: Parts and assembly for manufacturing a 2OC. The mould imprints the microfluidic channels into the liquid pre-PDMS (further elaborated in the detailed methodology on page 56). On the right side: example of an assembled setup with a selection of inserts. On the bottom of the AP the PDMS layer is bonded to a glass slide. (B) Explosion view of the 2OC's three layers (from top to bottom: AP, PDMS, glass slide). The red holder is an optional heat support for cultivation without an incubator. (C) Footprint of the 2OC with associated regions of interest (ROIs) and labelling of features, such as cultivation compartments (I) and pump membranes (M). (D) Footprint and ROIs of the 4OC.

Different to other organ and human-on-a-chip systems (Imura et al., 2010; Xu et al., 2012; Zhang et al., 2009) the MOC is a closed system with a minute volume (Fig. 2.01). There is no external tubing carrying medium into the system. There are also no external syringe or roller pumps. On one hand, external pumps allow precise control over their output rate. On the other hand, however, they inevitably increase the bulk volume of the medium and – in the case of syr inge pumps – may prohibit recirculating flow.

Instead, the MOC's microfluidic circuit comprises an intrinsic peristaltic micropump (Fig. 2.02A). The pump drives the medium in a pulsatile manner much like the heart (Schimek et al., 2013). Moreover, the tissue-to-fluid ratio is much higher in the MOC than in comparable systems. The enrichment of the medium with the cells' secretome is more accessible and allows actual crosstalk and interaction across several cultivation compartments that line the microfluidic circuit (Fig. 2.01C,D). This is not only closer to physiological conditions. It also enables the investigator to detect the very molecules cell cultures are exchanging and which might be diluted away in other devices (E.-M. Materne et al., 2015). In terms of toxicity and efficacy testing, the superior fluid ratio simplifies the adaptation of compound concentrations for the chip experiments.

However, compared to external pumps the design of the on-chip micropump complicates a direct correlation of simple parameters with the flow rate. A roller pump computes its output

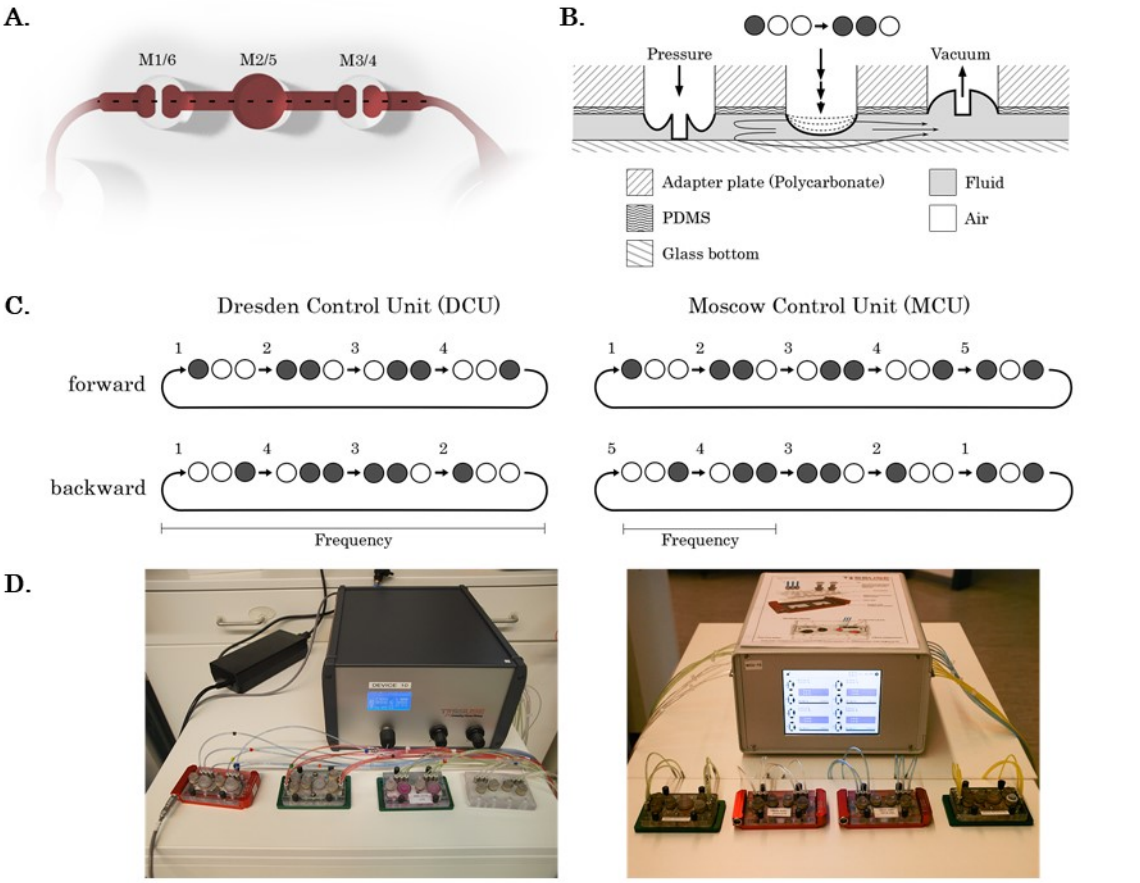

Figure 2.02: Pump cycle of different control units. (A) Footprint of the on-chip micropump. The outmost membranes are considered as valves. The central membrane is the main pumping element. The labelling respects that the two circuits of a 2OC are mirror-inverted. (B) Cross-sectional scheme of the micropump during the second transition. The pressure deflects the membranes towards the glass bottom; vacuum pulls them upwards. The throttling determines with which rate the membranes are actuated. (C) Scheme of the pump cycles in control units of different origin. The first, second and third circle represent the membranes M1/6, M2/5 and M3/4, respectively. Black circles depict lowered membranes; white circles illustrate lifted membranes. Each transition receives a number. It accounts for the actuation of a given membrane in both directions. For example, during transition 2 the membrane M2/5 is lowered in forward direction but raised in backward direction. Each transition has the same duration, which is set by the frequency. The term frequency is defined differently in both control units. The DCU describes it as complete cycle per second; for the MCU it is one transition per second. In this work the former terminology is commonly used. (D) Example pictures of the two different control units with connected chips.

from the angular velocity and the diameter of its head. A syringe pump, similarly, calculates the flow rate from the inner diameter of the incorporated syringe and its feeding rate. The MOC's micropump is, however, controlled by many more factors that may or may not be adjustable. For a scientifically accurate operation it is undeniably important to precisely control its output. For usability reasons the management of all factors should be done by an external control unit so that the operator does not necessarily need to know the underlying working principles.

In summary, information about the flow regime within the MOC is crucial to correlate it with the behaviour of the cells – especially the ECs – and to be able to alter it as well as to

recapitulate the *in vivo* flow dynamics. This part of the presented work is to explain the operation of the micropump, the impact of influential factors, the robustness of the flow within different chips, and implications for future designs.

2.1.1. Working Principle of the micropump

The on-chip micropump of the MOC platform was designed by our co-operation partner, Fraunhofer IWS, according to works published earlier (Wu et al., 2007). In its original form, the pump is a straight channel comprising three consecutive circular cavities with membranes at the top side (Fig. 2.02A). The membranes are aimed to be 500 µm thick. They are intrinsic to the PDMS of which the entire microfluidic system is made. All membranes can deflect either upwards or downwards if vacuum or pressure is applied, respectively (Fig. 2.02B). The medium below the membrane is, thus, either pulled towards or pushed away from the membranes. The middle membrane is the main pumping element. The two peripheral membranes incorporate ridge structures perpendicular to the channel that cut off the flow in either direction. Via tubings each membrane is separately connected to an external control unit and can be triggered independently.

The sequential deflections of the membranes perfuse the medium in the channel into the direction set by the operator (Fig. 2.02C). The three membranes are arranged in series (for the 2OC these are: M1, M2, M3; or in the mirrored circuit M6, M5, M4, respectively). Their coordinated up- and downwards deflection draws the fluid in or pushes it out. The procedure of the pump for a fluid flow from M1 to M3 (i.e. forward) is as follows:

1. Starting from an idle position the first membrane (M1) is lowered while the others are lifted.
2. The middle membrane (M2) now descends. The passage forward is free and is obstructed backwards. The fluid does its greatest leap downstream.
3. While M2 stays lowered, M1 lifts and M3 lowers simultaneously. Because M2 does not obstruct the channel (it does not have a ridge structure), some of the fluid beneath M3 is pushed back, some is pushed forward. Similarly, the fluid beneath M1 is drawn in from upstream of the micropump and some also from downstream.
4. Eventually, also M2 rises to fill the middle cavity again with upstream fluid. Since M3 blocks the channel, there is hardly any movement downstream.
5. The membranes M1 and M3 return to their original positions either simultaneously or successively depending on the manufacturer of the control unit. If the movements happen simultaneously, there is some back-streaming since for a short period all three membranes are in open position. Subsequently, the procedure starts anew.

The sequence and its speed are controlled by the external control unit, which also provides pressure and vacuum (Fig. 2.02D). Depending on the manufacturer from Dresden or Moscow the sequence is either a four-transitions- or five-transitions-cycle. For this work, generally, the control unit from Moscow is utilised. Due to its more approachable relation to the heart rate, the author defines frequency, however, in terms of complete pump cycles per second (i.e. the DCU's definition of frequency).

Another important parameter for pumping is the throttling. Throttles are situated right at the outlets of the control units. They control the amount of volume air entering or exiting the tubing that are connected to the membranes. Eventually, the throttles define the rate with which the membranes deflect into either direction.

No matter if lifting or lowering, each deflection transmits a pulse into the system and onto the cells within. The pulses can be visualised with micro particle image velocimetry (μPIV). Their shape, position and magnitudes are individually characteristic.

2.1.2. Particle Image Velocimetry (PIV) to determine the flow

To access the rheology of a given fluid several physical parameters need to be measured. One of them is the velocity. In bulk fluids, there are several ways to determine the flow rate, for example through turbines, pressure differences or ultrasound to name a few. Most of these techniques are not applicable or too costly in a microfluidic device such as the MOC. Micro particle image velocimetry is a rather inexpensive and versatile way to evaluate the flow velocity. It describes the application of the PIV technology in microfluidic devices. Due to constraints, such as the size, it must be altered.

The main principle behind PIV is the addition of particles to the fluid. The technique goes back to Ludwig Prandtl at the beginning of the 20th century (Raffel et al., 2007). Particles are admixed to visualise the streaming pattern of the fluid. In the beginning this allowed only qualitative descriptions of flows, which, however, laid the foundation for modern fluid mechanics. With adequate computational power digital evaluation of the particle clouds arose in the 1980s and allowed to measure quantitative responses (Westerweel, 1997). To correlate the visualised movement with the flowing liquid the particles should follow the liquid's motion as thoroughly as possible. This is the case for small particles with similar density and hydrophilicity as the fluid. Today, the particles are traced with high-speed cameras. To only record the 2D movement of the particles and prohibit disturbances from planes above and below the focus field, the stream is commonly illuminated with a light sheath only visualising the focal plane. Usually this is done by high-precision laser optics. The recording of the flowing particles can be analysed with arithmetic algorithms that compare the particle clouds in two consecutive pictures. From this a vector field is generated (Raffel et al., 2007). It allows time-resolved estimation of the fluid flow.

2.2. Basic methodology – Analysing the flow behaviour in the MOC

A concise overview of the µPIV analysis is given below. A more detailed methodology can be found in chapter 2.5 on page 56.

2.2.1. Adapting the PIV technology to the MOC format

Micro particle image velocimetry is carried out with a standard inverted microscope on which the MOC is positioned. The numerical aperture of the 2.5x-objective allows a sharp visualisation of the entire height of the microfluidic channels. Instead of a laser sheath the chip is illuminated with an LED light source opposite of the MOC. The particles appear as black spots on a bright background. The particle movement is recorded with a connected high speed camera. Every two consecutive images are analysed to extract information about the displacement of the particle cloud. Reducing the resolution as well as the area of acquisition increases the speed of the camera even more. High acquisition rates are required for the detection of rapid changes of the flow rate. In the chip these occur regularly during each deflection of a membrane. If the flow velocity was steadier, the resolution could be increased on the cost of a reduced acquisition rate. The higher resolution would also prevent the disguise of movement. This occurs if the particle displacement between two images is smaller than the pixel size. The movement would go astray during digitalisation. Eventually, acquisition speed and resolution must be evaluated and adapted for each region of interest (ROI) to determine the balance between spatial and temporal accuracy, amount of data and effort of the overall experimental setup.

In general, µPIV is always an approximation of the fluid behaviour. The better the particles follow and reflect to fluid movement the more accurate is the method. A microfluidic setting, such as the MOC, should comply with following recommendations:

- The particle diameter should lie between 1.7 and 4 pixels (px) (Raffel et al., 2007; Thielicke, 2014). Particles used in this thesis are chosen to be around 5 µm in diameter, which represents approximately the size of erythrocytes. With the given microscopic setup, the particles range between 1.15 to 2 px. Increasing the magnification would increase the digital particle size but – as described earlier – acquisition rate and temporal resolution would be reduced. The chosen size and magnification is a compromise between spatial and temporal resolution.
- The bulk density of the particles should lay between 5 to 20 particles per interrogation window (IW) for particles with a diameter of 3 px (Thielicke, 2014). As a rule of thumb, the optimum in any given IW is reached once the bright image components (i.e. the background) take up the same area as the dark components (i.e. the particles). For the MOC a density of 20 to 35 particles per IW are used. This agrees with the proposed convention as the particles are only about half the size.
- In medium, it is recommended to use particles with a hydrophilic surface and a similar volumetric mass density (Lindken et al., 2009).
- The particle response time should be well below the time between two consecutive images (Lindken et al., 2009). For particles of 5 µm diameter with a similar density to the fluid the response time is approximately 0.0014 ns at 20 °C whereas the time difference is about eight size units above that.

- The microscopic setup determines the depth of correlation (Lindken et al., 2009). This is the depth around the focal plane in which particles contribute to the μPIV calculations. The term is inspired by the depth of field in photography. For the given setup with a 2.5x-objective and a numerical aperture of 0.06 the depth of correlation is 827 μm, which is more than enough for the MOC's channels ranging from 100 to 300 μm height, only. Finding the proper focus is, hence, only of limited concern. Then again, this choice of magnification leads to incorporation of slower and faster particles depending on their height in the channel.

In the MOC platform two types of particles are commonly used. On the one hand, polystyrene (PS) beads with an average diameter of 5 μm are purchased (Thermo Fischer). Their surface is functionalised with aldehyde and sulphate groups. The high density of functional groups provides a hydrophilic character. Hence, adhesion of the particles is reduced especially to the chip's PDMS surfaces. The advantage of these particles is their ease of application especially in cell-free chips. Once biological material (e.g. cells or cell debris) is adsorbed in the chip or the surface of the channel lumen is altered, a subpopulation of the PS particles adheres to it. This can disturb or even preclude the recording.

Erythrocytes, or red blood cells (RBCs), can be used alternatively (Lima et al., 2008; Sugii et al., 2002). RBCs have a diameter like the PS beads. Their physiological surface potential prohibits the adhesion to plastic as well as to any biological material that might be present in the chip. Because the MOCs are envisioned to be perfused with full blood or a blood surrogate in the future, RBCs would be an appropriate tool to measure velocities in ongoing experiments. Thus, quality and stability as well as flow alterations could be evaluated almost online in future chip applications. A disadvantage of RBCs in comparison to PS beads is their rather complicated preparation as well as the more laborious recycling of some of the chip's components.

After the recording, analysing μPIV data is a three-step operation (Fig. 2.03). At first, image raw files are analysed for the displacement of the particle cloud in two consecutive pictures. From this a vector field of the moving particle cloud is generated. Depending on the software from every two pictures generally one vector field can be derived, effectively dividing the amount of data at least in half. The second layer of analysis comprises the data processing. Here, the spatially resolved vectors are averaged and the temporal values are reduced to

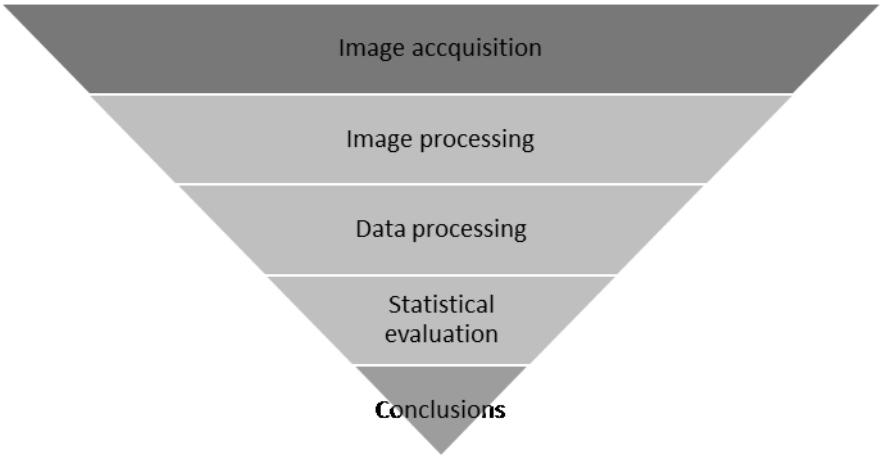

Figure 2.03: Procedure of analysing µPIV data.

general parameters such as flow rate or shear stress at the channel walls. At the very end, statistical analyses are performed that may vary in complexity depending on the scope of the experiment.

During this work a MATLAB (The Mathworks) routine has been programmed that processes the first two steps of the µPIV analysis automatically. For each recording, it summarises the results in an excel file as well as on a data sheet with a test image and key values (Fig. 2.04).

2.2.2. Step 1: images processing

For this work, the open-source toolbox PIVlab for MATLAB is used (Thielicke and Stamhuis, 2014). It was written for a variety of PIV applications and was found suitable for µPIV analysis. It allows the operator to choose from a variety of pre- and post-processing settings. Its precision is extraordinary, even at very low flow magnitudes. The processing time is considerable long, however. Including eventual data extraction, it can take up to 24 hours per recording. The effective processing time can be reduced to 3 hours per recording when analysing eight recordings in parallel. This is facilitated by PIVlab's (or particularly MATLAB's) command line access as well as its multithreading capabilities. Although generally unlimited, one analysis per processor is practicable. The use of this tool is, thus, encouraged especially when computing several recordings.

PIVlab's mode of operation is as follows:

Prior to calculating the particle displacement PIVlab enhances image quality to amplify accuracy. These enhancements are summarised by the term image pre-processing. It comprises several tweaks such as adaptive histogram equalization, intensity capping and Wiener filter for noise reduction, which are explained further in the detailed methodology.

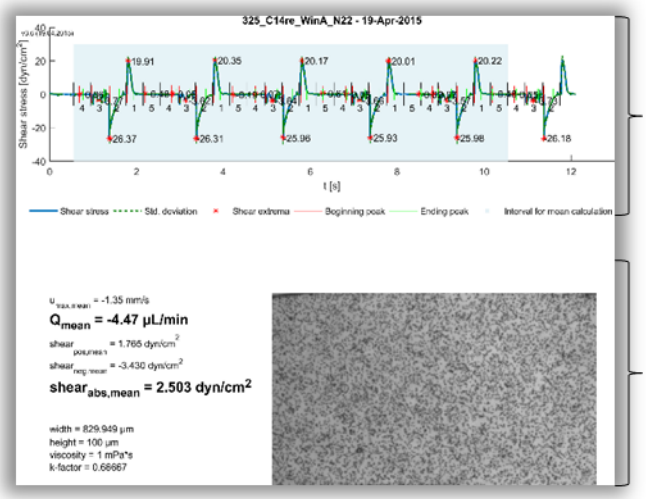

Plot of shear stress (dark blue) and its standard deviation (dark green) over time. The MATLAB routine automatically finds the transitions according to the used control unit as well as the beginning (red) and end (light green) of the peaks and the extrema in each transition.

The spatial and temporal average of the maximum velocity, the average flow rate, the average shear stress in positive and negative direction, as well as the absolute average shear stress within the light blue area are given. Additionally, basic parameters for the calculation are displayed together with an example recording to examine image quality.

Figure 2.04: Example of the output file from the MATLAB routine. Additionally, an Excel-file is created that comprises all data points as well as the entire metadata.

During the actual PIV analysis, the toolbox divides the image into a grid of IWs. The positions of the IWs are constant throughout the image stack. Using cross correlation, the software compares the most probable displacement within an IW and its respective IW in the next image. Cross correlation is a statistical method to find similarities in two signals. Originally, cross correlation was developed in signal processing to retrieve certain patterns in recordings; e.g. to distinguish a distinct word in a voice recording. PIVlab offers two algorithms to solve the correlation – *direct cross correlation* and *discrete Fourier transformation*. As a straight forward approach, the former is regarded as the most accurate but also the slowest computation. The latter is faster but also less precise. By using following provisions PIVlab enhances the discrete Fourier transformation:

- calculation of up to four passes (i.e. repetitions)
- forwarding of the numerical solution of the former pass to the next pass effectively introducing a bias
- refining the grid of IWs (i.e. downsizing the IW dimensions with each pass)

By doing so the vector field has a high spatial resolution, an improved signal-to-noise-ratio and a dynamically adapting velocity interval (Thielicke, 2014). Therefore, discrete Fourier transformation is commonly used throughout the work.

A disadvantage of discrete Fourier transformation is a scenario which results in the misinterpretation of the direction of the velocity. The algorithm, then, interprets the direction of flow just opposite to the actual flow. Its magnitude is also wrong. This happens especially if the flow is too rapid. In this work, such errors occurred especially at the onsets of very fast pulses. Increasing the acquisition rate (by means of reducing the magnification or the dimensional height of the ROI) could resolve the issue.

2.2.3. Step 2: data processing

Analysing linear segments of the microfluidics is least complicated and most accurate. If possible, linear parts are analysed before considering bended or dividing segments. The flow is presumed to be laminar (Busek et al., 2012). The flow, thus, only moves parallel to the channel walls rather than towards them. Due to friction, the flow is slowed down closer to the channel walls. In the two-organ-chip (2OC) the height of the rectangular channels of only 100 µm dominates the flow. Along the Z-axis a parabolic velocity profile establishes (Fig. 2.05C). The maximum velocity develops at the very centre of the channel, half way across the height. In the corresponding XY-plane a plug flow arises – in the central segment of the profile the maximum velocity is constant along the Y-axis and only drops close to the channel wall (Fig. 2.05B).

The movement of particles at different channel heights is not accounted for, here. Although, the discrimination would not be impossible it is certainly technically challenging.

For the data processing – the second part of µPIV analysis – the establishment of a plug flow is exploited: the constant velocity vectors along the Y-axis in the central part of the channel are averaged to derive the maximum velocity. A single velocity vector can be erroneous (especially close to the boundaries). Instead, the average over an adequate amount of data points in the centre greatly enhances the reliability of the data. Therefore, 25 % at the top and the bottom of the vector field are neglected, and the rest is averaged. Due to artefacts at the axial image borders, additionally, three columns of IWs on either side of the images are generally neglected (Fig. 2.05A).

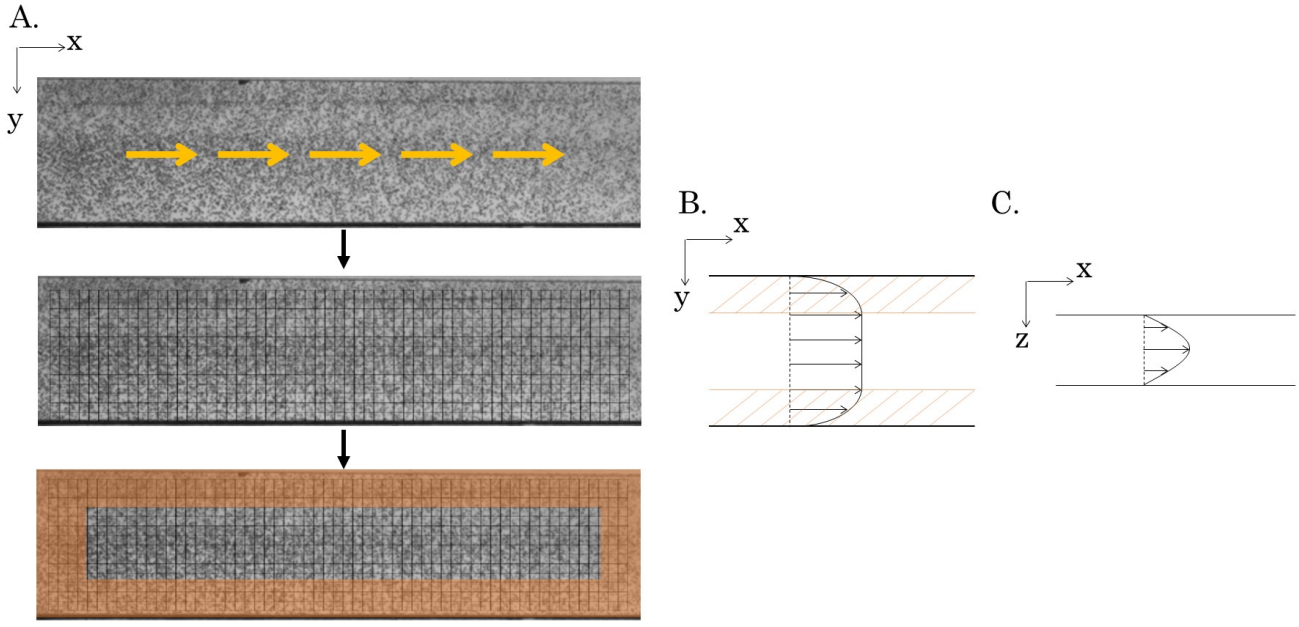

Figure 2.05: Foundation for µPIV measurement in a linear segment of the MOC. The liquid flows from left to right in all illustrations (yellow arrows). (A) Example of a recording of RBCs in a microfluidic channel (viewed from top). The image is segmented into overlapping IWs and particle displacement is calculated for each IW. The orange area highlights IWs that are then neglected during data processing. This area takes up 25 % in the top and bottom part of the image, respectively, as well as three columns of IWs on the left and right side of the image. Thus, only the central part of the plug flow is considered for all following calculations. (B) Presumed velocity profile along the Y axis (plug flow). The channels of the 2OC have a width of 500 or 1000 µm. (C) Presumed velocity profile along the Z axis (parabolic flow). The channels in the 2OC have a height of 100 µm.

The data is first averaged spatially to derive the maximum velocity for each time point. Next, the flow rate and wall shear stress (WSS) are derived. The shear stress-time-plot depicts the forces administrated to the channel walls and to the cells on its surface (usually ECs). The flow rate and WSS are eventually averaged temporally.

As mentioned before, the WSS is of physiological importance. In humans, it can vary heavily depending on the regarded vessel. It ranges from below 1 dyn/cm² (0.1 Pa) to above 70 dyn/cm² (7 Pa) (Kamiya et al., 1984; Papaioannou and Stefanadis, 2005). An average value of 15 dyn/cm² (1.5 Pa) is commonly accepted. *In vivo* measurements are, however, prone to error. The difficulty of determining the WSS emanates from the complexity of measuring the velocity but also varying vessel diameters and motions. Moreover, the simplification of a parabolic volume flow is thought to underestimate the shear stress up to 4-fold (Reneman et al., 2006). Particle image velocimetry improved the temporal and spatial accuracy in the last decade, even though plasma and RBCs might defer slightly in their respective speeds (Sugii et al., 2005; Vennemann et al., 2007).

2.2.4. Step 3: statistical evaluation

Setups that are meant to determine the flow rate require only a simple statistical analysis of the data points. More complex correlations can be found with *Design of Experiments* (DoE). It is a statistical method to screen factors for their effect on the overall process (Barrentine, 1999; Siebertz et al., 2010). Design of Experiments evaluates the responses from the process and determines the most influential factors. For the micropump's motion several factors are regarded worth screening for:

- frequency (i.e. amount of pump cycles per second),
- pressure (i.e. overpressure in the tubing),
- vacuum (i.e. negative pressure in the tubing),
- throttling (i.e. the constraint of the air flow in the tubing),
- direction of pumping (forward or backward),
- length of the tubing (the tube acts like a throttle by delaying the time until a specified pressure "arrives" at the chip's membranes),
- and liquid volume within the chip (as residual gas in the chip dampens the pulse transmission).

Even more external and internal factors are plausible (e.g. temperature, viscosity, materials, chip operator, order in which the lids of the chips are closed, etc.). Their alteration is, however, not feasible or not possible. Additionally, unknown factors might influence the pump's behaviour, too. Nevertheless, the author meant to pick the vital few out of the trivial many factors for the screening.

Instead of altering each factor at a time from a defined standard value, in DoE several factors are changed simultaneously following a defined logic. The pattern is written in matrices where -1 and +1 account for the factor's feasible minima and maxima, respectively, while 0 denominates the median (also known as central point). Other combinations are possible but uncommon. Changing several factors simultaneously not only reduces the amount of experiments to derive conclusions about their influence but also reveals combined effects of

factors. Two single effects might negate or amplify each other, which cannot be perceived in a single-change setup.

The pump cycle can be divided into several transitions according to each membrane deflection. For the MCU these are five transitions (Fig. 2.02C). Each transition has a recurring peak shape in the flow rate-time-plot from which following characteristics can be read:

- the peak maximum
- the peak's width (giving information about whether the pulse from the deflection is complete before the next pulse occurs)
- the peak's area (giving information about the volume of the pulse)

Because these parameters are acquired for every transition they sum up to 15 individual responses after data processing. Additionally, global values (i.e. spatial and temporal averages) are evaluated:

- the flow rate
- the WSS in the main direction
- the WSS against the main direction
- the absolute WSS

Each factor and each interaction produces an effect on each response that can be determined, statistically evaluated, and potentially used in a factorial model for the response. For a given factor the effect is calculated from all experiments where the factor was set to +1 *versus* all experiments where it was set to -1. An example for this can be found in table 2.1 on page 25.

2.3. Results – Flow patterns of the MOC

With the help of μPIV it is possible to recapitulate the deflections of the pump membranes and the cycle pattern with which they are controlled. The following measurements are based on the utilisation of the MCU. At the time, it allowed the precise and simple control of all described factors (in contrast to the DCU). Three ROIs were defined for the 2OC (WinA, WinB, WinC) and five ROIs for the 4OC (SpotA, SpotB, SpotC, SpotD, Spot E; compare to Fig. 2.01C,D).

2.3.1. Correlating membrane deflections with velocity peaks

One procedure during data processing is the reassignment of characteristic peaks to its respective membrane movement. In "normal" PIV this is commonly done with the help of a trigger that connects distinct time points of the actual flow with the flow graph. For the 2OC a trigger could, for example, start a measurement with the beginning of a pump cycle at transition 1. However, triggering was not possible in this work. A method based on pattern recognition via cross correlation was introduced instead. For this, a purely theoretical peak shape and its sequence was presumed for each ROI (Fig. 2.06A). If these patterns were recognised in the measurements (Fig. 2.06B) the peaks could be assigned to individual transitions.

If the sequence of the peak pattern deviated from the prediction it allowed conclusions about the chip's state. Using again the example of a circuit on the left side of the 2OC that is pumped backwards (i.e. anticlockwise): The shear stress-graph of the ROI WinA should not show notable flow in the fourth and fifth transition. The downward deflection of the rightmost membrane (M3) in this transition prohibits flow upstream of the pumping direction. If the measurement in WinA, however, indicates flow (Fig. 2.06A, grey peaks) it can be assumed that the pressure on M3 was insufficient to close this valve properly. It could also indicate the occurrence of bypasses around the membrane due to imperfect bonding. Similarly, if peaks occur in the first and second transition of WinC, the flow under or around the leftmost membrane (M1) is not prohibited. In both cases, these occurrences denote an inefficiency in pumping: The respective peaks in transition 2 (WinC) and 4 (WinA) are opposed to the main direction of flow.

2.3.2. Fundamental observations

Furthermore, following observations for the 2OC can be drawn from the shear stress-graphs:

- The circuit of the 2OC is not symmetrical. Reversing the direction of pumping influences the shape of the profile. This is especially true for the width of the peaks as revealed by DoE analysis later.
- If pumped by the MCU, two constitutional changes occur simultaneously in transition 3 visualised by a double peak of opposing directions in the time plot of WinA and WinC. With respect to the former example, that is caused by the concurrent lowering of M1 and lifting of M3. For the DCU, such peaks are similarly observable in transition 1 and 3.

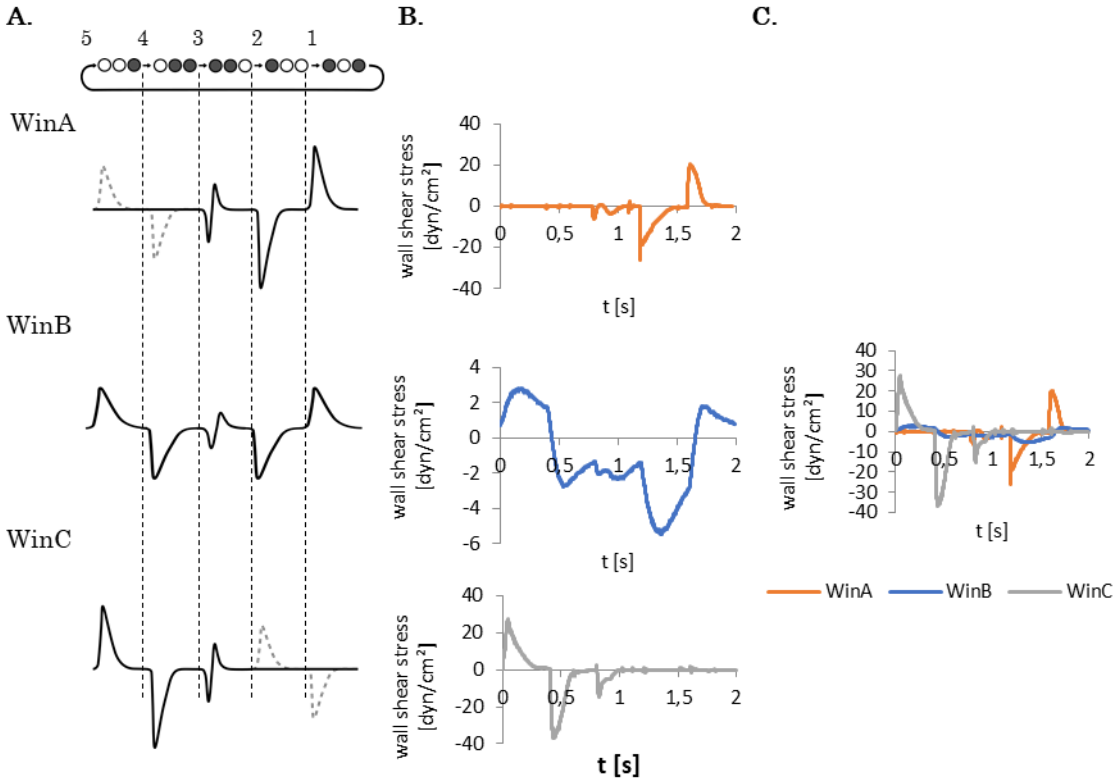

Figure 2.06: Principle of retrieving membrane deflections in µPIV data. (A) Purely theoretical comprehension of the pattern caused by the pump's membrane deflections illustrated by the time-resolved peak evolution in the µPIV data. It can be represented either by the linear velocity or its derivatives flow rate and WSS. The pumping direction of this example is backward, which is why the numbering is backwards, too (compare to Fig. 2.02C). Positive peaks are, thus, regarded as opposed to the main flow direction. Ideally, the peaks of WinA and WinC only overlap in the third transition. Grey dotted peaks may be produced if the pump's valves close insufficiently (see text for further detail). In these cases, the peaks from WinA and WinC may be opposed. (B) The patterns can be retrieved in the measurements. The peaks are correlated to distinct deflections without using external triggers. It turns out that the peak of transition 3 in WinB commonly has the same direction as the main flow. (C) Merge of the plots from B emphasising the dampening capacity of the cultivation compartments. Flow rate and WSS are on average 80 to 90 % lower in WinB.
Metadata: 2OC right circuit, particles: PS beads 20 % w/v, pumping direction: backward, frequency: 0.5 Hz, pressure: +47.5 kPa, vacuum: -40 kPa, throttling: 0.6 L/min @ +35 kPa, length of tubing: 2 m, objective: 2,5x, subsampling, max. acquisition rate: 1,858.736 fps.

- In the 2OC, WinA usually shows the highest velocities. This is because the section between M3 and the cultivation compartment is the shortest and widest of the microfluidic. Thus, the friction is low.
- However, the highest maximum shear stresses are measured in WinC. The section is less wide than WinA. Due to its influence (depicted in the detailed methodology in equation 2.12 on page 60) the WSS is elevated.
- The cultivation cavities act as phase dampeners. The strength of the pulses in WinB are reduced by five- to ten-fold compared to the respective pulses in WinA or WinC. This is due to the volume of air above the liquid in the cultivation cavities that is compressible and, thus, slows down the pulse. This is particularly obvious in the ROI SpotC of the 4OC, where the pulsatile flow gets dampened away by the adjacent

compartments. The circuitry of the 4OC comprises four linearly connected compartments instead of just two. One of them is exceptionally big.

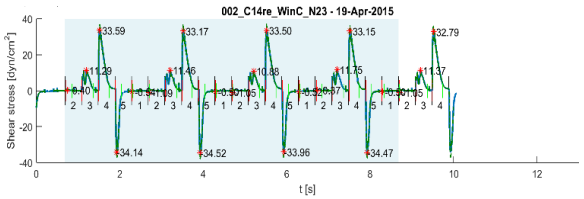

The ideal plot. The pump's valves close perfectly. The MATLAB routine finds all transitions correctly. In each transition, it finds the correct peak, pulse width and pulse area. 84 % of the image stacks are automatically processed with no or minor errors.
Metadata: 2OC right, WinC, forward, 0.5 Hz, +47.5 kPa, -40 kPa, 0.6 L/min @ +35 kPa, max. 2,732.24 fps.

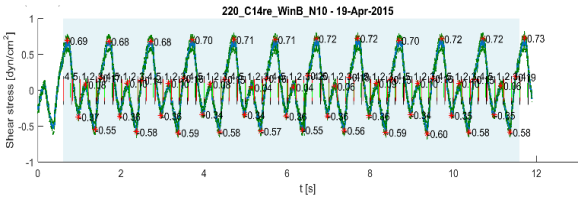

In this plot, only three of five peaks are found. Assigning the corresponding transition to the peak correctly is difficult for the routine. Therefore, solely global data (extrema, flow rate, average shear stress) are valid.
Metadata: 2OC right, WinB, forward, 1 Hz, +10 kPa, -70 kPa, 0.9 L/min @ +35 kPa, max. 2,732.24 fps.

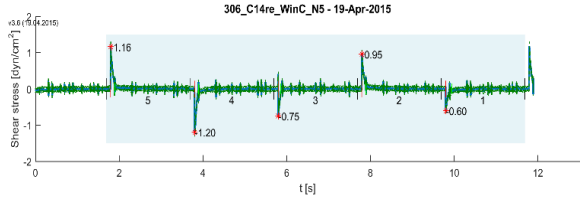

Example for poorly closed valve M6. Due to insufficient pressure peaks are visible in the first and second transition. The standard deviation appears bigger due to the small scaling.
Metadata: 2OC right, WinC, backward, 0.1 Hz, +10 kPa, -10 kPa, 0.3 L/min @ +35 kPa, max. 2,732.24 fps.

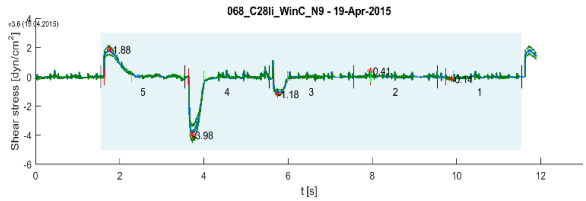

Even at very low pressure the valve M1 closes properly in this example. This property varies from chip to chip, but is also dependents on the main pumping direction.
Metadata: 2OC left, WinC, backward, 0.1 Hz, +10 kPa, -70 kPa, 0.9 L/min @ +35 kPa, max. 2,732.24 fps.

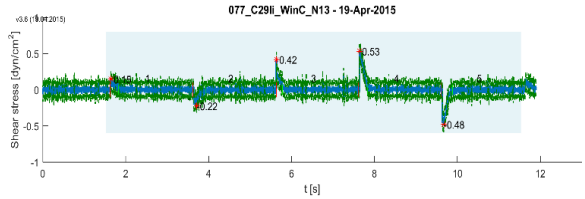

A rare case: the particle density is too low for a precise analysis. The flow is too low to prohibit settling of the particles in the big cultivation cavities. By shaking the chip before each measurement an even dispersion is pursued.
Metadata: 2OC left, WinC, forward, 0.1 Hz, +10 kPa, -10 kPa, 0.9 L/min @ +35 kPa, max. 2,732.24 fps.

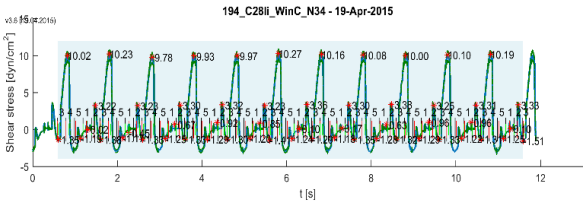

Complete failure of the MATLAB routine. The minima are not found, the width of the peaks as well as the beginning and end of the transitions are wrongly interpreted. 4 % of all processings contain non-evaluable responses. This example is an extreme, however.
Metadata: 2OC left, WinC, forward, 1 Hz, +25 kPa, -70 kPa, 0.9 L/min @ +35 kPa, max. 2,732.24 fps.

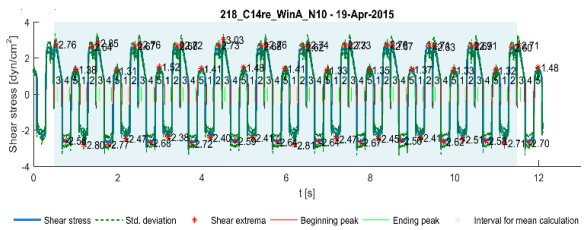

Due to low throttling, very steep peaks emerge. Nonetheless, the processing is almost flawless.
Metadata: 2OC right, WinA, forward, 1 Hz, +10 kPa, -70 kPa, 0.9 L/min @ +35 kPa, max. 1,858.736 fps.

Figure 2.07: Good and bad examples of µPIV data processing with PIVlab.
Metadata for all trials: PS beads 20 % w/v, 2 m tubing, 2,5x, subsampling

2.3.3. Screening factors for their impact on flow behaviour with the help of DoE

In all experimental designs of this work, the term *factor* describes the controllable variables, which are coded by the letters A to G. The output values are called *responses*. In a predefined manner, the factors' limits are combined to determine the influence of each factor. In DoE terminology, the limits are encoded with -1 and +1 describing the bottom and top limits of each factor. One combination of such limits is given a unique identification number – the design ID (a list of the design IDs and their settings can be found in the detailed methodology in the tables 2.6 on page 62 and 2.8 on page 64).

A total of two experimental designs has been created to characterise the 2OC. The first screening examines the parameters defined on page 13 for their influence and the robustness of the measurements. At the time point of the measurement the data processing was not able to distinguish extrema by their respective transition. Instead, the cycle-wide maxima and minima are evaluated. Moreover, the velocity information is not transformed into the flow rate and WSS. This does not affect the conclusions drawn from the Pareto charts. However, the comparability of the ROIs suffers. In the first screening, only main effects without interactions are examined.

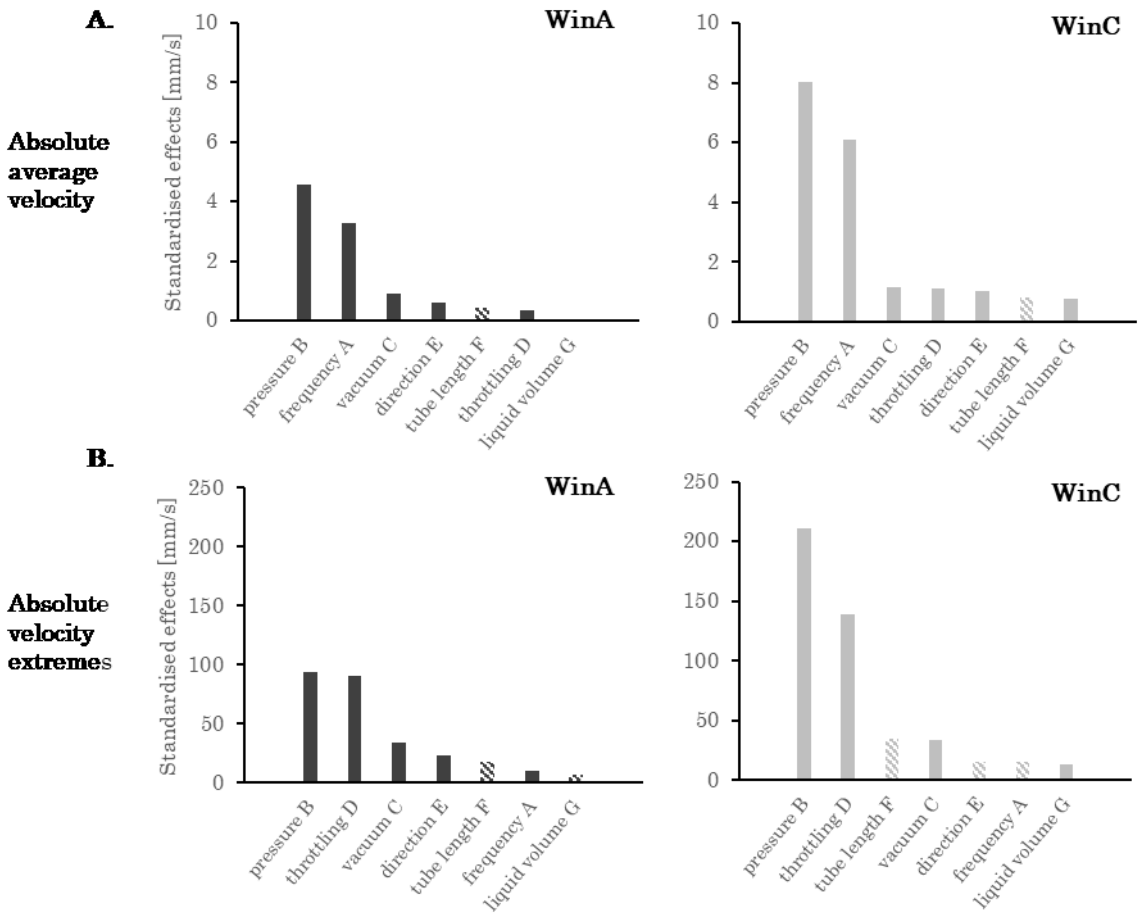

Figure 2.08: Pareto charts of the main effects in WinA and WinC of the first DoE screening. The responses for the absolute average velocity (A) and the absolute velocity extremes (B) are shown. The comparability of the two ROIs suffers from the illustration of the linear velocity rather than a more standardised parameter like flow rate or WSS. Dashed bars denote negative effects. Please note: Negative effects refer to a reciprocal relation between factor and response NOT to a rating.

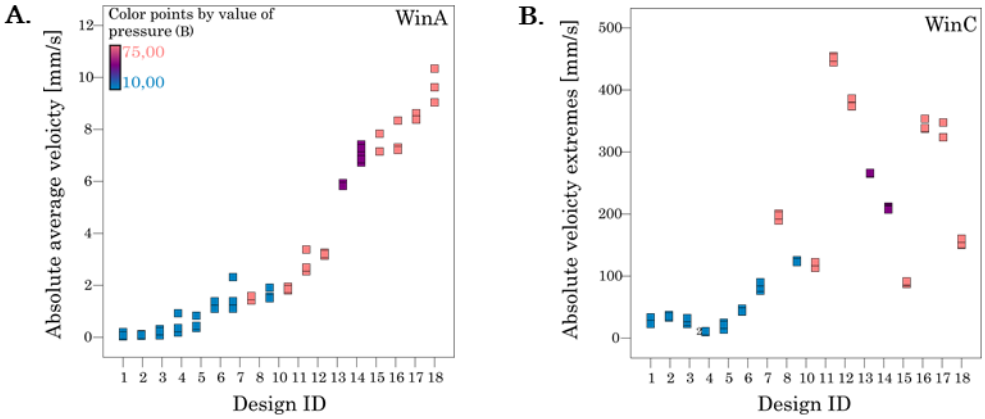

Figure 2.09: Replicability of responses from the first screening. (A) An exemplary depiction of the reproducibility of the average velocity in WinA. (B) The magnitude of the velocity extremes in WinC. Each combination of factor limits gets a unique design ID that is technically replicated three times. The design IDs are ordered after the experiments by the magnitude of the absolute average velocity to have an impression of the influence of the factor pressure on that response. The colouring of the squares is representative of the applied pressure.

Regarding the absolute average velocity significant effects can be found for the pressure (B) and the frequency (A). Their impact is more pronounced than the other factors' effects (Fig. 2.08A). No significant impact on the absolute average velocity is found for the throttling (D), the direction of pumping (E), the length of the tubing (F), and the liquid volume in the chip (G). Here, only the modulus of the values is analysed rather than the qualified velocities – with other words the actual direction of the flowing medium is not specially considered. This is to exclude the directional influence that would otherwise disguise the other effects. Interactions are not considered.

The modulus of the velocity extreme (Fig. 2.08B) is dependent on the pressure (B), too, as well as on the throttling (D). Whether the vacuum (C) influences the extremes cannot be concluded with certainty. In WinA the direction of pumping (E) and in WinC the length of the tubing (F) might have an impact. The frequency (A) and the liquid volume (G) are always insignificant for the extremes.

In conclusion, effects arising from the liquid volume are viewed as negligible for both responses – at least within the margins chosen for this screening (300 to 600 µL). Additionally, while the effect of the length of the tubing is not highly influential and its adaptation is rather difficult in an everyday setting it is excluded from the following experiments as well. The other factors are kept for the second round of DoE-screening.

The reproducibility of the measurements within the same chip is considerably high (Fig. 2.09), which conveys a high trust in the overall µPIV assessment. The variability between chips is not investigated, here. Moreover, whether the factors interact with one another is not explored in the scope of the first screening. Furthermore, influences of wearing

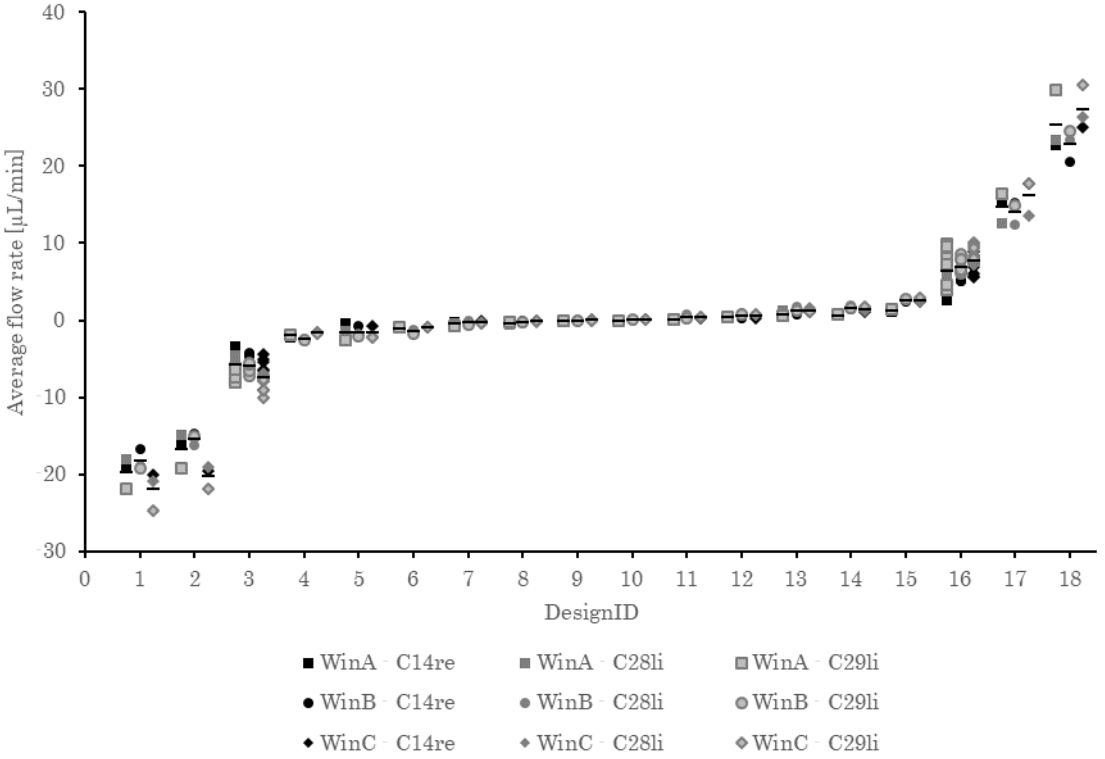

Figure 2.10: Reproducibility of measuring the average flow rate in the second screening. Each set of adjusted factors gets a unique design ID that is not replicated (except for the central points – design IDs 3 and 16) but reproduced in three different chips (C14re, C28li, C29li). The design IDs are ordered after the experiments by the average flow rate. In the closed circuitry of the chip the value should be equal in all ROIs. Differences can, however, occur and are discussed later. The different chips show deviations from another. The correlation value never exceeds 14 % for higher magnitudes, however.

are not regarded, which is part of a student research project discussed later. For the DoE-screenings it is, however, of no impact as it is stable over the course of a µPIV trial, which is usually shorter than five days.

2.3.4. Controlling the flow rate

The second DoE-screening checks the robustness among the chips and potential interactions between the main factors found in the first screening. The length of the tubing and the volume within the chip is not regarded separately anymore. During this work the data processing has been improved, which allows to evaluate much more responses. For example, it is possible to retrieve all information about velocity, pulse size, volume, and direction and to allocate these to specific pump transitions.

The average flow rate (that is proportional to the linear velocity from the first screening) can be assessed in all three ROIs with considerable accuracy. Regarding the average over three chips (C14re, C28li, C29li) it can be controlled from 19.98 ± 1.84 µL/min in backward direction and up to 25.20 ± 2.29 µL/min in forward direction.

The measurements are within an acceptable margin of error (Fig. 2.10). With higher flow rates deviations are recognisable. The correlation value never exceeds 14 % in high regions,

however. In other words, the standard deviation of the measured values has a magnitude of 14 % of the average value. Higher variances are mainly caused when frequency and pressure are set to their high limits. Taken all together the reproducibility over the course of the µPIV trial is not good but satisfactory.

If – in contrast to the first screening – not the absolute of the values but the qualified data is evaluated, the Pareto chart of effects shows a completely different pattern (Fig. 2.11). Additionally, factor interactions can be accessed. This is especially important for the main direction of pumping (E). It essentially determines the prefix of all values. The average effect of the set main direction is 14.88 ± 1.49 µL/min. This means that by just switching the direction, the flow rate will be altered on average by this magnitude. It predominates almost all other factors.

If, now, the frequency (A) or the pressure (B) are examined individually, they are found insignificant, which would not agree with the first screening. The reason for this is that the factors' positive and negative responses eliminate themselves when averaged. The impacts of the frequency and pressure only become clear by observing their *interactions* with the direction (AE and BE, respectively). For the flow rate following effects are clearly significant and, therefore, in agreement with the first screening: the direction of pumping (E), the pressure (BE) and the frequency (AE). Additionally – and this is new – the interaction of vacuum and throttling (CD) appears to have an effect.

Depending on the monitored ROI the vacuum (CE), the throttling (DE), the interaction of frequency or pressure with the throttling (AD and BD, respectively), as well as pressure and vacuum (BC) are alternating around the Bonferroni limit. Values surpassing this limit are regarded highly significant for the flow rate. Hence, CE and AD are included into the

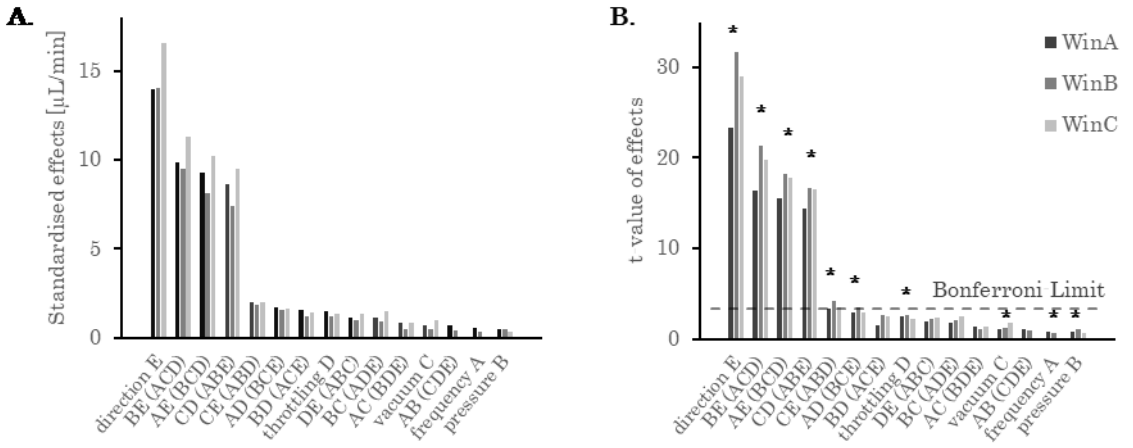

Figure 2.11: Pareto charts of the effects of main factors and their interactions on the average flow rate. (A) The Pareto chart shows the standardised effects that correlate with the model's coefficients for the respective factor. There are no negative effects. (B) The chart depicts the effects' t-values, which account for experimental errors. Furthermore, it allows to identify effects for modelling. Factors or interactions are chosen for the model, if they exceed the rather conservative Bonferroni limit ($p = 0.05 / 15$, $df = 71$). Chosen model terms are identified by an asterisk. The hierarchy rule for defining a model is applied leading to the incorporation of insignificant factors into the model (see text). Three-factor-interactions are not discovered. Some might be confounded by two-factor-interactions, however (parenthesis).

modelling. The significant factors chosen in figure 2.11 together with the corresponding main factors create a model with following factorial equation:

$$Q = 0.23 + 0.14 \cdot A + 0.22 \cdot B + 0.37 \cdot C + 0.67 \cdot D + 5.7 \cdot E$$
$$+0.83 \cdot A \cdot D + 4.61 \cdot A \cdot E + 5.06 \cdot B \cdot E + 4.26 \cdot C \cdot D + 0.98 \cdot C \cdot E \qquad (2.1)$$

To solve the equation for any setting the factors must be inserted in their encoded form, which can be found in table 2.7 on page 63. The coefficients derive from the average effects and represent the impact of the factor or interaction – the higher the coefficient, the higher the impact of the respective factor on the flow rate. Although they are mostly insignificant, main factors must be included into the equation due to the hierarchy rule for defining a model: For any involved interaction, every containing single factor and interaction must be included into the model as well. For example, to incorporate the two-factor-interaction CD, additionally the factors C and D must be considered although they are found insignificant.

The model can be plotted (Fig. 2.12A,B). Flow rates between -20.0 and 25.2 µL/min are adjustable. The analysis of variances (ANOVA) implies significance of the model ($p<0.0001$). Among others, correlation coefficients ($R^2=0.9844$) and signal to noise ratio (Adeq. Precision=50.4) indicate good prediction of the model. This is underlined by the residual plot (Fig. 2.12C). Moreover, the *Lack of Fit* is insignificant. Still, its insignificance is marginal and the model's linearity should be questioned: according to the *Lack of Fit*'s p-value there is only a chance of 5.86 % that the model is actually fitting. Likewise, the model fails to predict correctly at its limits. For example, at pressures below 30 kPa in combination with frequencies below 0.4 Hz the model predicts a low flow rate that is opposing to the set flow direction. The actual flow is very close to zero for such settings.

Three-factor-interactions are not found significant for the model. It should be noted, however, that all two-factor-interactions are confounding the interactions of the corresponding three uninvolved factors (AB aliases CDE, BC aliases ADE and so on). Three-factor-interactions are usually regarded as unlikely by statisticians. In this setting, they are not completely unimaginable, however. For example, the pressure might interact with the vacuum and the throttling (BCD): pressure and vacuum define the magnitude of pressure difference in the

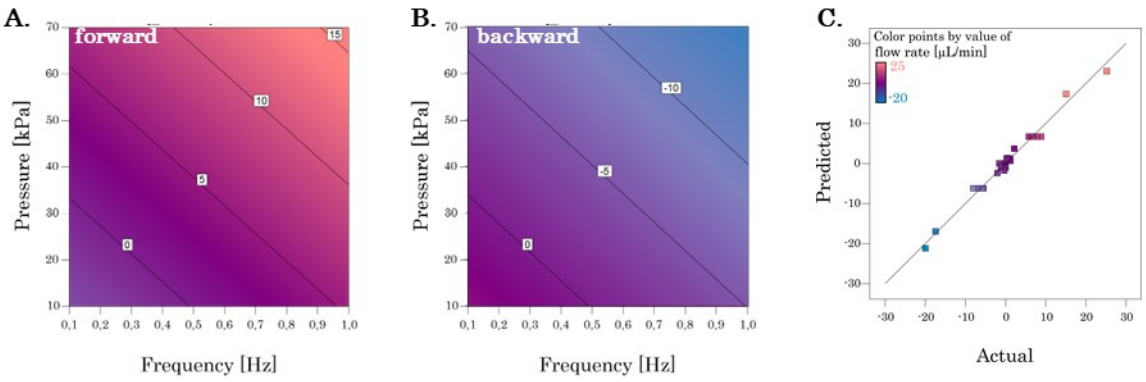

Figure 2.12: Modelling the average flow rate. Predicted flow rate if set to forward (A) and backward pumping (B). The plots are based on equation 2.1. The remaining factors are set to their respective central points (Tbl. 2.7). Especially at its lower limits (bottom left in both graphs) the model falsely predicts flow in opposing direction. (C) The residual plot depicts the deviation between predicted and measured flow rate.

tubing and the throttling determines the rate with which the pressure changes in the moment the con trol unit switches between to the two states. However, if the interaction BCD existed, it would not be recognised as it is disguised by the interaction AE. Then, the effect attributed to AE could in fact partially or completely emanate from BCD. Similarly, the interaction of pressure, vacuum and direction (BCE) could be confounded by the interaction of frequency and throttling (AD). The same is true for frequency, pressure and direction (ABE), which might be masked by vacuum and throttling (CD). Other three-factor-interactions are less likely or the aliasing two-factor-interaction is already insignificant. One way to resolve this dilemma at least for all interactions comprising the factor E is to exclude the main direction from all interactions.

In accordance with the first screening, using the absolute flow rate effectively removes the influence of the main direction from all interactions as it predominantly controls the values' prefixes. Different to what the model predicted, it never occurred that the flow is turned around by other factors than the set main direction. This observation allows the further proceeding. The absolute values (rather than the qualified values) simplify the analysis and the interpretation of the model considerably. They basically remove the factor E from all interactions – AE becomes A, BCE becomes BC and so on. The simplification also permits to account for the higher deviations at higher flow rates, which lead to an unbalanced distribution of the model's residuals. Transforming the data with the square root leads to a more homogeneous distribution. Furthermore, due to their relative concordance the data of all chips and all ROIs is averaged. This mostly affects the relativity towards the Bonferroni and t-value limits. The effects' t-values are substantially reduced.

The adapted Pareto chart (Fig. 2.13A) now reveals that the original interaction of vacuum and throttling (CD) is aliasing the interaction of frequency and pressure (AB, beforehand ABE). Due to averaging the impact of the vacuum (C) and the interaction of frequency and throttle (AD) are diminished. The direction of pumping (E) is found to have no significant role anymore.

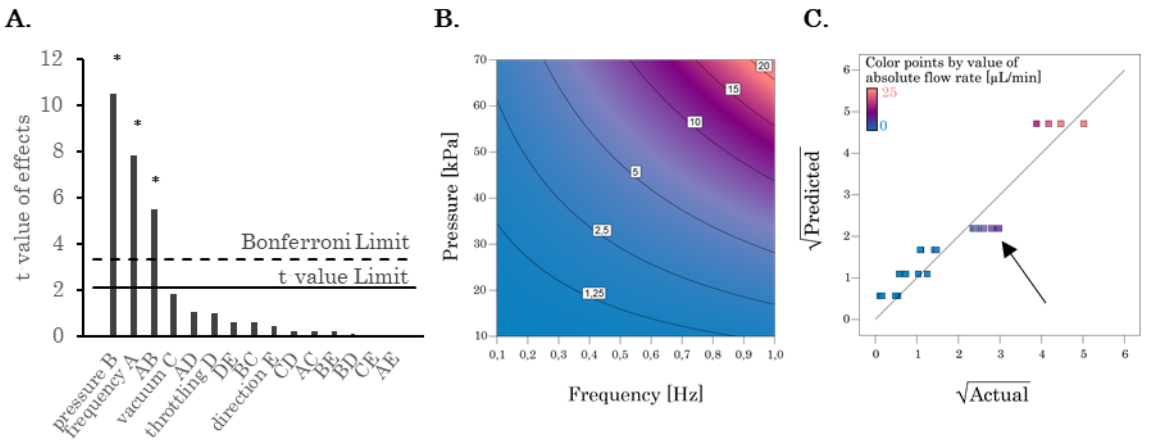

Figure 2.13: Analysis of the absolute average flow rate across all chips and ROIs. (A) Pareto chart of effects' t-values regarding the averaged absolute velocity. The models' terms are transformed with the square root to homogenise the distribution of residuals in the derived model. Dashed bars denote negative effects. Model terms are identified by an asterisk. (B) Predicted absolute flow rate regardless of the pumping direction. The model is based on equation 2.2. The remaining factors are set to their respective central points (Tbl. 2.7). (C) Residual plot of predicted vs. measured flow rate. The central points are presumably introducing unaccounted curvature into the model (arrow).

In concordance with the previous results, the pressure (B) and the frequency (A) influence the flow rate the most. Both show positive effects, which relates to an increase of the flow rate, if they are set to their positive limits. Their interaction (AB) has a significant positive effect, too. The interpretation of what causes this interaction is not trivial. Most likely this is due to the interference of high frequency with the complete development of pulses. A pulse emanates from the deflection of a specific membrane as explained before. If at a higher frequency the next deflection follows before the former finished, it might influence the overall output depending on the flow direction of each of the pulses.

It must be pointed out, again, that for all remaining two-factor-interactions confounding could still be an issue. Due to the predefined experimental design, main factors are not confounding. The likelihood of aliasing three-factor-interactions is, however, considered obsolete if not too many two-factors and main factors surface. Hence, the consideration of three-factor-interactions is not necessary, here.

The model derived from the remaining factors and interaction together with the transformation is resembled by following equation:

$$Q = E \cdot (2.01 + 0.89 \cdot A + 1.18 \cdot B + 0.63 \cdot A \cdot B)^2 \tag{2.2}$$

The set main direction (E) only influences the prefix. Evidently, the model has a very different appearance than the more complex version before. The expression is more concise and comprehensible. The model is significant ($p<0.0001$), the correlation coefficients are in reasonable agreement ($R^2=0.8928$), the random noise can be neglected (Adeq. Precision=24.05). The Lack of Fit is, however, significant ($p<0.001$). This is likely due to the curvature introduced by the central points. Still, the model is considered relatively accurate (Fig. 2.13B,C). More data regarding the inferential statistics of any model shown in this report can be found in the appendix starting at page 125.

Table 2.1: Ratio of the WSS extreme *against* vs. *in* direction of pumping. This table is intended as a replacement of an equivalent Pareto chart to illustrate the calculation and meaning of effects. The shown values are the average ± standard deviation of the factors at their respective limit. The standard deviation appears high. As it comprises all design IDs, it does not consider the alteration of other factors. Asterisks mark effects that are found significant. The standardised effects are computed by DesignExpert® and may deviate from the pure difference of top and bottom limits.

	WinA	WinB	WinC
average	79 ± 21 %	56 ± 24 %	72 ± 24 %
effect of frequency (A)			
1 Hz (+1)	67 ± 24 %	38 ± 25 %	66 ± 29 %
0.1 Hz (-1)	− 85 ± 27 %	− 74 ± 25 %	79 ± 27 %
standardised effect	-19 % *	-37 % *	-13 % *
effect of pressure (B)			
70 kPa (+1)	66 ± 30 %	37 ± 20 %	64 ± 32 %
10 kPa (-1)	− 87 ± 19 %	− 75 ± 28 %	− 82 ± 21 %
standardised effect	-19 % *	-38 % *	-18 % *
effect of pumping direction (E)			
forward (+1)	70 ± 16 %	58 ± 19 %	84 ± 21 %
backward (-1)	− 88 ± 22 %	− 54 ± 28 %	− 60 ± 22 %
standardised effect	-23 % *	+6 %	+29 % *
interactional effect of frequency and direction (AE)			
+1	89 ± 27 %	66 ± 35 %	59 ± 22 %
-1	− 64 ± 21 %	− 46 ± 24 %	− 86 ± 27 %
standardised effect	+24 % *	+20 % *	-28 % *
Additional effects found significant	BD (+17 %)	CD (+14 %)	BC (-23 %), DE (+22 %)

2.3.5. Controlling the maximum shear stress

The detailed data processing allows to analyse the impact of every single membrane deflection of the five-part pumping cycle of the MCU. Most importantly, the magnitude of shearing applied to the cells on the channel walls can be estimated. The WSS is dependent on the flow rate, the dimensions of the channel and the viscosity of the fluid as is explained in the detailed methodology. Due to the unsteady flow in the chip, there is also a dependency on the time point within the pumping cycle and the position in the chip. The channels close to the pump (i.e. the ROIs WinA and WinC) show WSS extrema approximately from 2- up to 25-fold above the simultaneous shear stresses in more distant regions (WinB). Besides the average WSS, for some experimenters the maximum WSS is of importance. Therefore, not every transition's WSS extreme is evaluated separately but the global minima and maxima. With respect to the set main pumping direction, these are recognised as extreme in and against the main direction of flow depending on their prefix. For example, if set to forward direction (which is clockwise pumping for a circuit on the left side of the 2OC) a positive peak is regarded as a pulse in the direction of flow and *vice versa*. If set to backward, a positive peak would represent a pulse against the main direction. Due to the nature of the micropump, a pump cycle will almost always contain positive and negative pulses.

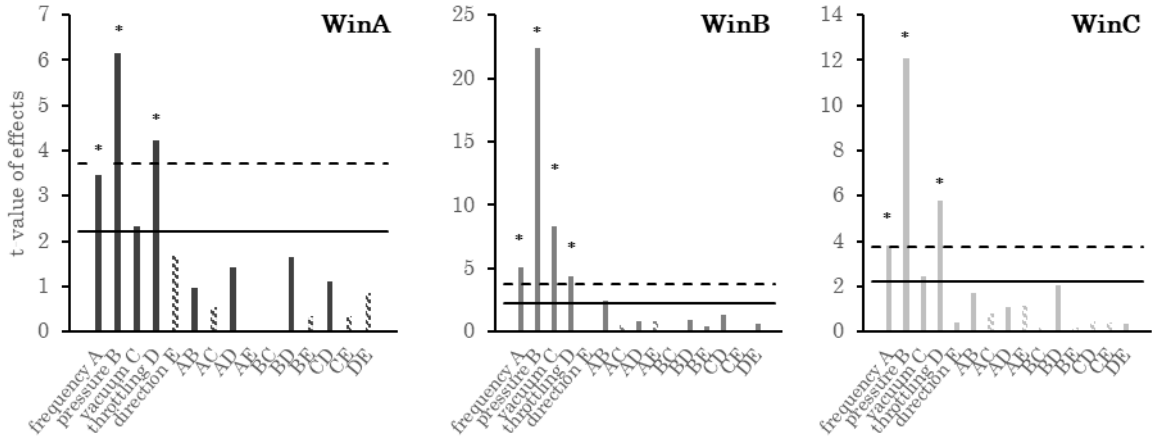

Figure 2.14: Pareto charts of the effects of main factors and their interactions on the WSS extremes *in* the main direction of pumping. The factors are not ordered as the ranking is different in each ROI. Dashed bars denote negative effects. For this analysis, the central points are disregarded, due to considerable curvature that they introduce (Fig. 2.16). The values for all ROIs are based on the square root of the terms to account for increasing residuals with size of the measured extreme. * for significant model terms ($p < 0.01$). Dashed and solid lines represent Bonferroni- and t-value limit, respectively.

It occurs that for WinA the extremes in the direction of flow are usually those visible in transition 2, while the opposing extremes can generally be observed in transition 1 (compare to Fig. 2.06 on page 16). In WinC, the extreme in the direction of flow always occurs in transition 4; the opposite extreme is in transition 5. Not surprisingly, the highest peak in the direction of pumping represent the discharge and inflation of the middle pumping chamber (i.e. the deflection of the main pumping element). Rarely, the highest WSS in WinA could emanate from the closure of the downstream valve if pumped forward (i.e. the closure of M3/4 in transition 3). Why the direction of pumping makes a difference will be discussed later.

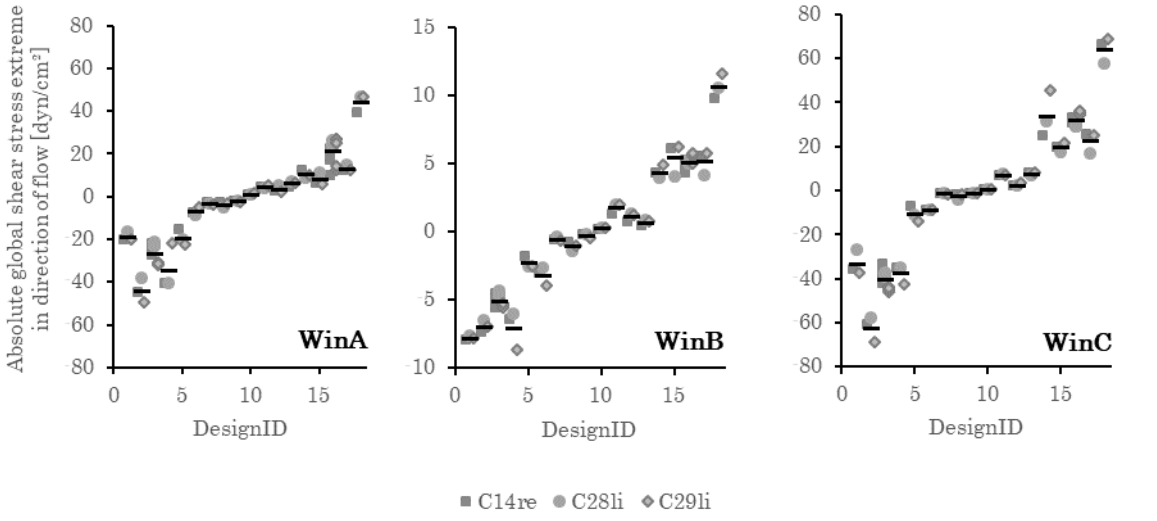

Figure 2.15: Replicability of measuring the WSS extremes *in* the main direction. Due to the dimensions of the corresponding channels and their position in the overall circuitry the extremes differ in the three ROIs. Divergences between the tested chips are obvious. The given design IDs correspond to those of figure 2.10. They are ordered after the experiments by the average flow rate.

Nevertheless, if the transition 3 contains the pulse with the WSS extreme, its magnitude is only briefly above the one in transition 2.

If perfectly closed, the WSS extrema opposing the direction of flow always occur due to the deflection of the valves close to the respective ROIs WinA and WinC. On average, it is about three quarters of the magnitude of the extreme in the direction of flow (Tbl. 2.1). To reduce unwanted flow and shearing in the opposing direction, one may attempt to reduce this ratio. Depending on the factor the effect is reversed in the two ROIs. For example, in WinA the direction of pumping (E) and the interaction of frequency and direction (AE) have a negative and positive effect, respectively. In WinC this is the other way around. This makes it hard to minimise the ratio as reducing the effect in one ROI increases it in the other. Raising the pressure has the highest overall effect on lowering the ratio of the opposing shear extremes. It is, however, obvious that certain backflow can hardly be avoided in any ROI.

Hence, the author concentrates on the WSS extreme in the direction of pumping. Like the flow rate hereafter. Only absolute values are regarded as the direction (E) almost exclusively influences the extreme's prefix. The absolute WSS maxima range from 1.17 to 44.33 dyn/cm² in WinA (0.12 to 4.43 Pa), from 0.24 to 10.64 dyn/cm² in WinB (0.02 to 1.06 Pa) and from 0.62 to 64.37 dyn/cm² in WinC (0.06 to 6.44 Pa). Ideally, values would be within physiological ranges, which in large vessels is on average below 20 dyn/cm² (2.0 Pa) (Papaioannou and Stefanadis, 2005).

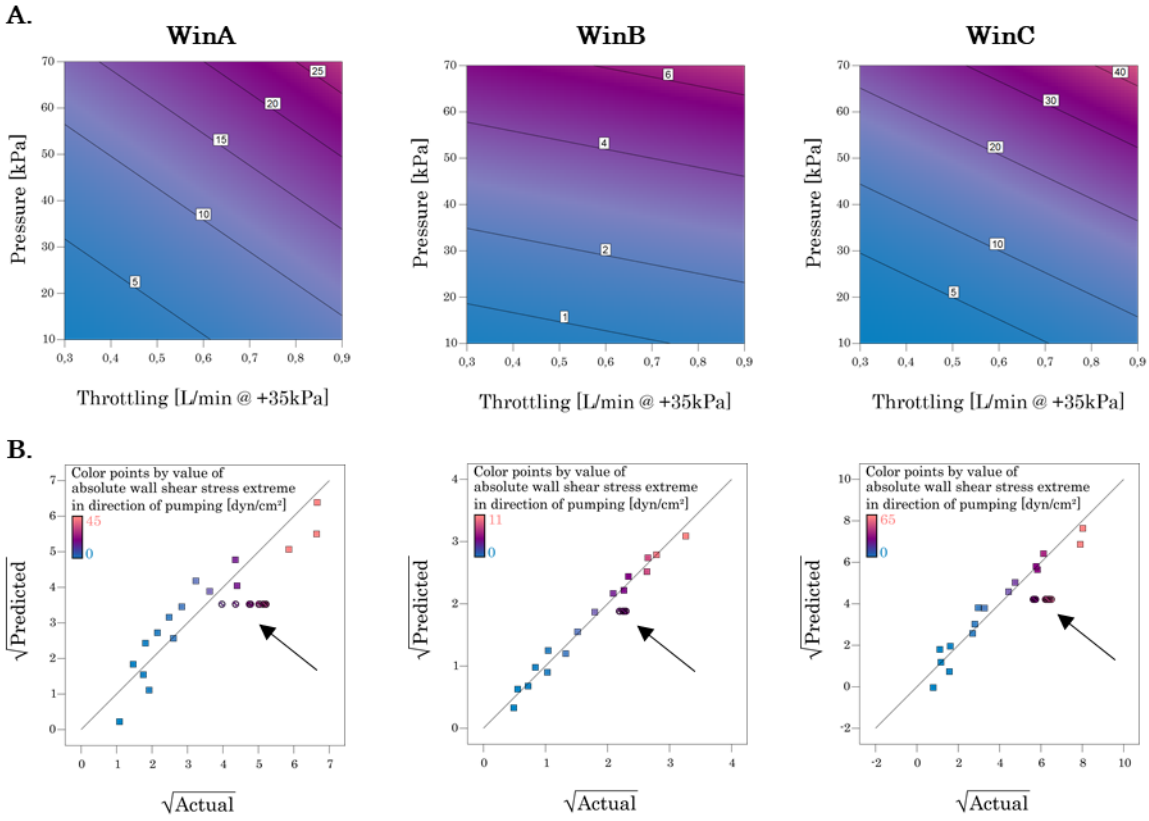

Figure 2.16: Modelling the WSS extreme *in* the main direction in each ROI. (A) Predicted WSS levels regardless of pumping direction. The remaining factors are set to their respective central points (Tbl. 2.7). All models are based on the square root of the terms to account for increasing residuals with increasing factors. Moreover, central points were excluded. The corresponding model equations and statistics can be found in the appendix 5.6.3 to 5.6.5. (B) The residual plots depict the deviation between predicted and measured WSS extremes. The circles represent central points that are excluded from the model (arrows).

If the central points are disregarded the influences of the main factors stand out (Fig. 2.14). Again, the pressure (B) shows the highest impact. It has a positive effect meaning that higher pressure will elevate the extreme. In the ROIs, close to the pump (WinA and WinC) also the throttling (D) has a major impact on the magnitude of the peaks – increasing the throttling (i.e. slowing down the membrane movement) lowers the peak. To a certain degree also vacuum plays a role in the development of the peak. More so in WinB than in the other ROIs. The vacuum's effect is positive, which for this factor means that a higher vacuum increases the peak's extreme. Just to clarify, the vacuum is given in positive values of pressure, although *de facto* it resembles a negative pressure. Surprisingly, and this is different to the first screening, the frequency positively affects the extreme.

Modelling this response is not very predictive. The discrepancy between the chips is too severe for some designIDs (Fig. 2.15). Depending on the ROI the correlation value ranges on average from 12 to 21 %, reaching up to 50 %. As the modelling is based on the average values of all chips the high correlation value introduces noise. The models that derive from the most influential factors (Fig. 2.16) are significant ($p<0.0001$). The correlation coefficients are robust ($R^2_{WinA}=0.8694$, $R^2_{WinB}=0.9826$, $R^2_{WinC}=0.9477$). As mentioned before, the central points are not considered, which simplifies the model. The signal-to-noise ratio supports the model (Adeq. $Precision_{WinA}=14.5$, Adeq. $Precision_{WinB}=36.1$, Adeq. $Precision_{WinC}=21.5$). As expected, the *Lack of Fit* is significant. This indicates that although the central points are excluded the data is still too noisy to explain all effects and interactions.

Depending on the ROI the models are considerably different. First and foremost, this relates to the respective location within the chip. The flow and, thus also, the WSS in WinA can be high as the friction in this part of the chip is lower. This is due to the wider dimensions and the shorter length of the corresponding channel. The opposite is true for WinC. Its microfluidic section is longer and narrower. Despite a retarded flow the rather narrow

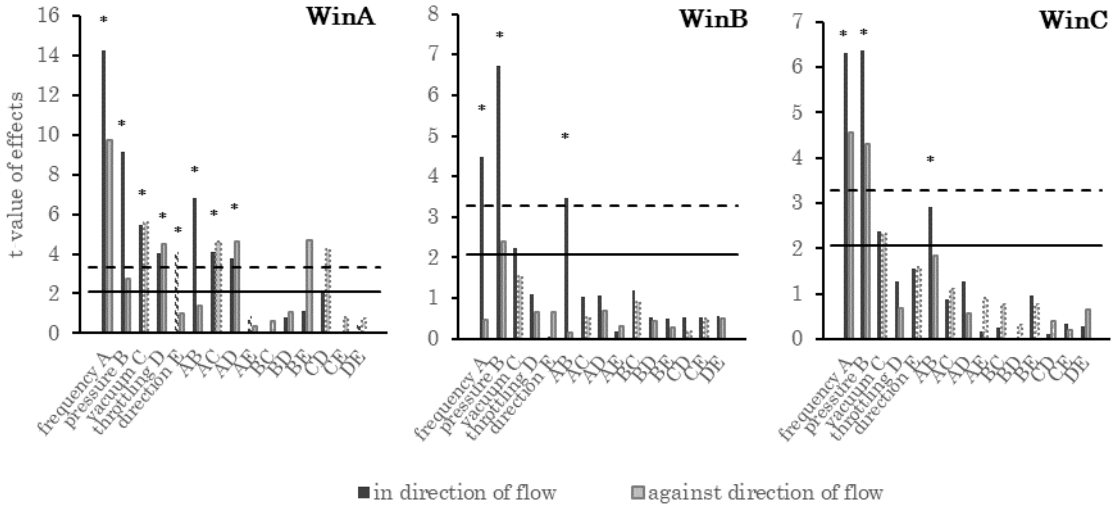

Figure 2.17: Pareto charts of the effects of main factors and their interactions on the average WSS *in* and *against* the main direction in each ROI. The factors are not ordered as the ranking is different in each ROI. Dashed bars denote negative effects. The values for WinC are based on the square root of the terms. Only for effects *in* the main direction of flow: * for significant model terms ($p < 0.01$). Dashed and solid lines represent Bonferroni- and t-value limit, respectively.

channel increases the WSS in comparison to WinA. In WinB, eventually, flow is considerably dampened down, creating an equally low WSS.

2.3.6. Controlling the average shear stress

The maximum WSS does not necessarily reflect the shear stresses perceived by the cells on the channels' walls. While the pulses have a duration of about 0.2 s, the extreme shear stresses last less than a quarter of this. Therefore, the average WSS is also analysed. Over the past decade literature acknowledges this by presenting also both, peak and mean WSS (Reneman et al., 2006).

Equal to the flow rate, the WSS can be distinguished into forces that act *in* and *against* the main direction of flow. Assessing the average WSS modulus has the premise that the direction of shearing does not matter to the perceiving cell and for its successive behaviour. The average WSS modulus has been used in former publications of the 2OC (Schimek et al., 2013). The highest average WSS is reached *in* the main direction of flow. It can be as high as 8.57 dyn/cm² (0.86 Pa) in WinA, 5.90 dyn/cm² (0.59 Pa) in WinB and 16.62 dyn/cm² (1.66 Pa) in WinC. At the central points the average values are 2.97 dyn/cm² (0.30 Pa) in WinA, 2.80 dyn/cm² (0.28 Pa) in WinB and 4.64 dyn/cm² (0.46 Pa) in WinC. Therefore, the 2OC can recapitulate the mean shear regime of an artery (Reneman et al., 2006).

Concerning the average WSS in both directions of pumping (Fig. 2.17): The influential factors are different in each ROI. They also differ depending on the examined shearing direction. In WinA for example, pressure (B), direction (E) and the interaction of frequency and pressure (AB) have no significant influence on the shearing *against* the direction of the overall flow, while they are significant for the shearing *in* the direction of flow. Especially in WinB the discrepancy between the directions is evident. This can be explained with the fact that the backflow in this ROI is considerably low and plainly does not create enough data to surpass the random error. Nonetheless, the frequency (A), the pressure (B) and their interaction (AB) impact the average WSS in the direction of flow the most. Moreover, their effects are positive meaning that high frequency and high pressure produce an increased average WSS.

For each ROI, a significant model ($p<0.0001$) can be formulated for the shear in the direction of flow (Fig. 2.18). However, they show significant *Lack of Fit* without exception, too. Among others, this may account for the evident curvature for WinB and WinC. Other modelling benchmarks are in reasonable range: the correlation coefficients ($R^2_{WinA}=0.9573$, $R^2_{WinB}=0.7801$, $R^2_{WinC}=0.8098$) and the random noises (Adeq. $Precision_{WinA}=29.0$, Adeq. $Precision_{WinB}=15.8$, Adeq. $Precision_{WinC}=18.1$).

Regarding the average WSS modulus, which comprises the information for both directions: The outcome is very similar to the average shearing *in* the direction of pumping (Fig 2.19). Overall, this modulus can be considered as a weighted average of the two shear stresses that distinguish between the directions of shearing. Accordingly, the identified influential factors for the modulus are a mixture of both formerly separately regarded responses. Moreover, the characteristics of the resulting models are similar. They are significant ($p<0.0001$), the

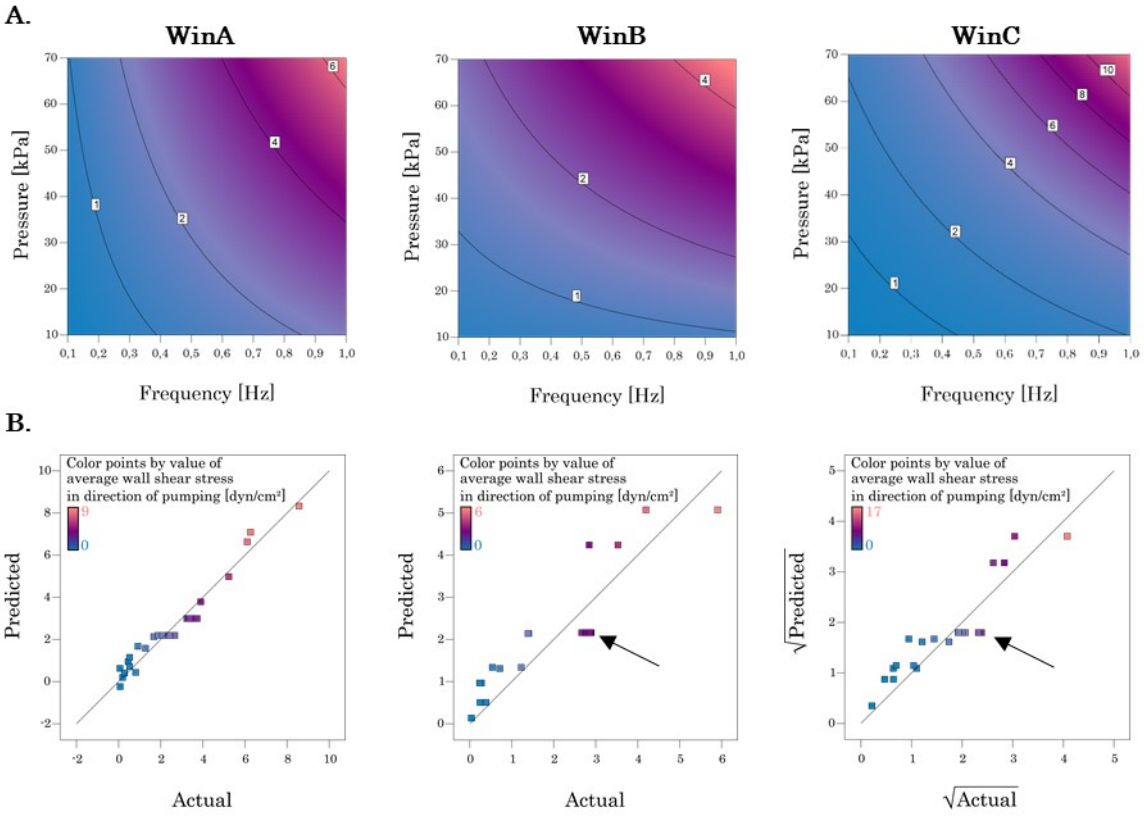

Figure 2.18: Modelling the average WSS *in* the main direction in each ROI. (A) Predicted shearing regardless of pumping direction (WinA shows directional impact). The remaining factors are set to their respective central points (Tbl. 2.7). The model for WinC is based on the square root of the terms to account for increasing residuals with increasing factors. The corresponding model equations and statistics can be found in the appendix 5.6.6 to 5.6.8. (B) The residual plot depicts the deviation between predicted and measured WSS. Especially, the models for WinB and WinC show deviations of the model at the central points (arrows) relating to unconsidered curvature.

correlation coefficients are acceptable (R^2_{WinA}=0.9684, R^2_{WinB}=0.8219, R^2_{WinC}=0.8157), as well as the random noise (Adeq. $Precision_{WinA}$=32.0, Adeq. $Precision_{WinB}$=17.6, Adeq. $Precision_{WinC}$=18.6). The *Lack of Fit* is always significant.

For both measures of the average WSS, there appears to be a nominal influence of the direction of pumping on the outcome in WinA. Especially, values in the opposing direction appear to be influenced by the interaction of pressure with the directional setting (BE).

2.3.7. Controlling the pulse shape

From an analytical perspective, two further characteristics of the flow profile are of interest: width and area of the pulses. As described before the observed pulses allow conclusions about the actuation of specific membranes. The pulses in the transition 1 and 5 always emanate from the movement of the membranes M3/4 and M1/6, respectively (compare to Fig. 2.06 on page 16). The transitions 2 and 4 are affiliated to the membrane M2/5. Under optimal conditions (i.e. the valves close properly) the transitions 1 and 2 are best observable in WinA while the transitions 4 and 5 show up in WinC. An overview about which membrane movement can be observed best during which transition and the respective orientation of the membranes is provided in table 2.2.

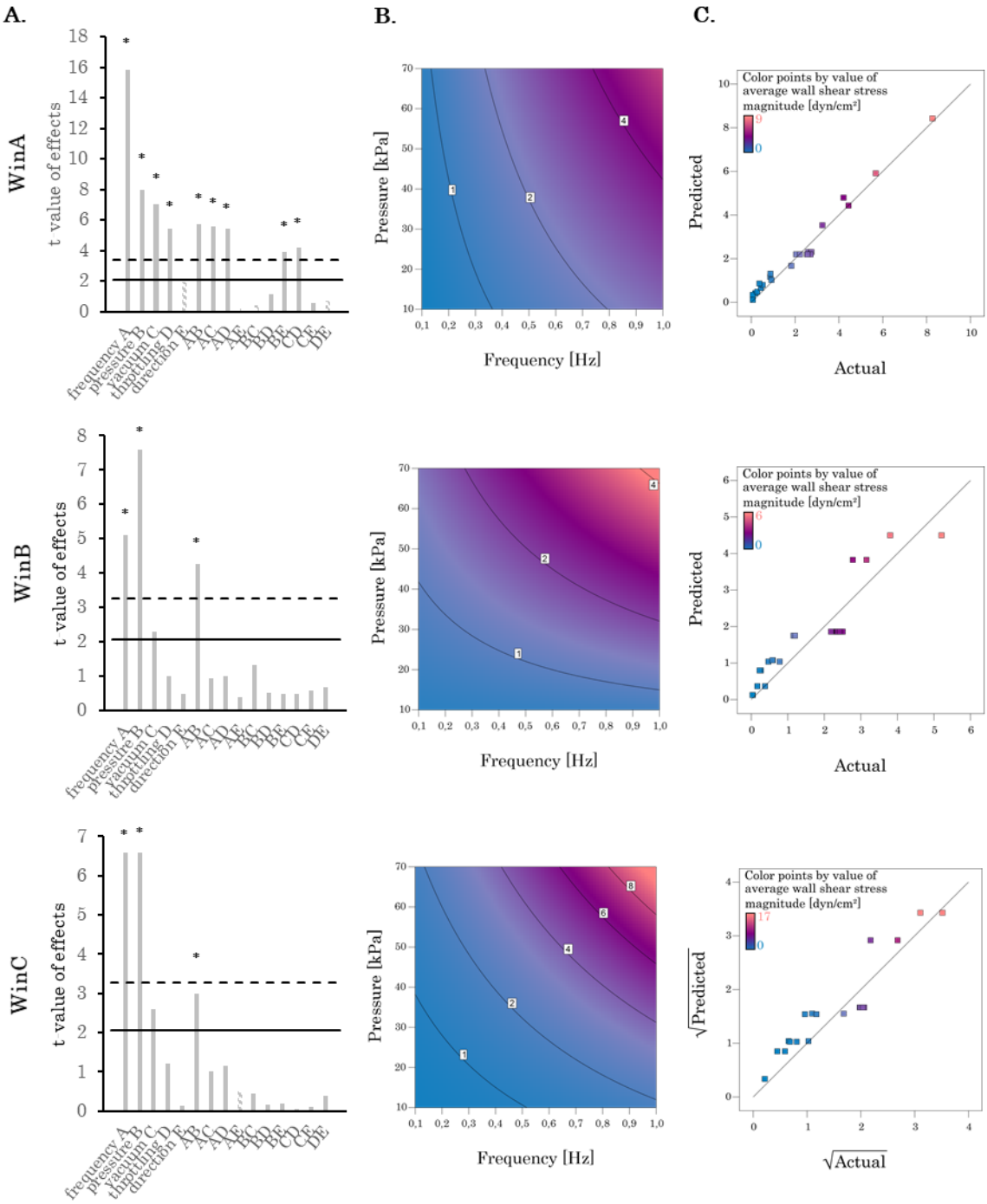

Figure 2.19: Analysis of the average WSS modulus in each ROI. (A) Pareto chart of effects' t-values. The factors are not ordered as the ranking is different in each ROI. Dashed bars denote negative effects. The values for WinC are based on the square root of the terms. * for significant model terms ($p < 0.01$). Dashed and solid lines represent Bonferroni- and t-value limit, respectively. (B) Predicted shearing regardless of pumping direction (WinA shows directional impact). The remaining factors are set to their respective central points (Tbl. 2.7). The corresponding model equations and statistics can be found in the appendix 5.6.9 to 5.6.11. (C) The residual plot depicts the deviation between predicted and measured average WSS magnitude.

The width of the pulse is calculated as duration (absolute) and as percentage of the timing between the transitions (relative). This period itself is determined by the frequency: the higher the frequency, the shorter the time between two pulses. The relative duration is to alert the operator whether the peak is fully developed before the next pulse is initiated. Full

Table 2.2: Direction of membrane actuation depending on the direction of pumping. This is to give a concise, yet, incomplete overview of the orientation of the membranes' movements regarding to figure 2.02 on page 5 during the respective transitions (parenthesis). It is meant to facilitate the interpretation of the found dependencies of the direction of pumping in figure 2.20.

	forward pumping	backward pumping
M3/4 (Transition 1)	lifting	descending
M2/5 (Transition 2)	descending	lifting
M2/5 (Transition 4)	lifting	descending
M1/6 (Transition 5)	descending	lifting

development of the pulse is arbitrarily defined if the relative value is below 85 %. With frequencies, as high as 1 Hz (i.e. a cycle duration of 1 s) each pulse can last at most 0.2 s. In such a case, it is very likely that a pulse is interrupted by the following pulse. Evaluating width and area of these respective pulses is not recommended as they provide an incomplete picture. Then, the tail of the pulse interferes with the following pulse. Pulses that are incomplete are excluded from the DoE analysis causing the data to be fragmented. Finding the influential factors for the duration and area with DoE, thus, must be regarded with care.

Moreover, the missing data complicates the evaluation by the statistics software as especially two-factor-interactions are now partially confounded by other two-factor-interactions. In the analysis of duration and area these usually show no significant impact except for the interaction of frequency and vacuum (AC), which is disguised by the involved main factors themselves. Also, the interaction of pressure and vacuum (BC) is partially masked by the interaction of throttling and pumping direction (DE).

For the duration of the pulse the medians of all investigated ROIs throughout the remaining designIDs lie at 0.18 to 0.20 s. The evaluation reveals that the throttling (D) has the highest leverage (Fig. 2.20A). For all membranes, less throttling (i.e. quicker membrane actuation) leads to shorter pulse durations. The vacuum (C) has a surprisingly high impact. A high degree of negative pressure leads to prolonged pulses. Pressure (B) on the other hand has only minor importance for the central membrane (M2/5). Again, higher values increase the width. The valves (M1/6, M3/4) are seemingly not affected by the pressure. Predictably, the frequency (A) has no influence on the pulse duration. Closer examination of the missing data points could, thus, be done at lower frequencies.

Most striking is the impact of the direction of pumping (E) on the pulse duration. Depending on the ROI and on the membrane, it has a significant positive or negative effect. In the logic of DoE, a positive effect describes that the duration is higher if pumped forward. This is, for example, the case for M3/4. Negative means an increased duration if pumped backwards, as seen for M1/6. A bit more intricate is the situation for M2/5, showing opposing effects depending on the ROI. The unusual effect of E originates from the nature of the corresponding membrane actuation. During forward pumping, for example, the regarded membrane M3/4 is being lifted during transition 1, while the membrane M1/6 is pushed down in transition 5 (Tbl. 2.2). Linking this back to the data of the Pareto charts clearly relates increased duration of the pulses to the raising of the membranes. In other words, lifting the membrane to its full extend takes longer than its full descent.

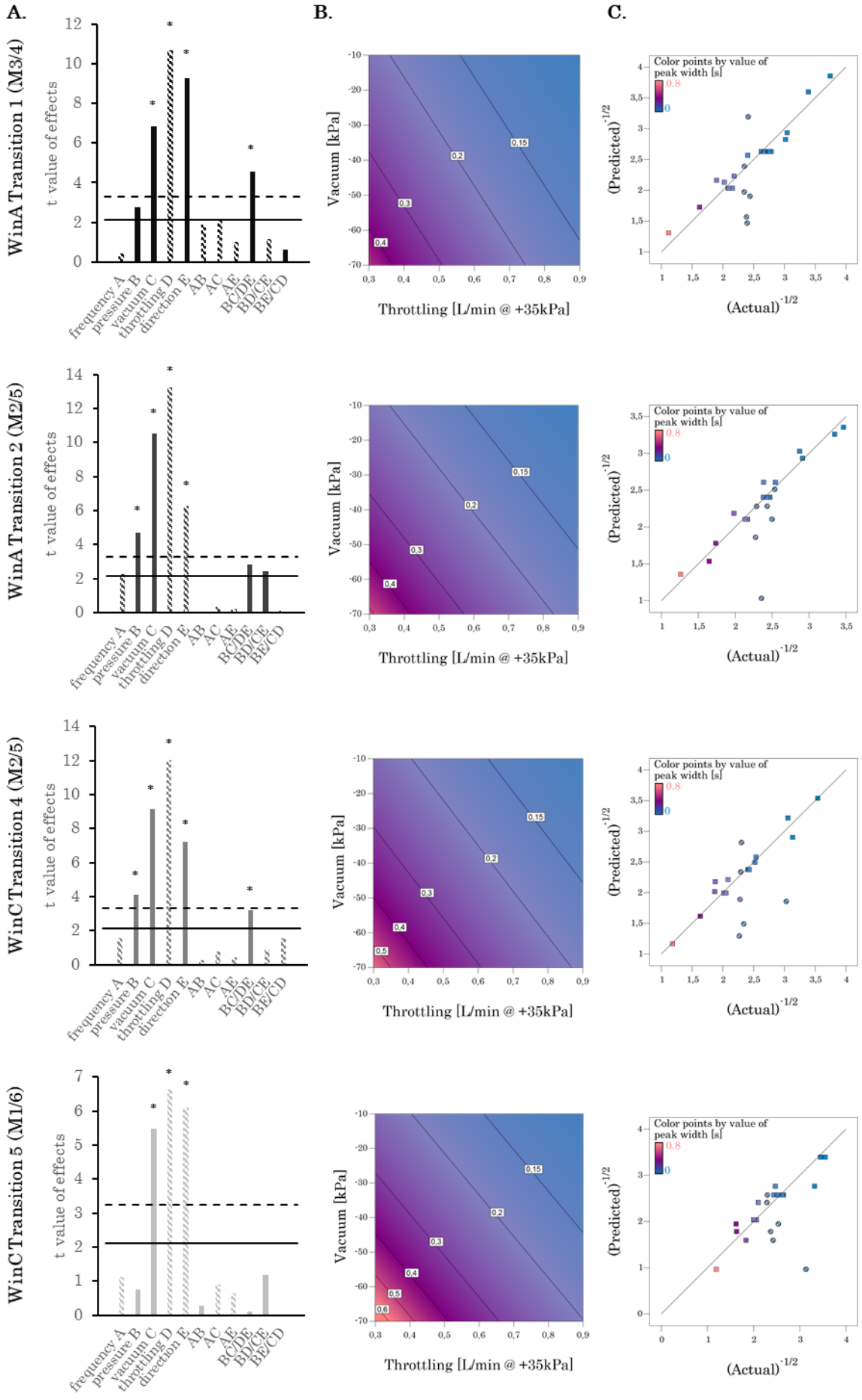
A.
B.
C.
WinA Transition 1 (M3/4)
WinA Transition 2 (M2/5)
WinC Transition 4 (M2/5)
WinC Transition 5 (M1/6)
t value of effects
frequency A
pressure B
vacuum C
throttling D
direction E
AB
AC
AE
BC/DE
BD/CE
BE/CD
Vacuum [kPa]
Throttling [L/min @ +35kPa]
Color points by value of peak width [s]
0.8
0
(Predicted)^-1/2
(Actual)^-1/2

(previous page)

Figure 2.20: Modelling the pulse duration in two distinct ROIs. The transitions are chosen as they provide a clear interpretation of the role of each membrane's actuation (see text). Corresponding to figure 2.06 on page 16 the transitions link to the membranes given in parentheses. (A) Pareto charts of effects' t-values. The factors are not ordered as the ranking is different in each ROI. The models' terms are transformed with the inverse square root to homogenise the distribution of residuals. Dashed bars denote negative effects of the untransformed data. * for significant model terms ($p < 0.01$). Dashed and solid lines represent Bonferroni- and t-value limit, respectively. (B) Predicted pulse duration regardless of the pumping direction (all ROIs show directional impact). The remaining factors are set to their respective central points (Tbl. 2.7). The corresponding model equations and statistics can be found in the appendix 5.6.12 to 5.6.15. (C) The residual plot depicts the deviation between predicted and measured duration. The circles represent points that are excluded from the model. The corresponding data is regarded as incomplete due to high pumping frequency that interrupted these pulses (see text).

As mentioned before, the data and the subsequent model (Fig. 2.20B,C) should be regarded with care. To homogenise the spreading of residuals the data is transformed with the inverted square root. The inferential statistics and the underlying formula can be found in the appendix. Although the Pareto charts for the models are not equivalent, the models have a similar appearance at the central points. It seems as if the predicted duration increases from membrane M3/4 over M2/5 to M1/6. The transitions 2 and 4 of WinA and WinC, respectively, should show high similarity due to their source. Similarly, the same should be true for the transitions 1 and 5 of the respective ROIs.

Regarding table 2.2 the direction should be considered when comparing the adjusted models. The model for the transition 2 of WinA is only comparable to the one of transition 4 of WinC, if the former is set to forward and the latter to backward pumping (graphs not shown). This is especially true when comparing models originating from descending membrane movements.

For lifting movements, there appears to be also an influence of the location of the ROI. For WinC the model suggests much increased durations (backward) than from the equivalent membrane in WinA (forward). This could be explained with the comparably longer channel at WinC.

The second characteristic for in depth analysis, the area of the peaks, is equivalent to the actual volume that is displaced by the actuation of either of the membranes. The author will use pulse volume synonymously to the area. The pulse volume of M2/5 (the main pumping element) is on average 0.23 µL in WinA. It can climb as high as 0.44 µL. In WinC the volume for the same membrane is on average 0.28 µL and up to 0.56 µL. The discrepancy probably originates from the different dimensions of the channels at the ROIs as discussed before. The pulse volume correlates with the pulse duration to some extent. As anticipated, pressure (B) and vacuum (C) have significant influences on this response (Fig. 2.21A). Both factors directly impact the shape of the membranes and, hence, the volume in the respective

chamber. For all ROIs, there is also an apparent contribution of the frequency (A) and a probably confound interaction of the frequency and vacuum (AC). However, this outcome is questionable. Of course, the frequency interferes at high rates with the full development of the pulse and could diminish the pulse volume. First, this would result in a negative effect and not – as it is here – in a positive action. Second, only two out of eight setups that contained the high (+1) frequency limit are considered of the analysis for the aforementioned reasons. Therefore, the shown influence is based on a rather low quantity of experiments.

Apart from these issues a model was created (Fig. 2.21B,C). The data is transformed with the square root and the respective statistics can be found in the appendix. Other than the duration, the pulse volume has a very similar appearance for the corresponding pulses emanating from membrane M1/6 and M3/4. Also, the two ROIs depicting the action of M2/5 are highly comparable.

2.3.8. Summary of the second DoE-screening

The readouts of the Pareto charts of all responses are summarised in table 2.3.

Not surprisingly, the **frequency (A)** has a major positive influence on all responses that are averaged over time. An increased frequency determines an increased flow rate and increased average WSS. However, there is an additional impact on almost all other investigated responses. Interesting especially for the reduction of the back flow: raising the frequency appears to reduce it especially in WinB. Nevertheless, its positive influence on the pulse volume and its interaction with the vacuum (AC), there, should be doubted.

By far the most influential factor is the **pressure (B)**. It shows up with high significance for almost every response. Most importantly, of course, is its effect on the WSS extreme and pulse volume. This is also the reason for its high impact on the flow rate (and heritably for the average WSS). Undoubtedly, these unexceptional positive effects are the reason for its contribution to a reduced back flow. The pressure interacts with the frequency (AB) especially on the level of global responses, where they amplify each other.

The **vacuum (C)** has a surprisingly low impact in comparison to the positive pressure. If it shows an effect in the Pareto charts, it commonly has a positive effect, meaning that a stronger vacuum promotes the respective response. The highest influence is found for the pulse duration and volume, which, both, are drawn from fragmented data sets. Its effect on the duration implies a broadening and flattening of the pulses. In turn, this should result in a decrease of the pulse's extreme. However, the increased pulse volume that comes with increased vacuum neutralises the flattening, which is why there is no effect on the extreme at least for WinA and WinC.

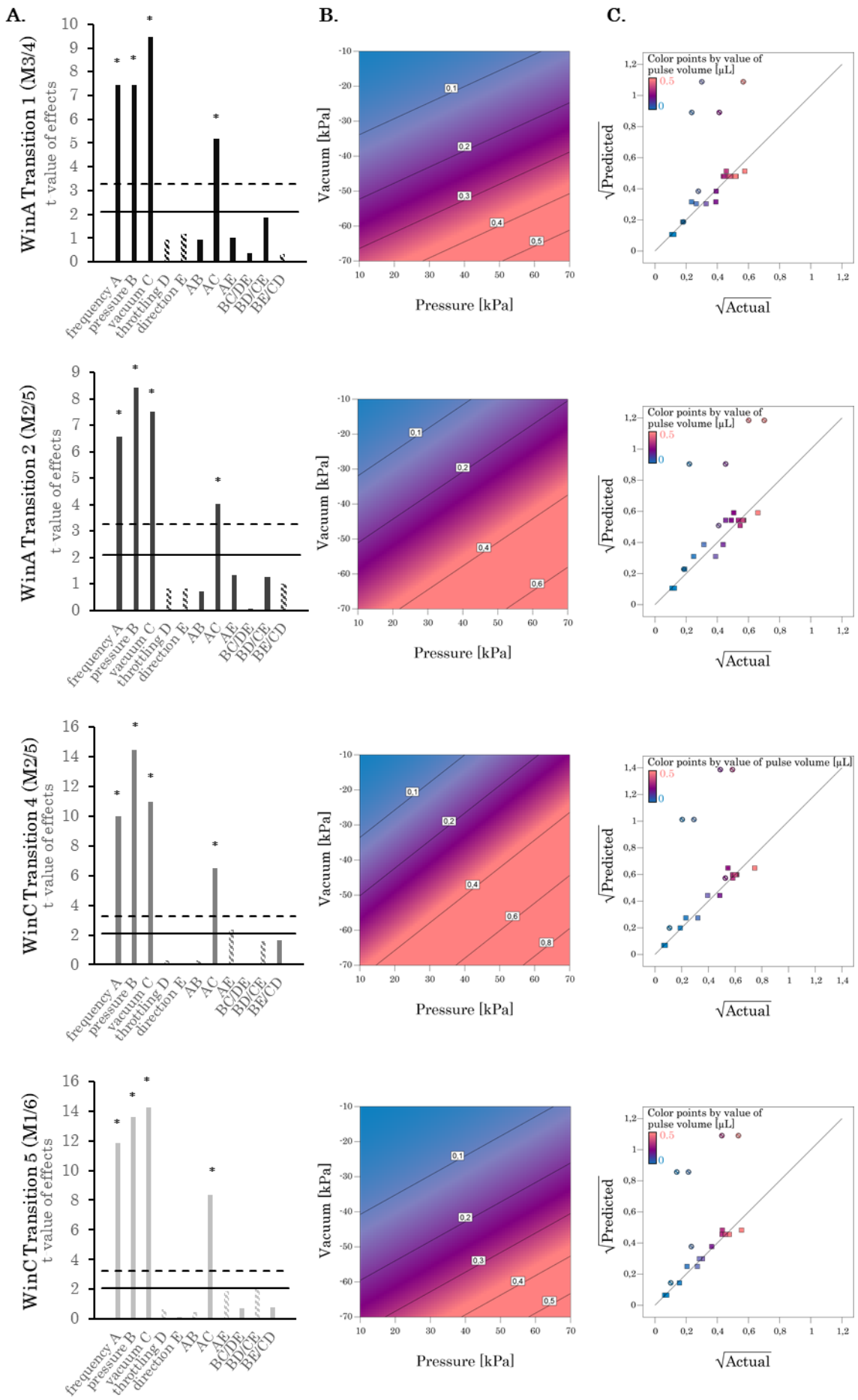
A.
B.
C.
WinA Transition 1 (M3/4)
WinA Transition 2 (M2/5)
WinC Transition 4 (M2/5)
WinC Transition 5 (M1/6)
t value of effects
frequency A
pressure B
vacuum C
throttling D
direction E
AB
AC
AE
BC/DE
BD/CE
BE/CD
Vacuum [kPa]
Pressure [kPa]
Color points by value of pulse volume [µL]
√Predicted
√Actual

(previous page)

Figure 2.21: Modelling the pulse volume in two distinct ROIs. The transitions are chosen an accordance with figure 2.20. (A) Pareto charts of effects' t-values. The factors are not ordered as the ranking is different in each ROI. The models' terms are transformed with the square root to homogenise the distribution of residuals. Dashed bars denote negative effects. * for significant model terms ($p < 0.01$). Dashed and solid lines represent Bonferroni- and t-value limit, respectively. (B) Predicted volume of the pulse regardless of the pumping direction. The remaining factors are set to their respective central points (Tbl. 2.7). The corresponding model equations and statistics can be found in the appendix 5.6.16 to 5.6.19. (C) The residual plot depicts the deviation between predicted and measured pulse volume. The circles represent points that are excluded from the model. The corresponding data is regarded as incomplete due to high pumping frequency that interrupted these pulses (see text).

The **throttling (D)** mainly influences the pulse duration. Increased throttling (i.e. a low flow rate in the air-carrying tubings) prolongs the pulses. Hence, it significantly reduces the WSS extremes. After the pressure, it is the second most influential factor on this response.

Doubtlessly, the set main **direction of pumping (E)** is the only determinant for the main direction of flow. Therefore, it determines nothing more than the prefix of most of the values. Only this permits the use of the modulus of the data, which is recommended as it simplifies the evaluation and interpretation tremendously. Not only the Pareto charts present effects clearer. Moreover, it simplifies the justification for the partial exclusion of complicated three-factor-interactions. The direction of pumping appears to impact only the pulse duration. Of course, as pointed out this is not caused by the direction *per se* but by the underlying orientation of the actuated membrane. Besides the interaction AB, the interactions with the direction of pumping – namely with the frequency (AE) and the throttling (DE) – are the only two-factor-interactions that show effects with a credible pattern.

Table 2.3: Summary of the factors' effects on the observed responses. The effects are classified as positive (+) or negative (–). The responses are subdivided into the respective ROI and to which membrane actuation the results can be attributed.

response	ROI	membrane	A	B	C	D	E	AB	AC	AD	AE	BC	BD	BE	CD	CE	DE
flow rate	all	all	++	+++				+									
WSS extreme in main direction (!)	WinA	M2/5 or M3/4	+	+	+?	+											
	WinB	mostly M2/5	+	+++	++	+		–?									
	WinC	M2/5	+	+++	+?	+											
ratio extreme against vs. in main direction	WinA	M3/4	–	–		(+)	–				+		+				
	WinB	M1/6 or M3/4	– –	– –	(+)	(–)	(+)				+				–		
	WinC	M1/6	(–)	–	(+)	(–)	+				–	+					+
average WSS in main direction	WinA	all	+++	++	+	+	–	++	+	+							
	WinB	all	+	++	+?			+									
	WinC	all	+	++	+?			+									
… against main direction	WinA	all	++	+?	+	+	(+)		+	+				+	+		
	WinB	all		+?													
	WinC	all	+	+	+?												
… modulus	WinA	all	+++	++	++	+	(–)	+	+	+				+	+		
	WinB	all	+	++	+?			+									
	WinC	all	++	++	+?			+									
pulse duration (!)	WinA	M3/4		+?	++	– – –	++										+ (BC?)
	WinA	M2/5		+	+++	– – –	–										+? (BC?)
	WinC	M2/5		+	++	– – –	++										+ (BC?)
	WinC	M1/6			+	– –	–										
pulse volume (!)	WinA	M3/4	++*	++	++				+*								
	WinA	M2/5	++*	++	++				+*								
	WinC	M2/5	+++*	+++	+++				+*								
	WinC	M1/6	+++*	+++	+++				++*								

+++/– – – effect is more than 3-fold above the Bonferroni limit (highly significant model term)
++/– – effect is at least 2-fold above the Bonferroni limit (very significant model term)
+/– factor is a significant model term ($p < 0.01$)
+?/–? factor is hardly significant ($p < 0.05$) – whether or not it has an influence is unclear
(+)/(–) the term had to be included into the model due to the hierarchy rule and is otherwise viewed as negligible
(!) results drawn from fragmented data set
* the effect is questionable (refer to text)

2.3.9. The 4-Organ-Chip (4OC)

The 4OC consists of two separate circuits that can communicate through a membrane in one of the cultivation compartments. For the excretory circuit two ROIs are evaluated (Spot D and E; Fig. 2.01D on page 4); for the surrogate blood flow circuit another three (Spot A, B, C). The measurements are, however, inconsistent due to the high variability in 4OC production at the time of investigation. The flow rate varies according to how tough the layers are clamped together to seal the microfluidics. The relatively soft PDMS channels are compressed and their dimensions are altered. As a rule of thumb: the stronger the fastening, the higher the velocities.

Nevertheless, a flow is inducible in both circuits by the incorporated micropumps. An almost linear correlation between frequency and flow rate is observable (Fig. 2.22). However, due to the previously mentioned reasons it should not be generalised for other 4OCs. For the given chip flow rates range from 0.51 µL/min (at 0.2 Hz) to 3.26 µL/min (at 1 Hz) in the surrogate blood circuit and from 0.58 µL/min to 4.24 µL/min in the excretory circuit. Due to the extended microfluidics and added phase dampening capacity in the cultivation compartments the flow rate, hence, is comparably reduced in the surrogate blood circuit. In the experimental setup, which led to the first publication on the 4OC (Maschmeyer et al., 2015b), the pumping frequency for this circuit is set to 0.8 Hz. It is comparable to 48 heart beats per minute and corresponds to two third of the physiological values of a resting adult. It is chosen this low to circumvent non-physiologic shear stresses for the liver equivalent. At this frequency, the flow rate is 2.58 µL/min for the given chip. It needs 5.3 hours to circulate the circuit's complete volume of 830 µL once. With its 0.3 Hz, the excretory circuit needs 10.4 hours for one turnover.

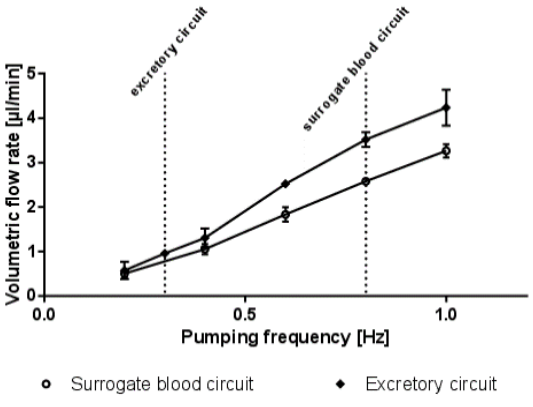

Figure 2.22: Average flow rate in dependency of the pump frequency. The averaged data of the spots A, B and C resemble the flow in the surrogate blood circuit. The spots D and E are depicting the excretory circuit. The actual 4OC experiments are conducted at 0.8 Hz (blood) and 0.3 Hz (excretory). This is emphasised by the dotted lines. Error bars show the standard error of the mean.

2.4. Discussion – Rationale behind the μPIV analysis and their implications

The evaluation of the μPIV data in combination with an experimental design comprising manifold factors and responses is only of value if the interpretation of the statistical results is met by reasonable interpretation and theory.

2.4.1. Why we perform measurements and statistics …

… rather than an analysis and modelling based on physical formulas.

The operation of the MOC is mainly based on the actuation of the micropump's membranes – on their amplitude, their geometry when lifted, their geometry when deflected downwards, the rate with which they deflect, and when they deflect. Multiple physical features with multiple implications and time-dependent regulation must be considered. Besides the aforementioned factors frequency, pressure, vacuum, throttling, and direction of pumping (i.e. membrane control) there are other relevant parameters such as material constants for the PDMS and the glass components, viscosity, temperature, compression and expansion of the air in the tubings and in the cultivation compartments, friction at the walls of the differently shaped microfluidic channels and compartments, as well as phase dampening in the cultivation cavities to name a few. With knowledge of the underlying processes and relationships it is possible to model the fluidic behaviour in the MOC.

Two of many possibilities to do so are mesh- and network-based simulation approaches. In fluid mechanics, the former is usually referred to as computational fluid dynamics (CFD). These are highly complex numerical calculations that solve physical formula separately for confined polygons in a 3D mesh and allow interactions of these polygons. Usually the outcome of the CFD analysis are 3D representations of the investigated physical strains. The preparation, programming and computation of such models is laborious for the operator and the computer and requires a decent amount of experience and knowledge. Due to the complexity, the models would never simulate the entire MOC system at once. Moreover, within the pump the expansion and complete closure of the valves can hardly be computed as the polygons size vary too much. Several CFD simulations of the 2OC's cultivation cavities have been conducted already (unpublished: Hsu, 2017; Sieber, 2017). This is of use for highly space-resolved evaluation of the fluidic flow to, for example, determine the distribution, penetration or turnover of nutrition, oxygen or added components.

Network-based simulations, on the other hand, view the system from a broader perspective without detailed knowledge of every geometry. The system is subdivided into various physical aspects (e.g. fluid mechanics, membrane movement, pneumatics, temporal control), which are all modelled separately but in exchange with one another. The computation is much less elaborate than the CFD calculations. Nevertheless, the setup of a network-simulation should be done with professional care. Devices similar to the MOC have been modelled by our co-operation partner, Fraunhofer IWS, with this approach before (Busek et al., 2015, 2016).

Nonetheless, a simulation just like a statistical evaluation is only as accurate as the underlying theory. What it cannot predict are factors that are hard if not impossible to describe or to control. Moreover, their impact might be hard to assign. To name a few: the

wearing of the moving parts, flaws during chip fabrication, micro-indentations from the aluminium mould, inconsistencies in membrane thickness, or complex volume changes, for example, if cell culture inserts are placed into the MOC.

In all these cases, µPIV is an approach for the cost-effective assessment of the fluid behaviour. Experimental design, further, allows the evaluation of the influence of controllable factors without in depth knowledge of the hidden physical parameters and processes. The DoE established and evaluated, here, is to show the potential and the disadvantages of such an approach and its future applicability for the MOC.

2.4.2. µPIV as an accurate tool to determine flow velocities in the MOC

Undoubtedly, µPIV is the most cost-efficient tool capable of assessing the flow within the MOC. Its setup is easy: additionally to a proper microscopic system (that should be readily available in a biotechnological laboratory), the µPIV requires only an appropriate high-speed camera and suiting particles. Though the addition of particles to the flow is somewhat invasive, it does not perturb the flow unlike to other flow sensors. Furthermore, for future applications using full blood or a blood surrogate, particles would be directly available as part of the biological system. Moreover, in contrast to artificial beads RBCs do hardly adhere to plastic surfaces, cells and cell debris in the MOC.

The acquisition of the footage is rather straightforward. Although some rules should be respected – like adjusting the ROI or triggering the initiation – it is not impossible to learn the basics within a day. The following analysis with the help of cross-correlation is more complex. However, with the help of an available toolset for PIV-analysis a certain degree of semi-automation has been achieved during this thesis. Admittedly, the dimensions and shape of the microfluidic channels facilitate the programming of such routines as the development of the flow in channels with an aspect ratio of 5 (500 µm wide, 100 µm high) follows comparable simple rules. The plug-like flow in the channels allowed for the averaging of the velocity vectors, which in turn increased accuracy and reproducibility.

Nevertheless, the system can be prone to error. For example, a visual separation of different planes within a channel is not conducted. Hence, the resulting recordings contain particles of different velocities depending on their height and proximity to the channel wall. Due to the high depth of correlation, all levels are fully included into the measurement. The slower particles close to the top and bottom wall possibly reduced the measured maximum velocity that is the basis for all further calculations. During the conversion of the digital data into relevant parameters a calibration is introduced that should account for this error (namely equation 2.4 on page 59). The applied calibration is drawn from previous works (Schimek et al., 2013). It can be assumed that for the given magnification of 2.5x the linear raw maximum velocities underestimate the true speed and should not be used. Increasing the magnification could decrease the error due to an enlarged numerical aperture, which in turn reduces the depth of correlation disproportionally. A higher magnification, however, reduces the acquisition rate, which is problematic for high velocities around the pulses' peaks.

For future MOC designs with altered aspect ratios and channel dimensions the calibration should be repeated with the help of reliable flow sources like syringe pumps.

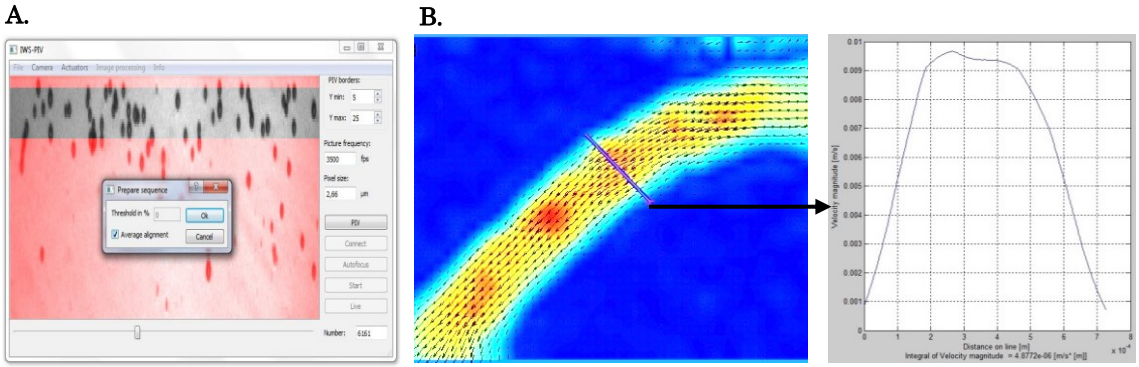

Figure 2.23: Exemplified image processing with two different programs. (A) uCam has a high speed but can only analyse linear segments and does not allow more than one instance at a time. (B) PIVlab comes with an optional graphical user interface that displays the generated vector field. Each vector represents an IW. PIVlab allows planar analysis as well as multiple instances. It is rather slow, however.

The variable particle speeds also introduce a certain degree of noise. An example: two particles are parallel to one another. From the camera's perspective one is hiding behind the other. If they travel with different velocities they will show up next to each other, eventually. Compared to a single particle in a different area they will produce a different speed and, thus, noise. This becomes striking and potentially interfering especially at a low overall speed (compare to figure 2.07 on page 17). Averaging of several consecutive recordings could reduce these deviations but would have to be deactivated around the peaks to not underestimate those. A feasible but not effortless improvement of a future analytical script.

Another issue of the μPIV analysis is the way of peak recognition during data processing. Occasionally, it is unprecise and prone to error. An actual physical trigger would be advantageous. It could especially improve the analysis of specific transitions. First, information is gained about the delay between the physical deflection of the membrane and the peak perception (i.e. the speed of the pulse). Second, it would allow high precision measurements of specific points within the flow rate-time-plots: instead of acquiring complete cycles – and, thus, produce thousands of images – the camera would just catch hundreds of images of defined moments of the cycle. This would allow to monitor the complete flow profile across the channel rather than only the maximum velocity in the centre.

For the image processing of the recordings our co-operation partner from the Fraunhofer IWS build an own solution – uCam (Fig. 2.23) – that is available to us in addition to PIVlab. The software is less complex as it is specially designed for the measurement of linear parts of the MOC's channels. The software determines the average displacement only in X-direction. The tremendous advantage of the program is its speed and usability. A stack of 20,000 single pictures can be processed within 10 to 15 min. Other than PIVlab, it can average a defined number of pictures (the default is five) and correlates them with the next average (*correlation averaging*). This is thought to increase the precision by reducing noise (Lindken et al., 2009). However, as already pointed out, during the deflection of a membrane this feature might reduce precision due to a steep temporary elevation of flow velocity that could be disguised by the averaging. Moreover, sub-pixel movements cannot be assessed. Thus, the software is rather quick and very precise only at specific range of velocities. Unfortunately, the program

is not intended for huge amounts of data, either. For example, a dataset of 3.2 GB would need to be divided in half to be processible. This obviously can become laborious at a certain number of experiments. Only one instance of the software is allowed at any time. In the author's opinion, this is the biggest disadvantage as it prohibits parallelised processing.

The two presented PIV-tools, uCam and PIVlab, both have advantages and depending on the domain their application can be justified. In terms of automation, accuracy and customisation the latter is favoured in this thesis. The former is simpler and faster, however. As the speed of analysis might matter to a human operator only in terms of convenience, it can be an issue, for example, for feedback control in an automated system. Both programs cannot give instantaneous results. However, if adapted, both tools could be of use in such a feedback control loop. For this, it is conceivable that the control unit does not only determine frequency, pressure and vacuum, but adapts them according to the µPIV measurements at specific ROIs of the MOC. This could be interesting in future MOCs where the biomass might change and alter the resistance of the microfluidics.

2.4.3. DoE helps in understanding the influential factors of the MOC's flow pattern

The great advantage of DoE is the easy accession of the influence of the factors at comparably low effort. In this thesis, fractional factorial designs are employed that immensely reduce the number of experiments. The rationale behind DoE has been established over decades already, which makes it a very standardised and reliable tool (Siebertz et al., 2010). With an adequate software, like DesignExpert®, the setup of an experimental design is easy and the tools for the interpretation are at hand. Nevertheless, the software requires a thorough preparation. Of course, the selection of the factors involves a certain degree of visualisation to predefine possible parameters that might have an impact on the flow. Feasible maxima and minima for the factors should be known as well as the precision of their regulation. The comprehensible presentation of the data in Pareto charts mediates clarity. There is no in-depth knowledge required to draw meaningful conclusions from the charts.

Especially, the design of the second DoE-screening suffers from the role of the pressure for the efficiency of pumping. If the pressure is too small, either or both valves (usually the upstream-lying) may not close properly during the discharge of the main pumping element. The interval between the minimum feasible pressure (10 kPa) and the pressure at which the valves close properly (~35 kPa) can have a very different rheological impact and pressure-dependent characteristic than the interval going up from that same pressure. For the benefit of interpretation these intervals should have been tested in two distinct experimental designs. However, the required pressure can be different for any chip. Probably depending on the quality of the bonding there are all kinds of chips, starting from those that pump efficiently at any pressure and those that have valves that never close properly. This issue will be discussed further below. In any case, in the interest of comparing three different circuits there is no discrimination of two pressure intervals. However, circuits are chosen with pumping efficiencies that are not too dissimilar.

In basic DoE only the maximum and minimum values of a given factor are tested and a linear relationship is presumed between factor and response. By transforming the responses or using polynomial models, a certain degree of non-linearity can be governed. To test the shape

of the relation of factor and response central points are introduced. These points are precisely half-way between the maximum and minimum value of the factor. They are influential for the outcome of the *Lack of Fit*-test. The *Lack of Fit* is commonly significant for the tested responses (except for the flow rate). It accounts for underlying curvature, outliers or models that are too big or small. Determining the concrete source of a significant *Lack of Fit* is not easy. The author suspects the discrepancies between the chips regarding specific responses and, ultimately, the two pressure intervals to be the underlying cause.

Hence, a sensitive interpretation of the outcome is required. This is especially true for the modelling of the responses. The factorial models used during this thesis cannot replace physical theory. Within the margins of the possible factor conditions they are regarded as sufficient, nonetheless. Particularly as the discrepancies between the chips do not allow a highly precise prediction anyway. Different to well-founded simulations the factorial models are also not able to incorporate the time-component. Network models, for example, will produce time-plots that bear high resemblance to actual graphs of the µPIV measurements (Busek et al., 2015).

Aside from the modelling, the interpretation of two- and three-factor-interactions can be tough occasionally. Supporting physical understanding is helpful. Nevertheless, the DoE results point at where to look more closely or, rather, where to be careful.

For future applications of DoE in the context of the MOC three things will highly simplify the evaluation process: First, the closer the experimenter sticks to the proposed experimental plan, the easier is the following interpretation with a specialised DoE-software. Alterations, like deviating the central points, complicate the identification of influential factors partially due to complex aliasing schemes. Second, the integration of the direction of pumping as a separate factor largely increased the effort for preparing the data to eventually enable proper interpretation. Using it on the background of this work helped to identify certain pump behaviours that will be discussed in the following. In further works on other chip layouts it might be advantageous to decide for a specific direction. Third, if the shape of the peaks is of interest a frequency should be chosen that is above the duration of the deflection.

2.4.4. The first DoE-screening – high technical reproducibility and exclusion of factors

The first DoE-screening utilises a resolution IV fractional factorial design (2^{7-3}), which allows an interpretation of the main effects with disregard of possible interactions. And although the data processing is not flawless (for example there is no localisation of extrema in distinct transitions) the results are comparable to those of the second screening.

Apart from the factors' influences two main conclusions can be drawn. First, the measurements are highly repeatable in the same chips. The runs are randomised, and the settings must be readjusted repeatedly. Still, the µPIV results are stable and the reliability of the technique is established. Therefore, no further technical repeats are conducted (except at the central points) to decrease the number of experiments.

Second, the factors length of the tubings and liquid volume within the 2OC are excluded due to their low influence on the average velocity and the velocity extremes. Both might be more influential with bigger differences. Here, the tubings are varied by 1 m and the liquid by 300

µL, only. Another rationale to exclude the length of the tubing as a factor is a very pragmatic one: The longer the tubing the more aggravating the handling of several chips can become. Shorter lengths, on the other hand, are not practical as they should cover the distance between control unit and incubator as well as control unit and microscope. Optimising the length is, therefore, more a matter of feasibility in everyday lab work rather than the flow behaviour in the chip. Moreover, the throttle's action is similar and much better to control. However, what cannot be assessed are the influences from squeezing the tubings in the incubator doors, which, again, can be interpreted as throttling.

The liquid volume in the chip is chosen to account for the gas volume that is inevitably below the lids in the cultivation compartments. Besides the flexible membranes these gas reservoirs are the main compressible volumes of a closed MOC. Hence, they account for the phase dampening effects seen especially in between the cultivation compartments in the ROI WinB. The influence of the liquid volume is not tested for WinB, however. In theory, bigger gas volumes are causing higher dampening. If the volume is big enough it will cancel out backflow in downstream lying channels and a steadier flow close to the average flow rate will be established. This effect can be observed at SpotC in the 4OC. Yet again, optimising the amount of liquid volume can be difficult as it should also account for the nourishment of the cells in the system that require a minimum amount of medium.

Likewise, the factor vacuum could have been excluded after the first screening as it does not show significant impact on the measured responses. At the time, this was regarded as erroneous. Just like the pressure, the vacuum determines the shape of the membranes during actuation. However, in contrast to the pressure the membrane's shape during lifting is not restricted by a glass bottom. This can be seen in the influence on pulse volume. Nevertheless, the insignificance of the vacuum on flow rate and extremes is supported by the findings of the second screening. The reason for this partially lies in its high impact also on the duration of the pulses, which flattens out the extremes.

2.4.5. The robustness of chip manufacturing and remaining factors in terms of flow rate

The extensive second screening specifically focuses on the robustness of the results from different chips as well as on the in-depth analysis of the remaining factors and their interactions towards precise features of the flow profile.

Concerning the average flow rate, the discrepancies between the tested chips are acceptable. The precision is, however, lagging behind other microfluidic pumps such as roller or syringe pumps. It is likely that every MOC works a little different due to hardly or not at all controllable issues during manufacturing:

- For example, the thickness of the membranes is determined by the depth of the membrane spacers during the curing of the PDMS. A highly manual process.
- Also, the depth of the spacers for the cultivation cavities is decisive for the success of the bonding. If screwed in to deeply they can cause bulging of the PDMS layer, which prohibits tight bonding, eventually. Especially for MOCs with several or bigger cavities (like the 4OC) this can be an issue.

- Another possible source for chip-to-chip differences occurs during disassembly of the casting unit: thin residual PDMS at the outlets of the cultivation cavities can impair the flow in one direction. This is sometimes perceived during the filling of the chips, when perfusing with a syringe is possible in one but not in the other direction.
- The most uncontrollable problem remains to be the bonding. Beginning with the impairment of the plasma treatment by unused PDMS monomers (Eddington et al., 2006), to imperfect and leaky bonding across the chip and even inactivated PDMS surfaces around the pump membranes possibly caused by the metal discs that are meant to mask the valves' ridges. The influence of the micropump on the variability between the chips is underlined by the findings that frequency and pressure have a positive effect on the variation.

Over the past years, the awareness towards these issues has been increased. The manufacturing is much more standardised, now. The documentation and further quality procedures help in reducing the rejection rate. Introducing further measures to reduce the manufacturer dependency will be beneficial as well, for example, by adopting ways to firmly determinate the membrane thickness, to condense individual manufacturing tasks and to remove the need for masking the membranes' ridges.

Even without further improvements the advantages of the on-chip micropump concerning the tissue-to-fluid ratio surpass alternative methods and difficulties during manufacturing.

Despite the robustness of the chip, partially troubling are the inconsistencies of the flow rates within the same chip in different ROIs. As the measurement is found to be stable for the same ROI in the first screening the differences must originate during data processing. Two assumptions for the calculation of the flow rate from the linear velocity might not be completely valid: the simplification that regards top and bottom of the channels to be infinite plates and the simplified rectangular shape of the channel's cross-section. Indentations from the aluminium mould or imperfect bonding can mediate bypasses that alter the cross-sectional area and distort the calculation of the flow rate. For a given chip the introduction of a correcting coefficient that equalises the flow rate between the different ROIs might improve the accuracy. If only interested in the average flow rate, it is advised to pursue the analysis in low-speed regions just behind bigger cultivation compartments, such as WinB or SpotC.

In a student research project, further nominal and ordinal factors that influence the flow rate in the 2OC were addressed (Zarske, 2015). Yet, the variability of the tested chips was comparably high and the measurement in the ROI WinA seemed flawed. From the findings for the other ROIs can be concluded, still, that wearing (i.e. aging) appears to be no issue for the MOC over the course of 14 days as the measured flow rates are relatively stable (Fig. 2.24A). Moreover, the influence of the membrane thickness was investigated (Fig. 2.24B). It appears that only a rather low thickness of 300 µm positively impacts the flow rate. A thickness of 500 µm and higher does not influence the output. However, the

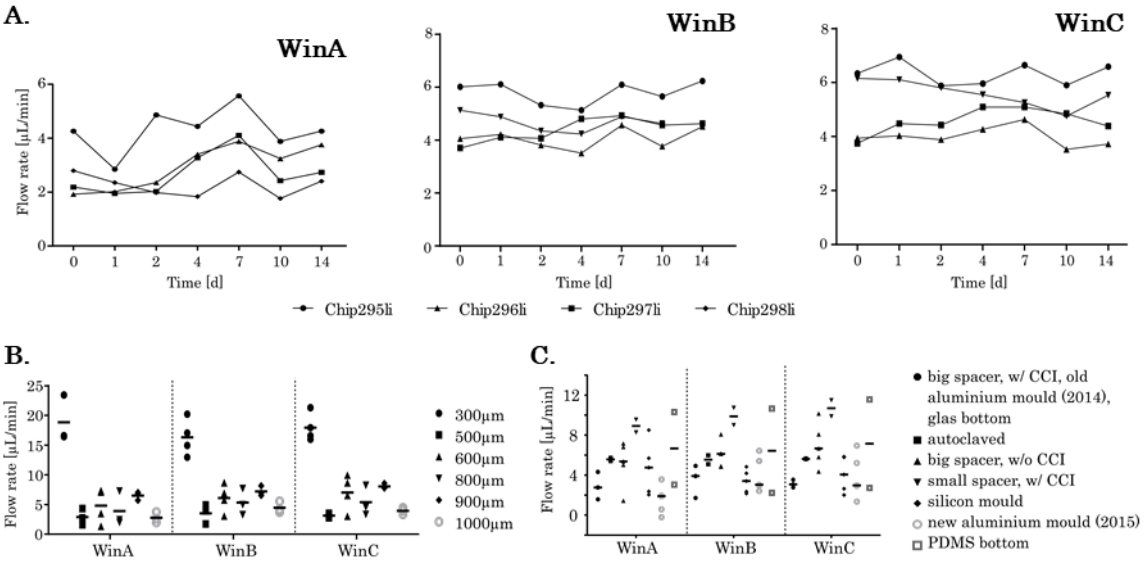

Figure 2.24: Flow rate in dependency of further factors. The graphs are adapted from a student research project (Zarske, 2015). (A) Change in flow rate due to possible wearing of the membranes with a thickness of 500 µm. (B) Variable membrane thicknesses. (C) Other nominal factors. The filled circles describe the standard setup. All other symbols depict deviations from the standard. If present cell culture inserts (CCIs) were placed in the cultivation cavity I2 (compare to figure 2.01C on page 4). For all graphs: The scales are not proportional to one another (n=2-5).

magnitude of the pulses' extrema almost linearly drops with increasing membrane thickness (data not shown). Hence, with increasing thickness the pulses are broadened due to a higher resistance of the membranes towards deformation.

The student, further, tested the influence of autoclaving the chip, of the cell culture inserts and of slight changes of the 2OC design over the past five years (silicon and aluminium moulds, Fig. 2.24C). However, the data is again highly variable allowing only speculations about the validity of the findings. Unclear are the changes on the flow rate for an autoclaved 2OC and a chip with a PDMS bottom instead of glass. Apparently no or only minor influences emanate from the type of mould or rather the three 2OC-designs. The liquid volume in the chip defined by the cell culture inserts and the shape of the respective spacer during curing supposedly has a critical impact that should be considered in future applications especially in automation.

2.4.6. The sealing of the valves is dependent on manufacturing, throttling and pumping direction

The control unit's sequence of membrane actuation defines the main direction into which the liquid is pumped. The MCU defines the two directions as forward and backward, which can be misleading. (Of course, the terms clockwise and anticlockwise are not accurate as well, as they depend on whether the 2OC is viewed from top or bottom and whether the left or right circuit is meant.) But does it matter into which direction the 2OC is pumped? – The answer is yes – the 2OC-circuit is not symmetrical. The flow profile must be different as the friction from the two channels up- and downstream of the micropump is different. Second, a reversal

of the main direction implies a reversal of pushing into pulling of each membrane actuation in the respective transition and *vice versa* (compare to table 2.2 on page 32). As will be explained in the next subsection, there is, however, a difference between pulling the liquid into and pushing it out of the micropump.

Most importantly, the role of the pressure divides the system's behaviour into two states. One where the pressure is high enough to close the valves (which might start somewhere between 20 and 40 kPa) and one where the valves do not close sufficiently leading to inefficient pumping. The pressure that divides these states is, however, not only different between the two valves and from chip to chip. Both of which are possibly caused by flaws during manufacturing. Making things even more complex, this 'dividing pressure' also depends on the throttling and the direction of pumping .

The pressure defines for each chip and valve individually when a valve – for example M3 – is properly closed (Fig. 2.25A,C). However, the pressure cannot be regulated for the membranes separately. Increasing the pressure in order to close the valve strengthens the output from the main pumping element and reinforces the problem. The throttling, on the other hand, defines how quick a deflection of the membrane occurs and, hence, influences the maximum strength and duration of the pulse (i.e. height and width of the peak). It is likely that a stronger pulse from the main pumping element rather than a weak pulse overcomes a

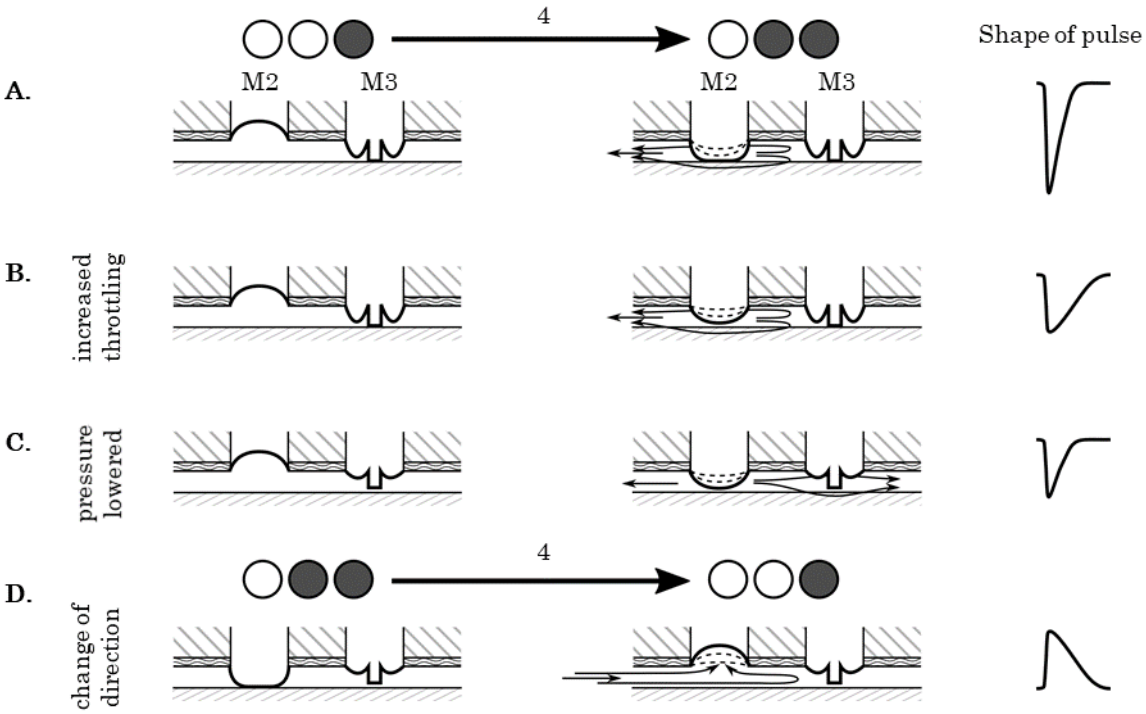

Figure 2.25: Scheme of flow due to membrane deflection in transition 4 of backward pumping. The shape of the pulse is equivalent to the measurement at the ROI WinC, which would be left of the scheme. (A) If the valve (here: M3) closes properly, it does not allow the flow to pass. Hence, the pulse from the deflection is fully transmitted to the left. (B) Increasing the throttling broadens the pulse. The valve closes (even at lower pressure) because the pulse maximum is lowered. The total force applied to the fluid (i.e. the area below the plotted pulse) should be the same as in A. (C) Lowering the pressure (instead or additionally) might lead to insufficient closing of the valve and the pulse is transmitted into both directions. On a side note: Because the magnitude of the pressure is the same for both membranes they both do not deflect as much as before. The pulse volume is smaller, because the pressure is smaller but also because certain volume is lost into the wrong direction. (D) Opposing direction – even at high magnitudes of vacuum its pulses are weaker (because they are broader) and the valve closes already at lower pressure.

closed valve (Fig. 2.25B). Higher throttling (at least of M2) will decrease the 'dividing pressure'. Moreover, during backward pumping the lowering of M2 in transition 4 enacts a higher force on the valve M3 than its lifting during the equivalent transition when pumped forward. Hence, the pressure that lowers M3 must be higher during backward pumping to close it sufficiently than in the opposite pumping direction (Fig. 2.25D). Changing the pumping direction affects the other valve (M1) just the other way around making it a bad measure to improve the closure of the valve, eventually.

2.4.7. Interactions and their implications

The second screening is a resolution V fractional factorial design (2^{5-1}). Besides an unobscured view on the main factors it allows an estimation of the interactions of these. In general, the two-factor-interactions of a resolution V design are potentially aliased by three-factor-interactions and *vice versa*. This means that in a design matrix a particular two-factor-interaction has the same or exactly the opposite set of experiments. In this case with five factors, any two-factor-interaction is confounded by an interaction of the remaining three factors – AB disguises CDE, BC disguises ADE and so on. This becomes a bit clearer with table 5.4 on page 120 in the appendix. Practically the aliasing means for the operator that conclusions about any two-factor-interaction cannot be drawn with last certainty as the effect could emanate at least partially from an underlying three-factor-interaction. The sparsity of these high-order interactions might make them negligible, however. Also, the fragmentation of the data (especially for pulse duration and volume) can lead to partial confounding of the effects. The elimination of the values' prefix in dependency of the set pumping direction excluded the likelihood for three-factor-interactions involving the factor E. For the flow rate, it revealed the aliasing of the interaction of frequency and pressure (AB).

Interactions with the frequency attribute to an interference of the duration between each deflection. As can be seen for the relative pulse duration, high frequencies disturb the complete development of a pulse. If the frequency is too high, the amplitudes of the membranes are not being build up to the extends defined by pressure and vacuum within a transition. For the flow profile this means, eventually, that a given peak interferes with the next one. If they both have the same direction the second is amplified; if they are opposed to one another the next pulse is weakened (Fig. 2.26). Moreover, the pressure acts quicker on

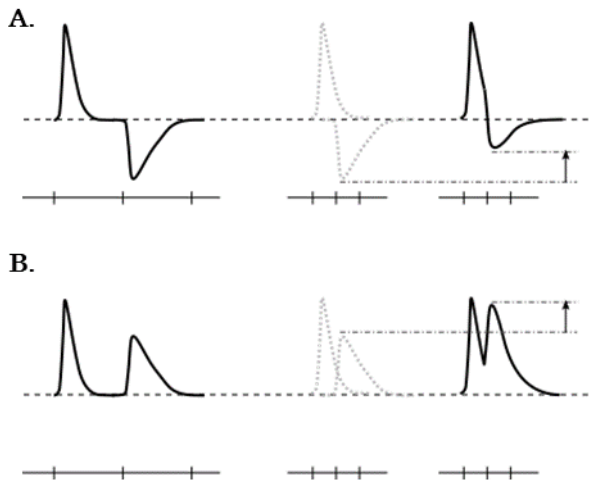

Figure 2.26: Scheme of overlapping pulses. The image depicts the implications of interfering pulses. At a low frequency (left) the pulses have enough time to develop. At a higher frequency (right) the development is impaired. (A) A second pulse is either lowered, if it is opposed to the former pulse, or (B) amplified, if both have the same direction. Pulses that emanate from vacuum (i.e. drawing) are wider and have a lower extreme than those that are attributed to pressure (i.e. discharge).

the membrane than the vacuum. Pushing the membrane down results in a shorter peak than its lifting. Possibly the glass surface mediates that the maximal downward amplitude is reached quicker. Vacuum-mediated pulses are, hence, more likely to be disturbed at a late stage of their development in comparison to pressure-mediated pulses. Therefore, the discharge of the fluid is – if at all – less often interrupted than its drawing.

In conclusion, frequency and pressure are augmenting each other's effects. This interaction is significant for the flow rate and is also reflected in the average WSS. The interaction also implies that if both factors are low there is almost no flow no matter of the settings for vacuum and throttling. On the other hand, either pressure or frequency can initiate flow even if the other is down.

Due to the interference of the pulses, the frequency has an impact on the WSS extremes in both directions, too. It amplifies the extreme in the direction of flow, while it decreases the extreme in the opposed direction. Increasing the frequency can, thus, be advantageous in terms of reducing the backflow, especially starting from the point of overlapping pulses at about 0.8 Hz. Of course, this leads to higher shearing and has implications on the flow rate, too, and should be considered when adjusting. The pressure decreases the backflow more efficiently.

The findings for the shear stress extremes can only describe tendencies, however. The variability of their actual magnitudes between different chips is too high to allow precise predictions. Especially, as only three chips are tested. More different chips could improve the correlation value. This attempt is laborious, however. The 'dividing pressure' referred to earlier should be respected for higher predictability as well.

Figure 2.27: Desired ranges, weightings and consequential values of the factors and selected responses. The graphs depict whether a parameter should be maximised, minimised or a target value should be reached. For each factor (A) the tested range is given; for each response (B) the discovered boundary (far-left and far-right values). The more a given parameter is raised above the baseline, the more it is desired. A detailed list of these values is given in the appendix 5.7 on page 151. The boxes and the values below each graph visualise the respective interval, which is feasible with the given restrictions. The greyer the more likely a value appears in the compromise solutions.

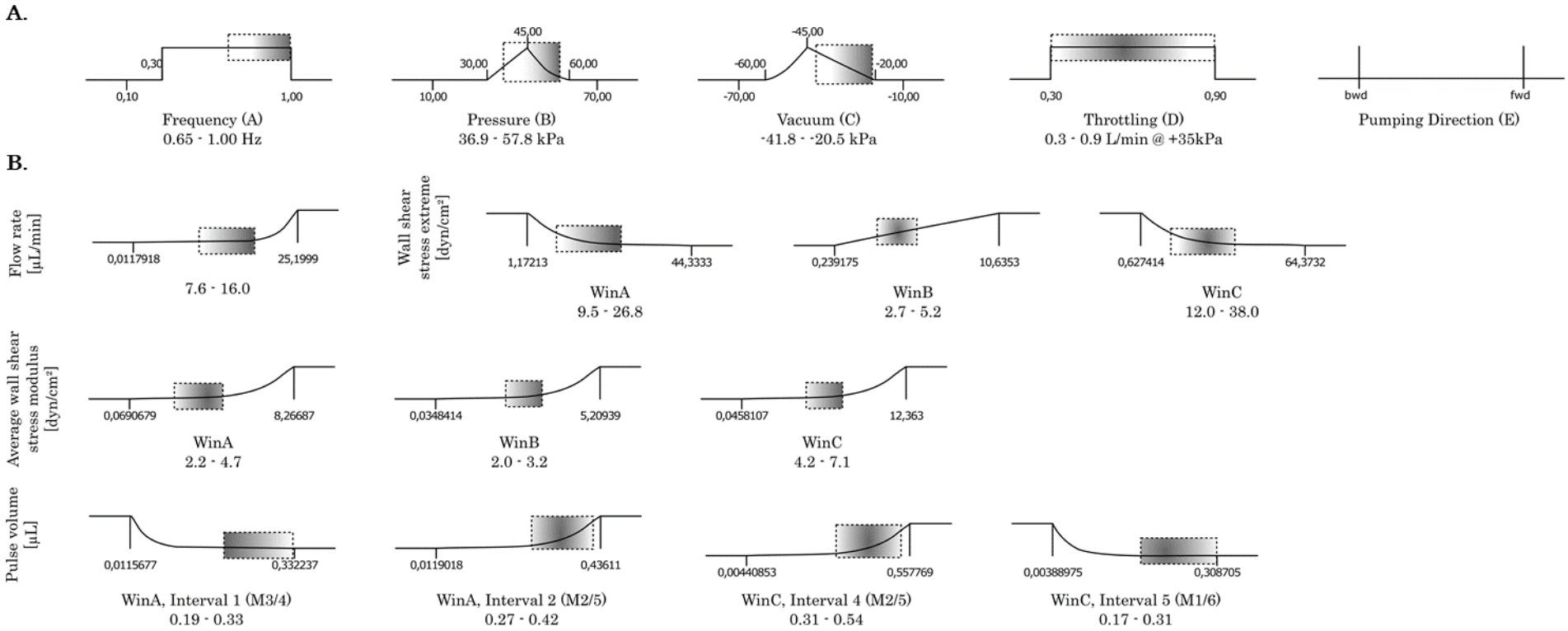

2.4.8. Optimising the flow

The DoE software, DesignExpert®, offers a tool that gives recommendations based on constraint input values and the discovered response models. As already pointed out, these are not well-founded on physical knowledge and do not take the improper closing of the valves into account. Nevertheless, it is a valuable instrument to break the findings down and to find compromises for all the optimising objectives.

For each factor and response, a target range as well as the importance may be defined (Fig. 2.27). For example, the frequency should not be used below 0.3 Hz because higher frequencies are closer to physiological heart rates. The pressure may not go below 30 kPa to increase the likelihood of proper closure of the valves. It is also capped at 60 kPa as several control units with chips share a single pressure source, which, in turn, might not be able to build up higher pressure. Reaching a mid-high magnitude is desirable. The same counts for the vacuum. Throttling and pumping direction are allowed over the whole range.

The task of optimising is to meet certain constraints for the responses, too. The flow rate should be maximised to enable proper turnover of the medium components. The WSS extremes in the ROIs close to the pump (WinA, WinC) may be minimised to be closer to physiological shear stresses. On the other hand, the extremes should be maximised between the cultivation cavities (WinB), because they are generally lower than physiological values. Furthermore, the average WSS should be maximised for the same reason. The duration of the pulses is not too important for optimisation. The pulse volume, eventually, should be as high as possible in the main direction of flow and as low as possible in the opposing direction.

These wishes are barely possible to realise with just these five factors, however. For instance, a high pressure increases the flow rate and raises the shear stress extremes at the same time. Based on the ranges and weightings the tool calculates a desirability value for each combination of settings and exploits the compromises. Proposed ranges for the factors and designated ranges for the responses are given in figure 2.27 and more condensed in figure 2.28. In a nutshell, the frequency and pressure, both, should be set to their upper end of the defined range, while the vacuum should be adjusted as low as reasonable. Throttling and direction of pumping influence some responses but can be freely adjusted to whatever has been defined for the former three factors. However, as throttling reduces the WSS extremes, higher throttling is recommended. The ranges for peak WSS are close to values

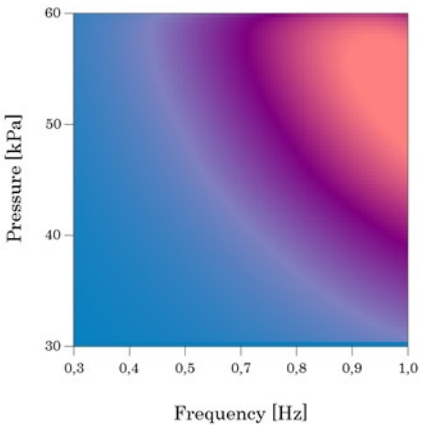

Figure 2.28: Desirability plot of the set factor boundaries. The plot is a condensed version of the results in figure 2.27. The warmer the colour, the better the desired constraints are met. For this graph the direction is forward, the vacuum is set to -25 kPa and the throttling to 0.6 L/min @ +35kPa.

measured in arteries of healthy human patients, which vary between 25 and 43 dyn/cm² (2.5 to 4.3 Pa) in carotid artery, 34 to 40 dyn/cm² (3.4 to 4.0 Pa) in femoral arteries and 27 to 39 dyn/cm² (2.7 to 3.9 Pa) in brachial arteries (Reneman et al., 2006). The mean values range from 4 to 14 dyn/cm² (0.4 to 1.4 Pa) for the same arteries.

It must be pointed out that the pictured optimisation is a rather holistic approach, where all ROIs are regarded as similarly important. This is particularly true for the 2OC as the more distant parts like WinB are only a minor fraction. In more complex chip designs with shorter channels next to the micropump and more dampening by the cultivation cavities (such as the 4OC) the optimisation might be more focused on certain ROIs. Furthermore, backflow will be less of an issue the more micropump and channels are separated by cultivation cavities.

2.4.9. Altering the pumping sequence

Up until recently, the provided control units, MCU and DCU, were relatively closed systems with only limited possibilities to alter the pumping sequence. Changing this sequence might prove to be beneficial. For example, an easy adaptation of the MCU's pumping sequence could be the exchange of the last step (both, forward and backward pumping) with a state where all membranes are lifted (Fig. 2.29). Without much effort that would introduce another peak in the main direction of pumping. Hence, the flow rate will be enhanced without changing WSS extremes. This state does, however, not occur in the *in vivo* heart sequence.

To improve the analogy to the physiological template – namely the beat of the heart – requires other measures. Of course, the heart is much more complex than the on-chip micropump. Nevertheless, there are some structural similarities that allow a comparison: if the main pumping element (i.e. the middle membrane and the cavity below) resembles the left chamber of the heart, then, the down- and upstream valves represent the mitral and aortic valve, respectively. The sequence of the cardiac cycle can easily be recapitulated with the micropump (Fig. 2.30A,B). Other than the original forward sequences the cardiac cycle is more like a 6-transition series.

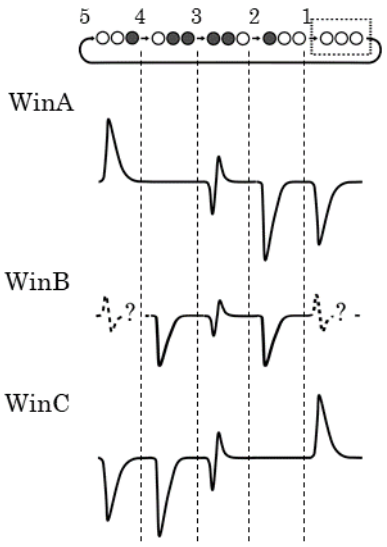

Figure 2.29: Easy improvement of the pumping sequence. The scheme is an adaptation of figure 2.6 on page 16, where the last step is exchanged with an all open state of the membranes (square). The main pumping direction is backwards. Therefore, negative peaks are regarded as pulses in the direction of flow, while positive peaks are considered as backflow. In contrast to the original scheme, another pulse in the main direction is introduced without much effort. In the distant ROI of WinB the overlapping pulses of WinA and WinC create mixed peaks that are hard to predict.

One of the main differences to the cardiac cycle is the duration of each transition. Closing and opening of the corresponding valves usually happens within little less than 100 ms while chamber discharge and refilling take up most of the time (Silverthorn, 2009). This can be recapitulated with the micropump by changing the length of the respective transitions, but also by increasing the throttling for the main chamber so that it does not discharge is entire content in an instant. Altering the frequency should affect the duration of the chamber's discharge and refilling and not necessarily the transitions for closing and opening of the valves. The duration of the isovolumic contraction (IVCT) and relaxation (IVRT) are considered constant (Barschdorff et al., 1995). Age- and disease-dependencies (such as hypertension) for both, IVCT and IVRT, have been described, however (Biering-Sørensen et al., 2016; Hirschfeld et al., 1976; Myreng and Nitter-Hauge, 1989). On a structural side, minimising the dimensions of the valves could decrease their impact in terms of backflow. Moreover, the integration of another chamber – the equivalent to an atrium – could be advantagous (Fig. 2.30C). It would have to move simultaneous but opposite to the main chamber. During the diastole the atrium discharges a bit later than the chamber. Hence, the atrium's membrane should be throttled to some lesser extend than the chamber's but still more than the valves' membranes. The flow profile due to these changes would be severe (Fig. 2.30D).

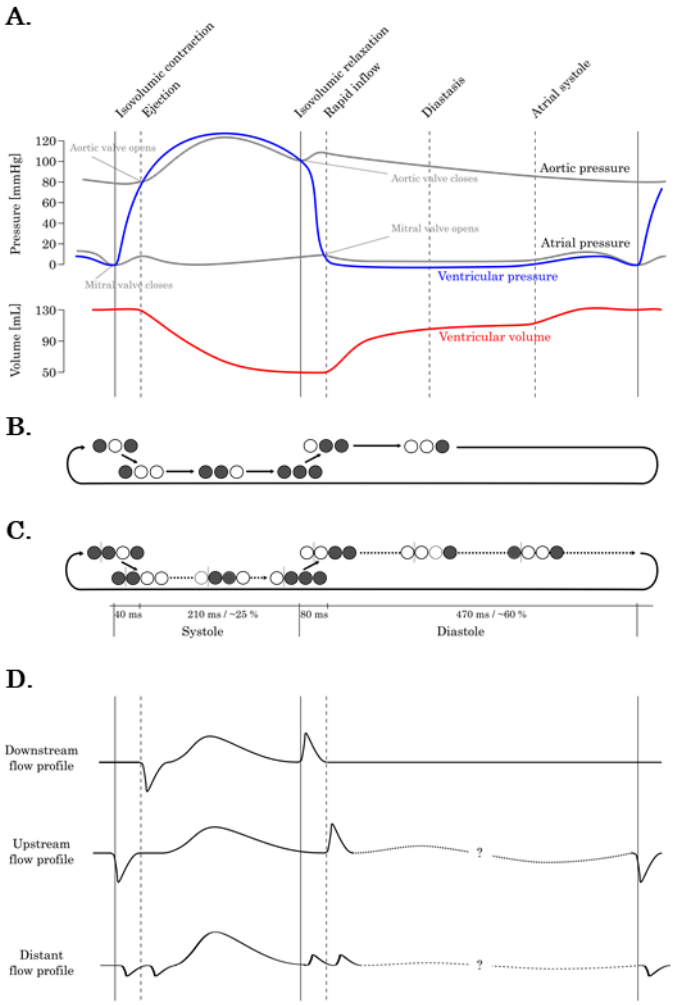

Figure 2.30: Cardiac physiology in comparison to the pumping sequence. (A) Scheme of a Wiggers diagram that relates blood pressure and volume as well as electrophysiological parameters to distinct events of the cardiac cycle. The images is adapted from Wikipedia (DestinyQx et al., 2012). (B) Correlating the sequence of the current 3-membrane micropump to the events during the cardiac cycle. Pumping from left to right, the left membrane represents the mitral and the right membrane the aortic valve. The middle membrane acts as the left heart chamber. (C) Enhancement of the micropump by another membrane on the far-left serving as an atrium. Furthermore, differential throttling is depicted by dotted circles and simultaneous movements by dotted arrows. The absolute and relative duration of each transition is given below. (D) Theoretical flow profiles behind and before the pump as well as in a distant (possibly dampened) channel. The former two only overlap in a single pulse.

2.4.10. Closing remarks

The on-chip micropump is the most important feature of the MOC platform. It is the feature that sets the system apart from most of the other current devices. Its control is, however, not readily comprehensible. And although a lot of influencing factors are now found and understood to some extent, it remains a less precise and less robust pump than other alternatives in the landscape of chip tools. Nevertheless, its benefits especially in terms of scale and tissue-to-fluid ratio are without competition. Comparable ratios are only achieved in pumpless MPS that convey a fluid stream through hydrostatic pressure that is not continuously re-circulating, yet (Kim et al., 2016; Sung et al., 2010). In future versions, the pump will further advance to create a more physiological flow pattern with reduced backflow. This will provide an organic stress pattern and pave the way for a more *in vivo*-like environment for the incorporated cells particularly for the ECs.

2.5. Detailed methodology

2.5.1. Multi-Organ-Chip fabrication

The 2OC contains two independent circuits, each with two fluidically interconnected cavities capable of embodying organoid constructs. Pulsatile perfusion of the system is created by a peristaltic on-chip micropump as described before. The volumetric flow rate in the chip can be controlled by the frequency of actuation, pressure and vacuum, which are externally applied to the membranes. The total volume of the chip is 600 µl, only. The 4OC, containing two overlapping circuits to incorporate four organoids, is considerably bigger. The surrogate blood circuit comprises 830 µL plus 250 µL above the intestinal cell culture insert. The excretory circuit has a volume of 600 µL.

The MOC's fabrication comprises several steps. First, the PDMS layer is casted and fused to the adapter plate (AP). For this a casting unit, the AP, a mould and several spacers are needed (compare to Fig. 2.01A, left, on page 4). The AP has access holes providing an opening for spacers, lid-, cell culture insert-holders and alike. Before the casting it is lubricated with Primer G790 (Wacker) and incubated for 5 min at room temperature. The primer mediates the adherence of the PDMS later. The casting unit arranges both, AP and mould, and defines the thickness of the PDMS layer. The AP, the casting unit and the mould are screwed together tightly. Spacers in the AP prevent distinct areas, like the cultivation compartments, to be filled with PDMS. The mould (also termed *master*) contains a positive of the microfluidic channel structure. For the 2OC the structure is only 100 µm high, which corresponds to the channel height later on. The master stamps the structure into the not-yet solid PDMS polymer (Sylgard® 184, Dow Corning), which is injected in between AP and mould. The polymer is a blend of 10 parts pre-polymer with 1 part of a light sensitive curing agent. A total of about 5 to 6 mL PDMS per chip is needed. Prior to injection, the blend is mixed vigorously until it becomes milky due to small air bubbles. It is, then, degassed in a desiccator until the mixture is clear again. The PDMS cures at 80 °C for 30 to 45 min or at room temperature for about 8 hours. A humid atmosphere (like an incubator) and latex residues from gloves impair the curing and should be avoided. Disassembly of the casting unit is, eventually, done in a laminar flow chamber to prevent dust and contaminations on the PDMS surface. Spacers and excessive PDMS are removed.

Next, the PDMS/AP composite is bonded to a glass slide (or alternatively to another PDMS layer) mediated by electromagnetic plasma – an excited gas that carries charged ions and electrons. The valves are masked by metal plates to prohibit bonding of their ridge structures. The plasma is created in a plasma chamber (Femto, Diener) by ionising air. Among others, ozone radicals form that generate reactive hydroxyl groups on the surface of glass and PDMS. The surfaces are, hence, activated. If two activated surfaces come into contact, they form covalent bonds between each other resulting in a fluid-tight composite. The plasma treatment has further favourable effects: it makes the surfaces hydrophilic which enhances cell attachment, reduces friction in the microfluidics against aquatic fluids and promotes wetting of the channels. However, the effect of activation vanishes if not conserved in an aqueous environment.

After bonding, the three-layer composite remains untouched for 1 to 2 min for the bonding reactions to fully conclude. Then, 80 % ethanol is injected into the chip and let for 5 to 20 min to wet the entire microfluidics and to sterilise it. Subsequently, the circuit is thoroughly rinsed with phosphate-buffered saline (PBS). Then, the desired medium and sterile screwings (compare to Fig. 2.01A, right, on page 4) are introduced depending on the experimental requirements. The medium remains inside the MOC for up to three days before the chip is actually used, thus, saturating the PDMS' surface with components of the medium. Leakages, improper bonding or obstructions should become evident before an experiment. Before its application, the medium is replaced once more and unwanted air bubbles, particularly in the micropump, are removed from the microfluidics. Eventually the chip is connected to a pump controller (MCU or DCU), which controls the pump procedure, its frequency as well as pressure and vacuum.

2.5.2. Preparation of the particles for μPIV

Polystyrene (PS) beads are acquired from ThermoFisher Scientific. Their surface is functionalised with aldehyde and sulphate groups. The optimal particle concentration usually lies at 20 % w/v or 1.3 x 10^8 particles/mL, accordingly. The beads are diluted with PBS.

The RBCs are obtained from venous blood and admixed with EDTA to prevent clogging. After donation, the blood is centrifuged for 10 min at 3,000 g. The plasma is carefully removed; if possible also the buffy coat. The density of RBCs is adjusted to a haematocrit (Ht) of 2.5 % or 2.8 x 10^8 RBCs/mL.

The microfluidics of a designated MOC should be prefilled with either PBS or media. Cell culture inserts or any other volumes should be considered as it will influence the outcome. For the DoE-screening experiments, there are no cell culture inserts incorporated into the MOC. Either particle solution is filled into the compartments according to the design (e.g. 300 μL per compartment in the 2OC). The system is closed with lids by which usually an even distribution of the particles is achieved. If not several minutes of pumping distributes the particles in the system. After some time, the particles might settle, which leads to a decrease of their density in the flowing fluid. If so, shaking will homogenise the solution again.

2.5.3. Recordings for μPIV

To analyse a chip, it is placed on a standard inverted microscope (Axio Vert.A1, Carl Zeiss) with the glass side facing down. A high-speed monochromatic camera (HXC40, Baumer) is positioned parallel to the direction of flow. Thus, it tracks the particle movement in X- and Y-direction. The Z-direction is not accounted for. In communication with a software (microDisplay, Silicon Software GmbH) the particle movement is recorded with high temporal resolution. By default, images are 2,048 x 2,048 px with a recording speed of about 180 frames per second (fps). Through the reduction of the image height the speed of recording can be enhanced. Often the image height is reduced to the width of the channel measuring about 500 μm in the 2OC. Thus, the acquisition rate is raised up to approximately 1,500 fps. Furthermore, it can be doubled by reading only every second photodiode of the camera sensor

in each direction (*subsampling*) causing a reduced maximum resolution of 1,024 x 1,024 px. For the given magnification of 2.5x with subsampling the pixel size is 4.32 µm/px.

The recording lasts between 1 to 15 s. Its length is chosen depending on the duration of a single pumping cycle of the chip's micropump. It should include at least one entirely. However, huge volumes of data might arise. An example: One recording of the ROI of the channel between the 2OC's cultivation compartments (WinB) measures 576 x 120 px (with subsampling and a 2.5x-objective). A single picture has a size of approximately 100 kB. If the pump has a cycle speed of 0.1 Hz (i.e. 1 cycle/10 s) the recording should last at least 12 s. Accordingly, 32,500 single images (2,732.24 fps) are recorded with an overall size of 3.2 GB.

2.5.4. Setting up PIVlab

Before PIVlab starts the image processing the images are edited to lift the contrast and facilitate the correlation later. Four enhancements can be done (Thielicke, 2014): (1) CLAHE is the most important improvement. It homogenises the distribution of pixel intensities in dozens of small parts of the image. Effectively it improves the contrast between background and particle even if both are not homogeneously illuminated. (2) The intensity high-pass excludes picture elements of very low intensity, which are supposed to be reflections or due to inhomogeneous particle density. It is, however, meant for PIV with a dark background and bright particles. As it is exac tly the opposite for the µPIV performed here, it is of no use. (3) Clipping or intensity capping eq ualises the intensity of very bright spots to the majority of bright pixels. It has a similar effect as CLAHE. For the µPIV of the MOC it has the same effect as intended for the high-pass filter. (4) The Wiener filter reduces noise on the expense of clarity. The standard settings for image pre-processing are given in table 2.4. According to the literature these processes could improve the detection of valid vectors by up to 5 %.

Table 2.4: Common settings for image processing in PIVlab.

Pre-Processing	
CLAHE size	20 px
High-pass size	off
Intensity capping	on
Wiener filter size	3
Processing	
Technique	DFT
Sequencing style	1-2, 3-4, 5-6, …
IW 1 size	64x64 px
IW 2 size	32x32 px
IW 3 size	16x16 px
Step size	50 %
Window deformation	spline
Subpixel estimation	Gaussian 2x3-point
Post-Processing	
Velocity limits	none
Standard deviation filter	8 x Std. dev.
Normalised median filter	Threshold = 5, ε=0.1 px

During the actual PIV analysis, the toolbox divides the image into a grid of interrogation windows (IWs). By default, one IW is initially 64 x 64 px in size. Each IW overlaps with the neighbouring IWs by 50 %. Then, with discrete Fourier transformation the movement of the particle cloud in each IW is computed and the numerical solution of this pass is forwarded to the next pass effectively introducing a bias. The IWs of the second pass have an area of 32 x 32 px, then 16 x 16 px, while incorporating the bias from the passes before. Eventually, from the procedure a vector field arises with vectors every 8 px (50 % overlap). Each contains information on the displacement in X- and Y-direction in [px/image pair]. This is converted to [mm/s] using the maximum acquisition rate in [fps] and the pixel size in [µm/px]. If particles move from right to left or from top to bottom the velocity has a positive value. The opposing direction has a negative prefix. The velocity in Z-direction is neglected.

Subsequently, PIVlab interpolates missing data and smooths the vectors. Vast outliers are just not realistic at such a high local resolution of the vectors. The tool allows to exclude vector sizes based on their absolute (realistic) value or semi-automated based on a maximum standard deviation from the median. The normalised median filter as described elsewhere (Westerweel and Scarano, 2005) is a more automatic filter with adapting limits based on local flow states.

2.5.5. Calculating the flow rate

During the image processing, for each pair of images results one vector field. The velocity of each vector is derived from its magnitude in X and Y. All central vectors (according to figure 2.5 on page 12) are then averaged:

$$v_{max} = \frac{\sum \pm \sqrt{v_x(i)^2 + v_y(i)^2}}{n} \tag{2.3}$$

where $v_x(i)$ and $v_y(i)$ are the velocities of the vector i of an IW along the X- and Y-axis, respectively. The prefix is chosen to be the same as v_x for each vector. Calculating the modulus seems unnecessary considering that linear segments of laminar flow should not show flow in Y. However, the modulus accounts for skewed recordings and allows the computation of more complex non-linear segments (e.g. curvatures) by including the flow in Y-direction. From each image pair results a value v_{max}. From this the flow rate Q is determined as:

$$Q = w \cdot h \cdot \bar{v} = w \cdot h \cdot k \cdot v_{max} \tag{2.4}$$

where w is the averaged channel width and h the channel height. The correction factor k with $k = 2/3$ was determined by our co-operation partner, Fraunhofer IWS (Schimek et al., 2013), and is specific for a channel of 500 x 100 µm. It describes the conversion of maximum velocity v_{max} into the mean velocity $\bar{v}$. The factor could also be determined through calibration with a (syringe) pump with known flow rate.

2.5.6. Calculating the shear stress

The following describes the derivation of the shear stress τ. To simplify, we assume two parallel, infinite plates and steady flow. Fluid flows along the X-axis between the plates. The shear stress profile in the XZ-plane is defined as:

$$\tau = \mu \frac{\partial v_x}{\partial z} \tag{2.5}$$

where μ is the dynamic viscosity. Here, it is presumed to be constant. The velocity v_x changes along the height but not along X and Y. Using the law of Navier and Stokes for incompressible fluids the velocity gradient can be resolved as:

$$\rho \frac{Dv}{Dt} = -\nabla p + \mu \nabla^2 \mathrm{v} + f$$

$$\rho \left(\frac{\partial v}{\partial t} + v_x \frac{\partial v}{\partial x} + v_y \frac{\partial v}{\partial y} + v_z \frac{\partial v}{\partial z} \right) = -\nabla p + \mu \left(\frac{\partial^2 \mathrm{v}}{\partial x^2} + \frac{\partial^2 \mathrm{v}}{\partial y^2} + \frac{\partial^2 \mathrm{v}}{\partial z^2} \right) + f \tag{2.6}$$

where ρ is the density of the fluid and ∇p is the pressure gradient between inlet and outlet of the described segment. The term f summarises all other forces (e.g. gravitation) that will be neglected in the following due to their insignificance. To simplify equation 2.6, it is presumed that the flow develops in X-direction and can be neglected in Y and Z. It is also presumed that there are no changes in velocity along X and Y (infinite plates) and the pressure gradient develops only along X:

$$\begin{aligned} v_y = 0, \quad v_z = 0 \\ \frac{\partial v}{\partial x} = 0, \quad \frac{\partial v}{\partial y} = 0 \\ \frac{\partial p}{\partial y} = 0, \quad \frac{\partial p}{\partial z} = 0 \end{aligned} \tag{2.7}$$

Thus, equation 2.6 can be reduced to:

$$\rho \frac{\partial v_x}{\partial t} = \frac{\Delta p}{L} + \mu \frac{\partial^2 v_x}{\partial z^2} \tag{2.8}$$

where L is the distance between inlet and outlet. Again, the flow is presumed steady between two consecutive pictures. The equation, thus, becomes time-independent. As a boundary condition, it is presumed that the velocity in the centre of the channel is at its maximum. Therefore:

$$\frac{\partial v_x}{\partial z} = \frac{1}{\mu} \frac{\Delta p}{L} \left(\frac{h}{2} - \mathrm{z} \right) \tag{2.9}$$

The Hagen-Poiseuille law for rectangular channels with a low height-to-width ratio (*h/w*) is as follows:

$$Q = \frac{h^3 \cdot w}{12 \cdot \mu} \cdot \frac{\Delta p}{L} \tag{2.10}$$

Integrating equations 2.9 and 2.10 into equation 2.5 results in:

$$\tau(z) = \frac{12 \cdot Q \cdot \mu}{h^3 \cdot w} \left(\frac{h}{2} - \mathrm{z} \right) \tag{2.11}$$

This describes the shear stress profile along the Z-axis. At the surface of the channel the WSS is as follows:

$$\tau(z = 0) = \frac{6 \cdot Q \cdot \mu}{h^2 \cdot w} \tag{2.12}$$

2.5.7. Basics of DoE

DoE is a statistical tool to reduce the amount of experiments with the goal to still determine influential factors of a given response. It is not meant for highly precise resolution of an underlying relation between factors and response, but to determine tendencies. For a comprehensive overview as well as deeper insights into the topic the author wants to refer to established literature (Barrentine, 1999; Siebertz et al., 2010; Westerweel, J. et al., 1993). In DoE, the term *factor* comprises the controllable variables, which are coded by the letters A to G, here. The output values are called *responses*.

From a set of factors, the experimenter chooses feasible limits that will define the range of the validity of the test. The factors are usually but not necessarily controllable. The lowest value of any given factor is coded with -1, the highest value with +1. The value in the very middle is called central point and is coded with a 0. All values in between can be coded accordingly and are fractions of 1. With the purpose to determine the influence of each factor and possible interactions an experimenter can test each combination of upper and lower limits with every other factors' limits. This is called a full factorial design. The amount of experiments is exponential for the number of factors. A full factorial design with seven factors comprises $2^7 = 128$ experiments. For three 2OCs with three ROIs this would result in 1,152 single measurements.

Among other concepts, DoE comprises fractional factorial designs. Here, not every combination has to be tested to still result in meaningful results. They exploit the sparsity-of-effects principle, which assumes that only main factors and only minimally factor interactions influence a given response. Higher order interactions are regarded as exceptional or non-existent. Hence, information of some factor interactions is not assessed depending on the design's resolution. Fractional designs are useful, if interactions are negligible or of no importance.

An example of a fractional design is given in table 2.6. It is a design matrix of a fractional 2^{7-3} design of resolution IV. This means 7 factors are assessed with a design that would fit a full factorial design of 4 factors ($2^4 = 16$ experiments). The first four factors are full combinations

Table 2.5: Coding of factors and responses of the first DoE-Screening of the 2OC. The coding can be resolved by inserting it into the equation below. The responses are analysed for the ROIs WinA and WinC only. Therefore, there are only four responses overall.

Factors / Coding	Frequency	Pressure	Vacuum	Direction	Throttling	Length of tubings	Liquid volume
1 (upper limit)	1.0 Hz	75 kPa	75 kPa	forward	0.9 L/min @ +35 kPa	2 m	600 µL
0 (central point)	0.6 Hz	42.5 kPa	42.5 kPa		0.6 L/min @ +35 kPa		450 µL
1 (lower limit)	0.2 Hz	10 kPa	10 kPa	backward	0.3 L/min @ +35 kPa	1 m	300 µL
Decoding	$0.4 \cdot x$	$32.5 \cdot x + 42.5$	$32.5 \cdot x + 42.5$		$0.3 \cdot x + 0.6$		$150 \cdot x + 450$

Responses	Absolute average velocity	Absolute extreme velocity
Unit	[mm/s]	[mm/s]

Table 2.6: Design matrix (2^{7-3}, resolution IV) of the first DoE-Screening. Each run is conducted on the same chip in two distinct ROIs in three independent replicates. This leads to 108 measurements that are conducted in a random order. The order of the designID derives from the corresponding flow rate (Fig. 2.09A).

Design ID	Frequency (A)	Pressure (B)	Vacuum (C)	Direction (E)	Throttling (D) *-ABC*	Length of tubing (F) *-ABE*	Liquid volume (G) *BCE*
1	-1	-1	-1	-1	1	1	-1
5	1	-1	-1	-1	-1	-1	-1
8	-1	1	-1	-1	-1	-1	1
16	1	1	-1	-1	1	1	1
3	-1	-1	1	-1	-1	1	1
9	1	-1	1	-1	1	-1	1
11	-1	1	1	-1	1	-1	-1
15	1	1	1	-1	-1	1	-1
2	-1	-1	-1	1	1	-1	1
4	1	-1	-1	1	-1	1	1
10	-1	1	-1	1	-1	1	-1
17	1	1	-1	1	1	-1	-1
6	-1	-1	1	1	-1	-1	-1
7	1	-1	1	1	1	1	-1
12	-1	1	1	1	1	1	1
18	1	1	1	1	-1	-1	1
13	0	0	0	-1	0	-1	0
14	0	0	0	1	0	-1	0

of all limits. The array that represents interactions of two factors are calculated by multiplying the array of these two factors. For example, in the design matrix the column for the interaction AB is produced by multiplying the individual entries of the columns A and B. Three-factor interactions are generated by multiplying three factor arrays and so on. Now, for the given design the columns A, B and C generate the experimental order for a fifth factor. BCE and ABE generate the array for the sixth and seventh factor, respectively. (The identity here is I = -ABCD = -ABEF = BCEG.) Hence, the order of the experiments for these three additional factors arises from the order of the former four. Simultaneously, any of the three-factor-interactions are disguised by the effects attributed to the newly prescribed main factors. Eventually, also the central points are tested to test whether factor and response correlate linearly and to additionally assess robustness of the measurements.

Every row of the design matrix is the blueprint for an experiment with the depicted variables. For each response, it creates a value. To now determine the effect of a factor on that response, the response array is split into those values deriving from an experiment where the factor's limit is set to +1 and all values for when it is set to -1. Both groups are averaged. The difference between these groups is the effect. It is positive if the +1-group has on average higher values than the -1-group. For visualisation purposes the factors' effects are ordered by their magnitude and depicted in a Pareto chart (which usually only shows the modulus of the effects). Here, significant effects and interactions usually stand out against the other effects and their interactions.

Besides the classical Pareto chart displaying the effects, in this thesis also the t-values of the effects are illustrated that derive from the significance of the factor (or interaction) for influencing the effect. The t-test assesses the risk of falsely confirming that a factor (or interaction) is significant. In this thesis, usually the t-value and Bonferroni limits are given in each Pareto chart that should be surpassed to be considered significant. The former represents the common 5 % alpha error. The latter is a conservative derivative from the t-statistics that uses the common probability divided by the number of all possible unique effects (p = 5 % / 15). As such, it is considered more conservative. Effects that surpass the Bonferroni limit are highly likely to be real. Both limits are, however, still susceptible to replications. If an experiment is repeated three times the relative height of the Bonferroni limit to the effect's t-value is much decreased compared to the average value of the same experiments. Hence, to increase confidence in the identification of effects, in most of the analysis the average values of the experiments are used. Effectively, fewer responses can then surpass the thresholds.

The specialised DoE software, DesignExpert®, helps not only in generating the design matrix and the creation of the Pareto chart. It also helps choosing significant factors as well as analysing their significance. From the significant factors, it produces a factorial model and determines its accuracy. Eventually, it assists in optimising the factors and confirming the effects.

The tables 2.5 to 2.8 depict the experimental setups of the first and second screening using the DoE principles.

Table 2.7: Coding of factors and responses of the second DoE-Screening of the 2OC. The coding can be resolved by inserting it into the equation below. The coding is a bit skewed for some central points, due to improper adjustment during experimentation. There are 19 responses per ROI (5 transitions x 3 responses + 4 global responses).

Factors / Coding	Frequency	Pressure	Vacuum	Throttling	Direction
1 (upper limit)	1 Hz	70 kPa	70 kPa	0.9 L/min @ +35 kPa	forward
0.25 (central point)		47.5 kPa			
0 (central point)			40 kPa	0.6 L/min @ +35 kPa	
0.111 (central point)	0.5 Hz				
-1 (lower limit)	0.1 Hz	10 kPa	10 kPa	0.3 L/min @ +35 kPa	backward
Decoding	$0.45 \cdot x + 0.5$	$30 \cdot x + 47.5$	$30 \cdot x + 40$	$0.3 \cdot x + 0.6$	

Responses per transition	Shear stress extreme	Pulse duration	Pulse volume
Unit	[dyn/cm²]	[%] or [s]	[µL]

Responses global	Average flow rate	Average shear stress in main dir.	Average shear stress against main dir.	Average shear stress modulus
Unit	[µL/min]	[dyn/cm²]	[dyn/cm²]	[dyn/cm²]

Table 2.8: Design matrix (2^{5-1}, resolution V) of the second DoE-Screening. With exception of the central points (6 replicates each) no run is replicated due to the high technical reproducibility found in the first screening. Instead three different chips with three ROIs each are tested. This leads to 252 measurements that are conducted in a random order. The order of the designID derives from the corresponding flow rate (Fig. 2.10). An extended version of the table can be found in the appendix 5.4.

DesignID	Frequency (A)	Pressure (B)	Vacuum (C)	Throttling (D)	Direction (E) *ABCD*
10	-1	-1	-1	-1	1
7	1	-1	-1	-1	-1
6	-1	1	-1	-1	-1
17	1	1	-1	-1	1
8	-1	-1	1	-1	-1
12	1	-1	1	-1	1
15	-1	1	1	-1	1
1	1	1	1	-1	-1
9	-1	-1	-1	1	-1
13	1	-1	-1	1	1
14	-1	1	-1	1	1
2	1	1	-1	1	-1
11	-1	-1	1	1	1
5	1	-1	1	1	-1
4	-1	1	1	1	-1
18	1	1	1	1	1
3	-0.11	0.25	0	0	-1
16	-0.11	0.25	0	0	1

2.5.8. Controlling the factors for DoE

For the 2OC seven factors are regarded worth testing. This section defines and explains the control of these factors.

There are two definitions for the *frequency* (A) depending on the control unit being used. The DCU describes frequency as the amount of pump cycles per second. However, the unit does not allow precise control of the frequency but has 10 set frequencies that rise exponentially. In contrast, the MCU defines the frequency as the amount of membrane deflections per second. In this thesis, the DCU's definition is used as it is more descriptive and relates closer to the heart beat. Furthermore, another difference between the DCU and MCU is the amount of membrane deflections per cycle, which is four and five, respectively (Fig. 2.02C on page 5). The MCU allows frequencies from 0.02 Hz to 1.0 Hz.

The *pressure* (B) describes the maximum overpressure that builds up in the tubing and deflects the pump's membrane downwards. Both control units can control the pressure. In theory, the maximum pressure is set by the used external compressor. The MCU, however, cuts off the pressure at about 70 kPa even if more is available. As the pressured air is also used to generate vacuum through a Venturi tube, it can fluctuate. Fluctuation increases during operation due to the permanent switching of pressure and vacuum in the tubes and due to leakage, which emerge from unconnected tubing as well as other control units on the same pressure supply.

Similarly, to pressure, *vacuum* (C) represents the maximum negative pressure in the tubing, which deflects the pump's membrane upwards. This value can be controlled by both control units but not in older versions of the DCU. The vacuum can fluctuate, too, and its maximum value is limited by the capacity of the Venturi tube. It usually cuts off at about -60 kPa for the MCU. If any leakage of the pressure supply occurs, this value might lie much lower. To stabilise the vacuum, one should, thus, prohibit leakage at all time.

The *throttling* (D) is one of the most delicate factors. It is a measure for the restriction of the flow at the output of the control unit, which results in delay until the set maximum pressure and vacuum values are reached. The throttling is usually controlled by a valve at or close to the very output port of the control unit leading to the micropump's membranes. Simplified, it is set by the size of an opening within the valve. The bigger the more air can pass within a defined time frame. This amount of air, however, is also dependent on the applied pressure or vacuum. In this work, the throttling is given in units of [L/min @ +35kPa]. High values are denoted as "low throttling" and *vice versa*. To adjust the throttling, all except the given output port are turned to vacuum. Then, the pressure of 35 kPa is set and the flow rate at the end of the tubing is measured with a flow sensor (AWM5000, Honeywell). The sensor passes a voltage that can be correlated to a volumetric flow. Depending on the valve the throttling can be precisely controlled with an adjustment bolt. The pressure might change during the adjustment and should be adapted.

The main *direction of pumping* (E) can be either forward or backward. On the left side of the 2OC (viewing from top) forward is defined as clockwise, on the right side it is anticlockwise. For both circuits of the 4OC forward describes clockwise pumping (viewing from top). Figure 2.02C on page 5 depicts the sequence of membrane deflections and their accounted labelling depending on forward or backward pumping for both control units.

When the control unit switches from pressure to vacuum or *vice versa*, the *length of the tubing* (F) influences the delay until the change "arrives" at the membrane. Furthermore, its volume influences how long it takes until the maximum pressure or vacuum is reached. It, hence, acts like a throttle.

The *liquid volume* (G) in the MOC indirectly defines the amount of residual gas phase in the chip. In contrast to the medium, this phase is compressible. It can absorb the energy from the pulsatile flow and release it slowly. Hence, it dampens the pulses, broadens the measured peaks and provides a steady flow, eventually.

Chapter 3

Vasculogenesis in the Multi-Organ-Chip

3.1. Introduction – Why we need to emulate the vasculature in the chip

The second part of the dissertation is subdivided into general aspects of why we need a vasculature in a microphysiological system (MPS) and what efforts have been made by others. Then, endeavours in the 2OC will be presented as well as approaches that go beyond, followed by discussing their outcome within the greater context and an outlook. The chapter is concluded by a description of the methodology.

3.1.1. Structure and haemodynamic influences in blood vessels

Endothelial cells (ECs) generate a confluent monolayer on the inner wall of arteries and veins. They constitute the innermost section – the intima – of the three layers that form a blood vessel. The other two layers are media and adventitia. These are mainly composed of smooth muscle cells (SMCs) and connective tissue, respectively. The constriction and dilation of arteries is due to the contraction and relaxation of the circumferentially aligned SMCs.

The ECs are the main driver for the creation of new vessels. Their action is summarised in the two processes angiogenesis and vasculogenesis (Carmeliet, 2002). The former describes the creation of new vessels by sprouting from existing ones. The latter is the *de novo* generation of a vascular network. For tissue engineers vasculogenesis is the prime scientific target. Still, once established both processes may occur.

The functionality of ECs is frequently influenced by several environmental conditions. For example, cytokines induce the expression of surface adhesion molecules like selectins, vascular cell adhesion molecule (VCAM) or intercellular adhesion molecules (ICAMs). This in turn mediates leukocyte rolling, adhesion and transmigration (Ley et al., 2007). Furthermore, ECs can produce chemokines and coagulation factors. They release vasoconstrictor agents like endothelin or angiotensin II, which not only induce the contraction, but also the proliferation of SMCs (Langheinrich and Bohle, 2005). On the other hand, ECs are capable to attenuate the rheological strain. Especially the production of the vasodilative factor nitric oxide (NO) is important. It primarily defines the vascular tone by mediating the relaxation of SMCs and consequently influences the WSS. Furthermore, NO influences immunological responses by inhibiting the adhesion and activation of leukocytes and thrombocytes as well as SMC migration and proliferation (Voetsch et al., 2004). Eventually, it reduces the oxidative stress within the cells and in the vicinity partly due to the degradation of oxidised low-density lipoprotein and its interaction with reactive oxygen species (Langheinrich and Bohle, 2005; Peters et al., 2013). Increased oxidative stress and the subsequent production of pro-inflammatory cytokines could lead to pathological conditions such as atherosclerosis, eventually.

Shear stress has an important impact on the functionality of the ECs. The first barrier for all blood-EC-interactions is the negatively charged glycocalyx. It is mainly composed of

glycoproteins (e.g. selectins, integrins or members of the immunoglobulin superfamily) and proteoglycans. In addition, soluble plasma molecules are embedded. The glycocalyx is constantly shed and subjected to altering conditions in WSS, frequency, pressure, and blood content. It does not represent a static layer but, rather, a fluid-like, slow-moving and dynamic structure of different ECM components (Reitsma et al., 2007). Depending on the vessel diameter, the glycocalyx is usually 0.2 µm thick in capillaries and up to 4.5 µm in murine carotid arteries (Megens et al., 2006; van den Berg et al., 2003). Shearing is transduced into the EC by a tight interplay of constituents of the glycocalyx with mechanosensors on and in the cells as well as in their cell membrane (Davies, 1995). The sensory complex of platelet endothelial cell adhesion molecule (PECAM-1, also cluster of differentiation 31, CD31), vascular endothelial cadherin (VE-cadherin, also CD144) and vascular endothelial growth factor receptor 2 (VEGFR-2) is probably the best understood structure out of many possible mechanotransducers (Gulino-Debrac, 2013). Among others, they mediate the regulation of genes (García-Cardeña et al., 2001; McCormick et al., 2001), as well as the production of extracellular matrix (ECM) and enzymes regulating vasodilation and vasoconstriction (Ando and Yamamoto, 2009; Barakat and Lieu, 2003; Busse and Fleming, 2006; Wilmer Nichols et al., 2011). For instance, WSS stimulates the upregulation of endothelial nitric oxide synthase (eNOS) as the main source of NO within ECs (Balligand et al., 2009; Florian et al., 2003; Kumagai et al., 2009; Kumar et al., 2010). Furthermore, the WSS effects the cytoskeleton and induces the elongation and orientation of the ECs with the direction of flow (Girard and Nerem, 1995; Levesque and Nerem, 1985; Schimek et al., 2013). Moreover, the healthiness of the glycocalyx and, hence, also the permeability of the entire endothelium (Sill et al., 1995) crucially depends on a proper WSS regime (van den Berg et al., 2006). In short: shearing is caring.

But not only the mere WSS has an impact on the ECs. Also, the pattern of the flow determines the healthiness of the vessel. Already in 1971 Caro *et al.* suggested that certain vascular regions, like bends or bifurcations, are prone to pathological developments due to a changed flow pattern in comparison to other vessels (Caro et al., 1971). Therefore, secondary, recirculating and oscillatory flow and their implications on behaviour of the cells have been intensively investigated (Chiu et al., 2009; Johnson et al., 2011; Kelly and Snow, 2007; Li et al., 2005; Ting et al., 2012).

3.1.2. Vasculature in tissue engineering

Understanding and recreating the vasculature has always been of scientific interest. Since August Krogh pioneered the topic in the early 20th century (Krogh, 1919; Poole et al., 2011) a lot has changed in the knowledge about the vasculature and with the possibilities that modern day cell culture systems offer. With the advent of MPS we are nowadays able to recreate a functional microvasculature that recapitulates the physiology, behaviour and function of the *in vivo* template. The MPS play a central role in recent advances as they not only represent platforms that potentially are able to mimic the appropriate dynamic environment (van Duinen et al., 2015). The development of tissue engineered organoid constructs and their incorporation into MPS has also risen the demand of perfusing them properly, preferably with the help of a microvascular system.

In fact, the lack of a vasculature has always limited the size and physiology of such constructs (Moya et al., 2013). The potential of 3D systems has been much appreciated. Their implementation is, however, slow due to the complexity, their visualisation and higher expenses in contrast to two-dimensional cell cultivation. Nonetheless, the human (or any organism's) physiology and functionality is 3D. Beginning with the processing of nutrients in the crypts and villi in the intestine, over the gradients in the liver lobules, the highly complex entanglements in the brain, or the filtering and reabsorption in the tubules of the kidney to name a few. In order to build models of these organs of relevant size and proper functionality a vascular network will be needed to promote the cell's supply as well as the depletion of waste products (Kolesky et al., 2016; Muehleder et al., 2014; Takebe et al., 2013; van Duinen et al., 2015; Zhang et al., 2016). Any 3D model will eventually require an enabling vascular network – either artificial or genuine – that also follows or even establishes their 3D orientation.

Furthermore, MPS developers inherently try to mimic human physiology. Recreating a vasculature within is only a logical step towards this goal. Evidently, the vasculature has several roles that are needed in any higher organism and that are beneficial in complex, systemic arrangements *in vitro*, as well. Despite supplying the tissues with oxygen and nutrients it enables system-wide communication (e.g. for the humoral system). As mentioned before, bigger *in vitro* models are limited as oxygen, glucose, amino acids, and other essential molecules can only reach the cells by diffusion through the entire construct. The longer the diffusion path the less likely a given molecule reaches the designated cell. If the cells in the aggregate's core are insufficiently supplied they become stressed or they die (Rouwkema et al., 2008a). Eventually they might release factors that negatively influence cells, which are otherwise well supplied (Zhou et al., 2006). To ascertain proper supply of the tissues in higher organisms, distances between capillaries range from some few micrometres in the liver up to 360 µm in the resting muscle (Forster, 1965; Hepple et al., 1996; Hunziker et al., 1979; Krogh, 1919). Tissue engineered constructs were found to have necrotic cores when reaching diameters of 500 µm or less depending on the cell type (Aleksandrova et al., 2016; Tolbert et al., 1980).

Another aspect of 3D constructs is the accumulation of waste products generated by all cells. These need to diffuse away to prevent toxic side effects. This is especially true for liver organoids. The liver has bile canaliculi on their apical side to get rid of any waste products in an orderly fashion (Nahmias et al., 2006). Although blood vessels are not directly involved in transportation of bile, they play a role in the orientation of the hepatocytes. Toxicological studies showed that during regeneration of the lobules hepatocytes reappear from their portal niche and grow towards the central vein using the endothelial sinusoid as guidance (Hoehme et al., 2010). Hence, blood vessels are an instrument for the orientation during regeneration and for the overall architecture of the liver lobules. Similar patterns can be found in several organs (Athanasiou et al., 2013; Baker et al., 2013). It underlines that integrating vasculature in tissue engineered constructs for MPS would not only serve as a mere route for tissue supply but also for cellular guidance. Whether this navigation emanates from direct interactions between the involved cells or whether it is an indirect process emerging from the diffusion of blood constituents is not important for the engineering.

Separate from supply and orientation, the MOC, furthermore, demands a continuous endothelium pervading the entire system. Eventually, the ECs should cover all surfaces that are in direct contact with the circulating medium or – at some point in the future – with a circulating blood surrogate including a model of the immune system. The interest in a continuous intima is, thus, twofold. First, as soon as erythrocytes and innate immune cells circulate through the chip, they need a physiological interface with which they can interact and which prohibits unwanted reactions of these cells like coagulation or inflammatory stimulation. This is especially important as – apart from the vasculature – the system is made of glass and plastics and, in this way, uncommon in a biological environment. Second, a continuous endothelium is also a barrier that controls diffusion of molecules from the lumen into the subjacent tissue. Recreating the barrier in a MPS could mimic effects of autocrine and paracrine communication more accurately. Besides glass, the MOC's main substrate is PDMS. Similar to, for example, fatty tissue PDMS absorbs small and especially hydrophobic molecules but also hydrophilic substances to some extend (Toepke and Beebe, 2006; Wang et al., 2012). Hence, drug metabolites from one organ could be absorbed before reaching the next compartment and false conclusion might be drawn. An endothelial barrier prevents this to some extent. On the other hand, some small lipophilic solutes and water can freely pass the endothelium *in vivo* (Nagy et al., 2008; Ono et al., 2005). In the MOC the PDMS would, hence, act as a sponge mimicking the *in vivo* subjacent (i.e. fatty) tissue.

Considering the flow dynamics in any MPS, dynamic forces are inevitably created by the circulating liquid (the extents are described in the previous chapter). Several tissue engineered constructs actually need external stimuli, like flow shear stress, to operate physiologically. The impact of WSS on ECs has been described before. Recreating these forces is, thus, crucial for the vitality and functionality of the *in vitro* model. There are cells, however, that are not used to physical stress. For example, hepatocytes have been shown to exhibit unfavourable behaviour when exposed to high WSS (Tanaka et al., 2006). Blood vessels or just an attenuating endothelium are, thus, also a protective buffer against harmful forces for the underlying tissues.

In summary, a continuous endothelial barrier penetrating tissue engineered organoids is required for the supply of 3D organoids with oxygen and nutrients as well as for the depletion of waste products. Endothelial cells, further, act as a barrier controlling diffusion of small and large hydrophilic molecules and protecting subjacent parenchymal cells from non-physiological mechanical strain. Moreover, blood vessels potentially provide guidance and orientation for other cells to properly align their respective organoid architecture.

3.1.3. Excurse: A common mistake

Occasionally following correlation is drawn: the distance of capillaries to one another in the body correlates with the diffusion distance of oxygen, substrates and waste products. Therefore, tissue engineered aggregates are limited in their radius to the same diffusion distance.

This, however, is not the case. It is commonly excepted that the oxygen diffusion distance is the limiting factor for artificial 3D constructs. But this distance cannot be derived from capillary distances. The scientific field usually concentrates on muscles as a model organ due

to the regular and almost linear orientation of the capillaries parallel to muscle fibres. Here, the smallest distance between two capillaries lies around 40 to 60 µm depending on the source (Hermansen and Wachtlova, 1971; Hunziker et al., 1979). The diffusion distance is, however, not to be mistaken with that 'average half-distance between two capillaries' (Hermansen and Wachtlova, 1971). This value is considerably different from the diffusive limit found in tissue engineered aggregates, which is accepted to be 100 to 200 µm (Aleksandrova et al., 2016; Carmeliet and Jain, 2000; Rouwkema et al., 2008b). The discrepancy arises from the inhomogeneous distribution of capillaries around muscle fibres. The diffusion from the capillary to the centre of the fibre can be much further than the distance between adjacent capillaries, especially after training (Hepple et al., 1996; Hermansen and Wachtlova, 1971). The centre of a fibre is supplied properly, nonetheless. Hence, the diffusion distance is defined as 'the average distance from a capillary to the most distant mitochondria' (Hepple et al., 1996). Because the number of capillaries per fibre increases with training, it is assumed that not the diffusion distance or capillary distance are of importance for the proper supply of the cells but rather the shared surface area of capillaries and muscle fibre.

Translating the problem back to a 3D aggregate it is obvious that the aggregate shares (idealised) its entire surface with the supplying environment. Therefore, aggregates can be much bigger than expected from the rationale depicted in the beginning. And this is although cultivation media in contrast to blood have a much smaller oxygen partial pressure (i.e. medium carries much less oxygen). If we recreate thick, vascularised tissue components the distance between the vessels should be in the physiological range of 40 to 60 µm.

Two more things should be mentioned within this context: In addition to oxygen, the cell survival in an *in vitro* aggregate can also be determined by the diffusion of a specific medium constituent or even by a specific waste product that accumulates within an aggregate's core. Second, cell survival should not be confused with physiological cell behaviour. The cell's behaviour can be altered, if its location exceeds a certain diffusion distance even though it might not decease. For instance, a cell in the centre of an aggregate might have enough glucose to survive but not enough oxygen to function physiologically (Zhou et al., 2006). The centre of the aggregate must not be necrotic, but the cell's stress signals might be similarly unwanted.

On the other hand, nutrient limitations could be just the right state from the perspective of a tissue engineer that tries to connect a construct to a vascular bed. In an unstressed state the cells might not attract blood vessels to maintain them. Only the stressed cells will release growth factors that, for example, stimulate ECs and incentivise them to sprout into the direction of the stressed cell (Carmeliet, 2002). Only this crosstalk can accomplish a proper connection to the vascular bed.

3.1.4. Existing models of the vasculature

Rebuilding the vasculature has been under intensive investigation over the past decade. Prime principle is to imitate biology as close as possible; using it as a template for any *in vitro* attempt. Straight forward approaches, for example, tried to mimic the actual structure of blood vessels by stacking vasculature-derived cell types within stripes of hydrogels (Tan and Desai, 2005). Combinations of a fibroblast, SMC and EC layer represented adventitia,

media and intima, respectively. Matrix-dependent cell interactions were observed. Also, the cell aligned and elongated revealing basic functionality. However, no real vessel formation was achieved. Others recognised the ability of ECs to form networks inside collagen hydrogels without predefined patterning (Sieminski et al., 2005). They treated outgrowth endothelial cells (OECs), human umbilical vein endothelial cells (HUVECs) and human dermal microvascular endothelial cells (HDMECs) with basic fibroblast growth factor (bFGF) and VEGF among others and monitored not only spreading and elongation but also the establishment of endothelial networks and lumen formation.

Ever since a variety of models for vascular systems arose. As has been reviewed recently, these can loosely be subdivided into two categories: artificially patterned (pre-vascularisation-based) and self-assembly models (Hasan et al., 2014). Both variants are overlapping to some degree.

The first category – pre-vascularisation-based attempts – comprises generally all 3D-bioprinting endeavours. Like the layering tactic described earlier, 3D-printing allows in theory the designated deposition of the right cell type at the right position relative to the other incorporated cell types. Often agarose (Bertassoni et al., 2014) or PEG derivatives like StarPEG (Chwalek et al., 2014) are used to embed and then deposit cells. Finding proper bio-inks is under heavy investigation depending on the requirements of the construct (Ranga et al., 2014). – Is it biocompatible? Shall it dissolve? If so, shall the cells break it down or shall it degenerate autolytically? Shall cells be able to migrate within? And what modulus should it exhibit? There is just more to it than the mere deposition of cells.

Another (due to its ease) promising approach of 3D-printing is the creation of scaffolds that will be sacrificed later in the process. Rather than printing vascular cells in a certain arrangement, this strategy lays the fluidic fundament for cell settlement and perfusion. The process was described for sugar (Miller et al., 2012) and thermo-responsive substrates, like PluronicF127 (Kolesky et al., 2016) or poly-N-isopropylacrylamide (Lee et al., 2016). The principle is as follows: A sacrificial lattice is created that has the 3D architecture of the emerging vessel structure. Then, a hydrogel, for instance gelatine or collagen, is casted around the mesh usually containing additional matrix elements. The scaffold can then be decomposed either by dissolution in water or by lowering the temperature. Subsequently, cells are flushed into the system if they were not embedded in the hydrogel already. These devices are potentially able to demonstrate sprouting of the introduced ECs (Zheng et al., 2012).

In a recently published study poly-octamethylene-maleate-anhydride-citrate (POMaC) layers were stacked on top of another (Zhang et al., 2016). The shape of the layers created a closed microfluidic network that is connected to the external space by micropores. The scaffold, hence, creates a hollow space into which ECs can be flushed. Additionally, an external space is formed that can be filled, again, with any hydrogel containing parenchymal cells like cardiomyocytes or hepatocytes. The device can be used inside a microfluidic chip or transplanted. POMaC decomposes over a long period of at least 28 days. Although a 3D printer is not required to create the lattice (in fact, the authors use several PDMS masters instead), printing surely would be an advantage for the benefit of convenience.

Other devices that fit into the first category of vascular models create lumen for instance by pulling out a needle or wire from a cured hydrogel (Seto et al., 2010), deposit ECs on membranes such as amnionic membranes using photolithographic techniques (Akahori et al., 2010) or recreate microvessels by populating microfluidic networks (Rosano et al., 2009; Schimek et al., 2013). The latter approach enables to control the fluid behaviour and, hence, the shear stress and mass transport phenomena.

The second category of vascular models, the self-organised models, rely on the EC's capability of *in vitro* network formation. Although ECs are not the sole constituent of blood vessels they are the driving force in sprouting, angiogenesis and vasculogenesis (Carmeliet, 2002; Fischer et al., 2006). However, ECs do not form vascular networks if they are not stimulated to do so. Due to their simplicity co-culture models became very popular among tissue engineers to induce vessel formation. Over the last few years, probably any kind of established EC type has been combined with any kind of stromal cell type (Tbl. 3.1). Almost all can form branching networks that interconnect ECs throughout the culture. The networks form *de novo*. Hence, these models tend to mimic vasculogenesis rather than angiogenesis. A recent review from our co-operation partner, the Ludwig Boltzmann Institute for Experimental and Clinical Traumatology (LBI), found that although there are a lot of co-cultivation approaches with distinct functionality and interaction of the cell types, none has proven to be superior to all the rest (Pill et al., 2015). However, the issue of over-vascularisation is only rarely regarded, meaning that the EC density – and possibly also the stromal cell density – is unphysiologically high (George, 2014). Still, the versatility of the co-cultures is not only attractive to study angiogenesis and vasculogenesis but also for tissue engineers trying to rebuild the network.

Table 3.1: Inconclusive overview of combinations of ECs and stromal cells.

EC	Stromal cell	Scaffold	Remarks	Reference
HAECs	SMCs	-	2D	(Wallace and Truskey, 2010)
HUVECs	ASCs	-	2D	(Huttala et al., 2015; Sarkanen et al., 2012; Vuorenpää et al., 2014)
HUVECs	ASCs	fibrin	sprouting assay	(Kachgal and Putnam, 2011)
HUVECs	ASCs	silk		(Kang et al., 2009)
HUVECs	lung fibroblasts	fibrin	sprouting assay	(Ghajar et al., 2006)
HUVECs	MSCs	fibrin	sprouting assay	(Ghajar et al., 2006)
HUVECs	MSCs	fibrin	sprouting assay	(Kachgal and Putnam, 2011)
HUVECs	pericytes	collagen I	in a microfluidic device	(Meer et al., 2013)
HUVECs	SHED	fibrin	mouse transplant	(Gorin et al., 2016)
OECs	ASCs	fibrin		(Holnthoner et al., 2015)
OECs	MPCs	fibrin, Matrigel, collagen I, PuraMatrix	mouse transplant	(Allen et al., 2011)
OECs	SMCs	-	2D	(Peters et al., 2013)

HAECs human arterial endothelial cells, HUVECs human umbilical vein endothelial cells, OECs outgrowth endothelial cells (also EPCs endothelial progenitor cells); ASCs adipose-derived stromal cells; MPCs mesenchymal progenitor cells; MSCs mesenchymal stromal cells; SHED dental pulp stem cells derived from deciduous teeth; SMCs smooth muscle cells

In 2013, two models were published that paved the way for the creation of vessels within MPS in the future. Jeon and colleagues developed a microfluidic platform that enabled the patterning of fibrin hydrogels (Huang et al., 2009). It allowed the loading of fibrin gels with different cell types that are placed in direct contact with a medium channel without mixing them. A delicate array of PDMS columns of defined dimensions delimited the gels. Despite the gaps between the pillars the surface tension of the uncured fibrin in concert with the hydrophobic surface of the PDMS prohibited the fibrin to exceed the boundary created by the pillars. This allowed an unrestricted exchange between adjacent channels at the gap positions. Although not completely new (Chung et al., 2009; Song et al., 2012) a sophisticated arrangement of such channels focused on the formation of endothelial networks (Kim et al., 2013). The design consisted of five compartments in a sandwich arrangement separated by the pillar arrays. The outer compartments held fibrin loaded with fibroblasts. The central area was filled with EC-containing fibrin. In between these compartments medium could move freely. Growth factors released by both cell types could now diffuse freely between the compartments. Without directly interacting, ECs and fibroblasts were still able to communicate. Over the course of four days ECs in the central compartment produced a vascular network, which would not establish without the fibroblasts. As it is the case *in vivo,* the ECs sprouted towards the morphogen gradient build up by the stromal cells. It was also shown that the artificial addition of growth factors such as VEGF could initiate sprouting, too. However, it could not emulate the co-culture environment entirely. The formed network was never as complex suggesting that further factors, the crosstalk of the different cell types or a specific range of concentrations is required to recapitulate the interplay. Furthermore, the directed ECs interconnected with the medium compartment. Without the guidance from the outer compartments this would have not occurred. The ECs would have no incentive to grow outbound. Most importantly, these conjunctions were direct connections into the *de novo* formed vasculature and enabled perfusion as well as polarisation of the microvessels.

Another investigation around George and colleagues created a microfluidic device with a distinct architecture (Hsu et al., 2013; Moya et al., 2013). As in other approaches, network formation was initiated by the co-cultivation of ECs and lung fibroblasts. Unlike the former approach, a pressure gradient across the cell-laden fibrin gel created anastomosis with the microfluidics. This suggested that not only biochemical interactions enable the interconnection of technical and biological vessels. The capillary network was also perfusable, especially at 'supraphysiological' pressure differences between in- and outlet. The magnitude of the pressure difference was shown to be more relevant than the absolute mean pressure. Whether the cells truly perceived the pressure difference or whether it initiated interstitial flow, convection of solutes or alignment of matrix elements remained unclear, eventually.

It is the author's notion that self-assembled networks, which are perfusable, would always surpass artificially created channels. The ECs' intrinsic knowledge should build vascular networks that adapt to the requirements of the tissue. It should control the perfusion of blood or its surrogate in terms of flow rate, shear stress and pressure as well as its permeability. It should organise branching, density and width much more profound than any investigator. It should adjust dynamically as it does *in vivo* – a feature synthetic channels can never meet.

Still, in any MPS artificial microfluidics will play an important role – whether moulded, printed or stacked. Nevertheless, interfacing the microfluidics with integrated organoid constructs must eventually be organised by the cells' programming itself. Hence, combining smart microfluidic design with self-assembling capillaries is the ultimate goal for any MPS engineer.

3.1.5. Fibrin as a hydrogel scaffold in tissue engineering

For the establishment of the vascular bed, hydrogels are optimal scaffold materials as they enable the cells to orientate freely in all directions. As already indicated, a whole range of hydrogels exist that are either of artificial or biological origin. In comparison to other gels, fibrin has several beneficial features:

- It is genuine. As fibrin is part of the blood coagulation cascade it is activated after an injury and prohibits wounds from bleeding. The fibrin mesh is then used as a scaffold for scar formation and eventual re-cellularisation and healing (Madri and Pratt, 1988). Although it is linked to an injured environment it is a scaffold that the repopulating cells recognise and shape to their needs.
- It is sticky. In fact, it is an approved surgical glue applied in clinics, for example in heart surgery where sutures are undesired or in patients with blood coagulation disorders (Canonico, 2003). The feature is also important in MPS for a fluid-tight incorporation into the microfluidics.
- Its curing is an easily controllable and tuneable process. Usually two equally-sized solutions of fibrinogen, the precursor of fibrin, and thrombin, a serine protease, are mixed which starts the enzymatic crosslinking reaction. The fibrin concentration defines the stiffness and the internal strain of the hydrogel. The activity of the thrombin mainly determines the speed of the curing but also its modulus (Weisel, 2007).
- It is of human origin. In contrast to common other hydrogels, like collagen I or Matrigel®, fibrin is extracted from human plasma donations. Due to the clinical application, it undergoes thorough screening for contaminants. Depending on the manufacturer its purity can vary. However, residual components like plasminogen or factor XIIIa (in the product from Baxter) can contribute to gel (in)stability (Weisel, 2007).
- It is degradable. Plasmin is the main driver of fibrinolysis *in vivo*. Its precursor is synthesised in the liver and brought into its active form by tissue plasminogen activator excreted by ECs on-site. Adding aprotinin to a fibrin mix or to the surrounding medium inhibits serine proteases such as plasmin, trypsin or thrombin. Furthermore, matrix metalloproteinases (MMPs) can degrade fibrin (Lafleur et al., 2002). Fibrin's degradability is advantageous to unmodified synthetic hydrogels. Simultaneously, it can be detrimental in long-term applications.

3.2. Results – Attempts to vascularise the 2OC

Besides the two organ equivalents that can be cultivated in the 2OC, its microfluidics can be populated with ECs basically mimicking a third organ – the vasculature (Schimek et al., 2013). Seeding of HDMECs into the chip's channels is not only feasible but also advantageous to simplistic culture dishes. Upon initiation of a volumetric flow the adherent ECs migrate, proliferate and elongate with the direction of flow. The characteristics suggest that the environment is suitable for a proper cell behaviour. The observation of abundant endothelial markers PECAM-1, VE-Cadherin and von Willebrand factor (vWF) provides evidence that the HDMECs are functional and close to their *in vivo* counterparts.

Developing the model further, this part of the thesis presents a possible approach of recreating a vascular bed within the organ compartments that could, eventually, anastomose with the existing vascular model and realise a continuous endothelium. The approach aims to comprise both categories of vascular modelling – artificial channels as well as self-assembled microvessels. As described before, this is regarded as the best way to meet the requirements towards an MPS. This work focuses primarily on the mere creation of microvessels; also, some first activities of organ model integration will be presented. As the experiments give a first insight into the obstacles and successes of vascular formation, it is an unfinished endeavour that concludes with the recommendations and an outlook for new approaches for the platform.

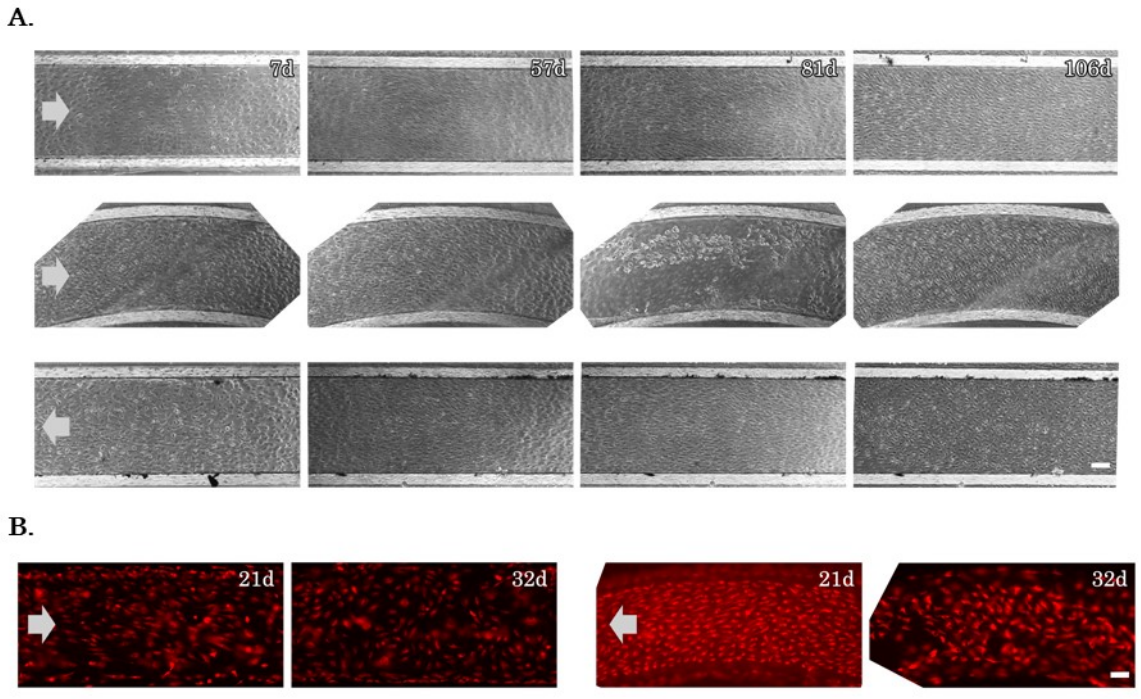

Figure 3.01: Long-term cultivation of primary ECs in the 2OC's microfluidics. (A) Primary HDMECs are cultivated over 106d. The cells elongate with the direction of flow. By the end of the period the cells appear less aligned but still viable. Scoured cells are replaced over time. (B) Primary HUVECs made visible by CalceinAM staining. The cells do not elongate by the shear stress profile emanating from the 2OC's micropump. In all images arrows depict the main pumping direction. The scale bars are 100 µm long.

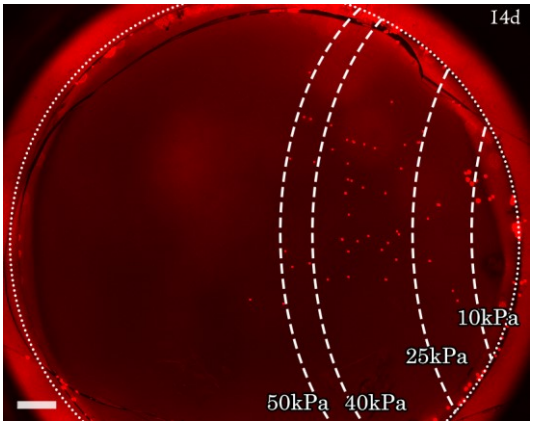

Figure 3.02: Casting of fibrin into the out-most compartment (I2) of the 2OC. Top view of red-fluorescent beads in a chip containing a 200 µL fibrin scaffold (dotted line) pumped for 14 days. Depending on the strength of the pump-driving pressure/vacuum, adhesion of the gel to the glass bottom is diminished and beads penetrate further under the scaffold (dashed lines). The scale bar is 500 µm long.

3.2.1. Considerations of shear on the alignment of endothelial cells

Seeding of ECs into the chip platform is easy and robustly repeatable. Given the groundwork that has been done before, HDMECs are successfully cultivated in further MOC designs (e.g. the 4OC). Furthermore, the cultivation of the HDMECs in the 2OC could be extended up to 106 days (Fig. 3.01A). The elongation of the cells is strongly dependent on the applied parameters of the control unit. Especially increasing the pressure can be beneficial. However, due to the variations in chip manufacturing (discussed in the previous chapter) the impact of these settings could vary from one chip to another. It should be considered that the WSS can be very different at different ROIs depending on the applied flow regime.

An addition to HDMECs as the prime EC type, also HUVECs are used to endothelialise the microfluidics. Especially in low passages they quickly cover all the surfaces of the 2OC. However, different to the HDMECs they do not appear to elongate with the direction of flow even after three weeks of dynamic cultivation (Fig. 3.01B). The nature of this atypical behaviour remains unknown as HUVECs are known to elongate and remodel due to flow (Chau et al., 2009; Inoguchi et al., 2007).

3.2.2. Fibrin hydrogels as a 3D scaffold for network formation

The vascularisation of the cultivation compartments is thought to be a twostep approach. First a vascular bed should be established that is – in an optimal case – connected to the chip's microfluidics. Then, the organoid culture should be integrated that connects to the vascular bed. Whether these steps happen simultaneously or consecutively remains to be investigated.

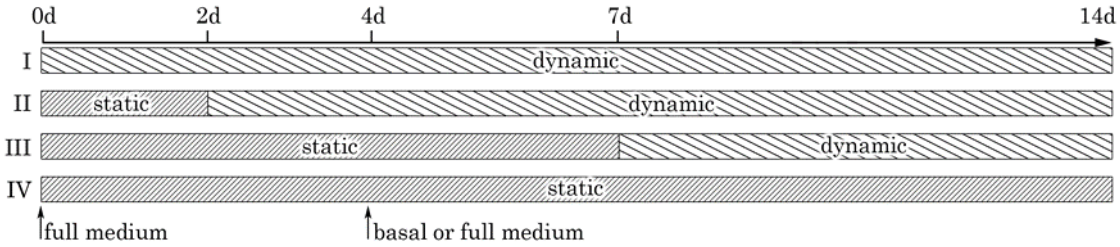

Figure 3.03: Schematic overview of cultivation conditions applied. In experiments with basal medium a complete medium exchange is conducted on day four. In all other cases half of the medium is exchanged either every or every other day.

First, it was assessed whether and how fibrin should be integrated into the chip. The 2OC's out-most compartments are chosen (I2, compare to figure 2.01 on page 4) as its inlet flow is dampened and exhibits less maximum strain to the gel (if the circuit's medium is pumped in forward direction). The fibrinogen concentration is 2.5 mg/mL to eventually allow cell spreading, which becomes more and more prohibited with increasing fibrinogen contents. Moreover, the gel's opaqueness correlates with the concentration of the fibrinogen impairing the visual evaluation, eventually. The thrombin activity is 0.2 IU/mL, which is comparably low (clinicians usually use 500 IU/mL). The gel is left to cure for 30 min. Two volumes, 200 and 300 µL, are used which result in hydrogels of 3.6 ± 0.26 and 5.6 ± 0.21 mm height. Equivalent to the 96-well-plate format, the area of the cultivation compartment is 6.5 mm. Therefore, the gel shrinks by 38 to 40 % during curing.

After initiation of the flow, the fibrin gel remains in place, although the fibrin prohibits the free passage through the compartment. This is important as it indicates that the gel is leak-proof. The medium must go through the fibrin mesh instead of circumventing it. Admixing particles to the medium reveals, however, that fibrin detaches from the glass bottom depending on the pumping strength. The chip's maximum output strength is mostly dependent on the applied pressure. The dependence of the detachment and the pressure is assessed at 10, 25, 40, and 50 kPa (Fig 3.02). At high magnitudes of pressure, the detaches from the bottom. For further experiments, the pressure is adapted to ± 25 kPa to account for the fragility of the given fibrin gel. The plain fibrin gels are cultivated as if cells were incorporated. They are stable in a perfused 2OC for at least 14 days, eventually. How the overall fluid dynamics are altered is not assessed.

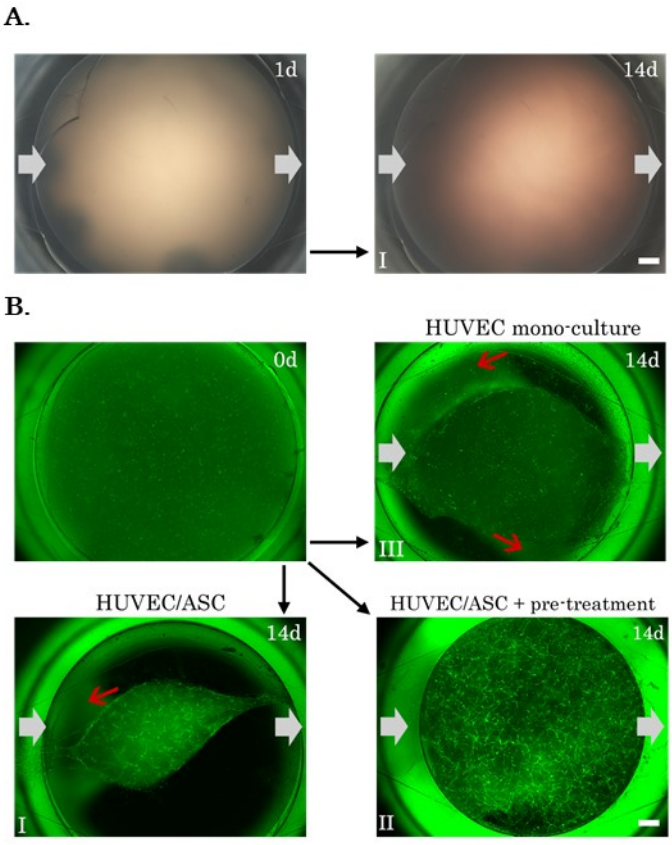

Figure 3.04: Comparison of cell-free and cell-laden fibrin gels. Representative images at 2x magnification of different gels. Grey arrows indicate the main direction of flow. Bottom left number corresponds to the conditions of figure 3.03. Scale bars are 500 µm. (A) Top view of a chip containing 200 µL of cell-free fibrin perfused for 14 days. No shrinkage is noticed. (B) Top left: Cell-laden fibrin gel at the day of the casting. GFP-expressing HUVECs are homogeneously distributed. If not pre-treated with a fibrinogen solution, gels tend to collapse due to the combined effects of flow and cellular actions over the course of 14 days. Gels contain either HUVEC mono-cultures or HUVEC/ASC co-cultures. Admixed ASCs are not visualised. The red arrows indicate the adhesion of fibrin to the PDMS side walls in the higher levels of the compartment.

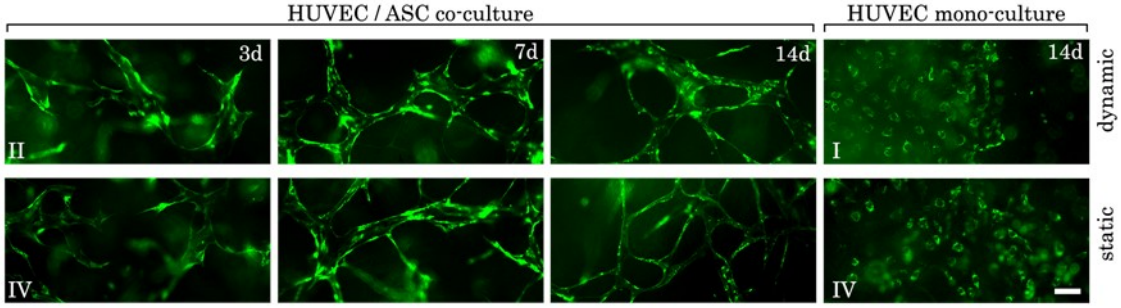

Figure 3.05: Formation of microvascular structures in fibrin gels under different flow conditions. The top row depicts dynamic cultivation in the 2OC; bottom row static in the 2OC. The HUVEC mono-cultures have a completely different morphology after 14 days. The images are representative for the specified day. They are taken at 10x magnification. Bottom left number corresponds to the conditions of figure 3.03. ASCs are not visualised. Scale bar is 100 µm long.

The fibrin appears to adhere better to the PDMS substrate on the side of the compartment than to the glass at the bottom. The PDMS gains a hydrophilic character through the treatment with physical plasma during bonding. This state can be conserved for several weeks in an aqueous environment (Morra et al., 1990). Losing the contact to the PDMS in addition to the glass usually results in a contraction of the gel towards the bulk fibrin revealing the internal strain that builds up within the gel after curing.

3.2.3. Depending on the culture system cells do or do not react to the flow regime

As a co-cultivation system, the combination of HUVECs and ASCs is chosen as both cells are established and well-characterised by our co-operation partner at the LBI. The HUVECs, used here, stably express the green fluorescent protein (GFP) to enable live-monitoring of the cell's morphology in the gel. Two types of cell-laden fibrin gels are compared: one holding the GFP-HUVEC/ASC co-culture and one containing a GFP-HUVEC mono-culture. All cultures are maintained for two weeks in the out-most compartments of the 2OC (I2). The gels are subjected to four different sets of flow pattern (Fig. 3.03) – pulsatile (i.e. dynamic) flow for the entire cultivation period, four days of static cultivation prior to the dynamic flow, seven days of static cultivation prior to the dynamic flow, and no perfusion at all. In all cases, medium is regularly exchanged, which allows continuous monitoring of glucose consumption and lactate dehydrogenase (LDH) activity to draw conclusions about cell viability. Additionally, lactate levels reveal the EC's primary route of metabolism. Eventually, the hydrogels are screened for their expression profile of distinct genes.

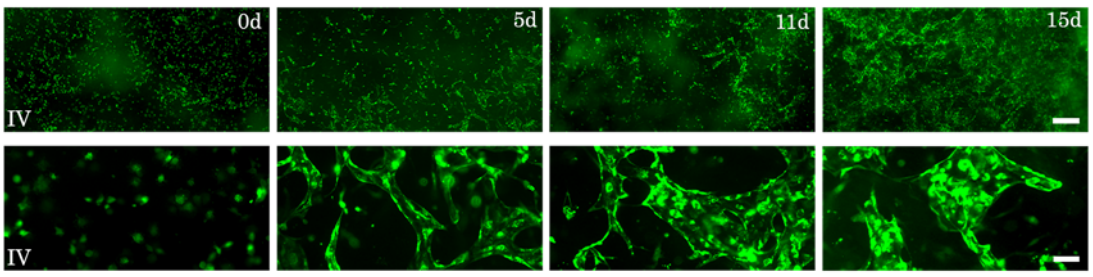

Figure 3.06: Spontaneous formation of tube-like structures in a static HUVEC mono-culture. An example of a rare, spontaneous network formation in a culture free of ASCs. Although still similar to co-cultures after 5 days, the morphology is considerably different at day 11. All pictures are from the same fibrin gel over the course of 15 days. Images in the upper panel are taken at 2x magnification; the scale bar is 500 µm long. The lower panel is taken at 10x magnification; the scale bar is 100 µm long.

In contrast to cell-free gels, the gels containing only HUVECs shrink towards the centre (Fig. 3.04). The cell-laden fibrin exposed to shear stress lose adhesion to the glass bottom, but not necessarily to the PDMS walls of the cultivation compartment. Hence, flow- and cell-mediated gel collapsing is driven primarily by the detachment from the glass surface and is partly a problem of adhesion rather than disintegration. Including the ASCs, however, leads to even further collapsing of the hydrogel especially starting from aside the outlets. The gels may even lose the contact to the edges of the cultivation cavity completely, which results in a spheroidal hydrogel. Pre-incubating the compartment with fibrinogen-enriched medium (2.5 mg/mL) prior to the casting of the gel improves the long-term stability.

Generally, the HUVEC mono-cultures are not able to form tube-like structures in the fibrin hydrogel (Fig. 3.05). Initially well distributed, the HUVECs in the gel appear to migrate towards the glass bottom, where they spread into an unaligned, cobblestone-like morphology and form a mono-layer without protrusions into the gel. This morphology is independent whether the chip is cultivated under static or dynamic conditions. In rare cases, however, spontaneous network formation can be observed (Fig. 3.06). It appears, however, considerably different to co-cultures at later stages. Moreover, it is neither controllable nor repeatable. Low levels of LDH throughout the cultivation suggest, both, viability and low turnover of the cells in any condition. Surprisingly, the expression of VEGFR2, VE-cadherin and PECAM-1 is significantly increased if the gels are cultivated in a dynamic environment for the entire 14 days in comparison to statically maintained gel mono-cultures (Fig. 3.07). They are elevated by two- to five-fold. On the other hand, no significant changes are found for the expression of VCAM-1, vWF, cyclooxygenase-2 (COX-2), or endothelial tyrosine kinase (TEK).

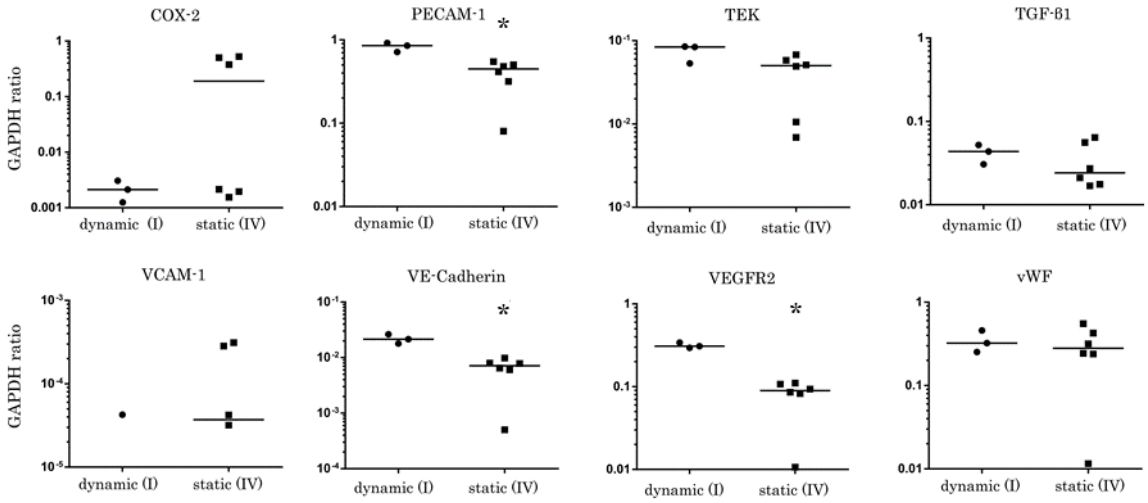

Figure 3.07: Ratio of mRNA expression in HUVEC mono-cultures of selected genes compared to GAPDH expression after 14 days of cultivation. Each point resembles the measurement of a distinct cell-laden fibrin gel from one circuit. The horizontal line depicts the median of each group. Expression levels of VCAM-1 are close to the detection limit. Preparations that are below the threshold are excluded from the graph due to the scaling. Asterisks indicates significant difference ($p < 0.05$) between dynamic and static cultivation conditions.

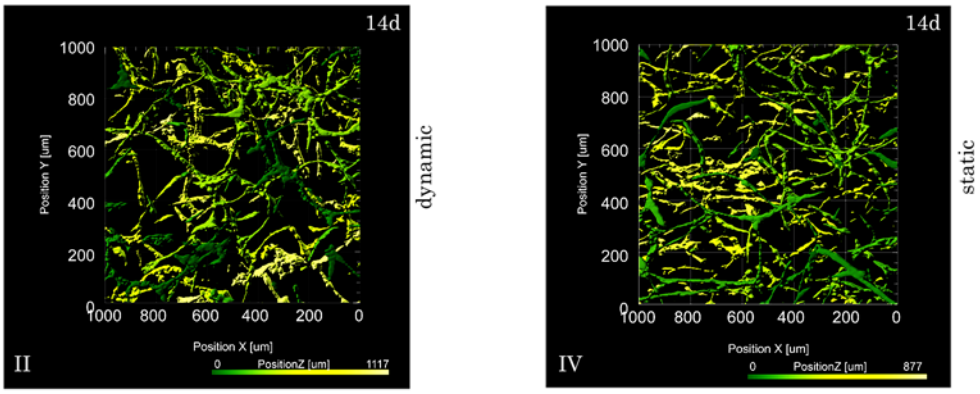

Figure 3.08: 3D rendering of co-cultures in different flow conditions. Image stacks are taken by 2PM. The Z-positions of the branches are colour-coded – darker coloured branches being closer to the glass bottom. The depth of the image acquisition is influenced by turbidity of the hydrogel.

The co-cultures of HUVECs and ASCs exhibit pronounced network formation within seven days. First connections of adjacent cells and small networks form within three days, already (Fig. 3.05). The outer diameter of the tube-like structures is 18.2 to 34.9 µm. Particularly in dynamic cultures, these are considerably stable until the end of the cultivation. The longest and thickest fibres usually form in the bottom fraction of the gel close to the glass surface. The observation of parallel fluorescent linings suggest that the branches are hollow. In any condition, network formation can be observed until a depth of up to 1.24 mm from the glass bottom (Fig. 3.08), which is the limit of the penetration depth of the 2-photon microscope (2PM). Throughout the cultivation singular cells disappear entirely. Subsets of networks remain separate, however. The network formation is found to be independent of the flow environment. Moreover, the flow appears to have no impact on the alignment of the HUVECs or the microvessels inside the gel.

A daily replenishment of half the medium is enough to prevent glucose limitation under, both, dynamic and static conditions (Fig. 3.09). A lower feeding rate is unfavourable as it leads to glucose limitation. In comparison to a static circuit, a continuous flow allocates the chip's entire content to the cells, which can be observed by the complete consumption of the glucose in dynamic chips (Fig. 3.09B). This might be the reason for the apparent earlier demise of the statically cultivated co-cultures. The limitation influences the network stability. Nevertheless, a delayed start (condition II) of the dynamic perfusion is thought to be beneficial for cell adaptation purposes. A daily exchange of 50 % of the medium elevates the glucose consumption to 1.88 ± 0.07 µmol per day and 1.71 ± 0.08 µmol per day in dynamic and static cultures, respectively. Lactic acid, as an indicator of anaerobic metabolism, is at comparably high levels (Fig. 3.10). A conversion rate of 100 % refers to a complete conversion of one molecule of glucose into two molecules of lactate. During the last week, on average 54.3 ± 4.3 % of glucose is converted to lactate in dynamic and 47.0 ± 3.9 % in static environments. In particular HUVECs are known for their high possible production of lactate *in vivo* and *in vitro* (Peters et al., 2009). On the other hand, it could be also an indication for

hypoxia in the gel. The LDH activity increases stably accounting for the cell turnover (Fig. 3.11).

The expressional levels are very different for co-cultures in comparison to mono-cultures. For PECAM-1 the expression elevated by up to fourfold in response to the flow. Apart from that the co-cultures do not exhibit any other significant flow-mediated changes in their expression (Fig. 3.14). The co-cultures, thus, show neither morphological, metabolic, nor expressional effects towards the dynamic flow within the 2OC, although the embedded HUVECs mono-cultures are clearly capable to react to volumetric flow.

3.2.4. The effect of additive-deprived medium conditions on the fibrin cultures

The question whether co-cultured cells are self-sufficient is addressed by supplying a subset of the cultures with medium containing no additives instead of the full endothelial medium starting from day four onward. This basal medium contains antibiotics and aprotinin, but no serum or additional growth factors (the composition of the full medium can be found in the detailed methodology). Interestingly, the network formation is unaffected by the deprivation of supplements in HUVEC/ASC co-cultures, while HUVEC mono-cultures fade. This suggests that during the interplay of the two cell types, factors are produced that are required to partly maintain the microvascular tubes and the viability of the cells (Fig. 3.12). Nevertheless, the branches of the networks thinned out from day ten onwards resulting in a collapse of the

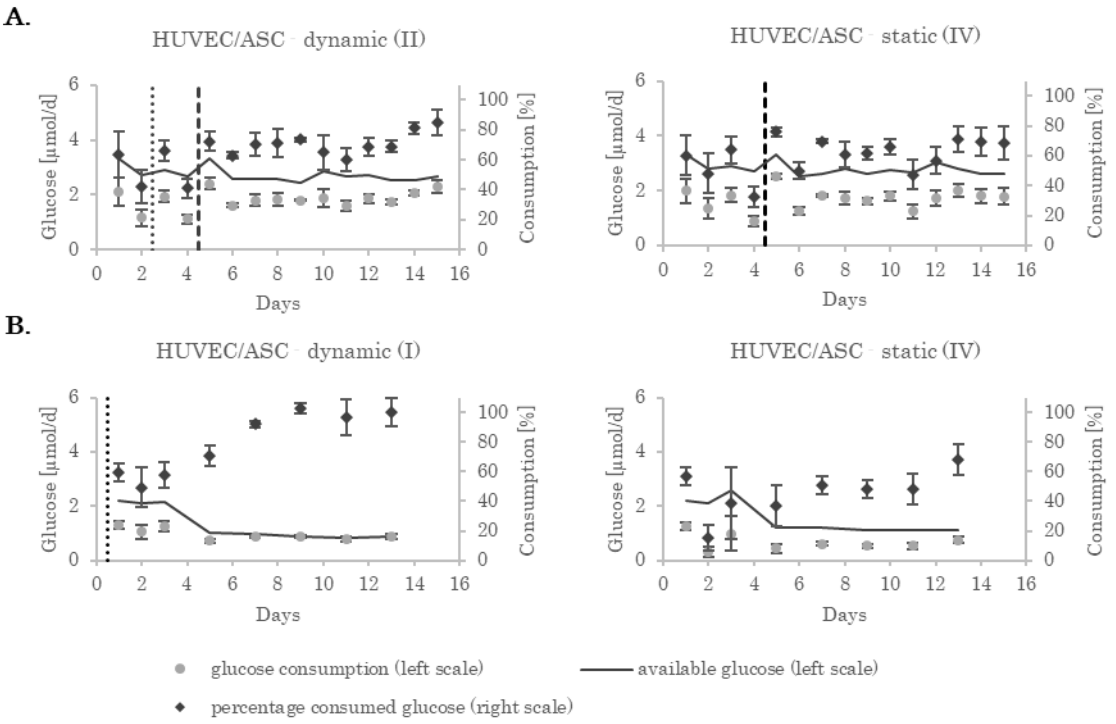

Figure 3.09: Absolute glucose consumption and consumption relative to glucose availability at two different feeding rates. Both absolute uptake and availability (left scales) are higher when exchanged daily (A) in contrast to a replenishment every other day starting at day 3 (B). The drop in glucose availability and consumption after three days is attributed to the reduced feeding rate. A low rate can lead to glucose limitation visible in a high relative consumption (right scale). In all cases half of the medium is replaced. Only on day four of the daily medium exchange regime the entire medium is replaced (dashed line). The values are derived from the supernatants of both cultivation compartments. In the static circuits the available glucose may be lower and, hence, the relative consumption higher. The dotted line depicts the onset of pumping. Error bars are standard deviations of technical repeats (n = 4 - 6).

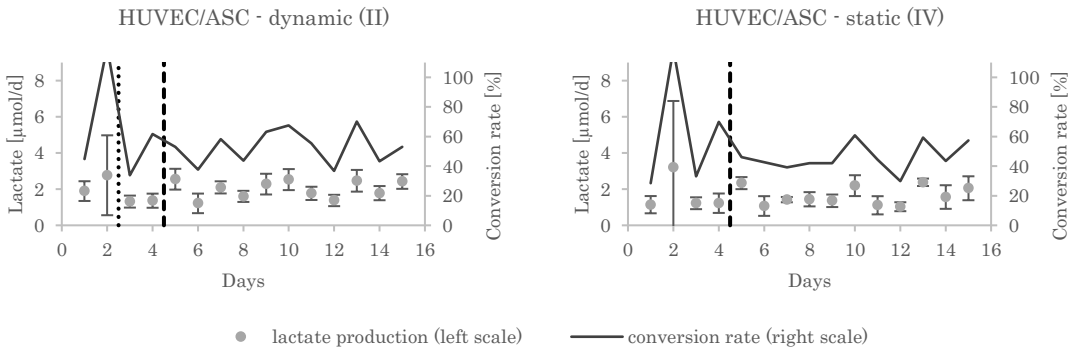

Figure 3.10: Lactate production and conversion rate of HUVEC/ASC co-cultures. The ECs exhibit a comparably high lactate production. For any other cell type this would be an indication for hypoxic conditions. However, HUVECs are known to produce lactate in the presence of oxygen (Peters et al., 2009). The dotted line depicts the onset of pumping; the dashed line marks an exchange of the entire medium content of the 2OC. Error bars are standard deviations of technical repeats (n = 4 - 6).

apparent lumen by day 14. In contrast, the HUVEC mono-cultures perish because of the shortage of medium constituents.

In comparison to the cultures in full medium, the glucose consumption and lactate production profile changes (Fig. 3.13). During the second week, the restricted cultures are consuming 1.59 ± 0.13 µmol glucose per day under dynamic conditions and 1.50 ± 0.15 µmol per day in static environments. Hence, the consumption is slightly lower. Also, the conversion rates for lactic acid is significantly lower in samples incubated with basal media. Only 34.1 ± 8.0 % of glucose is converted in dynamic and 31.5 ± 7.8 % in static cultures. The LDH release, on the other hand, increases two days after the change from full to basal medium (Fig. 3.11). By day nine the values return, however, to levels comparable to cultures in full medium. This may be attributed to an adjustment period to the new environment. The cells eventually re-establish a similar turnover rate as the counterparts in full medium.

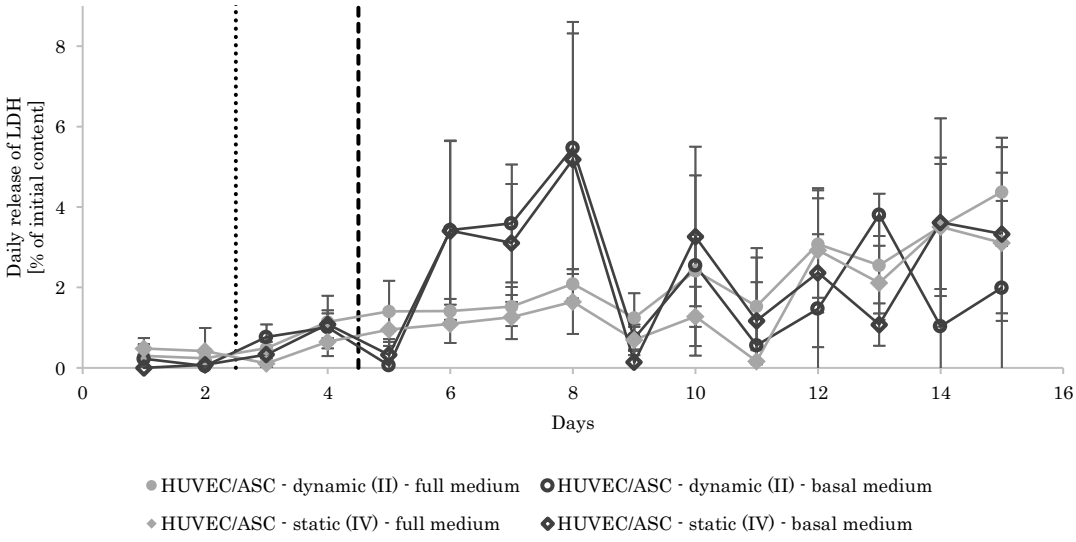

Figure 3.11: Relative LDH activity in media supernatants of HUVEC/ASC co-cultures in different media and different flow regimes. The dotted line marks the onset of dynamic cultivation; the dashed line indicates the complete change from full to basal medium. Error bars are standard deviations of technical repeats (n = 4 - 6).

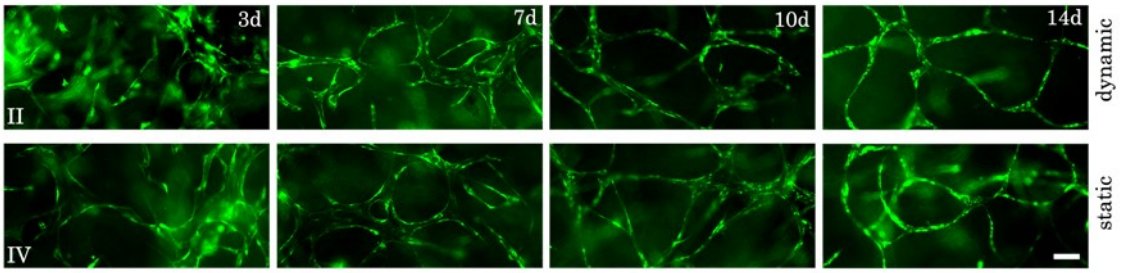

Figure 3.12: Formation of microvascular structures and their maintenance in basal medium in fibrin gels under different flow conditions. The top row depicts dynamic cultivation in the 2OC; bottom row static conditions in the 2OC. Culture medium is switched from full to basal at day three. The HUVEC mono-cultures do not endure these conditions (not shown). The images are representative for the specified day. They are taken at 10x magnification. The scale bar is 100 µm long.

Regarding the expression, VE-cadherin levels are significantly decreased under dynamic conditions. Again, no significant dependencies could be determined in the gene expression levels of the other genes (Fig. 3.14). A summary of the expressional changes in comparison to other published data is shown in table 3.2.

Table 3.2: Summary of qPCR results comparing static and dynamic cultivation conditions after 14 days of cultivation. Bold arrows indicate significant up- or downregulation or no change under dynamic conditions. Thin arrows indicate insignificant trends. * mRNA levels are close to the detection limit. See also figures 3.07 and 3.14. Please, pay attention that reported changes have been monitored after much shorter periods than those of this study, which is two weeks.

Gene	HUVEC mono-cultures, full medium	HUVEC/ASC co-cultures, full medium	HUVEC/ASC co-cultures, basal medium	Reported mRNA regulation (monitored period)	Reference
COX-2	↘	→	→	↗ (24h)	(Topper et al., 1996)
PECAM-1	↗	→	↘	→ (2h)	(Chlupac et al., 2014)
TEK	↗	→	→	↗ (24h)	(Zhao et al., 2002)
TGF-β1	→	→	→	↗ (12h)	(Ohno et al., 1995)
VCAM-1	↘*	→	→	↘ (6h)	(Ando et al., 1994)
VE-Cadherin	↗	→	↘	↗ (48h)	(Shoajei et al., 2014)
VEGFR2	↗	→	↘	↗ (48h)	(Shoajei et al., 2014)
vWF	→	→	↘	→ (6h)	(Galbusera et al., 1997)

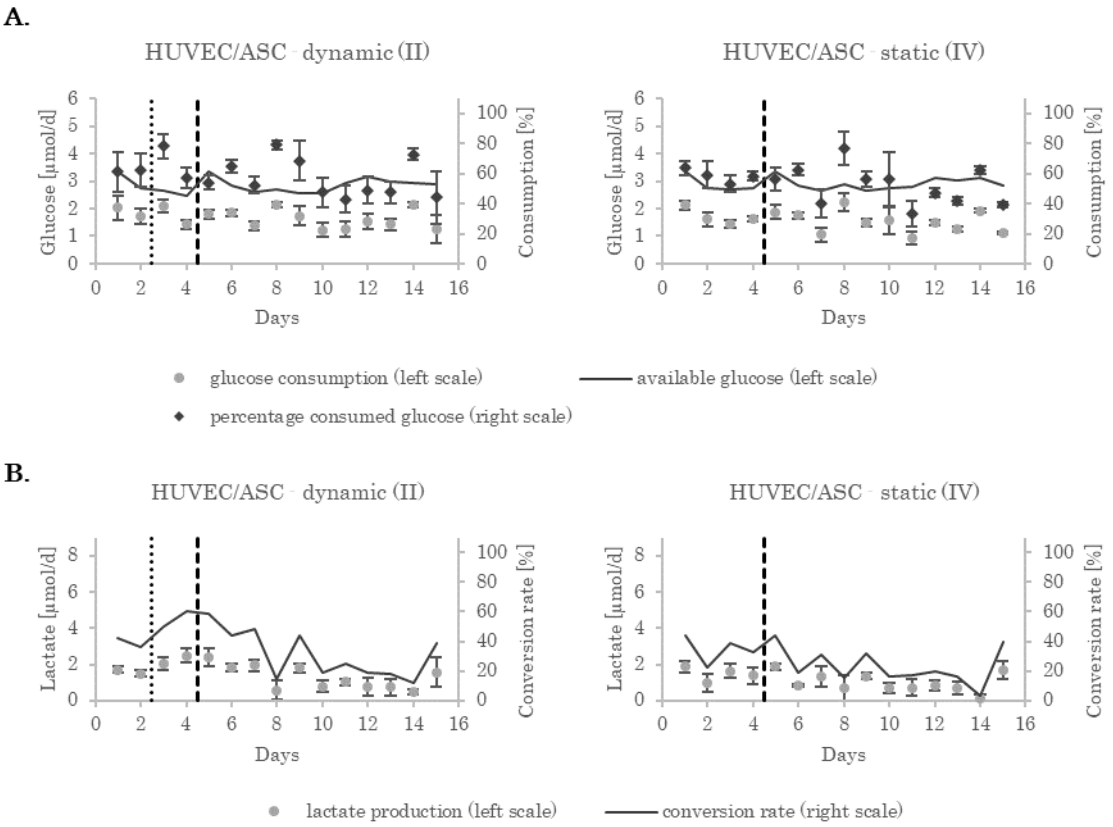

Figure 3.13: Metabolic parameters of HUVEC/ASC co-cultures in basal medium. (A) Absolute glucose consumption (left scales) and consumption relative to glucose availability at dynamic and static conditions (right scale). (B) Lactate production and conversion rate. In comparison to cells in full medium, the lactate production is diminished. The dotted line depicts the onset of pumping the dashed line indicates the complete change from full to basal medium. Error bars are standard deviations of technical repeats (n = 4 - 6).

3.3. Discussion – A HUVEC/ASC co-culture in a fibrin gel as a perspective for vasculogenesis in the MOC

The co-cultivation of ECs with stromal cells is known to mediate microcapillary vessel formation conveyed by the release of pro-angiogenic growth factors, including, but not limited to, VEGF, hepatocyte growth factor, bFGF and TGFß (Rohringer et al., 2014; Sieminski et al., 2005). The application of GFP-expressing HUVECs allows the on-line tracking of the network formation of such a co-culture. In addition to the biochemical interactions between both cell types, the flowing medium conveys a mechanical strain to the fibrin hydrogel. A pressure gradient across a gel and the shear on the surface of the HUVECs has been shown to be beneficial previously (Busse and Fleming, 2006; Johnson et al., 2011; Li et al., 2005). Moreover, interstitial flow can improve the development of capillaries and sprout formation (Helm et al., 2005; Moya et al., 2013), chemotactic cell migration (Shields et al., 2007) and remodelling of the ECM (Ng and Swartz, 2003).

As described earlier, the vascularisation strategy for the MOC platform comprises technically created microfluidics in combination with microtubule formation in the cultivation cavities. Besides established routes of endothelialising the 2OC (Schimek et al., 2013), the efforts and

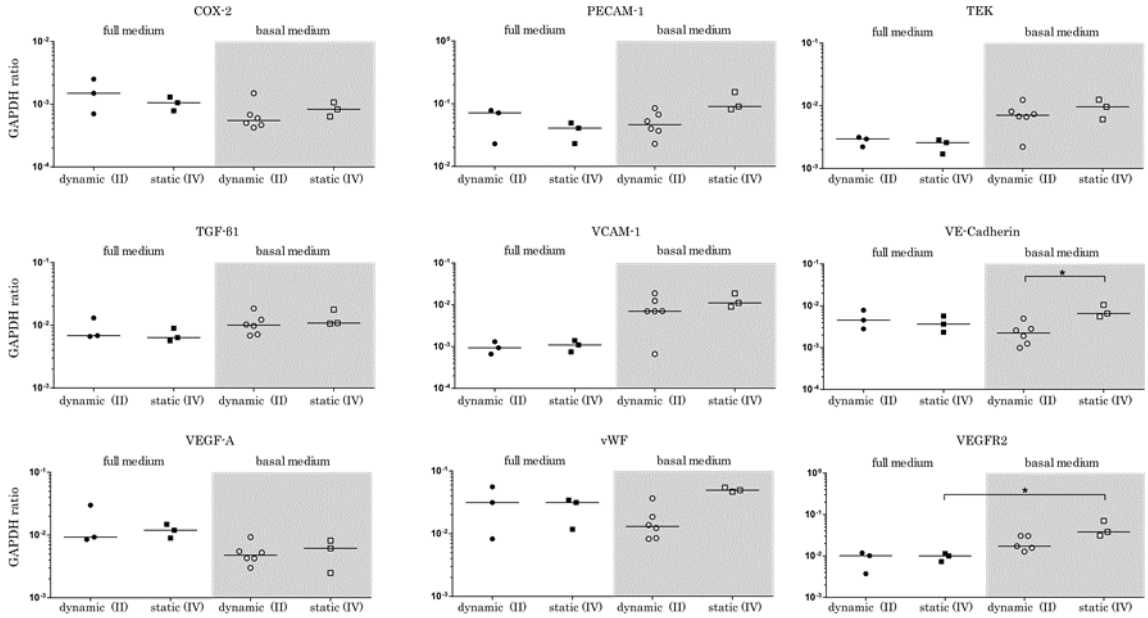

Figure 3.14: Ratio of mRNA expression in HUVEC/ASC co-cultures in different media of selected genes compared to GAPDH expression after 14 days of cultivation. Each point resembles the measurement of a distinct cell-laden fibrin gel from one circuit. The horizontal line depicts the median of each group. Asterisks specifies significant difference ($p < 0.05$) between indicated cultivation conditions.

findings thrive in terms of cultivation time and MOC design. To incorporate tubular networks into the cultivation compartments, the author focuses on the co-culture system of HUVECs and ASCs encapsulated in a fibrin hydrogel. The set-up can be incorporated into a dynamically cultivated 2OC, demonstrating the feasibility of this approach in the MOC platform. Additionally, the cells' ability to self-maintain their phenotype in medium containing no admixed growth factors, cytokines or serum and further concepts of realising perfused microvessels are viable.

3.3.1. Fibrin as a convenient biological scaffold

Hydrogels based on ECM components, such as collagen or Matrigel®, often serve as scaffold material for 3D co-cultivation. Although widely applied they are, however, known to have poor adhesion properties, particularly towards glass surfaces. Glutaraldehyde pre-treated glass slides have been reported to overcome this issue by promoting collagen-glass adhesion (Baker et al., 2013). Only this enables the utilisation of collagen hydrogels in microfluidics. During this thesis, also, an impaired adhesion of fibrin hydrogels to the glass surface of the 2OC has been observed when exposed to dynamic flow of particularly high strengths. The long-term stability of the incorporated fibrin can be improved considerably by pre-coating the cultivation compartments with fibrinogen. A minor disadvantage of this procedure is the potential occurrence of fibrin residues in the microfluidics upon curing of the actual hydrogel possibly due to the distribution of thrombin. These residues can serve as barrier for circulating debris or entirely obstruct the channels in rare cases. Therefore, other protein coatings that promote fibrin adherence might be desired.

A major influence on fibrin stability emanates from the incorporated cells. The HUVECs and ASCs can remodel the hydrogel through the excretion of specific proteases. Although, plasmin certainly is the main driver of fibrin depletion *in vivo*, it has been suggested that MMPs have a substantial influence on fibrin degradation *in vitro* (Ghajar et al., 2006). In vasculogenesis assays they are thought to be utilised for the shaping of the vessels. Moreover, the type of stromal cell in an EC co-culture may influence the set of matrix-modifying proteases employed by the EC (Kachgal and Putnam, 2011). Furthermore, the donor variability of ASCs is thought to have a major impact on tube formation of HUVECs (Rohringer et al., 2014). In any case, the combined efforts of both cell types (maybe even by pure consumption) weaken the fibrin ultrastructure, which leads to the collapse of the hydrogel, eventually. Higher fibrinogen concentrations as well as aprotinin in the medium strengthen the stability of the fibrin.

Our co-operation partner from the LBI assessed how different fibrinogen concentrations influenced the tube formation of the HUVEC/ASC co-culture. The fibrinogen content influences primarily the stiffness of the fibrin (Weisel, 2007). The vessel networks were quantified in terms of number of tubules and branch points. Fibrin gels with fibrinogen concentrations of 2.5, 5, 10, and 25 mg/mL were investigated. For all concentrations, the numbers plateaued after about seven days and slightly decreased until day 14. Smaller concentrations appeared to peak one to two days earlier. Already after four days of incubation fibrin gels containing 2.5 and 5 mg/mL of fibrinogen exhibited a significantly higher number of junctions and tubules than those with fibrinogen concentrations of 10 and 20 mg/mL. This relationship, then, remained over the course of the experiment. However, the detection might have been impaired at higher concentrations as the images became blurrier. Because not all vessels were, thus, accurately quantified in hydrogels with high concentrations the numbers of both, junctions and tubules, might have been underestimated. Although higher concentrations of fibrinogen did not prevent vascularisation they clearly impaired their maturation. In short, the choice of fibrinogen concentration is a compromise, eventually. While lower concentrations promote network formation, higher concentrations are less prone to collapsing and are easier to transfer.

Conveniently, fibrin does not limit the supply of the incorporated cells with nutrients. The production of lactate appears to be more affected by the chosen medium than by actual hypoxic conditions. Ultimately, network formation occurs in the very depth of the gel. The metabolic activity remains constant. This makes fibrin an adequate material for neo-vascularisation experiments. However, its long-term instability and its nature of being a scaffold in wound-healing – potentially conveying an inflammatory stress signal – might be disadvantageous. Whether the fibrin is exchanged with other ECM components over time has not been elucidated conclusively, yet. The addition of other matrix components, hydrogels or further extracellular matrix producers, such as fibroblasts or pericytes, might improve the situation (Kim et al., 2013).

3.3.2. The expression of genes in HUVEC/ASC co-cultures are not affected by the flow

The cell-laden fibrin gels are stable for at least two weeks in the 2OC. Unexpectedly, the mechanical strain of the circulating medium has only little long-term effect in co-cultures on

the expression of selected genes that are known to be involved in angiogenesis and/or mechanotransduction (Tbl. 3.2 on page 84). Proteins involved in shear stress-mediated cell behaviour are, for example, VEGFR-2 and VE-cadherin. Both have been reported to be upregulated in response to shear (Gulino-Debrac, 2013; Shoajei et al., 2014). Here, the direct comparison of dynamic *versus* static cultivation conditions at the end of the cultivation period does not surface any differences, however. In fact, if the co-cultures are supplied by normal full medium, none of the investigated genes exhibit significant changes in their expression pattern. This is in line with the overall morphology that is also not different whether flow is applied or not. In contrast, HUVEC mono-cultures clearly reveal upregulation in the expression levels of VEGFR-2 and VE-cadherin under dynamic cultivation conditions. The reason for the discrepancy is not fully clear. It must be pointed out, however, that the reported expressional changes have been monitored after much shorter time intervals before.

Other angiogenesis-related genes, such as COX-2 (Topper et al., 1996), eNOS (Johnson et al., 2011; Topper et al., 1996), TEK (McCormick et al., 2001; Zhao et al., 2002), or TGF-ß1 (Ohno et al., 1995) have been described to be increasingly expressed upon shear stresses. This could not be recapitulated in any culture over the long term in this study. Likewise, the intercellular adhesion molecule VCAM-1 has been found to be downregulated due to flow (Ando et al., 1994). Though there is a similar trend visible in the mono-culture, it is not significant due to its expression level close to the detection limits for the 2OC experiments. The expression of vWF has been described to be transiently upregulated due to flow, but then to return to its original level eventually (Galbusera et al., 1997; Shoajei et al., 2014). In any culture, here, the expression of vWF is unchanged and, hence, complies with the literature. Nevertheless, its expression is on a relatively high level and might be at its upper limit anyway. Finally, the expression levels of PECAM-1 have been reported not to change despite its involvement in mechanotransduction (Chlupac et al., 2014; Gulino-Debrac, 2013). This is also the case for the 2OC co-cultures. On the other hand, the mono-cultures exhibit a slight but significant increase. The upregulation of PECAM-1 might not be a direct response to shear, but could be attributed to gel invasion and tube formation (Yang et al., 1999). This is not directly observed, here.

On a long-term level, the HUVEC mono-cultures exhibit some expressional changes suggested by other publications. Moreover, their cobblestone-like morphology on the surface of the fibrin is particularly similar to 2D cultures (and these publications). HUVEC/ASC co-cultures, on the other hand, do not present any significant shear-related up- or downregulation albeit their pronounced microvascular structures within the fibrin scaffold.

Two aspects should be deliberated: First, although considered unlikely, opposing reactions of HUVECs and ASCs upon the flow could eliminate the overall effect in the expressional analysis. The individual patterns can only be analysed if both cells were sorted prior to the qPCR. Opposing effects are rather implausible, as ASCs have been reported to acquire an endothelial phenotype under, both, flow or VEGF stimulation (Colazzo et al., 2014).

Second: time-dependent changes in the expression of PECAM-1, VEGFR-2 and vWF in static HUVEC/ASC co-cultures have been described before (Rohringer et al., 2014) underlining the general ability to produce significant results in this system. Therefore, the author assumes

that other than the mono-cultures the co-cultured cells are just too distant and protected from the flow by the scaffold. It is plausible that the rheological strain is, thus, differently perceived by mono- and co-cultured HUVECs. Ultimately, their morphology (flat *versus* tube-like) and spatial location (on the fibrin surface *versus* within the fibrin) could explain the dissimilar perception of the flow. If this is the case, it is an indication that the tubular structures are not functionally connected to the volumetric stream. Either the pressure difference between in- and outlet is not high enough (Moya et al., 2013) and/or bypasses around the gel are created due to fibrin instability. Moreover, the lack of such a connection might be due to the absence of an appropriate guidance from outside of the hydrogel. Crosstalk with a stromal cell type alone is not sufficient for the HUVECs to form an interface to the exterior of the fibrin as has been shown before (Kim et al., 2013).

The competence of carrying flowing blood that exhibits a healthy strain on the ECs is not considered in many co-culture models. It is assumed that this lack of shearing is the reason for the degeneration of the formed networks and their retraction starting after about two weeks (Rohringer et al., 2014). The flow through functional capillaries has been shown to be necessary for the maturation of the network (Nunes et al., 2010). Hence, microvessels might be stable longer than two weeks as seen in transplanted and perfused fibrin scaffolds (Grainger et al., 2013). With other words, although it is clearly important for the initiation of sprouting the pure attraction of ECs with growth factors is insufficient as long as these neo-vessels are unused (McDougall et al., 2006). The networks are not vital vessels. They 'presume' unsuccessful anastomosis and abate – a normal process in *in vivo* network maturation (Carmeliet, 2002). Additionally, the endothelial barrier function cannot establish as long as it lacks a stimulating flow on its surface (Nagy et al., 2008). Eventually, flow is a measure to mediate polarisation of the ECs.

3.3.3. A basal medium as a sufficient supply for co-cultured HUVECs

The permanent crosstalk of HUVECs and ASCs is mediated by the secretion of known and possibly also unknown factors that are ultimately required for the endothelial tube formation. The withdrawal of foetal bovine serum (FBS) and growth factor supplements from the media is an attempt to investigate the self-sufficiency of the co-culture system. For this the co-cultures are incubated in full media for four days and then switched to basal media supply for additional ten days. While the removal influences the tube formation negatively, there are almost no significant effects on the gene expression levels in comparison to the full media equivalents. Only VEGFR2 is elevated in a static environment. Regarding the delayed increase of LDH it can be assumed that certain components of the full medium are retained in the fibrin gel or other voids of the 2OC such as the PDMS. Nevertheless, the full medium should be diluted away with every medium exchange. Moreover, like the LDH levels the cells' expression might adapt to the new environment, eventually, stabilising their expression over time. Whether this is the case would need to be assessed at further time points.

Nevertheless, the utilisation of basal instead of full medium is feasible at least after four days of settling and inducing first tube formation. The co-culture is, then, able to maintain its network. This finding is important for future applications of *de novo* microvessels in substance testing. Supplementation with FBS suffers from lot-to-lot variability, potential

interference with applied substances and an often not fully resolved composition. Hence, the outcome and reliability of assays involving FBS and other undefined additives impairs the validity. Furthermore, the stable phenotype of dynamically *versus* statically maintained co-cultures and full *versus* basal medium conditions reflect the model's capability to be combined with other organoids in the 2OC's circuitry in the future. If the HUVEC/ASC co-culture can maintain itself, it might facilitate the co-cultivation with further organoid cultures as the constraints on a common medium might diminish. Still, any medium composition must be evaluated on its suitability.

3.3.4. Integration of organ models into the created vascular bed

Like the effects of the ASCs on the co-culture, the organoids are meant to create a morphogen gradient that guides the ECs through the scaffold to them. Two things are vital for the success of such a vascular interconnection: the distance between ECs and the guiding cells should not be too high (Rohringer et al., 2014) and the interference of several stromal and parenchymal cell types should be considered.

In another student research project the incorporation of an organoid culture into the co-culture of HUVEC/ASC in a fibrin gel was investigated with regard to the technique of incorporation and behaviour of the cells within (Dotzler, 2016). As model organoid served the well-established liver aggregate (Maschmeyer et al., 2015a; E.-M. Materne et al., 2015; E. M. Materne et al., 2015; Wagner et al., 2013). First, a common medium was found that contained 70 % of the hepatocyte-specific medium (Williams' E with glutamine, hydrocortisone, insulin and 10 % FBS) and 30 % of the full endothelial medium. Then, two approaches to incorporate the aggregates into the gels were conducted. First, the hepatic spheres were injected into a curing fibrin gel. This resulted in the inhibition of the curing process, possibly due to the dilution of the fibrin with medium that inevitably came with the aggregates. Second, the aggregates were set into the cultivation compartment one day prior to the casting of the gel. However, the pre-treatment of the compartment with fibrinogen solution in combination with the aggregates created a thin fibrin mesh that, again, impaired the proper curing of the EC-laden fibrin gel later. Therefore, two techniques were suggested for an improved embedding of the organoids: Either the aggregates need to be admix to the fibrin pre-solution with an increased fibrinogen content to cope for the unknown amount of extra medium, or they are set on top of a cured gel.

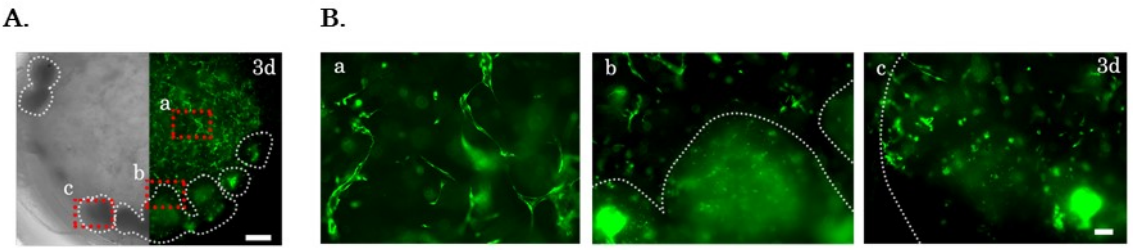

Figure 3.15: Liver aggregates in a HUVEC/ASC-laden fibrin gel. The graphs are adapted from a student research project (Dotzler, 2016). (A) Overview of the cultivation compartment showing the aggregates (highlighted by white dots) incorporated in the fibrin gel. The scale bar is 500 µm long. (B) Close-ups of the red squares. Network formation is visible offside of the aggregates (a), but not in their vicinity (b). The scale bar is 100 µm long.

Furthermore, the aggregates appeared to prohibit network formation in their vicinity independent of the technique being applied (Fig. 3.15). Whether this behaviour is a technical or a biochemical issue remained unclear, eventually. Nevertheless, it points out that the integration of organoids is less trivial than thought. The connection of organoids to a pre- or post-formed vascular network can only be successful if the ECs can be incentivised to grow to and even into this organoid. This might be prohibited, however, in an overstimulated EC/stromal cell co-culture with abundant and homogeneously distributed (i.e. undirected) growth factors. This is underlined by the following short experiment: Two fibrin gels were produced with one containing the commonly used HUVEC/ASC co-culture, while the other contained only HUVECs. After 12 days of maturation the gels were incorporated into the centre of another fibrin gel that was surrounded by an ASCs-containing gel with the purpose to attract the HUVECs from the former gel towards them. While there was clear sprouting visible from the mono-culture the co-culture did exhibit almost no sprouting (Fig. 3.16).

Taking all together, even though the co-culture of ECs and stromal cells is a convenient tool to investigate network formation it might not be the appropriate strategy for vascularising organoids. Given that the organoids likely use the same mechanics to attract the ECs and initiate tube formation as the stromal cell, the vascularisation of the organoid is prohibited. In the 'normal' co-culture setting the stromal cells are in direct contact and, thus, much closer to the ECs. Instead, tube formation may be initiated by the organoids themselves. But even then, stromal cells will be needed to direct the ECs towards the microfluidics as will be explained in the following section.

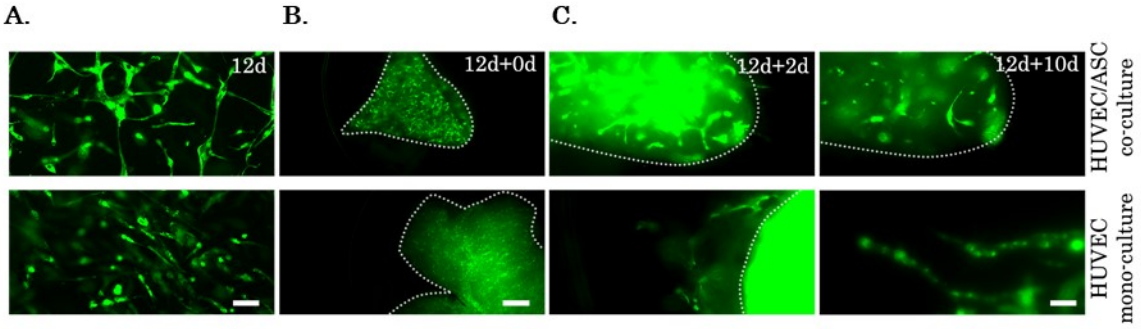

Figure 3.16: Sprouting assay of cell-laden fibrin gels. (A) Fibrin hydrogels containing either HUVEC/ASC co-cultures (top row) or HUVEC mono-cultures (bottom row) cultivated for 12d. Expectably, network formation is observed only for the former. Scale bar is 100 µm long. (B) The exact same gel is introduced into a cell-free fibrin gel that is surrounded by a gel containing only ASCs. The original gels (highlighted by white dots) collapse upon punching. The scale bar is 500 µm long. (C) Sprouting from the HUVEC-containing gel can only be observed for hydrogels containing only the mono-culture suggesting that the co-cultured HUVECs are unable to perceive growth factor gradients from outside the original gel. Scale bar is 100 µm long.

3.4. Creating a new design – Introducing the MOC4Xt

The formation of a vascular network is feasible in the 2OC. Still, the creation of connections to the microvessels cannot be achieved in a plain 2OC. The idea for an extended design of the 2OC (working title: MOC4Xt) is inspired by the publication of Jeon and colleagues (Kim et al., 2013). They reproduced perfusable microvessels *in vitro* with techniques that are accessible to the author and adaptable to the group's needs. Several design rules are applied:

- The patterning of the fibrin hydrogels is adapted from the publication template (Fig. 3.17B). The sandwich design has outer compartments (OCs), a central compartment (CC) and in between a medium channel (IM). The OCs hold fibrin loaded with fibroblasts or another sort of stromal cell type. The CC contains ECs in a fibrin hydrogel. As in the direct-contact co-cultures, network formation should occur due to the interaction of the cell types across the medium channel.
- The columns that delimit the compartments have a hexagonal footprint. It is thought to be an optimal shape to prohibit leaking of the gel into the other compartments (Huang et al., 2009). The surface tension forces that restrict the gels build up at the tips of the hexagon. The proximity of these tips is crucial and is chosen to be 100 µm.
- The filling of the chip must be done as in a normal 2OC; i.e. with two syringes attached to two cultivation cavities. Because it is not applicable to have the fibrin gel and the filling of the chip in the same place another cavity is included into the design. This compartment is solely meant to comprise the patterned fibrin gels.
- The medium should be allowed to flow freely in the IM. Its exchange throughout the cultivation period must be ensured. Hence, in the beginning of an experiment both IMs are connected to the rest of the circuitry.
- To, then, incentivise an interstitial flow across the EC-laden compartment valves ensure that the medium can only pass through the CC. These valves are designed bigger than usual to warrant that no bypass occurs as has been observed for the pump valves (see previous chapter).
- The size of the CC is adapted to the size of the spacers already in use in the laboratory.
- Access holes to the OCs are ensured by newly created spacers. Their screw diameter is chosen according to the syringe adapters. Originally, it was conceived to inject the liquid fibrin through a syringe.

As the dimensions of the hexagonal columns are essential to hold back the liquid fibrin the master must be created with precise photolithographic techniques. Our co-operation partners from the Technische Universität Braunschweig created a master mould from SU-8. The

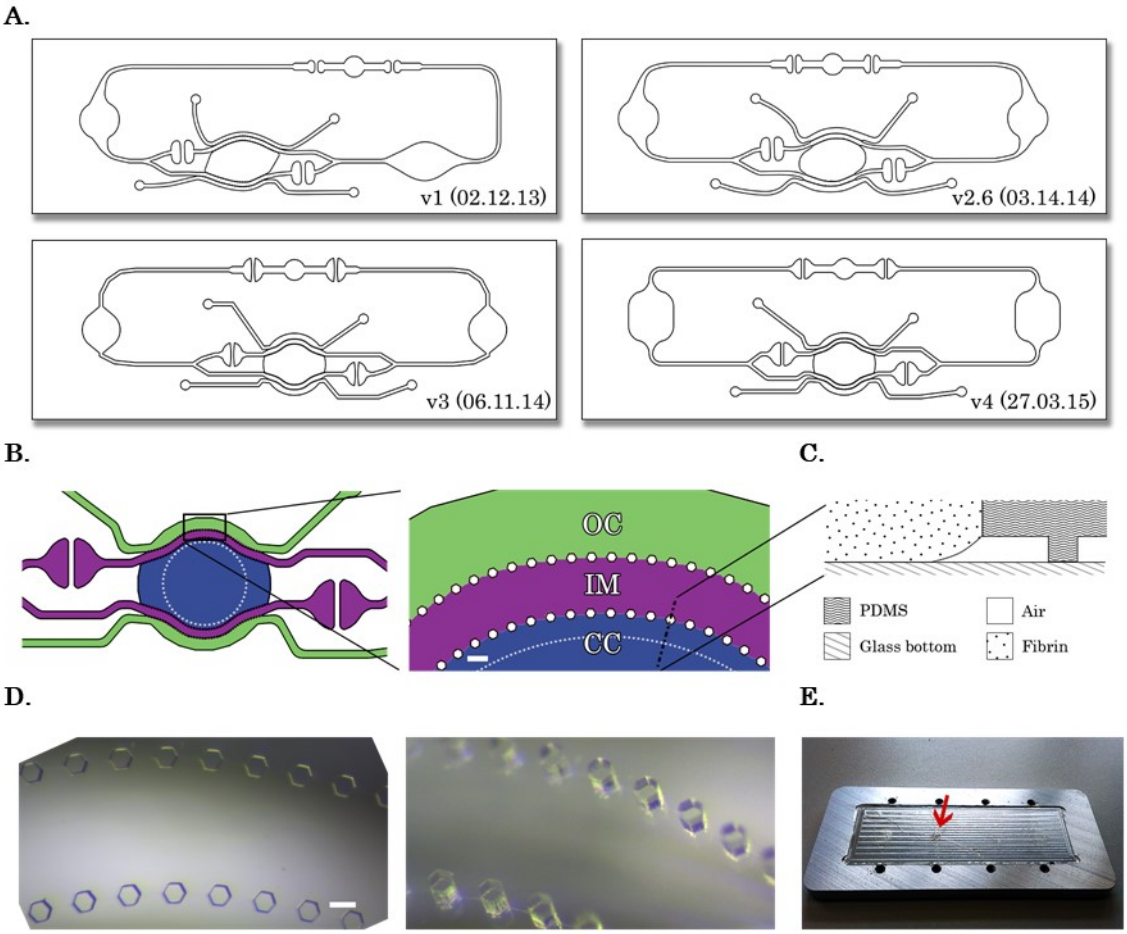

Figure 3.17: The MOC4Xt at a glance. (A) The version history of the design process. The compartment at the bottom centre is the functional heart of the chip. (B) Sandwich principle: the OC contains stromal cells in a fibrin gel; the IM is void of fibrin and contains medium only; the CC comprises ECs in a fibrin gel and will contain the *de novo* formed microvascular network. The white dotted circle represents the opening to the top created by the thin spacer during chip casting. Valves up- and downstream of the IM direct the medium through the CC as soon as required. The scale bar is 200 µm long. The colouring is according to the colours in the template publication (Kim et al., 2013). (C) Cross-sectional scheme of the surface tension created between hydrophobic PDMS and fibrin. In this particular case, the extend of the fibrin is defined by the spacer during chip casting. To overcome the surface tensions various strategies can be applied (see text). (D) Stereomicroscopic images of a PDMS mould shows the high precision of the SU8 master. The hexagonal columns of the hydrophobic PDMS in concert with the surface tension guide the curing fibrin through the compartments. Scale bar is 100 µm long. (E) The substrate of the master is glass and, thus, fragile (arrow) towards the pointy new spacers.

PDMS replica demonstrated the high precision of the master (Fig. 3.17D). Because the mould is immobilised on a glass substrate exceptional care must be taken during the insertion of the spacers. Too high forces on the pointy OC spacers could crack and destroy an entire master (Fig. 3.17E). The bonding of the PDMS layer to a glass slide is done corresponding to the bonding of a normal 2OC.

3.4.1. First proof of principle of the MOC4Xt

To enable the retention of fibrin the hexagonal PDMS columns had to be hydrophobic. Otherwise fibrin would easily pass them. Because the chip is hydrophilic after the bonding, hydrophobicity must be recovered overnight in the 80 °C oven. Then, fibrin gels can be filled into the chip. First, the OC are loaded with ASC-laden hydrogels. To do so, the still liquid fibrin is poured in one access hole and aspirated through the other with a pipette. The gel follows the channel-like compartment to the outlet. Filling EC-laden fibrin in the CC turned out to be more complex and will be addressed in the next subsection. Upon curing of the gel the microfluidics are filled with full EC medium via the other two cultivation compartments. For this the medium reservoir above the CC must be completely filled and tightly sealed to prohibit bubbles penetrating the central fibrin.

Within three days the GFP-HUVECs in the CC begin to form first microvascular structures that are interconnected (Fig. 3.18). Furthermore, the ECs establish a connection to the IM. Whether the network is perfusable cannot be assessed as there are always bypasses around the fibrin that served as routes of lesser resistance.

3.4.2. Obstacles in operating the MOC4Xt

Two problems arise from the hydrophobicity of the chip. First, the resistance of the channels to a fluid is problematic. High pressures to repeatedly inject medium via the syringes harm the delicate fibrin or even provoke leakage of the microfluidics. Second, during chip casting the CC's design is meant to host a thin spacer to create an accessible space with a diameter of 5.5 mm. If, later, fibrin is casted into this compartment the surface tension prohibits its migration to the PDMS columns that lie several microns offside (Fig. 3.17C). The resulting gaps at the edges of the CC allow an unrestrained bypassing flow of the medium instead of the perfusion of the IMs, only.

The first problem is addressed by injecting a fibronectin solution (50 µg/mL or 0.005 %) into the channels prior to the hydrophobic recovery. Fibronectin is widely used in cell culture for

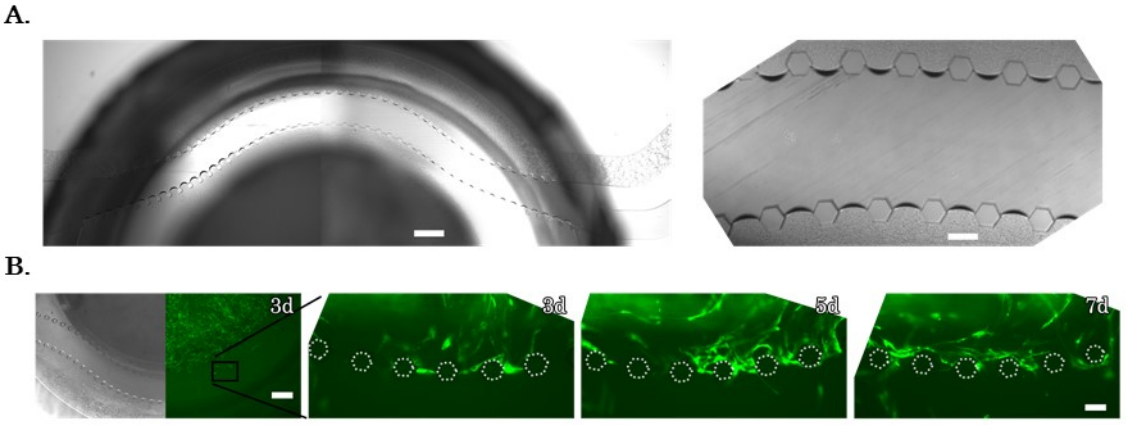

Figure 3.18: Proof of principle. (A) A cell-free fibrin gel can be filled into both compartments, CC and OC. Images are taken before medium is filled in, so that menisci are visible. The scale bars are 500 and 100 µm in the left and right image, respectively. (B) Cell-laden fibrin gels are filled into both compartments – HUVECs in the CC; ASCs in the OCs. Network formation can be observed in the ASC-free CC. The microvessels reach out to the border with the IM. The PDMS pillars are highlighted by white dots. In the left image, the scale bar is 500 µm long; in the other pictures, it is 100 µm.

mediating proper adherence especially of ECs to surfaces such as glass. In the hydrophobic chip the fibrillary fibronectin crystals serve as a facilitator for the wetting of the microfluidics.

To tackle the second problem two concepts are investigated. In the first approach the hydrophobic chip is treated with physical plasma again for some 5 to 10 seconds. The idea is to re-hydrophilies the CC but not the residual microfluidics including the PDMS columns. Fibrin with a fine-tuned fibrinogen concentration and thrombin activity should, thus, be soaked to but not beyond the delimiting columns. This approach is not effective, however. On the one hand, the plasma might bond the valves of the IMs effectively obstructing the passage to the microfluidics. On the other hand, the approach fails due to the substantial number of chips being lost to determine the parameters (time of plasma treatment, fibrinogen concentration, thrombin activity). The conditions for re-hydrophilization depended on unidentified external factors – one day's 5 seconds of plasma treatment could have the same effect as another day's 10 seconds. As the reproducibility is unsatisfactory there is always an inconvenient trial and error process, which at times results even in the complete loss of manufactured chips.

Another approach to address the filling of the CC is by applying just enough pressure to the fibrin to overcome the chamber's initial resistance. For this, the top of the CC is sealed with a thin PDMS layer that results if the spacer is not completely screwed in during chip casting. Two access holes are punched into the layer with a needle at the left and right side of the CC just enough to fit a 1 mL-pipette tip. Fibrin is introduced through one hole by gentle pipetting. The second hole releases the fibrin, which results in the filling of the CC to the columns. This technique is more precise and reproducible than the application of plasma but laborious nonetheless. Moreover, too much pressure can make the fibrin burst through the barrier resulting in a high failure rate, as well.

However, even if the CC and OCs are successfully filled with cell-laden fibrin gels (i.e. without leaking into the other compartments) further difficulties arise from the replacement of the air in the residual microfluidics with medium. After curing of the patterned fibrin gels the pure injection of medium through the other two cultivation compartments leads to an uncontrolled evacuation of the air – for example through the CC – so that the microstructure of the gel is either disrupted or that air bubbles are trapped inside the gel (Fig. 3.19).

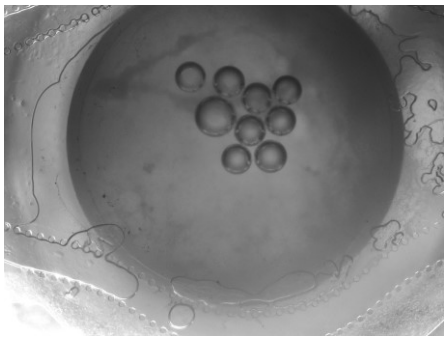

Figure 3.19: Bubbles trapped inside the fibrin gel. By pressing medium through the microfluidics to remove the air it could occur that bubbles find their way into the hydrogel instead of following the channels. Not only the bubbles may be trapped they also disrupt the fibrin's fine structure.

3.4.3. Improving the MOC4Xt

Developing the system further, the MOC4Xt design and its derivatives are meant to create a closed endothelial barrier throughout the MOC platform until the level of microcapillary supply of the organoids. Subtle design alterations are conceived to improve the MOC4Xt's functionality and usability. Generally, the chip's microfluidics should be reduced to a minimum to reduce channel resistance especially in case of a hydrophobic chip. Particularly, the rather long channel leading to the pumps could be shortened.

The loading of the OC is not an issue. However, the access openings in the AP could be revised. They are designed to hold the UNF 1/4"-28 thread of a syringe adapter. However, it turned out that the adapter is not required due to the aspiration of fibrin through the opposing access hole rather than its injection. Moreover, if still used the adapter does not seal properly at the interface to the PDMS layer. Instead, high forces when screwing might even detach the PDMS layer from the AP. The access holes could easily be smaller and, therefore, the OCs shorter, too.

The CC would need extended changes. Like the access holes for the OCs this compartment requires an access and outlet port to carry the liquid fibrin. The top of the compartment would need to be sealed with PDMS and later opened with a biopsy puncher. As this technique would not be precise and laborious, it would be also feasible to exclude the entire compartment from the design. As described before surface tension can be created at the small gap between PDMS and glass. If the design was adapted so that no liquid could pass this space other than through the fibrin the design could work without PDMS columns for the CC.

3.4.4. A step further: Separating the generation of the vascular bed from the chip

With regard to the upcoming chip models, in particular to the human-on-a-chip design, the vascularisation strategy of the MOC4Xt design cannot be adapted. The design relies on the OCs promoting guidance towards the IMs. However, the compartment consumes precious space. Furthermore, the failure rate is unexpectedly high and the assembly is laborious. Eventually, little is investigated on the long-term effect of medium-deprived stromal cells

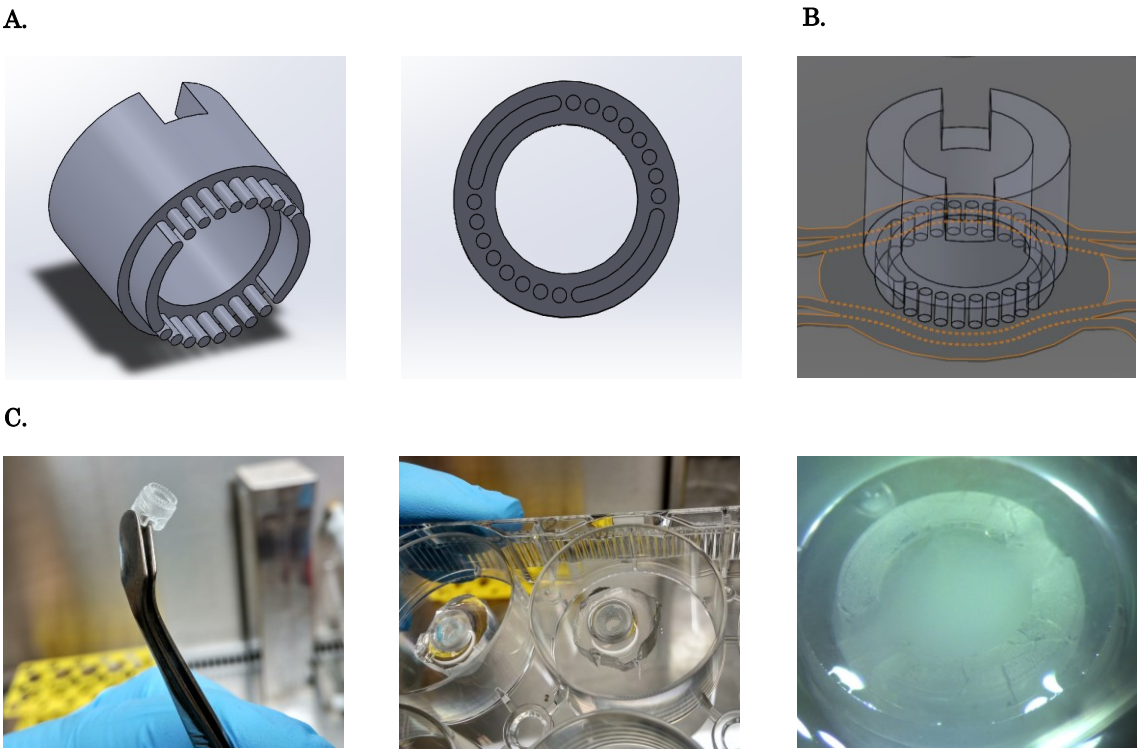

Figure 3.20: Next generation MOC4Xt. (A) A carrier designed to hold fibrin between the pillars and to place the gel in the desired MOC. (B) The underlying principle is still the same. The CC is now transferable, however. The OC is located in an external cultivation device. This possibly reduces labour, attrition, side effects of diminishing stromal cells, and – most importantly – space. (C) From left to right: photographs of prototype carrier placed in a self-build PDMS well and filled with fibrin, eventually.

offside of the IM near the access holes. The released factors from starving or even diminishing cells could lead to unwanted systemic artefacts.

Usually organoids for the MOC are assembled and pre-cultivated outside of the chip. This could be feasible for the vasculature, as well, bearing in mind that any approach needs to be connected to the microfluidics but otherwise leak-proof. Similar to the idea behind the MOC4Xt, the vessels need to form in an aligned manner in a co-culture system. For this the fibrin gel needs to be transportable without collapsing and without being harmed.

Adapted from developments by Sophie Bauer a fibrin carrier has been designed that could meet these requirements (Fig. 3.20). The cylindrical carrier has poles on its bottom that permit the adherence and mounting of a fibrin gel in between and throughout the inner perimeter. For the curing of the fibrin the carrier is placed in a firm, hydrophobic PDMS well. The fibrin hardly adheres to the PDMS. After curing and settling of the integrated ECs the carrier can be removed from the well without impairing the fibrin structure. It is, then, placed in a second well with a stromal outer compartment separated from the central carrier similar to the MOC4Xt design. This, again, should initiate network formation of the ECs. Moreover, outreaching of the cells is incentivised. These two steps could be combined in one device. Thereupon, the carrier is placed in the desired compartment of a common MOC. The current design of the carrier provides a diametric arrangement of the poles. Therefore, it should be

set in a compartment with diametrically opposing outlets, such as I2 of the 2OC. To prevent leaking the carrier might need to be glued with plain fibrin into the cultivation compartment.

The MOC4Xt design and its successors are thought to introduce the necessary incentives by using growth factor gradients emanating outside the HUVEC-laden fibrin gel. The created microcapillary network is of no use, if it is not eventually connected to the streaming medium or a potential blood surrogate. In affiliated change in the expression is expected, as well. Further developments will enable the cultivation of such a network in a form that allows the transfer into the desired MPS.

3.5. Detailed methodology

3.5.1. Cell culture

The HUVECs stably expressing GFP are purchased (Olaf Pharmaceuticals). The ASCs from one donor are isolated and selected by means of distinct characteristics described elsewhere (Rohringer et al., 2014; Wolbank et al., 2007). If not otherwise stated, both cell types are cultivated in full Endothelial Growth Medium MV2 (EGM MV2, Promocell), which contains growth factors (Tbl. 3.3) as well as 50 µg/mL gentamicin (Roth) and 0.5 µg/mL amphotericin B (PAA) to prevent contamination. The HUVECs are used up to passage 11 and the ASCs up to passage 7. All cell culture experiments are performed at 37 °C and 5 % carbon dioxide in a humid atmosphere.

3.5.2. Fabrication of the 2OC

The manufacturing of the 2OCs is described in chapter 2.5.1 on page 56.

3.5.3. Incorporating the cell-laden fibrin gel into the 2OC

The loading of the gels is heavily inspired by the works of our co-operation partner (Holnthoner et al., 2015; Rohringer et al., 2014). If not otherwise stated, all experiments in the 2OC are carried out using fibrin gels containing 2.5 mg/mL fibrinogen (Baxter) cross-linked by 0.2 IU/mL thrombin (Baxter). The HUVECs are usually embedded at a concentration of 5 x 10^5 cells per mL and ASCs at 2.5 x 10^5 cells per mL, resulting in a HUVEC to ASC ratio of 2:1. The gel is allowed to cure for 30 min at room temperature in the out-most cultivation compartment of the 2OC (I2). Both cultivation compartments are then filled with EGM MV2. The chip is tightly closed and incubated at 37 °C. The medium is, further, enriched with 100 KIU/mL aprotinin (Baxter) to inhibit serine protease-driven degradation of the fibrin. Half of the medium in each cultivation cavity is exchanged either every day or every other day. The 2OC is connected to the MCU on different days after fibrin incorporation (compare to figure 3.03 on page 77). The frequency is set to 0.3 Hz and pressure/vacuum ±25 kPa, if not stated otherwise. In cultures with basal medium the entire full medium is replaced on day four. The basal medium contains only antibiotics with no additional supplements or serum. Apart from the stated alterations all cultures are treated equally.

Table 3.3: Composition of EGM MV2.

Compound	Concentration
Ascorbic acid	1 µg/mL
bFGF	10 ng/mL
Epidermal growth factor	5 ng/mL
FBS	5 %
Hydrocortisone	0.2 µg/mL
Insulin-like growth factor	20 ng/mL
VEGF	0.5 ng/mL

3.5.4. Metabolic analysis

The glucose content in the medium supernatants is assessed colorimetrically using the Glucose LiquiColor® procedure (Stanbio). The assay is adapted using only 1/10 of the original volumes. Therein, glucose is oxidised in a two-step enzymatic reaction and a quinone dye is formed. Its intensity at 500 nm is directly proportional to the glucose content. Lactic acid content is determined with the colorimetric LAC 142 test (Diaglobal). Again, a two-step enzymatic reaction oxidises the reactant and creates a dye. The emission is measured at 520 nm. The LDH activity in the supernatants is quantified using the Pierce™ LDH Cytotoxicity Assay Kit (Thermo Fisher Scientific). According to the manufacturer's instructions, an amount of 12.5 µl of reagent is used and 12.5 µl of the supernatant is added for each measurement. Absorbance is assessed at 490 nm and subtracted from the absorbance at 680 nm to account for individual turbidity. Calculations are based on standards from a commercially available LDH positive control (Cayman).

3.5.5. Quantitative real-time polymerase chain reaction (qPCR)

After the experiment the cell-laden fibrin gels are dissolved in RA1 buffer (Machery-Nagel) with 1 % ß-mercaptoethanol and stored at -80 °C prior to total RNA isolation (NucleoSpin RNA II, Macherey-Nagel). The cDNA is synthesised with the TaqMan® Reverse Transcription Kit (Life Technologies). The qPCR is carried out with SensiFast SYBR No-ROX Kit (Bioline) on a light cycler (Mx3005P, Stratagene). Primers for COX-2, PECAM-1, TEK, TGF-ß1, VCAM-1, VE-cadherin, VEGFR2, VEGF-A, and vWF are synthesised by TIBMOL, Berlin (Tbl. 3.4). Cycle thresholds are normalised against those of glyceraldehyde 3-phosphate dehydrogenase (GAPDH). The expressional ratio towards GAPDH is compared using the Mann-Whitney U test for HUVEC mono-cultures and the Kruskal-Wallis one-way ANOVA on HUVEC/ASC co-cultures.

Table 3.4: List of primers.

Gene	Primer (5'→3')	
	forward	reverse
COX-2	TTgAAgAACTTACAggAgAAAAggA	CCAgTAggCAggAgAACATATAAC
GAPDH	TgTTgCCATCAATgACCCCTT	CTCCACgACgTACTCAgCg
PECAM-1	TCTgAgggTgAAggTgATAgCC	ggCTCTgTTgAAggCTgTgC
TEK	TgTCCCgAggTCAAgAggTg	gCACAAgTCATCCCgCAgTAg
TGF-β1	CCTggCgATACCTCAgCAAC	gCCATgAgAAgCAggAAAgg
VCAM-1	ACCCAAACAAAggCAgAgTACg	CCACAggATTTTCggAgCAg
VE-cadherin	AgCATCCAggCAgTggTAgC	gCACCgACACATCgTAgCTg
VEGF-A	AgCCTTgCCTTgCTgCTCTA	gTgCTggCCTTggTgAgg
VEGFR2	gACAACACAgCAggAATCAgTCAg	ggCAAgAACCATACCACTgTCC
vWF	CTgCCCACCCTTTgATgAAC	gCTTCCCACCTTgACATACTgC

3.5.6. Imaging

The images depicted are acquired either by fluorescence microscopy (Keyence) or 2PM (LaVision). Size measurements are carried out with the calibrated BZ-II Analyzer (Keyence). Image stacks and mosaics are processed and rendered with Imaris (Bitplane).

Chapter 4

Summary

The present work, investigated the feasibility of emulating the human vasculature in the MOC. As this is not only a pure biological effort, first, the rheology of the platform was assessed. Particularly, the behaviour of the chip's micropump was determined, which is influenced by a set of individual and interacting factors. For this, the μPIV technique was established in our laboratories. In addition, a collection of software tools was set up to achieve semi-automated processing of the footages and a first general analysis. Moreover, DoE was applied for the optimisation of the pumping to create in accommodating shear environment for the incorporated cells, but also to improve pumping efficiency and medium turnover of the device. In consideration of the findings, further general optimisations on the pumping sequence were proposed to advance the mimicking of the *in vivo* blood flow even more.

Then, the author focused on recreating human biology. The incorporation of a vascular network into the microfluidic platform was achieved by co-cultivating ECs with stromal cells. Here, the ASCs induced tube formation of GFP-HUVECs. A fibrin scaffold served as 3D space for cells to orientate and migrate in. The hydrogels were subjected to the chips perfusion for two weeks without interfering with the embedded cells. Interestingly, this incorporated network remained stable in serum- and supplement-depleted growth medium, which made this platform attractive for drug development and tissue engineering. The incorporation of organoids is of high interest especially considering ongoing developments of building a human-on-a-chip. However, the missing anastomosis of the *de novo* formed microcapillaries with the microfluidics demanded not only improved culturing strategies but also an overhaul of the platform. Ultimately, these vessels will need to be exposed to the optimised volumetric flow established in the former chapter. Therefore, the two cell types needed to be physically separated. The 2OC was extended to recapitulate the patterning of fibrin gels presented in work of others to achieve such a separation. Due to the complications in manufacturing and the overall space that was consumed by the extension, a re-examination of the approach was conducted leading to the proposition of using fibrin carriers in future developments.

Appendix

5.1. References

Akahori, T., Kobayashi, A., Komaki, M., Hattori, H., Nakahama, K.-I., Ichinose, S., Abe, M., Takeda, S., Morita, I., 2010. Implantation of capillary structure engineered by optical lithography improves hind limb ischemia in mice. Tissue Eng. Part A 16, 953–959. doi:10.1089/ten.tea.2009.0097

Aleksandrova, A. V., Pulkova, N.P., Gerasimenko, T.N., Anisimov, N.Y., Tonevitskaya, S.A., Sakharov, D.A., 2016. Mathematical and Experimental Model of Oxygen Diffusion for HepaRG Cell Spheroids. Bull. Exp. Biol. Med. 160, 857–860. doi:10.1007/s10517-016-3326-1

Allen, P., Melero-Martin, J., Bischoff, J., 2011. Type I collagen, fibrin and PuraMatrix matrices provide permissive environments for human endothelial and mesenchymal progenitor cells to form neovascular networks. J. Tissue Eng. Regen. Med. 5, e74–e86. doi:10.1002/term.389

Ando, J., Tsuboi, H., Korenaga, R., Takada, Y., Toyama-Sorimachi, N., Miyasaka, M., Kamiya, A., 1994. Shear stress inhibits adhesion of cultured mouse endothelial cells to lymphocytes by downregulating VCAM-1 expression. Am. J. Physiol. 267, C679-687.

Ando, J., Yamamoto, K., 2009. Vascular Mechanobiology. Circ. J. 73, 1983–1992. doi:10.1253/circj.CJ-09-0583

Athanasiou, K. a, Eswaramoorthy, R., Hadidi, P., Hu, J.C., 2013. Self-organization and the self-assembling process in tissue engineering. Annu. Rev. Biomed. Eng. 15, 115–136. doi:10.1146/annurev-bioeng-071812-152423

Baker, B.M., Trappmann, B., Stapleton, S.C., Toro, E., Chen, C.S., 2013. Microfluidics embedded within extracellular matrix to define vascular architectures and pattern diffusive gradients. Lab Chip 13, 3246–3252. doi:10.1039/C3LC50493J

Balligand, J.-L., Feron, O., Dessy, C., 2009. eNOS activation by physical forces: From short-term regulation of contraction to chronic remodeling of cardiovascular tissues. Physiol. Rev. 89, 481–534. doi:10.1152/physrev.00042.2007

Barakat, A., Lieu, D., 2003. Differential responsiveness of vascular endothelial cells to different types of fluid mechanical shear stress. Cell Biochem. Biophys. 38, 323–343. doi:10.1385/CBB:38:3:323

Barrentine, L.B., 1999. An introduction to design of experiments: A simplified approach. Amer Society for Quality, Milwaukee.

Barschdorff, D., Ester, S., Most, E., 1995. Phonocardiogram analysis of congenital and acquired heart diseases using artificial neural networks. pp. 271–288. doi:10.1142/9789812831187_0012

Bertassoni, L.E., Cecconi, M., Manoharan, V., Nikkhah, M., Hjortnaes, J., Cristino, A.L., Barabaschi, G., Demarchi, D., Dokmeci, M.R., Yang, Y., Khademhosseini, A., 2014. Hydrogel bioprinted microchannel networks for vascularization of tissue engineering constructs. Lab Chip 14, 2202–2211. doi:10.1039/c4lc00030g

Biering-Sørensen, T., Mogelvang, R., Schnohr, P., Jensen, J.S., 2016. Cardiac time intervals measured by tissue doppler imaging M-mode: Association with hypertension, left ventricular geometry, and future ischemic cardiovascular diseases. J. Am. Heart Assoc. 5. doi:10.1161/JAHA.115.002687

Busek, M., Gruenzner, S., Steege, T., Schmieder, F., Klotzbach, U., Sonntag, F., 2016. Design, characterization, and modeling of microcirculation systems with integrated oxygenators. J. Sensors Sens. Syst. 5, 221–228. doi:10.5194/jsss-5-221-2016

Busek, M., Polk, C., Albrecht, T., Marx, U., König, J., Sonntag, F., 2012. Automated micro-PIV measurement in Lab-on-a-Chip systems. Biomed. Tech. 57, 927–930. doi:10.1515/bmt-2012-4064

Busek, M., Rudolph, A., Grünzner, S., Schmieder, F., Sonntag, F., 2015. Design and regulation of complex microfluidic systems with simulationX.

Busse, R., Fleming, I., 2006. Vascular endothelium and blood flow. Handb. Exp. Pharmacol. 43–78.

Canonico, S., 2003. The use of human fibrin glue in the surgical operations. Acta Bio-Medica Atenei Parm. 74 Suppl 2, 21–25.

Carmeliet, P., 2002. The development of blood vessels: Cellular and molecular mechanisms, in: Tomanek, R.J. (Ed.), Assembly of the Vasculature and Its Regulation. Birkhäuser Boston, Boston, MA.

Carmeliet, P., Jain, R.K., 2000. Angiogenesis in cancer and other diseases. Nature 407, 249–257. doi:10.1038/35025220

Caro, C.G., Fitz-Gerald, J.M., Schroter, R.C., 1971. Atheroma and arterial wall shear observation, correlation and proposal of a shear dependent mass transfer mechanism for atherogenesis. Proc. R. Soc. London B Biol. Sci. 177, 109–133. doi:10.1098/rspb.1971.0019

Chau, L., Doran, M., Cooper-White, J., 2009. A novel multishear microdevice for studying cell mechanics. Lab Chip 9, 1897–1902. doi:10.1039/B823180J

Chiu, J.-J., Usami, S., Chien, S., 2009. Vascular endothelial responses to altered shear stress: Pathologic implications for atherosclerosis. Ann. Med. 41, 19–28. doi:10.1080/07853890802186921

Chlupac, J., Filova, E., Havlikova, J., Matejka, R., Riedel, T., Houska, M., Brynda, E., Pamula, E., Rémy, M., Bareille, R., Fernandez, P., Daculsi, R., Bourget, C., Bacakova, L., Bordenave, L., 2014. The gene expression of human endothelial cells is modulated by subendothelial extracellular matrix proteins: Short-term response to laminar shear stress. Tissue Eng. Part A 20, 2253–2264. doi:10.1089/ten.tea.2013.0153

Chung, S., Sudo, R., Mack, P.J., Wan, C.-R., Vickerman, V., Kamm, R.D., 2009. Cell migration into scaffolds under co-culture conditions in a microfluidic platform. Lab Chip 9, 269–275. doi:10.1039/B807585A

Chwalek, K., Tsurkan, M. V., Freudenberg, U., Werner, C., 2014. Glycosaminoglycan-based hydrogels to modulate heterocellular communication in in vitro angiogenesis models. Sci. Rep. 4. doi:10.1038/srep04414

Colazzo, F., Alrashed, F., Saratchandra, P., Carubelli, I., Chester, A.H., Yacoub, M.H., Taylor, P.M., Somers, P., 2014. Shear stress and VEGF enhance endothelial differentiation of human adipose-derived stem cells. Growth Factors 1–11. doi:10.3109/08977194.2014.945642

Davies, P.F., 1995. Flow-mediated endothelial mechanotransduction. Physiol. Rev. 75, 519–560.

DestinyQx, Daniel Chang, xavax, 2012. A Wiggers diagram, showing the cardiac cycle events occuring in the left ventricle. URL: https://commons.wikimedia.org/wiki/File:Wiggers_Diagram.svg (accessed 8.7.16).

Dotzler, A., 2016. Integration of a vascularizsed liver equivalent in a microfluidic multi-organ-chip platform. Technische Universität Berlin.

Duval, E., Baugé, C., Andriamanalijaona, R., Bénateau, H., Leclercq, S., Dutoit, S., Poulain, L., Galéra, P., Boumédiene, K., 2012. Molecular mechanism of hypoxia-induced chondrogenesis and its application in in vivo cartilage tissue engineering. Biomaterials 33, 6042–6051. doi:10.1016/j.biomaterials.2012.04.061

Eddington, D.T., Puccinelli, J.P., Beebe, D.J., 2006. Thermal aging and reduced hydrophobic recovery of polydimethylsiloxane. Sensors Actuators B Chem. 114, 170–172. doi:10.1016/j.snb.2005.04.037

Elder, B.D., Athanasiou, K.A., 2009. Hydrostatic pressure in articular cartilage tissue engineering: from chondrocytes to tissue regeneration. Tissue Eng. Part B. Rev. 15, 43–53. doi:10.1089/ten.teb.2008.0435

Engler, A.J., Sen, S., Sweeney, H.L., Discher, D.E., 2006. Matrix elasticity directs stem cell lineage specification. Cell 126, 677–689. doi:10.1016/j.cell.2006.06.044

Fischer, C., Schneider, M., Carmeliet, P., 2006. Principles and therapeutic implications of angiogenesis, vasculogenesis and arteriogenesis. Handb. Exp. Pharmacol. 157–212.

Florian, J.A., Kosky, J.R., Ainslie, K., Pang, Z., Dull, R.O., Tarbell, J.M., 2003. Heparan sulfate proteoglycan is a mechanosensor on endothelial cells. Circ. Res. 93, e136–e142. doi:10.1161/01.RES.0000101744.47866.D5

Forster, R.E., 1965. Oxygenation of the tissue cell. Ann. N. Y. Acad. Sci. 117, 730–735.

Galbusera, M., Zoja, C., Donadelli, R., Paris, S., Morigi, M., Benigni, A., Figliuzzi, M., Remuzzi, G., Remuzzi, A., 1997. Fluid Shear Stress Modulates von Willebrand Factor Release From Human Vascular Endothelium. Blood 90, 1558–1564.

García-Cardeña, G., Comander, J., Anderson, K.R., Blackman, B.R., Gimbrone, M.A., 2001. Biomechanical activation of vascular endothelium as a determinant of its functional phenotype. Proc. Natl. Acad. Sci. 98, 4478–4485. doi:10.1073/pnas.071052598

George, S.C., 2014. Vascularizing engineered tissues for in vivo and in vitro applications, in: Weisel, R.D. (Ed.), . Woodhead Publishing, pp. 283–298.

Ghajar, C.M., Blevins, K.S., Hughes, C.C.W., George, S.C., Putnam, A.J., 2006. Mesenchymal stem cells enhance angiogenesis in mechanically viable prevascularized tissues via early matrix metalloproteinase upregulation. Tissue Eng. 12, 2875–2888. doi:10.1089/ten.2006.12.2875

Girard, P.R., Nerem, R.M., 1995. Shear stress modulates endothelial cell morphology and F-actin organization through the regulation of focal adhesion-associated proteins. J. Cell. Physiol. 163, 179–193. doi:10.1002/jcp.1041630121

Gorin, C., Rochefort, G.Y., Bascetin, R., Ying, H., Lesieur, J., Sadoine, J., Beckouche, N., Berndt, S., Novais, A., Lesage, M., Hosten, B., Vercellino, L., Merlet, P., Le-Denmat, D., Marchiol, C., Letourneur, D., Nicoletti, A., Vital, S.O., Poliard, A., Salmon, B., Muller, L., Chaussain, C., Germain, S., 2016. Priming dental pulp stem cells with fibroblast growth factor-2 increases angiogenesis of implanted tissue-engineered constructs through hepatocyte growth factor and vascular endothelial growth factor secretion. Stem Cells Transl. Med. sctm.2015-0166. doi:10.5966/sctm.2015-0166

Grainger, S.J., Carrion, B., Ceccarelli, J., Putnam, A.J., 2013. Stromal cell identity influences the in vivo functionality of engineered capillary networks formed by co-delivery of endothelial cells and stromal cells. Tissue Eng. Part A 19, 1209–1222. doi:10.1089/ten.tea.2012.0281

Gulino-Debrac, D., 2013. Mechanotransduction at the basis of endothelial barrier function. Tissue barriers 1. doi:10.4161/tisb.24180

Hasan, A., Paul, A., Vrana, N.E., Zhao, X., Memic, A., Hwang, Y.-S., Dokmeci, M.R., Khademhosseini, A., 2014. Microfluidic techniques for development of 3D vascularized tissue. Biomaterials 35, 7308–7325. doi:10.1016/j.biomaterials.2014.04.091

Helm, C.-L.E., Fleury, M.E., Zisch, A.H., Boschetti, F., Swartz, M.A., 2005. Synergy between interstitial flow and VEGF directs capillary morphogenesis in vitro through a gradient amplification mechanism. Proc. Natl. Acad. Sci. U. S. A. 102, 15779–15784. doi:10.1073/pnas.0503681102

Hepple, R.T., Mackinnon, S.L.M., Thomas, S.G., Goodman, J.M., Plyley, M.J., 1996. Quantitating the capillary supply and the response to resistance training in older men. Pflügers Arch. Eur. J. Physiol. 433, 238–244. doi:10.1007/s004240050273

Hermansen, L., Wachtlova, M., 1971. Capillary density of skeletal muscle in well-trained and untrained men. J Appl Physiol 30, 860–863.

Hirschfeld, S., Meyer, R., Korfhagen, J., Kaplan, S., Liebman, J., 1976. The isovolumic contraction time of the left ventricle. An echographic study. Circulation 54, 751–756.

Hoehme, S., Brulport, M., Bauer, A., Bedawy, E., Schormann, W., Hermes, M., Puppe, V., Gebhardt, R., Zellmer, S., Schwarz, M., Bockamp, E., Timmel, T., Hengstler, J.G., Drasdo, D., 2010. Prediction and validation of cell alignment along microvessels as order principle to restore tissue architecture in liver regeneration. Proc. Natl. Acad. Sci. U. S. A. 107, 10371–10376. doi:10.1073/pnas.0909374107

Holnthoner, W., Hohenegger, K., Husa, A.M., Muehleder, S., Meinl, A., Peterbauer-Scherb, A., Redl, H., 2015. Adipose-derived stem cells induce vascular tube formation of outgrowth endothelial cells in a fibrin matrix. J. Tissue Eng. Regen. Med. 9, 127–136. doi:10.1002/term.1620

Hsu, H.-H., 2017. Methode zur Simulation und Charakterisierung von Diffusionsvorgängen in Hautmodellen in Multi-Organ-Chips (working title). TU Hamburg-Harburg.

Hsu, Y.-H., Moya, M.L., Hughes, C.C.W., George, S.C., Lee, A.P., 2013. A microfluidic platform for generating large-scale nearly identical human microphysiological vascularized tissue arrays. Lab Chip 13, 2990–2998. doi:10.1039/c3lc50424g

Huang, C.P., Lu, J., Seon, H., Lee, A.P., Flanagan, L. a, Kim, H.-Y., Putnam, A.J., Jeon, N.L., 2009. Engineering microscale cellular niches for three-dimensional multicellular co-cultures. Lab Chip 9, 1740–1748. doi:10.1039/b818401a

Huh, D., Matthews, B.D., Mammoto, A., Montoya-Zavala, M., Hsin, H.Y., Ingber, D.E., 2010. Reconstituting organ-level lung functions on a chip. Science 328, 1662–1668. doi:10.1126/science.1188302

Hunziker, O., Abdel'al, S., Schulz, U., 1979. The aging human cerebral cortex: A stereological characterization of changes in the capillary net. J. Gerontol. 34, 345–350. doi:10.1093/geronj/34.3.345

Huttala, O., Vuorenpää, H., Toimela, T., Uotila, J., Kuokkanen, H., Ylikomi, T., Sarkanen, J.-R., Heinonen, T., 2015. Human vascular model with defined stimulation medium - a characterization study. ALTEX 32, 125–136. doi:http://dx.doi.org/10.14573/altex.1411271

Imura, Y., Sato, K., Yoshimura, E., 2010. Micro total bioassay system for ingested substances: assessment of intestinal absorption, hepatic metabolism, and bioactivity. Anal. Chem. 82, 9983–9988. doi:10.1021/ac100806x

Inoguchi, H., Tanaka, T., Maehara, Y., Matsuda, T., 2007. The effect of gradually graded shear stress on the morphological integrity of a huvec-seeded compliant small-diameter vascular graft. Biomaterials 28, 486–495. doi:10.1016/j.biomaterials.2006.09.020

Johnson, B.D., Mather, K.J., Wallace, J.P., 2011. Mechanotransduction of shear in the endothelium: Basic studies and clinical implications. Vasc. Med. 16, 365–377. doi:10.1177/1358863X11422109

Kachgal, S., Putnam, A.J., 2011. Mesenchymal stem cells from adipose and bone marrow promote angiogenesis via distinct cytokine and protease expression mechanisms. Angiogenesis 14, 47–59. doi:10.1007/s10456-010-9194-9

Kamiya, a, Bukhari, R., Togawa, T., 1984. Adaptive regulation of wall shear stress optimizing vascular tree function. Bull. Math. Biol. 46, 127–137.

Kang, J.H., Gimble, J.M., Kaplan, D.L., 2009. In vitro 3D model for human vascularized adipose tissue. Tissue Eng. Part A 15, 2227–2236. doi:10.1089/ten.tea.2008.0469

Kelly, R.F., Snow, H.M., 2007. Characteristics of the response of the iliac artery to wall shear stress in the anaesthetized pig. J. Physiol. 582, 731–743. doi:10.1113/jphysiol.2007.128736

Kim, S., Chung, M., Jeon, N.L., 2016. Three-dimensional biomimetic model to reconstitute sprouting lymphangiogenesis in vitro. Biomaterials 78, 115–128. doi:10.1016/j.biomaterials.2015.11.019

Kim, S., Lee, H., Chung, M., Jeon, N.L., 2013. Engineering of functional, perfusable 3D microvascular networks on a chip. Lab Chip 13, 1489. doi:10.1039/c3lc41320a

Kolesky, D.B., Homan, K.A., Skylar-Scott, M.A., Lewis, J.A., 2016. Three-dimensional bioprinting of thick vascularized tissues. Proc. Natl. Acad. Sci. U. S. A. 113, 3179–3184. doi:10.1073/pnas.1521342113

Krogh, A., 1919. The supply of oxygen to the tissues and the regulation of the capillary circulation. J. Physiol. 52, 457–474. doi:10.1113/jphysiol.1919.sp001844

Kumagai, R., Lu, X., Kassab, G.S., 2009. Role of glycocalyx in flow-induced production of nitric oxide and reactive oxygen species. Free Radic. Biol. Med. 47, 600–607. doi:10.1016/j.freeradbiomed.2009.05.034

Kumar, S., Sud, N., Fonseca, F. V., Hou, Y., Black, S.M., 2010. Shear stress stimulates nitric oxide signaling in pulmonary arterial endothelial cells via a reduction in catalase activity: role of protein kinase Cδ. Am. J. Physiol. - Lung Cell. Mol. Physiol. 298, L105–L116. doi:10.1152/ajplung.00290.2009

Lafleur, M. a, Handsley, M.M., Knäuper, V., Murphy, G., Edwards, D.R., 2002. Endothelial tubulogenesis within fibrin gels specifically requires the activity of membrane-type-matrix metalloproteinases (MT-MMPs). J. Cell Sci. 115, 3427–3438.

Langheinrich, A.C., Bohle, R.M., 2005. Atherosclerosis: humoral and cellular factors of inflammation. Virchows Arch. 446, 101–111. doi:10.1007/s00428-004-1180-4

Lee, J.B., Wang, X., Faley, S., Baer, B., Balikov, D.A., Sung, H.J., Bellan, L.M., 2016. Development of 3D Microvascular Networks Within Gelatin Hydrogels Using Thermoresponsive Sacrificial Microfibers. Adv. Healthc. Mater. 5, 781–785. doi:10.1002/adhm.201500792

Levesque, M.J., Nerem, R.M., 1985. The Elongation and Orientation of Cultured Endothelial Cells in Response to Shear Stress. J. Biomech. Eng. 107, 341–347. doi:10.1115/1.3138567

Ley, K., Laudanna, C., Cybulsky, M.I., Nourshargh, S., 2007. Getting to the site of inflammation: the leukocyte adhesion cascade updated. Nat. Rev. Immunol. 7, 678–689. doi:10.1038/nri2156

Li, Y.-S.J., Haga, J.H., Chien, S., 2005. Molecular basis of the effects of shear stress on vascular endothelial cells. J. Biomech. 38, 1949–1971. doi:10.1016/j.jbiomech.2004.09.030

Lima, R., Wada, S., Tanaka, S., Takeda, M., Ishikawa, T., Tsubota, K., Imai, Y., Yamaguchi, T., 2008. In vitro blood flow in a rectangular PDMS microchannel: experimental observations using a confocal micro-PIV system. Biomed. Microdevices 10, 153–167. doi:10.1007/s10544-007-9121-z

Lindken, R., Rossi, M., Grosse, S., Westerweel, J., 2009. Micro-Particle Image Velocimetry (microPIV): recent developments, applications, and guidelines. Lab Chip 9, 2551–2567. doi:10.1039/b906558j

Madri, J.A., Pratt, B.M., 1988. Angiogenesis, in: Clark, R.A.F., Henson, P.M. (Eds.), The Molecular and Cellular Biology of Wound Repair. Springer US, pp. 337–358.

Marx, U., Andersson, T.B., Bahinski, A., Beilmann, M., Beken, S., Cassee, F.R., Cirit, M., Daneshian, M., Fitzpatrick, S., Frey, O., Gaertner, C., Giese, C., Griffith, L., Hartung, T., Heringa, M.B., Hoeng, J., De Jong, W.H., Kojima, H., Kuehnl, J., Leist, M., Luch, A., Maschmeyer, I., Sakharov, D., Sips, A.J.A.M., Steger-Hartmann, T., Tagle, D.A., Tonevitsky, A., Tralau, T., Tsyb, S., Van De Stolpe, A., Vandebriel, R., Vulto, P., Wang, J., Wiest, J., Rodenburg, M., Roth, A., 2016. Biology-inspired microphysiological system approaches to solve the prediction dilemma of substance testing. ALTEX 33, 272–321. doi:10.145/3/aitex.1603161

Maschmeyer, I., Hasenberg, T., Jaenicke, A., Lindner, M., Lorenz, A.K., Zech, J., Garbe, L.A., Sonntag, F., Hayden, P., Ayehunie, S., Lauster, R., Marx, U., Materne, E.M., 2015a. Chip-based human liver-intestine and liver-skin co-cultures - A first step toward systemic repeated dose substance testing in vitro. Eur. J. Pharm. Biopharm. 95, 77–87. doi:10.1016/j.ejpb.2015.03.002

Maschmeyer, I., Lorenz, A.K., Schimek, K., Hasenberg, T., Ramme, A.P., Hübner, J., Lindner, M., Drewell, C., Bauer, S., Thomas, A., Sambo, N.S., Sonntag, F., Lauster, R., Marx, U., 2015b. A four-organ-chip for interconnected long-term co-culture of human intestine, liver, skin and kidney equivalents. Lab Chip 15, 2688–2699. doi:10.1039/C5LC00392J

Materne, E.-M., Maschmeyer, I., Lorenz, A.K., Horland, R., Schimek, K.M.S., Busek, M., Sonntag, F., Lauster, R., Marx, U., 2015a. The Multi-organ Chip - A microfluidic platform for long-term multi-tissue coculture. J. Vis. Exp. doi:10.3791/52526

Materne, E.-M., Ramme, A.P., Terrasso, A.P., Serra, M., Alves, P.M., Brito, C., Sakharov, D.A., Tonevitsky, A.G., Lauster, R., Marx, U., 2015b. A multi-organ chip co-culture of neurospheres and liver equivalents for long-term substance testing. J. Biotechnol. 205, 36–46. doi:10.1016/j.jbiotec.2015.02.002

McCormick, S.M., Eskin, S.G., McIntire, L. V., Teng, C.L., Lu, C.-M., Russell, C.G., Chittur, K.K., 2001. DNA microarray reveals changes in gene expression of shear stressed human umbilical vein endothelial cells. Proc. Natl. Acad. Sci. 98, 8955–8960. doi:10.1073/pnas.171259298

McDougall, S.R., Anderson, A.R.A., Chaplain, M.A.J., 2006. Mathematical modelling of dynamic adaptive tumour-induced angiogenesis: Clinical implications and therapeutic targeting strategies. J. Theor. Biol. 241, 564–589. doi:10.1016/j.jtbi.2005.12.022

Meer, A.D. van der, Orlova, V. V., Dijke, P. ten, Berg, A. van den, Mummery, C.L., 2013. Three-dimensional co-cultures of human endothelial cells and embryonic stem cell-derived pericytes inside a microfluidic device. Lab Chip 13, 3562–3568. doi:10.1039/C3LC50435B

Megens, R.T.A., Reitsma, S., Schiffers, P.H.M., Hilgers, R.H.P., De Mey, J.G.R., Slaaf, D.W., oude Egbrink, M.G.A., van Zandvoort, M.A.M.J., 2006. Two-Photon Microscopy of Vital Murine Elastic and Muscular Arteries. J. Vasc. Res. 44, 87–98. doi:10.1159/000098259

Miller, J.S., Stevens, K.R., Yang, M.T., Baker, B.M., Nguyen, D.-H.T., Cohen, D.M., Toro, E., Chen, A.A., Galie, P.A., Yu, X., Chaturvedi, R., Bhatia, S.N., Chen, C.S., 2012. Rapid casting of patterned vascular networks for perfusable engineered three-dimensional tissues. Nat. Mater. 11, 768–774. doi:10.1038/nmat3357

Moreira, R., Neusser, C., Kruse, M., Mulderrig, S., Wolf, F., Spillner, J., Schmitz-Rode, T., Jockenhoevel, S., Mela, P., 2016. Tissue-engineered fibrin-based heart valve with bio-inspired textile reinforcement. Adv. Healthc. Mater. 5, 2113–2121. doi:10.1002/adhm.201600300

Morra, M., Occhiello, E., Marola, R., Garbassi, F., Humphrey, P., Johnson, D., 1990. On the aging of oxygen plasma-treated polydimethylsiloxane surfaces. J. Colloid Interface Sci. 137, 11–24. doi:10.1016/0021-9797(90)90038-P

Moya, M.L., Hsu, Y., Lee, A.P., Hughes, C.C.W., George, S.C., 2013. In vitro perfused human capillary networks. Tissue Eng. Part C. Methods 19, 730–7. doi:10.1089/ten.TEC.2012.0430

Muehleder, S., Ovsianikov, A., Zipperle, J., Redl, H., Holnthoner, W., 2014. Connections matter: channeled hydrogels to improve vascularization. Front. Bioeng. Biotechnol. 2, 52. doi:10.3389/fbioe.2014.00052

Myreng, Y., Nitter-Hauge, S., 1989. Age-dependency of left ventricular filling dynamics and relaxation as assessed by pulsed Doppler echocardiography. Clin. Physiol. 9, 99–106. doi:10.1111/j.1475-097X.1989.tb00961.x

Nagy, J.A., Benjamin, L., Zeng, H., Dvorak, A.M., Dvorak, H.F., 2008. Vascular permeability, vascular hyperpermeability and angiogenesis. Angiogenesis 11, 109–119. doi:10.1007/s10456-008-9099-z

Nahmias, Y., Berthiaume, F., Yarmush, M.L., 2006. Integration of technologies for hepatic tissue engineering, in: Advances in Biochemical Engineering/Biotechnology. pp. 309–329. doi:10.1007/10_029

Ng, C.P., Swartz, M.A., 2003. Fibroblast alignment under interstitial fluid flow using a novel 3-D tissue culture model. Am. J. Physiol. - Hear. Circ. Physiol. 284, H1771–H1777. doi:10.1152/ajpheart.01008.2002

Nunes, S.S., Greer, K.A., Stiening, C.M., Chen, H.Y.S., Kidd, K.R., Schwartz, M.A., Sullivan, C.J., Rekapally, H., Hoying, J.B., 2010. Implanted microvessels progress through distinct neovascularization phenotypes. Microvasc. Res. 79, 10–20. doi:10.1016/j.mvr.2009.10.001

Ohno, M., Cooke, J.P., Dzau, V.J., Gibbons, G.H., 1995. Fluid shear stress induces endothelial transforming growth factor beta-1 transcription and production. Modulation by potassium channel blockade. J. Clin. Invest. 95, 1363–1369. doi:10.1172/JCI117787

Ono, N., Mizuno, R., Ohhashi, T., 2005. Effective permeability of hydrophilic substances through walls of lymph vessels: roles of endothelial barrier. Am. J. Physiol. Heart Circ. Physiol. 289, H1676–H1682. doi:10.1152/ajpheart.01084.2004

Papaioannou, T.G., Stefanadis, C., 2005. Vascular wall shear stress: basic principles and methods. Hell. J. Cardiol. 46, 9–15. doi:15807389

Peters, E.B., Christoforou, N., Leong, K.W., Truskey, G. a, 2013. Comparison of mixed and lamellar coculture spatial arrangements for tissue engineering capillary networks in vitro. Tissue Eng. Part A 19, 697–706. doi:10.1089/ten.tea.2011.0704

Peters, K., Kamp, G., Berz, A., Unger, R.E., Barth, S., Salamon, A., Rychly, J., Kirkpatrick, C.J., 2009. Changes in human endothelial cell energy metabolic capacities during in vitro cultivation. the role of aerobic glycolysis and proliferation. Cell. Physiol. Biochem. 24, 483–492. doi:10.1159/000257490

Pill, K., Hofmann, S., Redl, H., Holnthoner, W., 2015. Vascularization mediated by mesenchymal stem cells from bone marrow and adipose tissue: a comparison. Cell Regen. 4, 8. doi:10.1186/s13619-015-0025-8

Poole, D.C., Copp, S.W., Hirai, D.M., Musch, T.I., 2011. Dynamics of muscle microcirculatory and blood-myocyte O(2) flux during contractions. Acta Physiol. (Oxf). 202, 293–310. doi:10.1111/j.1748-1716.2010.02246.x

Raffel, M., Willert, C.E., Wereley, S.T., Kompenhans, J., 2007. Particle Image Velocimetry. Springer Berlin Heidelberg, Berlin, Heidelberg. doi:10.1007/978-3-540-72308-0

Ranga, A., Gobaa, S., Okawa, Y., Mosiewicz, K., Negro, A., Lutolf, M.P., 2014. 3D niche microarrays for systems-level analyses of cell fate. Nat. Commun. 5, 4324. doi:10.1038/ncomms5324

Reitsma, S., Slaaf, D.W., Vink, H., Zandvoort, M.A.M.J. van, Egbrink, M.G.A. oude, 2007. The endothelial glycocalyx: composition, functions, and visualization. Pflügers Arch. - Eur. J. Physiol. 454, 345–359. doi:10.1007/s00424-007-0212-8

Reneman, R.S., Arts, T., Hoeks, A.P.G., 2006. Wall shear stress – an important determinant of endothelial cell function and structure – in the arterial system in vivo. J. Vasc. Res. 43, 251–269. doi:10.1159/000091648

Rohringer, S., Hofbauer, P., Schneider, K.H., Husa, A.M., Feichtinger, G., Peterbauer-Scherb, A., Redl, H., Holnthoner, W., 2014. Mechanisms of vasculogenesis in 3D fibrin matrices mediated by the interaction of adipose-derived stem cells and endothelial cells. Angiogenesis 17, 921–933. doi:10.1007/s10456-014-9439-0

Rosano, J.M., Tousi, N., Scott, R.C., Krynska, B., Rizzo, V., Prabhakarpandian, B., Pant, K., Sundaram, S., Kiani, M.F., 2009. A physiologically realistic in vitro model of microvascular networks. Biomed. Microdevices 11, 1051–1057. doi:10.1007/s10544-009-9322-8

Rouwkema, J., Rivron, N.C., van Blitterswijk, C.A., 2008. Vascularization in tissue engineering. Trends Biotechnol. 26, 434–441. doi:10.1016/j.tibtech.2008.04.009

Sarkanen, J.R., Vuorenpää, H., Huttala, O., Mannerstrm, B., Kuokkanen, H., Miettinen, S., Heinonen, T., Ylikomi, T., 2012. Adipose stromal cell tubule network model provides a versatile tool for vascular research and tissue engineering. Cells Tissues Organs 196, 385–397. doi:10.1159/000336679

Schimek, K., Busek, M., Brincker, S., Groth, B., Hoffmann, S., Lauster, R., Lindner, G., Lorenz, A., Menzel, U., Sonntag, F., Walles, H., Marx, U., Horland, R., 2013. Integrating biological vasculature into a multi-organ-chip microsystem. Lab Chip 13, 3588–3598. doi:10.1039/C3LC50217A

Seto, Y., Inaba, R., Okuyama, T., Sassa, F., Suzuki, H., Fukuda, J., 2010. Engineering of capillary-like structures in tissue constructs by electrochemical detachment of cells. Biomaterials 31, 2209–2215. doi:10.1016/j.biomaterials.2009.11.104

Shields, J.D., Fleury, M.E., Yong, C., Tomei, A.A., Randolph, G.J., Swartz, M.A., 2007. Autologous chemotaxis as a mechanism of tumor cell homing to lymphatics via interstitial flow and autocrine CCR7 signaling. Cancer Cell 11, 526–538. doi:10.1016/j.ccr.2007.04.020

Shoajei, S., Tafazzoli-Shahdpour, M., Shokrgozar, M.A., Haghighipour, N., 2014. Alteration of human umbilical vein endothelial cell gene expression in different biomechanical environments. Cell Biol. Int. 38, 577–581. doi:10.1002/cbin.10237

Sieber, S., 2017. Generation of a 3D bone marrow model. Technische Universität Berlin.

Siebertz, K., Bebber, D. van, Hochkirchen, T., 2010. Statistische Versuchsplanung. Springer Berlin Heidelberg, Berlin, Heidelberg.

Sieminski, a L., Hebbel, R.P., Gooch, K.J., 2005. Improved microvascular network in vitro by human blood outgrowth endothelial cells relative to vessel-derived endothelial cells. Tissue Eng. 11, 1332–1345. doi:10.1089/ten.2005.11.1332

Sill, H.W., Chang, Y.S., Artman, J.R., Frangos, J.A., Hollis, T.M., Tarbell, J.M., 1995. Shear stress increases hydraulic conductivity of cultured endothelial monolayers. Am. J. Physiol. 268, H535–H543.

Silverthorn, D.U., 2009. Das Herz als Pumpe, in: Physiologie. Pearson Education, München, p. 1357.

Song, J.W., Bazou, D., Munn, L.L., 2012. Anastomosis of endothelial sprouts forms new vessels in a tissue analogue of angiogenesis. Integr. Biol. 4, 857–862. doi:10.1039/C2IB20061A

Sonntag, F., Schilling, N., Mader, K., Gruchow, M., Klotzbach, U., Lindner, G., Horland, R., Wagner, I., Lauster, R., Howitz, S., Hoffmann, S., Marx, U., 2010. Design and prototyping of a chip-based multi-micro-organoid culture system for substance testing, predictive to human (substance) exposure. J. Biotechnol. 148, 70–75. doi:10.1016/j.jbiotec.2010.02.001

Sugii, Y., Nishio, S., Okamoto, K., 2002. In vivo PIV measurement of red blood cell velocity field in microvessels considering mesentery motion. Physiol. Meas. 23, 403–416.

Sugii, Y., Okuda, R., Okamoto, K., Madarame, H., 2005. Velocity measurement of both red blood cells and plasma of in vitro blood flow using high-speed micro PIV technique. Meas. Sci. Technol. 16, 1126–1130. doi:10.1088/0957-0233/16/5/011

Sung, J.H., Kam, C., Shuler, M.L., 2010. A microfluidic device for a pharmacokinetic–pharmacodynamic (PK–PD) model on a chip. Lab Chip 10, 446–455. doi:10.1039/B917763A

Takebe, T., Sekine, K., Enomura, M., Koike, H., Kimura, M., Ogaeri, T., Zhang, R.-R., Ueno, Y., Zheng, Y.-W., Koike, N., Aoyama, S., Adachi, Y., Taniguchi, H., 2013. Vascularized and functional human liver from an iPSC-derived organ bud transplant. Nature 499, 481–484. doi:10.1038/nature12271

Tan, W., Desai, T. a, 2005. Microscale multilayer cocultures for biomimetic blood vessels. J. Biomed. Mater. Res. A 72, 146–160. doi:10.1002/jbm.a.30182

Tanaka, Y., Yamato, M., Okano, T., Kitamori, T., Sato, K., 2006. Evaluation of effects of shear stress on hepatocytes by a microchip-based system. Meas. Sci. Technol. 17, 3167. doi:10.1088/0957-0233/17/12/S08

Thielicke, W., 2014. The flapping flight of birds: Analysis and application.

Thielicke, W., Stamhuis, E.J., 2014. PIVlab – Towards user-friendly, affordable and accurate digital Particle Image Velocimetry in MATLAB. J. Open Res. Softw. 2. doi:10.5334/jors.bl

Ting, L.H., Jahn, J.R., Jung, J.I., Shuman, B.R., Feghhi, S., Han, S.J., Rodriguez, M.L., Sniadecki, N.J., 2012. Flow mechanotransduction regulates traction forces, intercellular forces, and adherens junctions. Am. J. Physiol. - Hear. Circ. Physiol. 302, H2220–H2229. doi:10.1152/ajpheart.00975.2011

Toepke, M.W., Beebe, D.J., 2006. PDMS absorption of small molecules and consequences in microfluidic applications. Lab Chip 6, 1484–1486. doi:10.1039/b612140c

Tolbert, W.R., Hitt, M.M., Feder, J., 1980. Cell aggregate suspension culture for large-scale production of biomolecules. In Vitro 16, 486–490. doi:10.1007/BF02626461

Topper, J.N., Cai, J., Falb, D., Gimbrone, M.A., 1996. Identification of vascular endothelial genes differentially responsive to fluid mechanical stimuli: cyclooxygenase-2, manganese superoxide dismutase, and endothelial cell nitric oxide synthase are selectively up-regulated by steady laminar shear stress. Proc. Natl. Acad. Sci. 93, 10417–10422.

van den Berg, B.M., Spaan, J.A.E., Rolf, T.M., Vink, H., 2006. Atherogenic region and diet diminish glycocalyx dimension and increase intima-to-media ratios at murine carotid artery bifurcation. Am. J. Physiol. - Hear. Circ. Physiol. 290, H915–H920. doi:10.1152/ajpheart.00051.2005

van den Berg, B.M., Vink, H., Spaan, J.A.E., 2003. The endothelial glycocalyx protects against myocardial edema. Circ. Res. 92, 592–594. doi:10.1161/01.RES.0000065917.53950.75

van Duinen, V., Trietsch, S.J., Joore, J., Vulto, P., Hankemeier, T., 2015. Microfluidic 3D cell culture: from tools to tissue models. Curr. Opin. Biotechnol., Chemical biotechnology • Pharmaceutical biotechnology 35, 118–126. doi:10.1016/j.copbio.2015.05.002

Vennemann, P., Lindken, R., Westerweel, J., 2007. In vivo whole-field blood velocity measurement techniques. Exp. Fluids 42, 495–511. doi:10.1007/s00348-007-0276-4

Voetsch, B., Jin, R.C., Loscalzo, J., 2004. Nitric oxide insufficiency and atherothrombosis. Histochem. Cell Biol. 122, 353–367. doi:10.1007/s00418-004-0675-z

Vuorenpää, H., Ikonen, L., Kujala, K., Huttala, O., Sarkanen, J.-R., Ylikomi, T., Aalto-Setälä, K., Heinonen, T., 2014. Novel in vitro cardiovascular constructs composed of vascular-like networks and cardiomyocytes. In Vitro Cell. Dev. Biol. Anim. 50, 275–286. doi:10.1007/s11626-013-9703-4

Wagner, I., Materne, E.-M., Brincker, S., Süßbier, U., Frädrich, C., Busek, M., Sonntag, F., Sakharov, D.A., Trushkin, E. V., Tonevitsky, A.G., Lauster, R., Marx, U., 2013. A dynamic multi-organ-chip for long-term cultivation and substance testing proven by 3D human liver and skin tissue co-culture. Lab Chip 13, 3538–3547. doi:10.1039/C3LC50234A

Wallace, C.S., Truskey, G. a, 2010. Direct-contact co-culture between smooth muscle and endothelial cells inhibits TNF-alpha-mediated endothelial cell activation. Am. J. Physiol. Heart Circ. Physiol. 299, H338–H346. doi:10.1152/ajpheart.01029.2009

Wang, J.D., Douville, N.J., Takayama, S., ElSayed, M., 2012. Quantitative analysis of molecular absorption into PDMS microfluidic channels. Ann. Biomed. Eng. 40, 1862–1873. doi:10.1007/s10439-012-0562-z

Weisel, J.W., 2007. Structure of fibrin: impact on clot stability. J. Thromb. Haemost. 5, 116–124. doi:10.1111/j.1538-7836.2007.02504.x

Westerweel, J., Nieuwstadt, F.T.M., TU Delft, TU Delft, Delft University of Technology, 1993. Digital particle image velocimetry: theory and application.

Westerweel, J., 1997. Fundamentals of digital particle image velocimetry. Meas. Sci. Technol. 8, 1379–1392. doi:10.1088/0957-0233/8/12/002

Westerweel, J., Scarano, F., 2005. Universal outlier detection for PIV data. Exp. Fluids 39, 1096–1100. doi:10.1007/s00348-005-0016-6

Wilmer Nichols, Michael O'Rourke, Charalambos Vlachopoulos, 2011. McDonald's blood flow in arteries: Theoretical, experimental and clinical principles.

Wolbank, S., Peterbauer, A., Fahrner, M., Hennerbichler, S., van Griensven, M., Stadler, G., Redl, H., Gabriel, C., 2007. Dose-dependent immunomodulatory effect of human stem cells from amniotic membrane: a comparison with human mesenchymal stem cells from adipose tissue. Tissue Eng. 13, 1173–1183. doi:10.1089/ten.2006.0313

Wu, M.-H., Huang, S.-B., Cui, Z., Cui, Z., Lee, G.-B., 2007. A high throughput perfusion-based microbioreactor platform integrated with pneumatic micropumps for three-dimensional cell culture. Biomed. Microdevices 10, 309–319. doi:10.1007/s10544-007-9138-3

Xu, H., Wu, J., Chu, C.-C., Shuler, M.L., 2012. Development of disposable PDMS micro cell culture analog devices with photopolymerizable hydrogel encapsulating living cells. Biomed. Microdevices 14, 409–418. doi:10.1007/s10544-011-9617-4

Yang, S., Graham, J., Kahn, J.W., Schwartz, E.A., Gerritsen, M.E., 1999. Functional roles for PECAM-1 (CD31) and VE-cadherin (CD144) in tube assembly and lumen formation in three-dimensional collagen gels 155, 887–895.

Zarske, V., 2015. Untersuchung der Flüssigkeitsströmungen im Multi-Organ-Chip. Technische Universität Berlin.

Zhang, B., Montgomery, M., Chamberlain, M.D., Ogawa, S., Korolj, A., Pahnke, A., Wells, L.A., Massé, S., Kim, J., Reis, L., Momen, A., Nunes, S.S., Wheeler, A.R., Nanthakumar, K., Keller, G., Sefton, M. V., Radisic, M., 2016. Biodegradable scaffold with built-in vasculature for organ-on-a-chip engineering and direct surgical anastomosis. Nat. Mater. doi:10.1038/nmat4570

Zhang, C., Zhao, Z., Rahim, N.A.A., Noort, D. van, Yu, H., 2009. Towards a human-on-chip: Culturing multiple cell types on a chip with compartmentalized microenvironments. Lab Chip 9, 3185–3192. doi:10.1039/B915147H

Zhao, Y., Chen, B.P.C., Miao, H., Yuan, S., Li, Y.-S., Hu, Y., Rocke, D.M., Chien, S., 2002. Improved significance test for DNA microarray data: temporal effects of shear stress on endothelial genes. Physiol. Genomics 12, 1–11. doi:10.1152/physiolgenomics.00024.2002

Zheng, Y., Chen, J., Craven, M., Choi, N.W., Totorica, S., Diaz-Santana, A., Kermani, P., Hempstead, B., Fischbach-Teschl, C., López, J.A., Stroock, A.D., 2012. In vitro microvessels for the study of angiogenesis and thrombosis. Proc. Natl. Acad. Sci. 109, 9342–9347. doi:10.1073/pnas.1201240109

Zhou, J., Schmid, T., Schnitzer, S., Brüne, B., 2006. Tumor hypoxia and cancer progression. Cancer Lett. 237, 10–21. doi:10.1016/j.canlet.2005.05.028

5.2. Abbreviations

µPIV	micro particle image velocimetry
2OC	two-organ-chip
2PM	two-photon microscopy
3D	three-dimensional
4OC	four-organ-chip
ANOVA	analysis of variance
AP	adapter plate
ASC	adipose-derived stroma cell
bFGF	basic fibroblast growth factor
CC	central compartment (of the MOC4Xt)
CCI	cell culture insert
CD31	cluster of differentiation 31 (also PECAM-1)
CD144	cluster of differentiation 144 (also VE-cadherin)
CD202B	cluster of differentiation 202B (also TEK)
CD309	cluster of differentiation 309 (also VEGFR-2)
CFD	computational fluid dynamics
CLAHE	contrast limited adaptive histogram equalisation
COX-2	cyclooxygenase-2
DCU	Dresden control unit
DoE	design of experiments
EC	endothelial cell
ECFC	endothelial colony-forming cell (also OEC)
ECM	extracellular matrix
EGM	endothelial growth medium
eNOS	endothelial nitric oxide synthase
EPC	late endothelial progenitor cell (also OEC)
FBS	foetal bovine serum
Flk1	foetal liver kinase 1 (also VEGFR-2)
fps	frames per second
GAPDH	glyceraldehyde 3-phosphate dehydrogenase
GFP	green fluorescent protein
HAEC	human arterial endothelial cell
HDMEC	human dermal microvascular endothelial cell
HUVEC	human umbilical vein endothelial cell
Ht	haematocrit
ICAM	intercellular adhesion molecule
ID	identification
IM	medium channel in between the OC and the CC (of the MOC4Xt)
IVCT	isovolumic contraction time (others also use ICT)
IVRT	isovolumic relaxation time
IW	interrogation window
KDR	kinase insert domain (also VEGFR-2)
LBI	Ludwig Boltzmann Institute for Experimental and Clinical Traumatology

LDH	lactate dehydrogenase
MCU	Moscow control unit
MMP	matrix metalloproteinase
MOC	multi-organ-chip
MPC	mesenchymal progenitor cell
MPS	microphysiological system
MSC	mesenchymal stroma cell
NO	nitric oxide
OC	outer compartment (of the MOC4Xt)
OEC	outgrowth endothelial cell (others also use EPC, ECFC)
PBS	phosphate-buffered saline
PDMS	polydimethylsiloxane
PECAM-1	platelet endothelial cell adhesion molecule (also CD31)
PIV	particle image velocimetry
POMaC	poly-octamethylene-maleate-anhydride-citrate
PS	polystyrene
px	pixel
qPCR	quantitative real-time polymerase chain reaction
RBC	red blood cell
ROI	region of interest
SHED	dental pulp stem cell derived from deciduous teeth
SMC	smooth muscle cell
TEK	endothelial tyrosine kinase a.k.a. angiopoietin-1 receptor (others also use CD202B)
TGF-ß	transforming growth factor beta
VCAM	vascular cell adhesion molecule
VE-cadherin	vascular endothelial cadherin (also CD144)
VEGF	vascular endothelial growth factor
VEGFR-2	vascular endothelial growth factor receptor 2 (others also use KDR, CD309, Flk1)
vWF	von Willebrand factor
WSS	wall shear stress

5.3. Supplementary compilation

Videos:

- macroscopic view on a pumping 2OC
- microscopic view on the micropump
- example µPIV recordings (with and without vector fields)
- flow disrupts fibrin adhesion in dependency of applied pressure (related to figure 3.02)
- 3D rendering of in-depth grown microvessels (related to figure 3.08)

Scripts (all running in MATLAB R2015a):

- PIVlab_commandline_edited_incl subfolder.m – running PIVlab from the MATLAB shell with standardly applied settings (©Thielicke) and continuing through the folder after completion
- PIVAnalyse_v3_7.m – extraction of the flow profile from MATLAB-file and creating analysable output files
- startPIVAnalyse_v3_7.m – running the extraction for a complete set of experiments and summarising the data
- Int_assign.m – finding the control unit's sequence in the flow profile
- third party scripts: PIVlab 1.41, ipeak6, xlwrite, fastsmooth.m, xls_check_if_open.m

5.4. Extended design matrix of the second DoE-screening

The table is an extended version of table 2.8 on page 64. The value 1 symbolises the upper limit of a factor, -1 describes the lower limit. Through column multiplication of the factors or interactions the values for the corresponding interaction is produced. The designID is created after the experiments and orders the experiments by their average flow rate (Fig. 2.10, page 20).

DesignID	A	B	C	D	E	AB	AC	AD	AE	BC	BD	BE	CD	CE	DE
10	-1	-1	-1	-1	1	1	1	1	-1	1	1	-1	1	-1	-1
7	1	-1	-1	-1	-1	-1	-1	-1	-1	1	1	1	1	1	1
6	-1	1	-1	-1	-1	-1	1	1	1	-1	-1	-1	1	1	1
17	1	1	-1	-1	1	1	-1	-1	1	-1	-1	1	1	-1	-1
8	-1	-1	1	-1	-1	1	-1	1	1	-1	1	1	-1	-1	1
12	1	-1	1	-1	1	-1	1	-1	1	-1	1	-1	-1	1	-1
15	-1	1	1	-1	1	-1	-1	1	-1	1	-1	1	-1	1	-1
1	1	1	1	-1	-1	1	1	-1	-1	1	-1	-1	-1	-1	1
9	-1	-1	-1	1	-1	1	1	-1	1	1	-1	1	-1	1	-1
13	1	-1	-1	1	1	-1	-1	1	1	1	-1	-1	-1	-1	1
14	-1	1	-1	1	1	-1	1	-1	-1	-1	1	1	-1	-1	1
2	1	1	-1	1	-1	1	-1	1	-1	-1	1	-1	-1	1	-1
11	-1	-1	1	1	1	1	-1	-1	-1	-1	-1	-1	1	1	1
5	1	-1	1	1	-1	-1	1	1	-1	-1	-1	1	1	-1	-1
4	-1	1	1	1	-1	-1	-1	-1	1	1	1	-1	1	-1	-1
18	1	1	1	1	1	1	1	1	1	1	1	1	1	1	1
3	-0.1	0.3	0	0	-1	-0,03	0	0	0,1	0	0	-0,3	0	0	0
16	-0.1	0.3	0	0	1	-0,03	0	0	-0,1	0	0	0,3	0	0	0
Aliases					ABCD	CDE	BDE	BCE	BCD	ADE	ACE	ACD	ABE	ABD	ABC

A – frequency; B – pressure; C – vacuum; D – throttling; E – main pumping direction

(continued)

DesignID	ABC	ABD	ABE	ACD	ACE	ADE	BCD	BCE	BDE	CDE	ABCD	ABCE	ABDE	ACDE	BCDE	ABCDE
10	-1	-1	1	-1	1	1	-1	1	1	1	1	-1	-1	-1	-1	1
7	1	1	1	1	1	1	-1	-1	-1	-1	-1	-1	-1	-1	1	1
6	1	1	1	-1	-1	-1	1	1	1	-1	-1	-1	-1	1	-1	1
17	-1	-1	1	1	-1	-1	1	-1	-1	1	1	-1	-1	1	1	1
8	1	-1	-1	1	1	-1	1	1	-1	1	-1	-1	1	-1	-1	1
12	-1	1	-1	-1	1	-1	1	-1	1	-1	1	-1	1	-1	1	1
15	-1	1	-1	1	-1	1	-1	1	-1	-1	1	-1	1	1	-1	1
1	1	-1	-1	-1	-1	1	-1	-1	1	1	-1	-1	1	1	1	1
9	-1	1	-1	1	-1	1	1	-1	1	1	-1	1	-1	-1	-1	1
13	1	-1	-1	-1	-1	1	1	1	-1	-1	1	1	-1	-1	1	1
14	1	-1	-1	1	1	-1	-1	-1	1	-1	1	1	-1	1	-1	1
2	-1	1	-1	-1	1	-1	-1	1	-1	1	-1	1	-1	1	1	1
11	1	1	1	-1	-1	-1	-1	-1	-1	1	1	1	1	-1	-1	1
5	-1	-1	1	1	-1	-1	-1	1	1	-1	-1	1	1	-1	1	1
4	-1	-1	1	-1	1	1	1	-1	-1	-1	-1	1	1	1	-1	1
18	1	1	1	1	1	1	1	1	1	1	1	1	1	1	1	1
3	0	0	0,03	0	0	0	0	0	0	0	0	0	0	0	0	0
16	0	0	-0,03	0	0	0	0	0	0	0	0	0	0	0	0	0
Aliases	DE	CE	CD	BE	BD	BC	AE	AD	AC	AB	E	D	C	B	A	I

A – frequency; B – pressure; C – vacuum; D – throttling; E – main pumping direction

5.5. Raw data…

5.5.1. …of the first DoE-screening

ID	Run	A [Hz]	B [kPa]	C [kPa]	D [L/min @ +35kPa]	E	F [m]	G [µL]	average velocity (WinA) [mm/s]	average velocity (WinC) [mm/s]	absolute extreme (WinA) [mm/s]	absolute extreme (WinC) [mm/s]
1	11	1	10	10	0.9	fwd	2	300	0.11	0.14	41.30	30.04
2	4	1	10	10	0.9	bwd	1	600	0.09	0.11	36.24	35.21
3	22	1	10	75	0.3	fwd	2	600	0.21	1.21	30.18	27.16
4	2	5	10	10	0.3	bwd	2	600	0.49	0.72	13.39	10.84
5	39	5	10	10	0.3	fwd	1	300	0.55	1.42	25.51	20.15
6	3	1	10	75	0.3	bwd	1	300	1.27	0.68	49.48	44.51
7	1	5	10	75	0.9	bwd	2	300	1.60	2.76	110.69	82.58
8	9	1	75	10	0.3	fwd	1	600	1.52	3.04	74.10	196.09
9	16	5	10	75	0.9	fwd	1	600	1.66	3.67	124.42	123.94
10	13	1	75	10	0.3	bwd	2	300	1.87	2.67	78.29	116.51
11	26	1	75	75	0.9	fwd	1	300	2.87	3.89	203.60	450.44
12	40	1	75	75	0.9	bwd	2	600	3.20	6.63	250.08	377.87
13	44	3	42.5	42.5	0.6	fwd	1	450	5.88	10.34	133.07	265.74
14	15	3	42.5	42.5	0.6	bwd	1	450	7.02	11.55	167.93	209.62
15	21	5	75	75	0.3	fwd	2	300	7.38	11.67	66.94	89.68
16	7	5	75	10	0.9	fwd	2	600	7.62	13.72	144.86	343.32
17	12	5	75	10	0.9	bwd	1	300	8.46	16.45	255.50	331.77
18	23	5	75	75	0.3	bwd	1	600	9.67	16.86	105.78	154.07

A – frequency; B – pressure; C – vacuum; D – throttling; E – main pumping direction; F – length of tubing; G – liquid volume in chip

5.5.2. …of the second DoE-screening

The responses are the averaged data points of three independent circuits. Additionally, the given flow rate Q is the average of the three ROIs WinA, WinB and WinC. Crossed out values are neglected in the evalutation (see respective text passages).

ID	Run	A	B	C	D	E	Q_mean	abs(Q_mean)	WSS extreme in main dir (WinA)	WSS extreme in main dir (WinB)	WSS extreme in main dir (WinC)	ratio extremes (WinA)	ratio extremes (WinB)	ratio extremes (WinC)	WSS_mean in main dir (WinA)	WSS_mean in main dir (WinB)	WSS_mean in main dir (WinC)
		[Hz]	[kPa]	[kPa]	[L/min @ +35kPa]		[µL/min]	[µL/min]	[dyn/cm²]	[dyn/cm²]	[dyn/cm²]	[1]	[1]	[1]	[dyn/cm²]	[dyn/cm²]	[dyn/cm²]
1	7	1	70	70	0.3	bwd	-19.981	19.981	18.9181	7.78196	33.2179	0.265032	0.203228	1.08238	6.2659	4.19614	9.22797
2	13	1	70	10	0.9	bwd	-17.4295	17.4295	44.1252	6.94473	62.4172	0.64974	0.105057	0.295094	6.10704	3.53145	8.02794
3	2	0.5	47.5	40	0.6	bwd	-8.02826	8.02826	~~26.9793~~	~~4.83639~~	~~42.308~~	0.901109	0.447897	0.462961	3.53253	2.74037	4.26226
3	14	0.5	47.5	40	0.6	bwd	-6.58061	6.58061	~~26.4096~~	~~5.07679~~	~~40.4272~~	0.888735	0.509629	0.499814	3.32384	2.8941	4.01082
3	16	0.5	47.5	40	0.6	bwd	-6.68585	6.68585	~~27.1753~~	~~5.10004~~	~~41.1434~~	0.877484	0.500958	0.499876	3.48113	2.87872	4.07697
3	19	0.5	47.5	40	0.6	bwd	-5.53558	5.53558	~~25.2607~~	~~5.13763~~	~~38.6632~~	0.904522	0.547544	0.554499	3.24121	2.79707	3.70093
3	20	0.5	47.5	40	0.6	bwd	-5.56038	5.56038	~~26.6962~~	~~5.073~~	~~39.4391~~	0.884794	0.559219	0.552424	3.37679	2.75979	3.75382
3	28	0.5	47.5	40	0.6	bwd	-5.80745	5.80745	~~26.7879~~	~~5.14163~~	~~39.689~~	0.885674	0.537043	0.544547	3.72739	2.80564	3.74438
4	5	0.1	70	70	0.9	bwd	-2.02696	2.02696	34.3298	7.02811	37.523	1.17339	0.600435	0.33888	1.27586	1.40334	0.895242
5	12	1	10	70	0.9	bwd	-1.56138	1.56138	19.352	2.30184	10.6899	0.933918	0.381002	0.656709	5.23089	1.22652	3.02695
6	23	0.1	70	10	0.3	bwd	-1.16981	1.16981	6.78092	3.22131	8.78578	1.02302	0.555785	0.583967	0.525008	0.712613	0.486933
7	10	1	10	10	0.3	bwd	-0.332585	0.332585	3.081	0.518815	1.35772	0.781401	0.410068	0.89427	0.810529	0.243742	0.408946
8	8	0.1	10	70	0.3	bwd	-0.234473	0.234473	3.67897	1.06284	2.47637	1.10272	1.14772	0.58029	0.456838	0.234323	0.219273
9	26	0.1	10	10	0.9	bwd	-0.0117918	0.0117918	2.15428	0.304759	1.23224	1.05124	1.0819	0.878938	0.0669108	0.041281	0.0474238
10	9	0.1	10	10	0.3	fwd	0.026889	0.026889	1.17213	0.239175	0.627414	0.836238	0.818068	1.01941	0.0768336	0.036656	0.0466443
11	3	0.1	10	70	0.9	fwd	0.294479	0.294479	4.63049	1.75939	7.2781	0.590367	0.715401	1.10917	0.196105	0.279031	0.412607
12	24	1	10	70	0.3	fwd	0.540152	0.540152	3.29269	1.08785	2.61036	1.01722	0.80092	0.535748	1.67482	0.539135	1.46266
13	4	1	10	10	0.9	fwd	1.07405	1.07405	6.15878	0.701745	7.86462	0.622473	0.670295	0.848182	0.919511	0.388946	1.2088
14	11	0.1	70	10	0.9	fwd	1.20578	1.20578	10.4788	4.37296	33.9955	0.562703	0.46461	0.873002	0.284031	0.714943	1.0854
15	22	0.1	70	70	0.3	fwd	2.16895	2.16895	8.06186	5.45959	19.6519	0.498391	0.575774	0.975694	0.527217	1.38693	2.09158
16	1	0.5	47.5	40	0.6	fwd	8.86327	8.86327	~~25.3264~~	~~5.27992~~	~~32.7844~~	0.589826	0.428449	0.87675	2.61116	2.85275	5.6883
16	15	0.5	47.5	40	0.6	fwd	6.82576	6.82576	~~18.9903~~	~~5.10809~~	~~32.5689~~	0.745242	0.586981	0.892478	2.09182	2.85393	5.39604
16	17	0.5	47.5	40	0.6	fwd	7.82312	7.82312	~~25.1231~~	~~5.14682~~	~~32.9443~~	0.70504	0.571406	0.890842	2.66552	2.87718	5.57136
16	18	0.5	47.5	40	0.6	fwd	6.27088	6.27088	~~22.8553~~	~~5.08216~~	~~31.7383~~	0.819708	0.695202	0.907163	2.42355	2.77303	5.38972
16	21	0.5	47.5	40	0.6	fwd	6.60597	6.60597	~~22.5516~~	~~4.80564~~	~~31.9383~~	0.798034	0.657634	0.902149	2.35915	2.66712	5.40593
16	27	0.5	47.5	40	0.6	fwd	5.80682	5.80682	~~15.7741~~	~~5.06014~~	~~31.9164~~	0.850865	0.693287	0.929519	1.87667	2.79909	5.41951
17	6	1	70	10	0.3	fwd	15.0793	15.0793	13.1521	5.12879	22.5966	0.447596	0.158905	0.257795	3.90281	2.84497	6.84302
18	25	1	70	70	0.9	fwd	25.1999	25.1999	44.3333	10.6353	64.3732	0.672791	0.284089	0.717865	8.56561	5.9048	16.6163

A – frequency; B – pressure; C – vacuum; D – throttling; E – main pumping direction

(continued)

ID	WSS_mean against main dir (WinA) [dyn/cm²]	WSS_mean against main dir (WinB) [dyn/cm²]	WSS_mean against main dir (WinC) [dyn/cm²]	WSS_mean modulus (WinA) [dyn/cm²]	WSS_mean modulus (WinB) [dyn/cm²]	WSS_mean modulus (WinC) [dyn/cm²]	pulse duration (WinA. Int1) [s]	pulse duration (WinA. Int2) [s]	pulse duration (WinC. Int4) [s]	pulse duration (WinC. Int5) [s]	pulse volume (WinA. Int1) [µL]	pulse volume (WinA. Int2) [µL]	pulse volume (WinC. Int4) [µL]	pulse volume (WinC. Int5) [µL]
1	1.99603	0.964332	10.9405	4.21044	3.80342	9.64702	0.174432	0.18023	0.194621	0.101885	0.0903855	0.361621	0.239013	0.184399
2	2.56984	0.558195	5.34446	4.43793	3.15454	7.19875	0.0870663	0.118001	0.106974	0.164168	0.154259	0.298802	0.339558	0.132723
3	1.75858	1.20006	4.12343	2.6447	2.18508	4.22009	0.128941	0.212976	0.170312	0.25049	0.220098	0.323677	0.374396	0.18935
3	1.87841	1.45114	4.11311	2.5946	2.3306	4.04081	0.132121	0.215379	0.170312	0.240381	0.240864	0.310064	0.353449	0.199869
3	1.95879	1.46108	4.13918	2.7122	2.32471	4.09399	0.132707	0.215858	0.169661	0.239364	0.250868	0.321087	0.358857	0.202477
3	2.03968	1.6983	4.40284	2.62658	2.36619	3.91283	0.144543	0.217232	0.172386	0.235663	0.260681	0.301647	0.338678	0.208957
3	2.11935	1.71384	4.51976	2.73265	2.34907	3.98136	0.145188	0.21508	0.171451	0.235379	0.271453	0.315063	0.345823	0.214268
3	1.93596	1.68512	4.57038	2.7429	2.36549	3.97475	0.140454	0.219564	0.169621	0.246643	0.267035	0.319135	0.343812	0.210333
4	0.557004	0.815649	0.984079	0.867332	1.15793	0.922795	0.107959	0.254295	0.15738	0.381616	0.332237	0.43611	0.298832	0.186816
5	6.36748	0.438434	2.61895	5.68212	0.777956	2.82914	0.17216	0.155617	0.188856	0.155585	0.170381	0.205776	0.0850867	0.046143
6	0.230875	0.375797	0.433197	0.371283	0.580211	0.46939	0.244252	0.331408	0.2867	0.376492	0.107592	0.191331	0.155428	0.081282
7	1.08598	0.0997651	0.461084	0.920257	0.16655	0.430759	0.181246	0.160264	0.190666	0.178303	0.0333555	0.0343488	0.0118839	0.0102449
8	0.428424	0.219892	0.178311	0.443393	0.228085	0.19991	0.380545	0.62946	0.375028	0.705892	0.15281	0.151377	0.0535924	0.0423399
9	0.0718311	0.0410623	0.0444624	0.0690679	0.0412287	0.0458107	0.0713747	0.089308	0.079788	0.090768	0.0115677	0.0119018	0.00440853	0.00388975
10	0.0669083	0.0316235	0.0461098	0.0713199	0.0348414	0.046359	0.20982	0.175747	0.230336	0.22692	0.0147615	0.0155525	0.00592872	0.00570705
11	0.167316	0.241938	0.285172	0.181443	0.2628	0.348682	0.277608	0.154585	0.284504	0.16836	0.0550535	0.0615874	0.10305	0.0739424
12	2.02114	0.401357	0.983598	1.82727	0.468926	1.19864	0.17586	0.193132	0.182665	0.170714	0.0557231	0.0485989	0.0416305	0.0195744
13	0.829076	0.328639	0.879869	0.875972	0.376971	1.05381	0.109814	0.0832406	0.101877	0.0842244	0.0320958	0.0362961	0.0357432	0.0247239
14	0.248337	0.379481	0.332751	0.269944	0.588053	0.652704	0.173236	0.121229	0.155184	0.0793	0.0702657	0.0985752	0.23565	0.0928789
15	0.510342	0.893025	0.79697	0.520473	1.19918	1.38202	0.799827	0.368351	0.716628	0.297192	0.20944	0.255509	0.557769	0.308705
16	2.65552	1.28872	2.51339	2.62382	2.35298	4.19128	0.230264	0.164054	0.242292	0.142679	0.197344	0.320835	0.371338	0.185367
16	2.5373	1.66175	2.76178	2.22848	2.41947	4.14816	0.228052	0.16935	0.238876	0.145717	0.197506	0.240003	0.359888	0.204699
16	2.81104	1.63548	2.77435	2.70911	2.42789	4.2462	0.218548	0.16397	0.238063	0.145375	0.221704	0.316906	0.368659	0.204484
16	2.89492	2.04702	2.92789	2.56553	2.48834	4.18277	0.2152	0.166003	0.242089	0.159088	0.231973	0.286346	0.358522	0.225391
16	2.96709	1.83277	2.97748	2.5414	2.35965	4.25014	0.222015	0.167438	0.243577	0.156746	0.226488	0.288333	0.361943	0.222569
16	2.45618	2.02451	3.01184	2.0471	2.50138	4.2523	0.22859	0.176584	0.24644	0.156404	0.192641	0.206089	0.360604	0.228005
17	2.09805	0.180209	1.88695	3.24679	2.77989	4.75599	0.181599	0.168887	0.192577	0.191008	0.0774763	0.167192	0.277814	0.0544227
18	7.68221	2.07686	7.53255	8.26687	5.20939	12.363	0.167946	0.190631	0.108946	0.189544	0.321013	0.492061	0.336555	0.286535

5.6. Inferential statistics to the second DoE-screening

5.6.1. Flow rate

ANOVA for selected factorial model

Analysis of variance table [Partial sum of squares - Type III]

Source	Sum of Squares	df	Mean Square	F Value	p-value Prob > F
Model	2096,99	10	209,70	106,95	< 0.0001
A-f	*0,32*	*1*	*0,32*	*0,16*	*0,6926*
B-+p	*0,76*	*1*	*0,76*	*0,39*	*0,5406*
C--p	*2,22*	*1*	*2,22*	*1,13*	*0,3024*
D-thr	*7,08*	*1*	*7,08*	*3,61*	*0,0744*
E-dir	*890,15*	*1*	*890,15*	*453,98*	*< 0.0001*
AD	*11,07*	*1*	*11,07*	*5,64*	*0,0295*
AE	*341,55*	*1*	*341,55*	*174,19*	*< 0.0001*
BE	*420,12*	*1*	*420,12*	*214,26*	*< 0.0001*
CD	*290,51*	*1*	*290,51*	*148,16*	*< 0.0001*
CE	*15,36*	*1*	*15,36*	*7,83*	*0,0123*
Residual	33,33	17	1,96		
Lack of Fit	*22,49*	*7*	*3,21*	*2,96*	*0,0586*
Pure Error	*10,85*	*10*	*1,08*		
Cor Total	2130,32	27			

Std. Dev.	1,40	R-Squared	0,9844
Mean	0,24	Adj R-Squared	0,9751
C.V. %	573,23	Pred R-Squared	0,9182
PRESS	174,33	Adeq Precision	50,378
-2 Log Likelihood	84,34	BIC	121,00
		AICc	122,84

Factor	Coefficient Estimate	df	Standard Error	95% CI Low	95% CI High	VIF
Intercept	0,23	1	0,27	-0,34	0,79	
A-f	0,14	1	0,35	-0,60	0,88	1,00
B-+p	0,22	1	0,35	-0,51	0,94	1,00
C--p	0,37	1	0,35	-0.37	1.11	1,00
D-thr	0,67	1	0,35	-0,073	1,40	1,00
E-dir	5,70	1	0,27	5,14	6,27	1,02
AD	0,83	1	0,35	0,093	1,57	1,00
AE	4,61	1	0,35	3,87	5,35	1,00
BE	5,06	1	0,35	4,33	5,79	1,02
CD	4,26	1	0,35	3.52	5.00	1,00
CE	0,98	1	0,35	0.24	1.72	1,00

Final Equation in Terms of Coded Factors:

Q_mean =
+0,23
+0,14 * A
+0,22 * B
+0,37 * C
+0,67 * D
+5,70 * E
+0,83 * AD
+4,61 * AE
+5,06 * BE
+4,26 * CD
+0,98 * CE

Final Equation in Terms of Actual Factors:

dir bwd
Q_mean =
+19,31541
-13,62523 * f
-0,16138 * +p
-0,30432 * -p
-20,10850 * thr
+6,16071 * f * thr
+0,47346 * -p * thr

dir fwd
Q_mean =
+3,35899
+6,85644 * f
+0,17577 * +p
-0,23900 * -p
-20,10850 * thr
+6,16071 * f * thr
+0,47346 * -p * thr

5.6.2. Flow rate (modulus)

Transform: Square Root **Constant:** 0,000000

ANOVA for selected factorial model

Analysis of variance table [Partial sum of squares - Type III]

Source	Sum of Squares	df	Mean Square	F Value	p-value Prob > F
Model	41,53	3	13,84	66,65	< 0.0001
A-f	*12,76*	*1*	*12,76*	*61,41*	*< 0.0001*
B-+p	*22,91*	*1*	*22,91*	*110,30*	*< 0.0001*
AB	*6,31*	*1*	*6,31*	*30,36*	*< 0.0001*
Residual	4,99	24	0,21		
Lack of Fit	*4,60*	*14*	*0,33*	*8,51*	*0,0009*
Pure Error	*0,39*	*10*	*0,039*		
Cor Total	46,52	27			

Std. Dev.	0,46	R-Squared	0,8928
Mean	2,09	Adj R-Squared	0,8794
C.V. %	21,82	Pred R-Squared	0,8517
PRESS	6,90	Adeq Precision	24,052
-2 Log Likelihood	31,14	BIC	44,47
		AICc	40,88

Factor	Coefficient Estimate	df	Standard Error	95% CI Low	95% CI High	VIF
Intercept	2,01	1	0,087	1,83	2,19	
A-f	0,89	1	0,11	0,66	1,13	1,00
B-+p	1,18	1	0,11	0,95	1,41	1,00
AB	0,63	1	0,11	0,39	0,86	1,00

Final Equation in Terms of Coded Factors:

Sqrt(abs(Q_mean)) =
+2,01
+0,89 * A
+1,18 * B
+0,63 * AB

Final Equation in Terms of Actual Factors:

Sqrt(abs(Q_mean)) =
+0,37221
+0,11922 * f
+0,013794 * +p
+0,046499 * f * +p

5.6.3. Wall shear stress extreme in direction of flow (WinA)

Transform: Square Root **Constant:** 0,000000

These designIDs were ignored for this analysis.
3, 16

ANOVA for selected factorial model

Analysis of variance table [Partial sum of squares - Type III]

Source	Sum of Squares	df	Mean Square	F Value	p-value Prob > F
Model	42,50	4	10,62	18,31	< 0.0001
A-f	*6,98*	*1*	*6,98*	*12,03*	*0,0053*
B-+p	*21,96*	*1*	*21,96*	*37,85*	*< 0.0001*
C--p	*3,14*	*1*	*3,14*	*5,42*	*0,0400*
D-thr	*10,41*	*1*	*10,41*	*17,95*	*0,0014*
Residual	6,38	11	0,58		
Cor Total	48,88	15			

Std. Dev.	0,76	R-Squared	0,8694
Mean	3,31	Adj R-Squared	0,8220
C.V. %	23,04	Pred R-Squared	0,7238
PRESS	13,50	Adeq Precision	14,476
-2 Log Likelihood	30,70	BIC	44,56
		AICc	46,70

Factor	Coefficient Estimate	df	Standard Error	95% CI Low	95% CI High	VIF
Intercept	3,31	1	0,19	2,89	3,72	
A-f	0,66	1	0,19	0,24	1,08	1,00
B-+p	1,17	1	0,19	0,75	1,59	1,00
C--p	0,44	1	0,19	0,024	0,86	1,00
D-thr	0,81	1	0,19	0,39	1,23	1,00

Final Equation in Terms of Coded Factors:

Sqrt(abs(extreme in dir WinA)) =
+3,31
+0,66 * A
+1,17 * B
+0,44 * C
+0,81 * D

Final Equation in Terms of Actual Factors:

Sqrt(abs(extreme in dir WinA)) =
-1,26840
+1,46775 * f
+0,039054 * +p
+0,014775 * -p
+2,68909 * thr

5.6.4. Wall shear stress exteme (WinB)

Transform: Square Root Constant: 0,000000

These designIDs were ignored for this analysis.
3, 16

ANOVA for selected factorial model

Analysis of variance table [Partial sum of squares - Type III]

Source	Sum of Squares	df	Mean Square	F Value	p-value Prob > F
Model	11,62	4	2,91	155,67	< 0.0001
A-f	*0,49*	*1*	*0,49*	*26,19*	*0,0003*
B-+p	*9,47*	*1*	*9,47*	*507,20*	*< 0.0001*
C--p	*1,31*	*1*	*1,31*	*69,96*	*< 0.0001*
D-thr	*0,36*	*1*	*0,36*	*19,34*	*0,0011*
Residual	0,21	11	0,019		
Cor Total	11,83	15			

Std. Dev.	0,14	R-Squared	0,9826
Mean	1,71	Adj R-Squared	0,9763
C.V. %	8,00	Pred R-Squared	0,9633
PRESS	0,43	Adeq Precision	36,135
-2 Log Likelihood	-24,29	BIC	-10,42
		AICc	-8,29

Factor	Coefficient Estimate	df	Standard Error	95% CI Low	95% CI High	VIF
Intercept	1,71	1	0,034	1,63	1,78	
A-f	0,17	1	0,034	0,100	0,25	1,00
B-+p	0,77	1	0,034	0,69	0,84	1,00
C--p	0,29	1	0,034	0,21	0.36	1,00
D-thr	0,15	1	0,034	0,075	0,23	1,00

Final Equation in Terms of Coded Factors:

Sqrt(abs(extreme in dir WinB)) =
+1,71
+0,17 * A
+0,77 * B
+0,29 * C
+0,15 * D

Final Equation in Terms of Actual Factors:

Sqrt(abs(extreme in dir WinB)) =
-0,21178
+0,38846 * f
+0,025641 * +p
+9,52283E-003 * -p
+0,50064 * thr

5.6.5. Wall shear stress extreme (WinC)

Transform: Square Root **Constant:** 0,000000

These rows were ignored for this analysis.
3, 16

ANOVA for selected factorial model

Analysis of variance table [Partial sum of squares - Type III]

Source	Sum of Squares	df	Mean Square	F Value	p-value Prob > F
Model	81,02	4	20,25	49,86	< 0.0001
A-f	*5,96*	*1*	*5,96*	*14,68*	*0,0028*
B-+p	*59,16*	*1*	*59,16*	*145,62*	*< 0.0001*
C--p	*2,39*	*1*	*2,39*	*5,88*	*0,0337*
D-thr	*13,51*	*1*	*13,51*	*33,25*	*0,0001*
Residual	4,47	11	0,41		
Cor Total	85,49	15			

Std. Dev.	0,64	R-Squared	0,9477
Mean	3,80	Adj R-Squared	0,9287
C.V. %	16,77	Pred R-Squared	0,8894
PRESS	9,45	Adeq Precision	21,547
-2 Log Likelihood	25,00	BIC	38,86
		AICc	41,00

Factor	Coefficient Estimate	df	Standard Error	95% CI Low	95% CI High	VIF
Intercept	3,80	1	0,16	3,45	4,15	
A-f	0,61	1	0,16	0,26	0,96	1,00
B-+p	1,92	1	0,16	1,57	2,27	1,00
C--p	0,39	1	0,16	0,036	0,74	1,00
D-thr	0,92	1	0,16	0,57	1,27	1,00

Final Equation in Terms of Coded Factors:

Sqrt(abs(extreme in dir WinC)) =
+3,80
+0,61 * A
+1,92 * B
+0,39 * C
+0,92 * D

Final Equation in Terms of Actual Factors:

Sqrt(abs(extreme in dir WinC)) =
-1,86137
+1,35677 * f
+0,064095 * +p
+0,012878 * -p
+3,06268 * thr

5.6.6. Average wall shear stress in main direction (WinA)

ANOVA for selected factorial model

Analysis of variance table [Partial sum of squares - Type III]

Source	Sum of Squares	df	Mean Square	F Value	p-value Prob > F
Model	115,82	8	14,48	53,30	< 0.0001
A-f	*55,30*	*1*	*55,30*	*203,62*	*< 0.0001*
B-+p	*22,96*	*1*	*22,96*	*84,54*	*< 0.0001*
C--p	*8,27*	*1*	*8,27*	*30,44*	*< 0.0001*
D-thr	*4,42*	*1*	*4,42*	*16,26*	*0,0007*
E-dir	*4,52*	*1*	*4,52*	*16,63*	*0,0006*
AB	*12,77*	*1*	*12,77*	*47,01*	*< 0.0001*
AC	*4,51*	*1*	*4,51*	*16,60*	*0,0006*
AD	*3,93*	*1*	*3,93*	*14,48*	*0,0012*
Residual	5,16	19	0,27		
Lack of Fit	*4,55*	*9*	*0,51*	*8,25*	*0,0014*
Pure Error	*0,61*	*10*	*0,061*		
Cor Total	120,98	27			

Std. Dev.	0,52	R-Squared	0,9573
Mean	2,56	Adj R-Squared	0,9394
C.V. %	20,38	Pred R-Squared	0,8709
PRESS	15,62	Adeq Precision	28,977
-2 Log Likelihood	32,11	BIC	62,10
		AICc	60,11

Factor	Coefficient Estimate	df	Standard Error	95% CI Low	95% CI High	VIF
Intercept	2,53	1	0,100	2,32	2,74	
A-f	1,85	1	0,13	1,58	2,13	1,00
B-+p	1,18	1	0,13	0,91	1,45	1,00
C--p	0,72	1	0,13	0,45	0,99	1,00
D-thr	0,53	1	0,13	0,25	0,80	1,00
E-dir	-0,40	1	0,098	-0,61	-0,20	1,00
AB	0,89	1	0,13	0,62	1,17	1,00
AC	0,53	1	0,13	0,26	0,80	1,00
AD	0,50	1	0,13	0,22	0,77	1,00

Final Equation in Terms of Coded Factors:

shear mean in dir of flow (WinA) =

+2,53
+1,85 * A
+1,18 * B
+0,72 * C
+0,53 * D
-0,40 * E
+0,89 * AB
+0,53 * AC
+0,50 * AD

Final Equation in Terms of Actual Factors:

dir bwd

shear mean in dir of flow (WinA) =
+0,61147
-2,30186 * f
+3,02156E-003 * +p
+2,33105E-003 * -p
-0,26847 * thr
+0,066160 * f * +p
+0,039324 * f * -p
+3,67221 * f * thr

dir fwd
shear mean in dir of flow (WinA) =
-0,19189
-2,30186 * f
+3,02156E-003 * +p
+2,33105E-003 * -p
-0,26847 * thr
+0,066160 * f * +p
+0,039324 * f * -p
+3,67221 * f * thr

5.6.7. Average wall shear stress in main direction (WinB)

ANOVA for selected factorial model

Analysis of variance table [Partial sum of squares - Type III]

Source	Sum of Squares	df	Mean Square	F Value	p-value Prob > F
Model	44,60	4	11,15	20,40	< 0.0001
A-f	*10,95*	*1*	*10,95*	*20,04*	*0,0002*
B-+p	*24,76*	*1*	*24,76*	*45,30*	*< 0.0001*
C--p	*2,77*	*1*	*2,77*	*5,06*	*0,0343*
AB	*6,55*	*1*	*6,55*	*11,99*	*0,0021*
Residual	12,57	23	0,55		
Lack of Fit	*12,52*	*13*	*0,96*	*195,58*	*< 0.0001*
Pure Error	*0,049*	*10*	*4,925E-003*		
Cor Total	57,17	27			

Std. Dev.	0,74	R-Squared	0,7801
Mean	2,05	Adj R-Squared	0,7419
C.V. %	36,08	Pred R-Squared	0,6508
PRESS	19,96	Adeq Precision	15,806
-2 Log Likelihood	57,04	BIC	73,70
		AICc	69,77

Factor	Coefficient Estimate	df	Standard Error	95% CI Low	95% CI High	VIF
Intercept	1,96	1	0,14	1,67	2,26	
A-f	0,83	1	0,18	0,44	1,21	1,00
B-+p	1,23	1	0,18	0,85	1,61	1,00
C--p	0,42	1	0,18	0.034	0,80	1,00
AB	0,64	1	0,18	0,26	1,02	1,00

Final Equation in Terms of Coded Factors:

shear mean in dir of flow (WinB) =
+1,96
+0,83 * A
+1,23 * B
+0,42 * C
+0,64 * AB

Final Equation in Terms of Actual Factors:

shear mean in dir of flow (WinB) =
-0,19287
-0,061704 * f
+0,014857 * +p
+0,013866 * -p
+0,047394 * f * +p

5.6.8. Average wall shear stress in main direction (WinC)

Transform: Square Root **Constant:** 0,000000

ANOVA for selected factorial model

Analysis of variance table [Partial sum of squares - Type III]

Source	Sum of Squares	df	Mean Square	F Value	p-value Prob > F
Model	18,86	4	4,72	24,48	< 0.0001
A-f	*7,73*	*1*	*7,73*	*40,14*	*< 0.0001*
B-+p	*8,56*	*1*	*8,56*	*44,43*	*< 0.0001*
C--p	*1,10*	*1*	*1,10*	*5,74*	*0,0251*
AB	*1,67*	*1*	*1,67*	*8,67*	*0,0073*
Residual	4,43	23	0,19		
Lack of Fit	*4,41*	*13*	*0,34*	*172,90*	*< 0.0001*
Pure Error	*0,020*	*10*	*1,962E-003*		
Cor Total	23,29	27			

Std. Dev.	0,44	R-Squared	0,8098
Mean	1,74	Adj R-Squared	0,7767
C.V. %	25,15	Pred R-Squared	0,7055
PRESS	6,86	Adeq Precision	18,095
-2 Log Likelihood	27,83	BIC	44,49
		AICc	40,56

Factor	Coefficient Estimate	df	Standard Error	95% CI Low	95% CI High	VIF
Intercept	1,70	1	0,084	1,53	1,88	
A-f	0,69	1	0,11	0,47	0,92	1,00
B-+p	0,72	1	0,11	0,50	0,95	1,00
C--p	0,26	1	0,11	0,036	0,49	1,00
AB	0,32	1	0,11	0,096	0,55	1,00

Final Equation in Terms of Coded Factors:

Sqrt(shear mean in dir of flow (WinC)) =

+1,70
+0,69 * A
+0,72 * B
+0,26 * C
+0,32 * AB

Final Equation in Terms of Actual Factors:

Sqrt(shear mean in dir of flow (WinC)) =

+0,070460
+0,58383 * f
+0,010902 * +p
+8,75978E-003 * -p
+0,023921 * f * +p

5.6.9. Average wall shear stress modulus (WinA)

ANOVA for selected factorial model

Analysis of variance table [Partial sum of squares - Type III]

Source	Sum of Squares	df	Mean Square	F Value	p-value Prob > F
Model	89,60	10	8,96	52,17	< 0.0001
A-f	*43,32*	*1*	*43,32*	*252,21*	*< 0.0001*
B-+p	*10,93*	*1*	*10,93*	*63,62*	*< 0.0001*
C--p	*8,61*	*1*	*8,61*	*50,12*	*< 0.0001*
D-thr	*5,11*	*1*	*5,11*	*29,73*	*< 0.0001*
E-dir	*0,64*	*1*	*0,64*	*3,74*	*0,0701*
AB	*5,63*	*1*	*5,63*	*32,78*	*< 0.0001*
AC	*5,38*	*1*	*5,38*	*31,30*	*< 0.0001*
AD	*5,15*	*1*	*5,15*	*29,98*	*< 0.0001*
BE	*2,63*	*1*	*2,63*	*15,30*	*0,0011*
CD	*3,02*	*1*	*3,02*	*17,59*	*0,0006*
Residual	2,92	17	0,17		
Lack of Fit	*2,57*	*7*	*0,37*	*10,51*	*0,0007*
Pure Error	*0,35*	*10*	*0,035*		
Cor Total	92,52	27			

Std. Dev.	0,41	R-Squared	0,9684
Mean	2,25	Adj R-Squared	0,9499
C.V. %	18,41	Pred R-Squared	0,8741
PRESS	11,65	Adeq Precision	31,993
-2 Log Likelihood	16,16	BIC	52,82
		AICc	54,66

Factor	Coefficient Estimate	df	Standard Error	95% CI Low	95% CI High	VIF
Intercept	2,25	1	0,079	2,08	2,42	
A-f	1,64	1	0,10	1,42	1,86	1,00
B-+p	0,82	1	0,10	0,60	1,03	1,00
C--p	0,73	1	0,10	0,51	0,95	1,00
D-thr	0,56	1	0,10	0,35	0,78	1,00
E-dir	-0,15	1	0,079	-0,32	0,014	1,02
AB	0,59	1	0,10	0,37	0,81	1,00
AC	0,58	1	0,10	0,36	0,80	1,00
AD	0,57	1	0,10	0,35	0,79	1,00
BE	0,40	1	0,10	0,18	0,62	1,02
CD	0,43	1	0,10	0,22	0,65	1,00

Final Equation in Terms of Coded Factors:

shear mean magn (WinA) =
+2,25
+1,64 * A
+0,82 * B
+0,73 * C
+0,56 * D
-0,15 * E
+0,59 * AB
+0,58 * AC
+0,57 * AD
+0,40 * BE
+0,43 * CD

Final Equation in Terms of Actual Factors:

dir bwd
shear mean magn (WinA) =
+2,19031
-2,34893 * f
-0,010307 * +p
-0,028135 * -p
-2,35938 * thr
+0,043932 * f * +p
+0,042939 * f * -p
+4,20224 * f * thr
+0,048284 * -p * thr

dir fwd
shear mean magn (WinA) =
+0,81794
-2,34893 * f
+0,016359 * +p
-0,028135 * -p
-2,35938 * thr
+0,043932 * f * +p
+0,042939 * f * -p
+4,20224 * f * thr
+0,048284 * -p * thr

5.6.10. Average wall shear stress modulus (WinB)

ANOVA for selected factorial model

Analysis of variance table [Partial sum of squares - Type III]

Source	Sum of Squares	df	Mean Square	F Value	p-value Prob > F
Model	36,72	4	9,18	26,53	< 0.0001
A-f	*8,99*	*1*	*8,99*	*25,99*	*< 0.0001*
B-+p	*19,99*	*1*	*19,99*	*57,77*	*< 0.0001*
C--p	*1,81*	*1*	*1,81*	*5,24*	*0,0316*
AB	*6,29*	*1*	*6,29*	*18,17*	*0,0003*
Residual	7,96	23	0,35		
Lack of Fit	*7,92*	*13*	*0,61*	*142,50*	*< 0.0001*
Pure Error	*0,043*	*10*	*4,273E-003*		
Cor Total	44,68	27			

Std. Dev.	0,59	R-Squared	0,8219
Mean	1,76	Adj R-Squared	0,7909
C.V. %	33,41	Pred R-Squared	0,7176
PRESS	12,62	Adeq Precision	17,600
-2 Log Likelihood	44,24	BIC	60,90
		AICc	56,96

Factor	Coefficient Estimate	df	Standard Error	95% CI Low	95% CI High	VIF
Intercept	1,69	1	0,11	1,45	1,92	
A-f	0,75	1	0,15	0,44	1,05	1,00
B-+p	1,10	1	0,15	0,80	1,40	1,00
C--p	0,34	1	0,15	0,032	0,64	1,00
AB	0,63	1	0,15	0,32	0,93	1,00

Final Equation in Terms of Coded Factors:

shear mean magn (WinB) =
+1,69
+0,75 * A
+1,10 * B
+0,34 * C
+0,63 * AB

Final Equation in Terms of Actual Factors:

shear mean magn (WinB) =
-0,12651
-0,19547 * f
+0,011237 * +p
+0,011220 * -p
+0,046425 * f * +p

5.6.11. Average wall shear stress modulus (WinC)

Transform: Square Root **Constant:** 0,000000

ANOVA for selected factorial model

Analysis of variance table [Partial sum of squares - Type III]

Source	Sum of Squares	df	Mean Square	F Value	p-value Prob > F
Model	15,82	4	3,95	25,45	< 0.0001
A-f	*6,75*	*1*	*6,75*	*43,44*	*< 0.0001*
B-+p	*6,78*	*1*	*6,78*	*43,62*	*< 0.0001*
C--p	*1,05*	*1*	*1,05*	*6,77*	*0,0159*
AB	*1,41*	*1*	*1,41*	*9,05*	*0,0063*
Residual	3,57	23	0,16		
Lack of Fit	*3,57*	*13*	*0,27*	*652,75*	*< 0.0001*
Pure Error	*4,207E-003*	*10*	*4,207E-004*		
Cor Total	19,39	27			

Std. Dev.	0,39	R-Squared	0,8157
Mean	1,62	Adj R-Squared	0,7837
C.V. %	24,31	Pred R-Squared	0,7138
PRESS	5,55	Adeq Precision	18,570
-2 Log Likelihood	21,82	BIC	38,48
		AICc	34,55

Factor	Coefficient Estimate	df	Standard Error	95% CI Low	95% CI High	VIF
Intercept	1,59	1	0,075	1,43	1,74	
A-f	0,65	1	0,098	0,44	0,85	1,00
B-+p	0,64	1	0,097	0,44	0,84	1,00
C--p	0,26	1	0,099	0,053	0,46	1,00
AB	0,30	1	0,099	0,093	0,50	1,00

Final Equation in Terms of Coded Factors:

Sqrt(shear mean magn (WinC)) =
+1,59
+0,65 * A
+0,64 * B
+0,26 * C
+0,30 * AB

Final Equation in Terms of Actual Factors:

Sqrt(shear mean magn (WinC)) =
+0,080199
+0,56132 * f
+9,33440E-003 * +p
+8,54918E-003 * -p
+0,021958 * f * +p

5.6.12. Pulse duration (WinA – M3/4)

Transform: Inverse Sqrt **Constant:** 0,000000

These designIDs were ignored for this analysis.
1, 5, 7, 12, 17, 18

ANOVA for selected factorial model

Analysis of variance table [Partial sum of squares - Type III]

Source	Sum of Squares	df	Mean Square	F Value	p-value Prob > F
Model	6,96	5	1,39	61,96	< 0.0001
B-+p	*0,16*	*1*	*0,16*	*7,28*	*0,0158*
C--p	*1,04*	*1*	*1,04*	*46,46*	*< 0.0001*
D-thr	*2,52*	*1*	*2,52*	*112,17*	*< 0.0001*
E-dir	*1,89*	*1*	*1,89*	*84,02*	*< 0.0001*
DE	*0,45*	*1*	*0,45*	*20,05*	*0,0004*
Residual	0,36	16	0,022		
Lack of Fit	*0,33*	*6*	*0,055*	*19,98*	*< 0.0001*
Pure Error	*0,028*	*10*	*2,766E-003*		
Cor Total	7,32	21			

Std. Dev.	0,15	R-Squared	0,9509
Mean	2,42	Adj R-Squared	0,9355
C.V. %	6,18	Pred R-Squared	0,8568
PRESS	1,05	Adeq Precision	32,555
-2 Log Likelihood	-28,09	BIC	-9,55
		AICc	-10,49

Factor	Coefficient Estimate	df	Standard Error	95% CI Low	95% CI High	VIF
Intercept	2,36	1	0,033	2,29	2,43	
B-+p	-0,13	1	0,048	-0,23	-0,028	1,05
C--p	-0,33	1	0,049	-0,43	-0.23	1,04
D-thr	0,52	1	0,049	0,41	0,62	1,04
E-dir	-0,30	1	0,032	-0,37	-0,23	1,03
DE	-0,22	1	0,049	-0,32	-0,11	1,05

Final Equation in Terms of Coded Factors:

1/Sqrt(width WinA Int1) =
+2,36
-0,13 * B
-0,33 * C
+0,52 * D
-0,30 * E
-0,22 * DE

Final Equation in Terms of Actual Factors:

dir bwd

1/Sqrt(width WinA Int1) =

+1,80989

-4,30294E-003 * +p

-0,011059 * -p

+2,44431 * thr

dir fwd

1/Sqrt(width WinA Int1) =

+2,08639

-4,30294E-003 * +p

-0,011059 * -p

+0,99246 * thr

5.6.13. Pulse duration (WinA – M2/5)

Transform: **Inverse Sqrt** **Constant:** **0,000000**

These designIDs were ignored for this analysis.
1, 5, 7, 12, 17, 18

ANOVA for selected factorial model

Analysis of variance table [Partial sum of squares - Type III]

Source	Sum of Squares	df	Mean Square	F Value	p-value Prob > F
Model	5,16	5	1,03	86,13	< 0.0001
B-+p	*0,26*	*1*	*0,26*	*21,78*	*0,0003*
C--p	*1,33*	*1*	*1,33*	*110,86*	*< 0.0001*
D-thr	*2,14*	*1*	*2,14*	*178,77*	*< 0.0001*
E-dir	*0,48*	*1*	*0,48*	*39,90*	*< 0.0001*
DE	*0,099*	*1*	*0,099*	*8,24*	*0,0111*
Residual	0,19	16	0,012		
Lack of Fit	*0,19*	*6*	*0,031*	*49,28*	*< 0.0001*
Pure Error	*6,266E-003*	*10*	*6,266E-004*		
Cor Total	5,35	21			

Std. Dev.	0,11	R-Squared	0,9642
Mean	2,35	Adj R-Squared	0,9530
C.V. %	4,66	Pred R-Squared	0,8522
PRESS	0,79	Adeq Precision	34,968
-2 Log Likelihood	-41,93	BIC	-23,38
		AICc	-24,33

Factor	Coefficient Estimate	df	Standard Error	95% CI Low	95% CI High	VIF
Intercept	2,30	1	0,024	2,24	2,35	
B-+p	-0,16	1	0,035	-0,24	-0,089	1,05
C--p	-0,37	1	0,036	-0,45	-0,30	1,04
D-thr	0,48	1	0,036	0,40	0,55	1,04
E-dir	0,15	1	0,024	0,099	0,20	1,03
DE	-0,10	1	0,036	-0,18	-0,027	1,05

Final Equation in Terms of Coded Factors:

1/Sqrt(width WinA Int2) =
+2,30
-0,16 * B
-0,37 * C
+0,48 * D
+0,15 * E
-0,10 * DE

Final Equation in Terms of Actual Factors:

dir bwd
1/Sqrt(width WinA Int2) =
+1,70777
-5,43370E-003 * +p
-0,012474 * -p
+1,92390 * thr

dir fwd
1/Sqrt(width WinA Int2) =
+2,41480
-5,43370E-003 * +p
-0,012474 * -p
+1,24417 * thr

5.6.14. Pulse duration (WinC – M2/5)

Transform: Inverse Sqrt **Constant:** 0,000000

These designIDs were ignored for this analysis.
1, 5, 7, 12, 17, 18

ANOVA for selected factorial model

Analysis of variance table [Partial sum of squares - Type III]

Source	Sum of Squares	df	Mean Square	F Value	p-value Prob > F
Model	5,29	5	1,06	71,97	< 0.0001
B-+p	*0,25*	*1*	*0,25*	*17,33*	*0,0007*
C--p	*1,24*	*1*	*1,24*	*84,13*	*< 0.0001*
D-thr	*2,12*	*1*	*2,12*	*143,79*	*< 0.0001*
E-dir	*0,78*	*1*	*0,78*	*52,88*	*< 0.0001*
DE	*0,15*	*1*	*0,15*	*10,52*	*0,0051*
Residual	0,24	16	0,015		
Lack of Fit	*0,23*	*6*	*0,039*	*344,47*	*< 0.0001*
Pure Error	*1,133E-003*	*10*	*1,133E-004*		
Cor Total	5,53	21			

Std. Dev.	0,12	R-Squared	0,9574
Mean	2,28	Adj R-Squared	0,9441
C.V. %	5,32	Pred R-Squared	0,8455
PRESS	0,85	Adeq Precision	37,447
-2 Log Likelihood	-37,39	BIC	-18,85
		AICc	-19,79

Factor	Coefficient Estimate	df	Standard Error	95% CI Low	95% CI High	VIF
Intercept	2,23	1	0,027	2,17	2,28	
B-+p	-0,16	1	0,039	-0,24	-0,079	1,05
C--p	-0,36	1	0,039	-0,44	-0,28	1,04
D-thr	0,47	1	0,039	0,39	0,56	1,04
E-dir	-0,19	1	0,026	-0,25	-0,14	1,03
DE	-0,13	1	0,039	-0,21	-0,044	1,05

Final Equation in Terms of Coded Factors:

1/Sqrt(width WinC Int4) =
+2,23
-0,16 * B
-0,36 * C
+0,47 * D
-0,19 * E
-0,13 * DE

Final Equation in Terms of Actual Factors:

dir bwd

1/Sqrt(width WinC Int4) =

+1,91337

-5,37299E-003 * +p

-0,012046 * -p

+2,00051 * thr

dir fwd

1/Sqrt(width WinC Int4) =

+2,04233

-5,37299E-003 * +p

-0,012046 * -p

+1,14917 * thr

5.6.15. Pulse duration (WinC – M1/6)

Transform: Inverse Sqrt **Constant:** 0,000000

These designIDs were ignored for this analysis.
1, 5, 7, 12, 17, 18

ANOVA for selected factorial model

Analysis of variance table [Partial sum of squares - Type III]

Source	Sum of Squares	df	Mean Square	F Value	p-value Prob > F
Model	6,34	3	2,11	42,22	< 0.0001
C--p	*1,56*	*1*	*1,56*	*31,20*	*< 0.0001*
D-thr	*2,25*	*1*	*2,25*	*44,91*	*< 0.0001*
E-dir	*0,99*	*1*	*0,99*	*19,70*	*0,0004*
Curvature	0,095	2	0,047	0,94	0,4096
Residual	0,80	16	0,050		
Lack of Fit	*0,78*	*6*	*0,13*	*59,27*	*< 0.0001*
Pure Error	*0,022*	*10*	*2,192E-003*		
Cor Total	7,24	21			

Std. Dev.	0,22	R-Squared	0,8879
Mean	2,33	Adj R-Squared	0,8668
C.V. %	9,60	Pred R-Squared	0,7003
PRESS	2,14	Adeq Precision	20,779
-2 Log Likelihood	-10,44	BIC	1,92
		AICc	-0,088

Factor	Coefficient Estimate	df	Standard Error	95% CI Low	95% CI High	VIF
Intercept	2,18	1	0,073	2,02	2,33	
C--p	-0,41	1	0,073	-0,56	-0,25	1,05
D-thr	0,49	1	0,073	0,34	0,65	1,05
E-dir	0,31	1	0,071	0,16	0,46	2,20
Ctr Pt 1	0,17	1	0,14			
Ctr Pt 2	0,082	1	0,14			

Final Equation in Terms of Coded Factors:

1/Sqrt(width WinC Int5) =
+2,18
-0,41 * C
+0,49 * D
+0,31 * E

Final Equation in Terms of Actual Factors:

dir bwd
1/Sqrt(width WinC Int5) =
+1,53217
-0,013246 * -p
+1,59698 * thr

dir fwd
1/Sqrt(width WinC Int5) =
+2,11186
-0,013246 * -p
+1,59698 * thr

5.6.16. Pulse volume (WinA – M3/4) (modulus)

Transform: Square Root **Constant:** 0,000000

These designIDs were ignored for this analysis.
1, 5, 7, 12, 17, 18

ANOVA for selected factorial model

Analysis of variance table [Partial sum of squares - Type III]

Source	Sum of Squares	df	Mean Square	F Value	p-value Prob > F
Model	0,35	4	0,088	48,83	< 0.0001
A-f	*0,099*	*1*	*0,099*	*54,63*	*< 0.0001*
B-+p	*0,097*	*1*	*0,097*	*53,81*	*< 0.0001*
C--p	*0,16*	*1*	*0,16*	*90,49*	*< 0.0001*
AC	*0,048*	*1*	*0,048*	*26,51*	*< 0.0001*
Residual	0,031	17	1,807E-003		
Lack of Fit	*0,027*	*7*	*3,871E-003*	*10,66*	*0,0006*
Pure Error	*3,630E-003*	*10*	*3,630E-004*		
Cor Total	0,38	21			

Std. Dev.	0,043	R-Squared	0,9199
Mean	0,40	Adj R-Squared	0,9011
C.V. %	10,61	Pred R-Squared	0,8366
PRESS	0,063	Adeq Precision	20,061
-2 Log Likelihood	-82,19	BIC	-66,73
		AICc	-68,44

Factor	Coefficient Estimate	df	Standard Error	95% CI Low	95% CI High	VIF
Intercept	0,47	1	0,014	0,44	0,50	
A-f	0,16	1	0,022	0,12	0,21	2,09
B-+p	0,099	1	0,013	0,070	0,13	1,03
C--p	0,23	1	0,024	0,18	0,28	3,13
AC	0,12	1	0,024	0,073	0,17	3,13

Final Equation in Terms of Coded Factors:

Sqrt(abs(pulse vol WinA Int1)) =
+0,47
+0,16 * A
+0,099 * B
+0,23 * C
+0,12 * AC

Final Equation in Terms of Actual Factors:

Sqrt(abs(pulse vol WinA Int1)) =
+0,039370
-2,15268E-003 * f
+3,28716E-003 * +p
+2,57428E-003 * -p
+9,15093E-003 * f * -p

5.6.17. Pulse volume (WinA – M2/5)

Transform: Square Root **Constant:** 0,000000

These designIDs were ignored for this analysis.
1, 5, 7, 12, 17, 18

ANOVA for selected factorial model

Analysis of variance table [Partial sum of squares - Type III]

Source	Sum of Squares	df	Mean Square	F Value	p-value Prob > F
Model	0,48	4	0,12	42,95	< 0.0001
A-f	*0,12*	*1*	*0,12*	*42,41*	*< 0.0001*
B-+p	*0,20*	*1*	*0,20*	*70,64*	*< 0.0001*
C--p	*0,15*	*1*	*0,15*	*54,68*	*< 0.0001*
AC	*0,044*	*1*	*0,044*	*15,69*	*0,0010*
Residual	0,047	17	2,784E-003		
Lack of Fit	*0,037*	*7*	*5,341E-003*	*5,37*	*0,0089*
Pure Error	*9,940E-003*	*10*	*9,940E-004*		
Cor Total	0,53	21			

Std. Dev.	0,053	R-Squared	0,9100
Mean	0,46	Adj R-Squared	0,8888
C.V. %	11,56	Pred R-Squared	0,7972
PRESS	0,11	Adeq Precision	19,279
-2 Log Likelihood	-72,69	BIC	-57,23
		AICc	-58,94

Factor	Coefficient Estimate	df	Standard Error	95% CI Low	95% CI High	VIF
Intercept	0,53	1	0,018	0,49	0,57	
A-f	0,18	1	0,027	0,12	0,24	2,09
B-+p	0,14	1	0,017	0,11	0,18	1,03
C--p	0,22	1	0,030	0,16	0,28	3,13
AC	0,12	1	0,030	0,055	0,18	3,13

Final Equation in Terms of Coded Factors:

Sqrt(pulse vol WinA Int2) =
+0,53
+0,18 * A
+0,14 * B
+0,22 * C
+0,12 * AC

Final Equation in Terms of Actual Factors:

Sqrt(pulse vol WinA Int2) =
+0,020391
+0,048507 * f
+4,67438E-003 * +p
+2,53445E-003 * -p
+8,73546E-003 * f * -p

5.6.18. Pulse volume (WinC – M2/5)

Transform: Square Root **Constant:** 0,000000

These designIDs were ignored for this analysis.
1, 5, 7, 12, 17, 18

ANOVA for selected factorial model

Analysis of variance table [Partial sum of squares - Type III]

Source	Sum of Squares	df	Mean Square	F Value	p-value Prob > F
Model	0,74	4	0,18	106,14	< 0.0001
A-f	*0,17*	*1*	*0,17*	*100,12*	*< 0.0001*
B-+p	*0,35*	*1*	*0,35*	*202,19*	*< 0.0001*
C--p	*0,20*	*1*	*0,20*	*117,73*	*< 0.0001*
AC	*0,072*	*1*	*0,072*	*41,85*	*< 0.0001*
Residual	0,029	17	1,731E-003		
Lack of Fit	*0,029*	*7*	*4,108E-003*	*60,69*	*< 0.0001*
Pure Error	*6,768E-004*	*10*	*6,768E-005*		
Cor Total	0,76	21			

Std. Dev.	0,042	R-Squared	0,9615
Mean	0,49	Adj R-Squared	0,9524
C.V. %	8,46	Pred R-Squared	0,9093
PRESS	0,069	Adeq Precision	29,236
-2 Log Likelihood	-83,14	BIC	-67,68
		AICc	-69,39

Factor	Coefficient Estimate	df	Standard Error	95% CI Low	95% CI High	VIF
Intercept	0,58	1	0,014	0,55	0,61	
A-f	0,22	1	0,022	0,17	0,26	2,09
B-+p	0,19	1	0,013	0,16	0,21	1,03
C--p	0,25	1	0,023	0,21	0,30	3,13
AC	0,15	1	0,023	0,10	0,20	3,13

Final Equation in Terms of Coded Factors:

Sqrt(pulse vol WinC Int4) =
+0,58
+0,22 * A
+0,19 * B
+0,25 * C
+0,15 * AC

Final Equation in Terms of Actual Factors:

Sqrt(pulse vol WinC Int4) =
-0,031182
+0,032055 * f
+6,23641E-003 * +p
+2,30368E-003 * -p
+0,011252 * f * -p

5.6.19. Pulse volume (WinC – M1/6) (modulus)

Transform: Square Root **Constant:** 0,000000

These designIDs were ignored for this analysis.
1, 5, 7, 12, 17, 18

ANOVA for selected factorial model

Analysis of variance table [Partial sum of squares - Type III]

Source	Sum of Squares	df	Mean Square	F Value	p-value Prob > F
Model	0,39	4	0,098	124,78	< 0.0001
A-f	*0,11*	*1*	*0,11*	*138,47*	*< 0.0001*
B-+p	*0,14*	*1*	*0,14*	*174,77*	*< 0.0001*
C--p	*0,16*	*1*	*0,16*	*201,99*	*< 0.0001*
AC	*0,055*	*1*	*0,055*	*70,04*	*< 0.0001*
Residual	0,013	17	7,821E-004		
Lack of Fit	*0,011*	*7*	*1,592E-003*	*7,41*	*0,0027*
Pure Error	*2,149E-003*	*10*	*2,149E-004*		
Cor Total	0,40	21			

Std. Dev.	0,028	R-Squared	0,9671
Mean	0,37	Adj R-Squared	0,9593
C.V. %	7,52	Pred R-Squared	0,9254
PRESS	0,030	Adeq Precision	31,372
-2 Log Likelihood	-100,62	BIC	-85,16
		AICc	-86,87

Factor	Coefficient Estimate	df	Standard Error	95% CI Low	95% CI High	VIF
Intercept	0,45	1	9,498E-003	0,43	0,47	
A-f	0,17	1	0,015	0,14	0,20	2,09
B-+p	0,12	1	8,844E-003	0,098	0,14	1,03
C--p	0,22	1	0,016	0,19	0,26	3,13
AC	0,13	1	0,016	0,099	0,17	3,13

Final Equation in Terms of Coded Factors:

Sqrt(abs(pulse vol WinC Int5)) =
+0,45
+0,17 * A
+0,12 * B
+0,22 * C
+0,13 * AC

Final Equation in Terms of Actual Factors:

Sqrt(abs(pulse vol WinC Int5)) =
-3,66016E-003
-0,010249 * f
+3,89722E-003 * +p
+2,09557E-003 * -p
+9,78393E-003 * f * -p

5.7. Desired factor, response ranges and weightings

		Constraints						Descriptive statics of 99 solutions					
		Goal	Lower limit	Upper limit	Lower weight	Upper weight	Importance	Minimum	Lower quantile	Median	Mean	Upper quartile	Maximum
Frequency		is in range	0.3	1	1	10	3	0.654	1	1	0.993	1	1
Pressure		is target = 45	30	60	1	2	3	36.91	55,437	56.466	55.322	56,733	57.847
Vacuum		is target = 45	20	60	2	1	3	20.482	20.695	20.715	21.091	20,796	41.793
Throttling		is in range	0.3	0.9	1	1	3	0.3	0,473	0.556	0.569	0,642	0.9
Direction of Pumping		is in range	bwd	fwd			3						
Flow rate		maximize	0.018	25.200	10	1	5	7.589	14,821	15.386	14.762	15,512	16.042
Wall shear stress extreme in main direction (!)	WinA	minimize	1.172	44.333	1	5	3	9.546	16,502	18.159	18.333	20,130	26.751
	WinB	maximize	0.239	10.635	1	1	2	2.669	4,231	4.398	4.349	4,531	5.203
	WinC	minimize	0.627	64.373	1	5	3	12.026	23,783	26.077	26.126	28,763	37.954
Average wall shear stress in main direction	WinA	maximize	0.067	8.567	5	1	3	2.363	4,026	4.445	4.430	4,963	6.132
	WinB	maximize	0.037	5.905	5	1	4	2.376	3,471	3.547	3.464	3,564	3.633
	WinC	maximize	0.047	16.616	5	1	3	4.814	7,803	8.042	7.782	8,096	8.313
... modulus	WinA	maximize	0.069	8.267	5	1	3	2.244	3,481	3.664	3.678	3,934	4.701
	WinB	maximize	0.035	5.209	5	1	4	2.075	3,095	3.166	3.088	3,182	3.245
	WinC	maximize	0.046	12.363	5	1	3	4.162	6,640	6.838	6.622	6,884	7.063
Pulse duration (!)	WinA. Int1	is target = 0.2	0.071	0.800	1	5	2	0.078	0,142	0.193	0.187	0,227	0.281
	WinA. Int2	is target = 0.2	0.083	0.629	1	5	2	0.109	0,150	0.169	0.176	0,201	0.341
	WinC. Int4	is target = 0.2	0.080	0.717	1	5	2	0.096	0,163	0.198	0.202	0,238	0.304
	WinC. Int5	is target = 0.2	0.079	0.706	1	5	2	0.096	0,140	0.164	0.184	0,239	0.393
Pulse volume (!)	WinA. Int1	minimize	0.012	0.332	1	10	3	0.187	0,216	0.218	0.217	0,219	0.33
	WinA. Int2	maximize	0.012	0.436	5	1	3	0.265	0,318	0.323	0.320	0,325	0.424
	WinC. Int4	maximize	0.004	0.558	5	1	3	0.311	0,395	0.403	0.398	0,406	0.535
	WinC. Int5	minimize	0.004	0.309	1	10	3	0.169	0,202	0.205	0.204	0,206	0.309

5.8. Contribution to publications

Parts of this work have been pre-published in the following works:

Hasenberg, T., Mühleder, S., Dotzler, A., Bauer, S., Labuda, K., Holnthoner, W., Redl, H., Lauster, R., Marx, U., 2015. Emulating human microcapillaries in a multi-organ-chip platform. J. Biotechnol. 216, 1–10. doi:10.1016/j.jbiotec.2015.09.038

Maschmeyer, I., Hasenberg, T., Jaenicke, A., Lindner, M., Lorenz, A.K., Zech, J., Garbe, L.-A., Sonntag, F., Hayden, P., Ayehunie, S., Lauster, R., Marx, U., Materne, E.-M., 2015. Chip-based human liver–intestine and liver–skin co-cultures – A first step toward systemic repeated dose substance testing in vitro. Eur. J. Pharm. Biopharm. doi:10.1016/j.ejpb.2015.03.002

Maschmeyer, I., Lorenz, A.K., Schimek, K., Hasenberg, T., Ramme, A.P., Hübner, J., Lindner, M., Drewell, C., Bauer, S., Thomas, A., Sambo, N.S., Sonntag, F., Lauster, R., Marx, U., 2015. A four-organ-chip for interconnected long-term co-culture of human intestine, liver, skin and kidney equivalents. Lab Chip. doi:10.1039/C5LC00392J

Acknowledgments

With this I want to thank everybody who helped me and supported me during all these years of my PhD studies. With so many people coming and going through our lab over the years, it is almost impossible to thank everybody individually. Nonetheless, I am grateful for everyone's help, insights and ideas regardless of the brevity of some of our encounters. Some of these truely stand out as without them there would be no thesis or at least not a thesis of this quality. Above all, I want to express my gratitude once again to Dr. Uwe Marx and Professor Roland Lauster, who believed in my strengths and invited me to the Department of Medical Biotechnology and later to TissUse to prepare my dissertation.

Naturally, a great deal of help came from my three students Sophie Bauer, Andrea Dotzler and Victoria Zarske. Thanks for your truly valuable feedback, which helped my thesis to grow. I consider myself lucky to have worked with you. Also my colleagues have a fair share on this thesis. I appreciate their help and guidance as I know that my thoughts are sometime here and there and, thus, not always the easiest to follow. But apart from all the professional contributions, all of them became real friends and best-Sekt-buddies. First and foremost, Eva was a huge aid to my work – especially throughout the reviewing phase. Moreover, I also would like to express my gratitude to Alex, Anja, Anna, Annika, Beren, Chris, Daniel, Enrico, Ilka, Isi, Jule, Kathi, Lutz, Mark, Reyk, Stefan, Thommy and Tobias (who can never be named separately), as well as all the rest of the lab folks. Everybody had their part in creating this excellent working environment. And no one was ever mad when I forget to cook again… Thank you all for making our time together pleasant and enjoyable.

Furthermore, I want to thank all our collaborators – especially the people at the Ludwig Boltzmann Institute, namely Heinz, Severin, Wolfgang and the rest of the team. Also the Fraunhofer IWS as well as the TU Braunschweig have a major share in this work, since they supplied me with knowledge and technology. Professor Ute Römisch helped me substantially with creating the DoE schemes. Kerstin Schirmann always had an open ear for my rheological problems. And Philip Saunders was there for grammatical correction. To all of them: thank you very much!

Eventually, my biggest and 'specialest' thanks go to my family. Three and a half years is a long time, which does not always pass by easily. But they made it go easy. In fact, the most beautiful moment was when I married Sybille, who is the most precious person to me – I love you. Thank you for your continued support in the darkest hours and your joy in the brightest. Sybille, my parents and my new family always had my back and even helped me with substantial bits of this thesis. Thank you all – you are the best!